CRANFIELD UNIVERSITY

CHRIS SUNGKYUN BANG

AEROELASTIC ANALYSIS ON A MULTI-ELEMENT COMPOSITE WING IN GROUND EFFECT USING FLUID-STRUCTURE INTERACTION

SCHOOL OF APPLIED SCIENCES
PhD

PhD
Academic Year: 2017 - 2021

Supervisor: Mr Clive Temple
Associate Supervisor: Dr Laszlo Konozsy
August 2021

CRANFIELD UNIVERSITY
PhD

SCHOOL OF APPLIED SCIENCES
PhD

Academic Year 2017 - 2021

CHRIS SUNGKYUN BANG

AEROELASTIC ANALYSIS ON A MULTI-ELEMENT COMPOSITE WING IN GROUND EFFECT USING FLUID-STRUCTURE INTERACTION

Supervisor: Mr Clive Temple
Associate Supervisor: Dr Laszlo Konozsy
August 2021

This thesis is submitted in partial fulfilment of the requirements for the degree of PhD

ABSTRACT

The present research focuses on an advanced coupling of computational fluid dynamics (CFD) and structural analysis (FEA) on the aeroelastic behaviour of a multi-element inverted composite wing with the novelty of including the ground effect. Due to the elastic properties of composite materials, Formula One (F1) car's front wing may become flexible under fluid loading, modifying the flow field and eventually affecting overall aerodynamics. This research investigates the influence of elastic behaviour of the wing in ground proximity on the aerodynamic and structural performance by setting up an accurate the Fluid-Structure Interaction (FSI) modelling framework.

A steady-state two-way coupling method is exploited to run the FSI simulations using ANSYS, which enables simultaneous calculation by coupling CFD with FEA. A grid sensitivity study and turbulence model study are preferentially performed to enhance confidence of the numerical approach. The FSI study encompasses everything from basic examination and measurement of the interaction phenomena using a single and double element inverted wing to the creation of a multi-objective wing design optimisation procedure. The computational results obtained from FSI simulations are assessed and compared with the experimentation with respect to surface pressure distribution, aerodynamic associated forces, and wake profiles. Concerning structure layups, ply orientation and core materials, the effect of various composite structure configurations on the wing performance is extensively studied. An efficient and unique decomposition-based optimisation framework utilising the response surface model is provided based on the aero-structural coupled analysis in order to enhance the wing design process' accuracy and efficiency while tackling aeroelastic phenomena.

Keywords:

Two-way coupling, Aeroelastic tailoring, Response Surface Methodology, numerical solution

ACKNOWLEDGEMENTS

Firstly, I would like to thank my supervisors Mr. Clive Temple and Dr. Laszlo Konozsy for their continuous support throughout my PhD period. Despite the unprecedented first year with bit of turbulence, they kept me encouraged all the time and motivated me to complete this long journey.

I would like to give special thanks to Dr. Zeeshan Rana and Dr. Veronica Marchante for their dedicated support and guidance, sharing their expertise for my project and accepting my relentless meeting requests. I am grateful that I can learn from them not only engineering knowledge, but also mindset as an individual researcher who needs to lead the project on their own.

My gratitude extends to the staff at Cranfield University, especially Dr. Michael Knaggs in IT department for his technical support and advice every time I had issue on HPC. In addition, many thanks to my friends at Cranfield, Laura and Sangjun, for accompanying me on this PhD journey all along and getting through all ups and downs together.

Finally, I would like to thank my family back in South Korea for their encouragement and support over a long period of time. Also, many thanks to my friends, OhBangKimLeeAn in South Korea and Hopeless, in the UK for sharing positive vibes and a lot of fun. Special thanks to my other half, Yoojung, who has provided me endless love and substantial support throughout the study time to pursue my dream.

TABLE OF CONTENTS

LIST OF FIGURES

LIST OF TABLES

NOMENCLATURE

AR	Wing aspect ratio
b	Wing span
c	Wing chord
C_D	Drag coefficient
C_L	Lift coefficient
C_P	Pressure coefficient
E	Young's modulus
G	Shear modulus
h	Wing ride height above ground
P	Pressure
q	Dynamic pressure, $q = 1/2\rho V^2$
Q	Q criterion, second invariant of ΔU
Re	Reynolds number
t	Timestep
U_∞	Freestream velocity
u_{min}	Minimum u velocity component in wake
u, v, w	Velocity components in x, y, z axes system
$u'u', v'v', w'w'$	Turbulent stresses in x, y, z axes system
x, y, z	Cartesian right handed coordinates
y^+	Non-dimensional normal wall distance

Greek Symbols

α	Incidence
δ_{99}	Wake thickness, as measured by 99% displacement thickness
δ_{bottom}	Bottom of wake thickness
δ_{top}	Top of wake thickness

ε	Turbulence dissipation rate
k	Turbulent kinetic energy
ρ	Density
η	Non-dimensionalised span from wing tip
μ	Viscosity
ν	Poisson ratio
ω	Planar vorticity for tip vortex

LIST OF ABBREVIATIONS

CAD	Computer Aided Design
CFD	Computational Fluid Dynamics
CSD	Computational Structure Dynamics
DES	Detached Eddy Simulation
DNS	Direct Numerical Simulation
FANS	Finite Analytic Navier-Stokes
FEM	Finite Element Method
FSI	Fluid-Structure Interaction
GCI	Grid Convergence Index
LDA	Laser Doppler Anemometry
LES	Large Eddy Simulation
LHS	Latin Hypercube Sampling
MDO	Multidisciplinary Design Optimisation
MOO	Multi-Objective Optimisation
PIV	Particle Image Velocimetry
RANS	Reynolds Averaged Navier-Stokes
RNG	Renormalisation Group theory ($k-\varepsilon$ turbulence model)
RMS	Root Mean Square
RMSE	Root Mean Square Error
RSM	Response Surface Methodology
S-A	Spalart - Allmaras
SRANS	Steady Reynolds Averaged Navier-Stokes
SSE	Error Sum of Squares
SSR	Sum of Squares
SST	Total Sum of Squares

1 Introduction

1.1 Background for this research

Aerodynamics began to be included as part of the design process in the aircraft industry. As road vehicles have been developed in terms of speed, aerodynamic performance of the ground vehicles should be taken into consideration at preliminary development stage. In fact, it is of little importance for passenger cars to enhance aerodynamic performance, since other elements appealing to customers such as aesthetic look, might be considered more essential. On the other hand, in the motorsport industry, especially in the Formula One (F1) racing series, one of the primary aspects that has a considerable impact on overall performance of open-wheel racing vehicles is aerodynamics, concerning acceleration, deceleration, and cornering speed. While there is limited space to a certain extent for the development on engine, tyres and other mechanical components in order to improve the car performance, aerodynamics is a factor that engineers can manipulate with for this purpose. Lowering drag, which enhances top speed, or boosting downforce, which increases cornering speed, can improve a racing car's aerodynamic performance. It is important not only to maximise the aerodynamic efficiency by increasing the downforce as well as by diminishing the drag, but also to achieve correct aerodynamic balance of downforce distribution between front and rear [1]. The position of the front wing is modified as the car accelerates or stops owing to suspension movement, resulting in a substantial shift in the amount of front downforce and, ultimately, the car's drivability.

In the past, Formula One (F1) was a pinnacle of motorsport and its technical development. Until aerodynamics in F1 was introduced in 1967 [2], streamlined body was used in aerodynamics but most of performance was achieved from the engine and power improvement. The first inverted wing, directly mounted on the front and rear axles, was introduced in 1968 when engineers realised that the effect of aerodynamics could make the car faster by increasing cornering speed and acceleration and braking performance. However, the following year, the technical regulation changed due to the fatal accident caused by structural failure of the wing mountings [2]. In 1977, Lotus introduced Lotus type 778 with a big breakthrough in aerodynamic development by introducing full ground effect using aerofoil shaped underbody and side skirt seals to produce more downforce. Unfortunately, this idea was replaced with a flat-bottom undertray in 1989 and since then small details of the car started to be focused for aerodynamic improvement.

The front wing of modern F1 racing cars operate in ground effect, which its distance from the ground is typically 70-100mm, producing 25-30% of total downforce [3,4]. As the first component directly involving with the oncoming airflow, the front wing not only produces downforce to push the car to the ground, but also influences the flow going towards downstream components such as undertray, barge boards, and rear wing by controlling it to keep high-energy flow contained with low turbulence intensities. Thus, the flow around the wing is important to understand its characteristic by optimising the wing configuration and to make the most performance out of it.

In 2010, a ‘flexi-wing’ of the Red Bull RB6 was captured in the German GP where the tips of the front wing were bent far closer to the ground compared to others [5]. From the on-board camera, it also showed that the wing becomes lowered towards the ground as the car accelerated and in reverse it comes back to the original position as the car brakes losing speed and the aero load applied to the wing reduces. It was believed that the wing was deflected under fluid loading throughout the speed range in order to contribute to additional aerodynamic benefits such as decreased drag, improved balance, or increased downforce. Since the 1990s, F1 engineers have exploited this phenomenon called ‘Aero Elasticity’ where aerodynamic components, mainly the wings, become flexible and alter flow field characteristics. At the beginning, the whole rear wing assembly was designed to flex and lean backwards to minimise drag by lowering incidence of the wing. However, due to several big accidents during the pre-season testing, the Fédération Internationale de l'Automobile (FIA) introduced bodywork flexibility rules which limit this effect and indicate that the cars are allowed to race as considered legal if passed. Aeroelasticity of the front wing was also exploited not to reduce drag (as the front wing produces little drag), but to increase downforce. Ground effect enhances when the tips of the front wing run closer to the ground. The pressure differential between the wing’s top and bottom surfaces is improved as the endplate approaching to the ground acts like the side skirt seal preserving the airflow within. To prohibit excessive movement of the front wing which might lead to potential accident, FIA introduced additional mandatory deflection test to check how much the front wing is deformed under a certain load applied. As presented about how aeroelasticity has been used in F1

industry, the F1 teams put significant effort to make the most aerodynamic advantage out of the constrained situation given by the regulation so as to maximise the performance.

Several techniques, including wing tunnel tests, computational fluid dynamics (CFD), and track testing, can be used to design the aerodynamics of F1 vehicles. Wind tunnel testing provides for the rapid testing of a range of model variants as well as the measurement of forces and pressures. Furthermore, the flow around components can be visualised for better understanding of its characteristics through several approaches such as Particle Image Velocimetry (PIV) technique, Laser Doppler Anemometry (LDA) system, or flow-viz, all of which are limited, and high cost is expected to use the wind tunnel facility. Thanks to the development of computational analysis technologies in terms of cost-effectiveness and reliability, numerical methods have been exploited more frequently, enabling studying complex flow physics around sophisticated geometries that cannot be captured by experimentation. Therefore, in order to increase comprehension of phenomenon of the aeroelastic behaviour of the wing component described previously, Fluid-Structure Interaction (FSI) concept can be employed, which is defined as a phenomenon where the fluid flow and structural integrity are interactively dependent.

The flow behaviour of a structure is determined by its shape and motion, and the associated structural deformation is determined by the fluid loading applied on it. [6]. Fluid modelling should incorporate a structural analysis as part of the method to characterise the influence of aerodynamic loads on the structure and to improve structural deformation accuracy. In many industries, it has been able

to demonstrate the practicality and effectiveness of performing aeroelastic analysis by means of FSI modelling, which couples computational fluid dynamics (CFD) with computational structure dynamics (CSD)[7–9]. In the motorsport industry, open-wheel racing cars' front wing is generally composed of composite materials due to qualities including lights weight and high specific strength and stiffness and possibility to tailor the loads and aeroelastic behaviour compared to conventional materials such as metal of which stiffness is uniform. It is speculated that a wing constructed of laminated composite materials may include elastic couplings which can be exploited to improve flexible components in line with the regulations such as optimising aerodynamic efficiency of elastic wing. In addition, the effect is probably dependent upon the structural integrity of the composite lamination, for example ply orientation, ply thickness or stacking sequence. Thus, the goal of this study is to exploit the FSI technique to explore the influence of front wing flexibility on aerodynamic performance while taking into consideration the structural properties of composite materials.

1.2 Motivation and methodology

There exist lots of studies that performed extensive investigation into the wing performance in ground effect both experimentally and numerically thanks to its substantial benefit in racing car application [10–14]. However, as opposed to the real situation, those studies regarded the wing as a rigid body where aeroelastic characteristics of the wing was not incorporated. As the design of the flexible front wing is inevitable and widely exploited in the development of F1 racing cars in order to enhance the ground effect and ultimately overall aerodynamic

performance, it is important to investigate and quantify its effect on the performance and to gain profound knowledge of the flow field generated around this flexible component.

In preliminary stage of design process of the front wing of F1 cars, it is necessary to predict level of performance that the wing is able to generate and to optimise its configuration in terms of physical wing geometry and structural parameters. Composite material used to manufacture the wing has the potential to tailor its characteristics such as strength and stiffness by morphing the structural parameters and it can lead to controlling capability of wing deflection, affecting the overall car performance. Hence, it is required to develop an optimisation routine to find a wing configuration that can produce maximum aerodynamic efficiency with the minimum weight.

To the extent of my knowledge, there have been little comparative research obtained to predict accurate aeroelastic behaviour of an inverted multi-element wing in ground proximity considering nonlinear structural characteristics of composite materials. Due to the fact that the aero-structural interaction is too complicated to be dealt with by analytical approach and experiments are limited in scope owing to its strong nonlinearity and multidisciplinary nature, a computational solution should be more relevant to demonstrate better understanding of the associated flow features in this research which are unfeasible to study experimentally.

The current work presented in this thesis can be composed of two parts – analysis and optimisation. The first part focuses on investigation into aeroelastic behaviour of the wings in ground effect and the wings are modelled based on

Zerihan's single element and double element wings [13], which is a representative of simplified version of the F1 front wing. The experimental studies carried out by Zerihan [13] and Mahon [14] can be used extensively to validate computational results. Fluid-Structure Interaction method is chosen to better describe complex phenomenon between flow physics and structural dynamics. The wings are constructed with various configuration of composite laminate structure as it proves to be capable of reproducing nonlinearity of composite material. In the second part, a multi-objective optimisation (MOO) routine is created in order to study the effect of wing configuration and composite laminate structure on the wing performance in ground proximity by utilising a response surface methodology (RSM) in conjunction with Fluid-Structure Interaction modelling.

1.3 Aim and objectives

The flow field influenced by the movement of the elastic wing could have potential to have an impact on the aerodynamic performance in an either positive or negative way according to the literature which will be discussed in the next chapter. The fluid-structure interaction is too complicated to analyse using available resources in the public domain and this study would be an underlying step to evaluate its effectiveness with a help of the Fluid-Structure Interaction modelling which provides comprehensive understanding of the dynamic phenomenon and the associated results. This research aims to assess the aeroelastic behaviour of a multi-element composite wing in ground proximity focusing on a novel coupling of computational fluid dynamics (CFD) and structural

analysis (FEA). Further research will attribute development of a design optimisation process of the composite wing in ground effect considering aeroelastic characteristic. The following objectives are taken into account in order to fulfil the research's goal:

- To perform verification and validation study on the FSI model and numerical method.

- To establish a framework of FSI modelling workflow in connection with high performance computing system.

- To investigate and quantify the effect of aeroelastic behaviour of a single element inverted composite wing in ground effect on aerodynamic performance with regard to surface pressure distribution, aerodynamic forces, and wake profiles in comparison with experiments and non-FSI rigid wing.

- To evaluate and quantify the impact of a double element inverted composite wing's aeroelastic behaviour in ground proximity on aerodynamic performance in terms of surface pressure distribution, aerodynamic forces, and wake profiles in comparison with experiments and non-FSI rigid wing.

- To analyse the influence of ride height variation on the wing aeroelasticity performance of a multi-element wing in ground effect concerning.

- To generate a meta model to be employed for the Response Surface Methodology (RSM) by using FSI modelling.

- To develop a multi-objective optimisation (MOO) process to find a wing configuration that maximises aerodynamic performance and minimised the wing weight under structural constraint in accordance with the technical regulation.

1.4 Scientific contributions and list of publications

The contributions of this study to the knowledge can be summarised as below:

- Quantifying the influence of aeroelastic behaviour of a multi-element wing working in ground effect on structural and aerodynamic performance using the FSI technique.

- Establishment of an FSI modelling framework in connection with high performance computing system to improve computational calculation time.

- Carrying out the grid convergence study and assessing the effect of various engineering turbulence models, uncertainty of numerical solutions could be reduced, and reliability of the associated results increased.

- In comparison with the results of the non-FSI model, the flexible wing,

caused by the structural elasticity under the aerodynamic load, provides changes in the fluid flow field around the wing including the characteristics of the wing tip vortices, leading to affecting the overall wing performance.

- Successful creation of a surrogate model based on the results of FSI numerical analysis using the response surface, considering multiple objectives such as aerodynamic efficiency and structural weight.

- Development of a multi-objective optimisation approach to determine a F1 front wing configuration to achieve maximum aerodynamic efficiency with minimum weight under structural constraint.

- The multi-objective optimisation method was found to be an accurate and efficient way of solving a complicated design problem of aerodynamic components when considering fewer functions over a great number of design variables.

- Bang, C. S., Rana, Z. A., Könözsy, L., Rodriguez, V. M., and Temple, C. (February 7, 2022), “Aeroelastic Analysis of a Single Element Composite Wing in Ground Effect using Fluid-Structure Interaction”, ASME.*J. Fluids Eng.* April 2022; 144(4): 041202.

- Bang, C. S., Rana, Z. A., Könözsy, L., Rodriguez, V. M., and Temple, C. 2022. “Numerical Investigation and Fluid-Structure Interaction (FSI) Analysis on a Double-Element Simplified Formula One (F1) Composite

Wing in the Presence of Ground Effect" *Fluids* 7, no. 2: 85.

1.5 Thesis structure

There are seven chapters in this thesis. The study's background and objectives are described in the first chapter. Previous investigations and literature relevant to this topic of research is reviewed in Chapter 2. The following part, in Chapter 3, presents the framework of the numerical analysis including detailed computational setup for FSI and fundamental theory of optimisation algorithm. It is followed by the FSI analysis on a single element inverted composite wing in Chapter 4. Chapter 5 focuses on a double element inverted composite wing. The next Chapter 6 focuses on a discussion of the multi-objective optimisation routine using FSI coupled modelling. Chapter 7 concludes with a conclusion and recommendations for further research.

2 Literature review

Following the introduction of the background and aim of the study presented, this chapter provides relevant research carried out in the past. The literature review consists of four parts. The first part looks at preceding research on the wing aerodynamics including ground effect experimentally and numerically. The fluid's interaction with the structure is too complex to be analysed and the importance lies in evaluating the individual aspect of the phenomenon. The next section then focuses on the concept of the Fluid-Structure Interaction modelling and aeroelasticity, which has been widely utilised in a variety of sectors including aerospace and marine. It helps to better understand the fundamentals of FSI, its industrial applications, and the coupling methods. Finally, the optimisation methods used for the aeroelastic modelling is reviewed in terms of Response Surface Methodology (RSM) and Multi-Objective Optimisation (MOO), which will be utilised in this study. The final section concludes the chapter with summary of all sections mentioned above.

2.1 Wing aerodynamics

The Formula One car's front wing, being composed of an inverted aerofoil and additional flaps, is considered one of the most important aerodynamic components with respect to generating downforce as well as affecting other aerodynamic elements downstream (wheels, underbody, rear wing, etc). Overall performance might be influenced by small perturbation in the environment.

Therefore, it is crucial to take a look at the flow behaviour around the wing as the first step.

2.1.1 Single element wing

There have been numerous experimental studies investigating the front wing aerodynamics including ground effect. Initially, a single element wing was considered. In 1994, experimental study of the single element wing with variation of ground height was performed at moving ground wind tunnel facility by Knowles et al [11]. It was discovered that with reduction in the height, the pressure on the wing's lower surface rises, implying that the wing induces greater amount of downforce due to the accelerated flow between the wing and the ground. The force reduction effect was not caught as not enough ride heights were studied.

In the same year, comparable studies with symmetric NACA aerofoil were carried out using fixed ground facility by Ranzenbach and Barlow [15]. For comparison, they repeated the experiment the following year using cambered NACA aerofoils in road condition [16,17]. Both cases were successful to capture the force reduction phenomenon. The cambered aerofoil, on the other hand, had a significant larger ground height than the symmetric one. It was discovered that the boundary layer merging reduces the flow velocity under the aerofoil while also increasing the pressure in that area.

Investigation on the aerodynamic characteristic of a single element wing with endplates attached was carried out by Zerihan and Zhang in a moving ground system in a series of studies [13,18–21]. The effect of ground clearance on aerodynamic performance such as surface pressure distribution, sectional forces

and wake surveys were evaluated, and it showed a similar trend that observed by Ranzenbach and Barlow who nevertheless arrived at a different conclusion. The impact of force reduction was connected to the trailing edge boundary layer separation rather than the merging of the two boundary layers [13]. It was discovered that the flow behaviour is not accurately predicted at the low heights [19]. Zhang and Zerihan [18] also studied the centre-positioned wake using a Laser Doppler Anemometry (LDA) system. The wake developed with increasing the ground proximity the force reduction phenomenon is produced by the boundary layer separation according to this study. They assessed vortices generated at the edge of a cambered wing at various ride height using a variety of experimental approaches such as Particle Image Velocimetry (PIV), LDA and surface flow visualisation [21]. It was revealed that the streamwise peak suction position on the lower surface at the endplate edge is where the edge vortex begins to form. The edge vortex created more suction, and because of the lower effective angle of attack, the trailing edge separation was delayed. The vortex became stronger until it reached the maximum, with the size remaining unchanged. At further lower ride heights the vortex began to break down and expanded. The enhancement of force was attributed to the edge vortex existence, which is not the primary cause.

In addition to the experiments mentioned above, the single element wing has also been studied from a numerical approach. Ranzenbach and Barlow performed a numerical analysis on the same aerofoils used in their experiments [15,17]. With a Reynold-Averaged Navier-Stokes (RANS) model in the structured grid, the computation was carried out in a condition of both fixed and moving

ground effect. It was showed that the results with the moving ground produced increase in downforce with increasing the ground proximity. It indicates that the fix ground case did not give accurate results. In order to make a comparison with the experiments, the computational study on the two-dimensional single aerofoil was carried out by Zerihan and Zhang [20]. The two turbulence models, Spalart-Allmaras (S-A) model and the k – ω SST model, were tested in a domain with full structure grid of roughly 30,000 cells. The S-A model accurately predicted general trends in the surface pressure over the whole range of heights, but the wake thickness was overpredicted by both models. Mahon and Zhang [14] extended the previous study further, applying six different turbulence models (i.e. S-A, Standard k – ε, k – ε RNG, Realizable k – ε, Standard k – ω and k – ω SST) in order to investigate the main flow characteristic. The computation domain was created with both structured and unstructured grids. The RANS model was shown to be capable of properly producing variations in the flow field around the aerofoil near to the ground.

Numerical study on a three-dimensional single element wing was conducted to assess the effect of compressibility for low subsonic Mach numbers [22]. Although compressibility of the flow was neglected in most studies, it is evident that the rapidly accelerated flow between the wing and the ground causes compressibility effects, which change the flow and result in dramatically different lift and drag forces than incompressible models. It was discovered that the incompressible simulations underpredict the aerodynamic forces such as lift and drag with increase in Mach number due to the lower density region between the lower surface and the ground. Diasinos performed a computational study on the

impact of the wing span on the single element inverted wing in ground effect [23]. Furthermore, they developed the associated results to investigate the influence of the ground effect on aerodynamic interaction between the wing and a racing car wheel [24]. Both studies were based on RANS modelling and steady-state solutions. As the vortex characteristics were significantly affected by the ground clearance and the wing span, it was shown that the loss of peak downforce with a narrower wing was observed and the wheel lift interacted with the wider wing was markedly decreased with reducing the ride height.

Following the extensive studies on the single element wing experimentally and numerically, they have been limited to a certain test condition of a straight-line. Keogh [25] performed a numerical investigation on the effect of steady-state cornering condition on the flow behaviour developed in the wake of a single element inverted wing in close ground proximity. With the RANS turbulence model, the pressure-based implicit solver was used and compressibility effects at given Mach numbers were negligible. It turned out that the cornering condition causes the change in the pressure distribution near the endplate, resulting in unbalanced strength of the vortices, its vertical position and the overall wing performance. Along with Keoph's research, experimental and numerical studies on the influence of yaw angle on flow structures around a racing car's front wing and nose section in ground effect were conducted [26]. By using three-equation $k - k_L - \omega$ transitional turbulence model, the existence of a laminar bubble could be taken into account along with a steady-state, incompressible and segregated solver. On- and off-surface flow structures were well analysed despite lack of accuracy of capturing the turbulent attachment point. Utilising the equivalent wind

tunnel test single element wing, Roberts researched the impact of the boundary layer transition and Reynolds number dependency on the fundamental flow characteristics [27–29]. With extensive experimental and computational analysis, it was revealed that the force production and flow separation are markedly attributed to different trip positions. Therefore, it was crucial to set a correct placement of the boundary layer trip in order to achieve more accurate representation in a wind tunnel testing.

2.1.2 Double element wing

In Formula one, addition of extra element on the wing can be an option to enhance aerodynamic performance by delaying trailing edge separation. Following the single element wing study, the investigation was thoroughly carried out on the double element wing. It was started by Ranzenbach and Barlow conducting an experimental work on a two dimensional NACA $63_2 - 215$ Mod B aerofoil with a 30% of flap gap at the fixed ground facility [30]. It was observed that additional downforce is obtained compared to that of single element wing and a region of force decrease was captured at large heights. Jasinski and Selig [31] conducted another experiment with the double element wing. The ride height was fixed for 0.3 chord length and the ground was not moving. It was shown two trailing edge vortices at the endplate were created and its size increased with higher flap angle.

Followed by their single element wing experiment, Zhang and Zerihan also investigated the ground effect of a two element wing [32], which is a combination of the single element wing extracted from the previous work [13] with an extra

flap downstream. The results obtained from LDA, PIV and oil flow visualisation presented the surface pressure on both elements and the sectional forces with the ride height variation. The downforce increase was mainly attributed to the main element with a help of significant circulation caused by the flap. As the wing was approached, the downforce increased up to the maximum and fell off due to the vortex breakdown at the small height.

The double element wing in ground proximity was tested experimentally by Mahon [33] with various configurations of flap position and ride heights. Different experimental techniques such as force measurement, PIV, flow viz and pitot tubes were utilised. It was found that the forces generated by a wing with multiple elements in ground proximity were largely insensitive to variation in flap location. However, extreme values of flap gap and flap location resulted in significant reductions in aerodynamic forces (downforce and drag) and pitching moment due to the flap stalling. One of the novel findings in this study was the existence of potential lift limiting mechanism caused by the reversed flow within the lower wake. However, the experiments did not confirm the phenomenon as the results was only concluded from the pitot tube readings. Two edge vortices were captured by the PIV technique. The lower vortex close to inner side of the endplate was stronger than the top vortex at the top outside of the endplate. The feet attached underneath the endplate caused to increase downforce by generating an extra vortex below.

The same model as Mahon's was experimentally tested by Van den Berg [34] with a goal of ensuring and refuting Mahon's hypotheses. In line with Mahon's results, he used the PIV to demonstrate the flow recirculation and observed the

sudden force drop at high ride height due to the vortex breakdown. However, unlike Mahon's idea, he claimed that the cause of reduction in downforce is mainly from the edge vortex breakdown instead of the reversed flow within the lower wake. A region of larger flow reversal occurred as the edge vortex broke down.

Pegrum [35] performed the experiments to investigate the influence of vortices generated by a Formula One (F1) front wing in conjunction with a rotating wheel using flow visualisation, total pressure wake surveys and PIV technique. It was discovered that the vortex strength is attributed to how vortices are merged downstream depending on the right height of the wing. Also, the conclusion lied to the fact that the behaviour of the vortex, such as strength and separation, generated by the F1 front wing are markedly affected by the ground height and proximity to the rotating wheel.

Computational studies have been extensively performed on the double element wing in ground effect. Ranzenbach and Barlow also examined the flow field around their double element aerofoil using variants of the Standard k – ε model in a structured domain including a moving ground [12]. At low ride heights, they only noticed minor variations in downforce, but this did not affect their original conclusion on the cause of force reduction. The influence of various turbulence models was evaluated by Mahon and Zhang [14] using Zerihan's double element aerofoil [32]. Comparing Ranzenbach and Barlow's study, a computational domain consisting of about 200,000 cells was utilised, yielding $y^+ \approx 1$. It was noted that more than 80% of total downforce is generated by the primary element, whereas the flap creates a great deal of drag. With the limited dimensionality, it

was argued that the numerical solution anticipates the boundaries of the wake inaccurately.

Mahon also used a three-dimensional double element wing to undertake a thorough computational examination [33]. The underestimated lower surface suction pressure caused weaker edge vortices and they showed close relationship with the pressure discrepancy between the wing's bottom and upper surfaces. The three-dimensionality helped to better predict the wake profile compared to the two-dimensional result. Gird limitation allowed simulations only to be carried out at small ride heights within the force increase range.

In succession to Mahon's work, the same wing model was numerically studied by Van den Berg [36], focusing on changing the domain for better results. More accurate computational wing model was achieved by scanning the wing data and removing excessively thin trailing edge. The fully structured grid was expanded with 3.8 million cells. As the best alternative, the Spalart – Allmaras turbulence model was selected owing to better prediction and reliability. Consequently, correlation between experiment and numerical solution was significantly improved when compared to Mahon's work. However, the SRANS results failed to converge for a region of $0.158 < h/c < 0.317$ due to limitation to capture unsteady characteristic of flow caused by the vortex breakdown.

Heyder-Bruckner conducted computational study on a double element wing in ground proximity with ride height variation using RANS and Detached Eddy Simulation (DES) [37]. He created a fully structured 3D domain and the finest mesh included 8.7 million cells. The DES produced better prediction of general feature of downforce and breakdown of main edge vortex than that of RANS.

Furthermore, at large heights, the wing generated constant flow field and it turned to show unsteadiness at small heights induced by the main vortex break down. However, the wing downforce was only influenced at higher ride heights before the vortex breakdown occurred. At considerably lower ride heights, the main edge vortex was dissipated further upstream and with great intense.

Table 1 presents an overview of the computational study on an inverted wing under the ground effect condition which has been discussed. It is concluded that three-dimensionality should be included to better predict the influence of the wing tip vortices and the SRANS has limitation to model the vortex breakdown despite accurately representing the surface pressure and velocity profile.

Table 1 Summary of numerical studies on an inverted wing in ground proximity

Author	Ref.	Re-number	Wing	Grid	No. cells	Solvers
Ranzenbach & Barlow	[15]	1.5×10^6	Single/Double	2D structured	3.0×10^4	FANS
Zerihan & Zhang	[13]	4.6×10^5	Single	2D structured	3.0×10^4	SRANS
Mahon & Zhang	[33]	4.6×10^5	Single	2D hybrid	3.5×10^5	SRANS
Mahon & Zhang	[38]	7.9×10^5	Double	2D hybrid	3.8×10^5	SRANS
Van den Berg	[34]	5.8×10^5	Double	3D structured	4.0×10^6	SRANS
Heyder-Bruckner	[37]	5.8×10^5	Double	3D structured	8.7×10^6	SRANS/DES

2.2 Aeroelasticity

2.2.1 Background

Aerodynamic forces are prone to deform and interact with the elastic structure, altering the fluid flow field, which is one of the primary problems when designing sophisticated aero components. It is regarded as aeroelasticity. Aeroelastic phenomena may be defined according to the Collar's triangle of forces shown in Figure 2.1. The three forces, typically dynamic aeroelastic phenomena, are depicted in the inner circles and the sides of the triangle illustrates the interaction between the forces of certain areas of mechanics, such as aeroelasticity. The unidirectional deformation of the structure characterises static aeroelastic events that are free of inertial forces. Dynamic aeroelasticity involving inertial forces, on the other hand, are known for rhythmic feature of structural deformation. Aeroelasticity has traditionally been used primarily in the aerospace sector. However, civil engineering including infra structures and transportation engineering (vehicles) have both benefited from aeroelastic research.

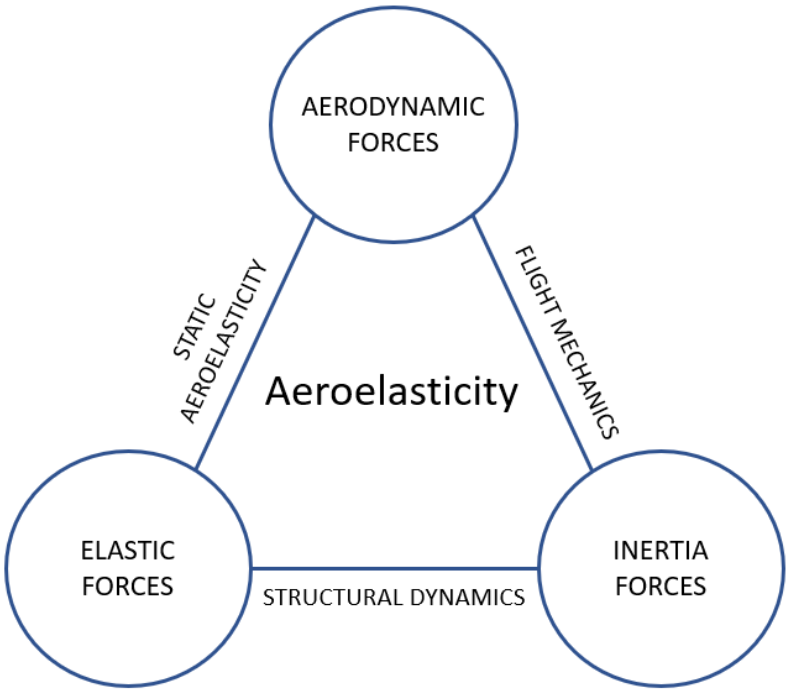

Figure 1 Collar's triangle of forces

2.2.2 Fluid-Structure Interaction (FSI)

2.2.2.1 Overview of FSI

Even though this interaction between fluid flows and immersed flexible structures plays an important role in industry, because of their significant nonlinearity and interdisciplinary character, they are challenging to comprehend [39–41]. It is impossible to acquire analytical solutions to the model equations and the scope of experiments is restricted. As a result, a numerical technique known as Fluid-Structure Interaction (FSI) may be used to explore the underlying physics involved in the intricate interactions between fluids and solid bodies. Furthermore, as computer technology has advanced, scientific and engineering

numerical solutions have become significantly complicated and intricate, necessitating the use of an efficient computational method to solve them.

One of the most important things to consider throughout the aerospace design process is aeroelasticity to avoid aeroelastic problems such as divergence or flutter [42–44]. In wind engineering, in construction of bigger turbines that are more vulnerable to aeroelastic reaction, appropriate FSI modelling of wind turbine blades is critical [8,45,46]. Large blades under aerodynamic loading can cause additional vibration that could result in unbalanced load alteration and instability problems so that ultimately it could have a significant impact on the whole wind turbine system. In the automotive sector, research has been undertaken related to aeroelastic behaviour of car components. Gayland et al. [47] used a one-way coupling to model the interaction of transient flow characteristic with a vehicle hood structure, continuously developing a method that may be used early in the vehicle design process to identify and resolve possible panel vibration concerns. Ratzel and Dias [48] used a coupled transient FSI simulation to investigate a elastic flap at the back of a standard car model. Several flap shape changes that reduced maximum deflection are found and an optimisation routine to find a flap design with the least amount of displacement is accordingly used. Similarly, Patil et al. [49] used a two-way weakly coupled method to simulate an FSI model of a chin spoiler around the airflow. The interplay between the local and global flow fields was modified, and the vehicle drag effect was examined. The numerical results were validated by experiments carried out in a wind tunnel. Andreassi et al. [50] presented an example of FSI approach in the study of a Formula One car

front wing with different speed and angle of attack. However, the ground effect was not applied as the bottom was stationary.

The computational techniques for solving the FSI-related matters may be divided into two categories: monolithic and partitioned approach, which are also known as strongly coupled approach and loosely coupled approach respectively. Strong coupling with matching interface discretisation is a term used to describe monolithic coupling. The solution techniques for both approaches are shown in Figure 2. The monolithic technique utilises an integrated algorithm to solve a single equation which combines fluid and structural dynamics into for the whole problem. The solution technique includes the interfacial conditions. It can be beneficial to improve accuracy for a multidisciplinary problem, but developing and maintaining such a specialised code may necessitate significantly more resources and knowledge [51,52]. The partitioned technique calculates the fluid mechanics, structural mechanics, and mesh movement equations in order. In a typical partitioned coupling algorithm, the fluid mechanics equations are first solved with the velocity boundary conditions derived from the extrapolated structure displacement rate at the interface, then the structural mechanics equations are solved with the updated fluid mechanics interface traction for a given time step. A major benefit of using this method is to utilise existing both fluid and structural solvers. Convergence issues can arise, especially with light structure in heavy fluid, or when the structure is entirely enclosing an incompressible fluid [53].

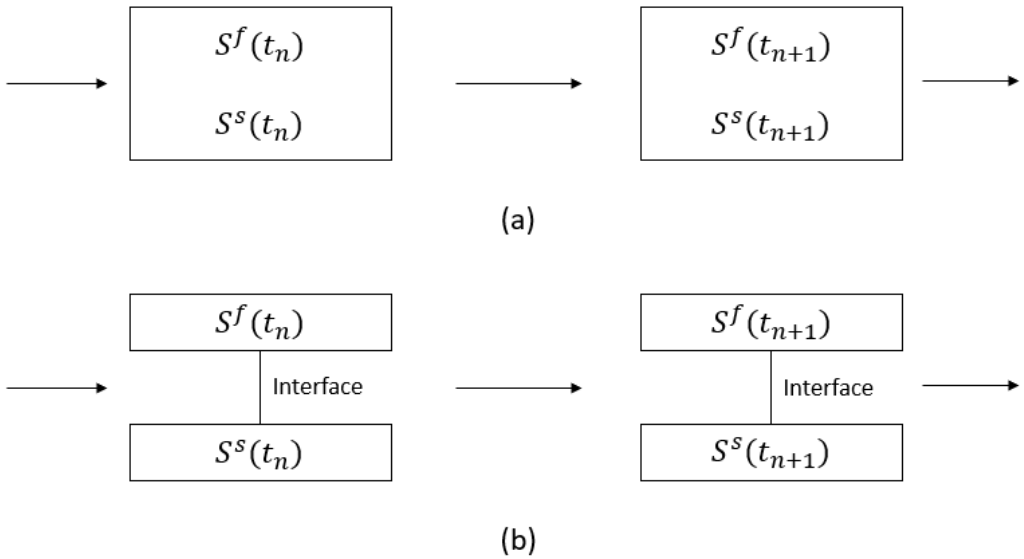

Figure 2 Numerical approaches for FSI problems; (a) monolithic approach (b) partitioned approach where S^f and S^s denote structure system and fluid system respectively

2.2.2.2 FSI in ANSYS

The partitioned method was applied in this investigation using ANSYS package, which is one of the most widely used computational software for purpose of academic research and engineering industry. The ANSYS facilitates the creation of multidisciplinary analyses through ANSYS System Coupling. Multiple separate investigations may be combined via System Coupling, enabling one integrated system to handle diverse solver and other data sources. A study of the combined findings of multiple analyses may demonstrate more complicated interactive phenomenon than an analysis of the results of those analyses separately, which results in increase in accuracy and better results. The schematic steps of the System Coupling analysis in ANSYS is presented in Figure 3 [54]. First, the physics needs to be set up for coupling participants, for example fluid and structure modelling. For each participant, data transfer

variables, regions and coupling related settings are set up to be coupled, which enable a combined analysis. Next, it is necessary to set up the System Coupling for the analysis, specifying iteration settings, and defining data transfers. Once all setups are completed, the System Coupling is used to start the combined analysis, and each solver participated is operated within the system. While running, calculation progress can be kept track of, or the analysis can be paused and restarted. Once the calculation is finished, a review of each solver and coupled analysis results is carried out and the decision make to terminate the analysis.

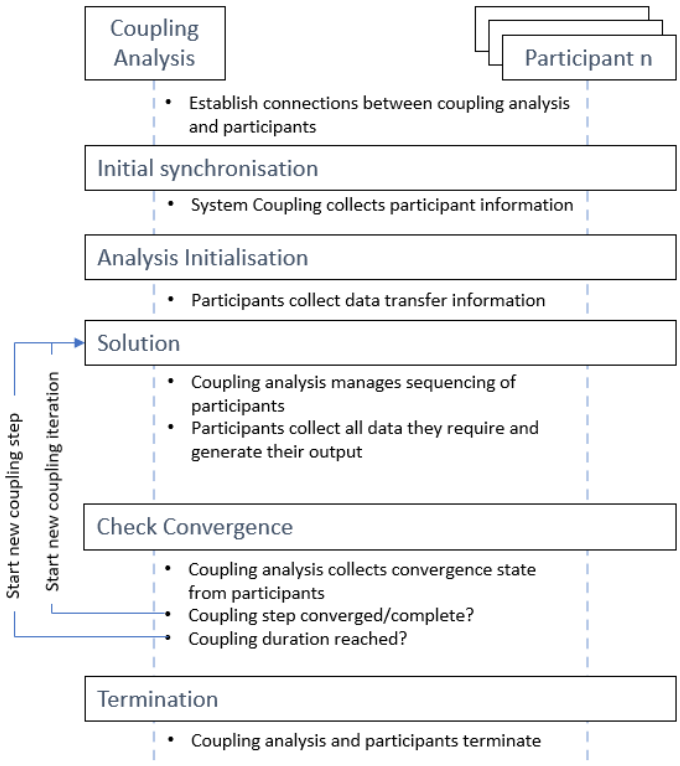

Figure 3 Schematic diagram of ANSYS System Coupling approach

Assessment of convergence of all coupling stages is performed once each literation is finished by providing Root Mean Square (RMS) values for all individual solvers (target side and source side). It is needed that the target side RSM value meet the convergence requirements given in the System Coupling setup input and the required minimum number of coupling iteration is fulfilled. Depending on the convergence status, a fresh coupling iteration can be started, or a new coupling step can be begun up to reaching the convergence criteria. Each iteration is compared to the preceding iteration in order to assess data transfer convergence. Between these two repetitions, the difference in all data transfer values is reduced to a value that has been normalised. The data transmitted has converged when a normalised value produced by two consecutive iterations is less than the convergence objective. The RMS is the standard metric for determining convergence. The range of the normalised value may be adjusted through the input file for System Coupling. The definition of RMS value is shown as:

$$RMS = \sqrt{\frac{1}{n}\sum_{i=1}^{n} \hat{\Delta}_i^{\,2}} \qquad \textbf{(2-1)}$$

Where $\hat{\Delta}_i$ is the normalised change in the data transfer value between successive iterations within/across a given coupling step, and is calculated as:

$$\hat{\Delta}_i = \frac{1}{0.5 \times ((max|\varphi| - min|\varphi|) + |\bar{\varphi}|_{ave})} \Delta \quad \textbf{(2-2)}$$

where φ is the data transfer value. Δ is the un-normalised change between consecutive iterations, and is expressed as:

$$\Delta = \frac{1}{\omega}(\varphi - \varphi_{pre}) \quad \textbf{(2-3)}$$

where φ and φ_{pre} correspond to the current and previous iterations respectively, and ω is the under-relaxation factor that is used to create the final result for the current iteration.

Data transfers between target and source sides during a combined analysis are handled by the System Coupling. The following categories of data are currently managed by the System Coupling: Force, Motion and Thermal. The communication between target and source regions is appropriately achieved to transfer the date from one side to another. For force and motion example for the fluid-structure interaction, the date transfer between each physics is proceeded, where a structure solver is updated with fluid loading from a fluid solver transferred and the fluid solver receives deflection of the structure. By calculating the mesh locations on both target and source sides, all data exchanges in System Coupling are achieved. More details can be found in ANSYS User's Guide [54].

2.3 Optimisation for aeroelastic modelling

2.3.1 Background

In engineering design process, optimisation is inevitably taken into consideration these days. Various mechanical structures aim to be constructed with a goal of less weight and improved strength under reasonable budget. In aerospace industry, anisotropic materials are popular to be used to design aerodynamic components, leading to structural advantage under the fluid loading and it is defined as aeroelastic tailoring. Munk first applied the aeroelastic tailoring concept in propeller blades made of wood [55]. He utilised wood ply laid up in specific orientations so as to exploit the anisotropic properties of the material to twist the blade favourably as the thrust changed. The US Air Force Research Laboratory recently introduced the Variable Camber Compliant wing, of which camber can be adjusted by an actuator [56]. Significant increase in efficiency was achieved employing a continuous and non-stretchable skin where aeroelastic tailoring is applied. The Grumman X-29 aircraft with the forward swept wing was a famous example of aeroelastic tailoring [57]. Despite being sensitive to aeroelastic divergence caused by its unusual structure, adjustment of the wing incidence was achieved by modifying the wing bending and torsion with a help of considerable change in material layers. Without a large weight penalty, the aeroelastic divergence would be prevented [58].

Since then, the aeroelastic tailoring (morphing) ideas have been progressively being investigated in the aerospace industry to improve aerodynamic performance and feasibility. An aeroplane wing, for instance, may reduce fuel

load and extend flight range by optimising its configuration during flight, which results in drag reduction keeping the same level of lift. More efficient aircraft structure design using aeroelastic tailoring alone increases its performance fulfilling the design requirement [59–66] or in combination with structural optimisation [67]. However, the coupled aerodynamic-structural idea should be considered within the design loop to apply to the aeroelastic design. However, inside the design loop, the creation of such aeroelastic design ideas necessitates the consideration of aerodynamic-structure interaction. Composite materials can be good resources for the morphing technique which have benefit to adjust stiffness. The laminate stacking sequence, laminate volume fractions, and ply percentage composition can all impact anisotropic characteristics or elastic coupling terms in composites.

With the aeroelastic tailoring concept used in the aerospace industry in mind, it has been increasingly applied to other industrial sectors such as marine engineering, especially marine lifting surfaces. Compared to the aerospace engineering, the designs of marine lifting surfaces require different considerations due to different governing flow physics. For marine lifting surfaces, cavitation bubble and hydro-elastic instabilities can have an adverse influence on performance and less effectiveness while working in high velocities or near surface conditions. In order to avoid or mitigate cavitation, composite materials have advantages of specific strength, seawater corrosion resistance, and fatigue performance compared to traditional metallic materials.

When operating under off-design circumstances, traditional metallic alloy maritime propellers can experience considerable performance degradation.

Beyond the pre-defined condition, considerable performance degradation of traditional metallic alloy marine propellers can be found. However, using composite materials poses challenges in the design process, as the fluid and structural responses are highly coupled due to the increased flexibility. Hence, the designs of composite lifting surfaces require a more careful consideration and a better understanding of the complex coupling effects [68,69]. In addition, to minimise cavitation and maintain structural integrity while retaining high efficiency, lower aspect ratio of maritime lower surfaces is expected with complicated geometries than that of aerodynamic lifting surfaces. Due to the complex geometry, variation of geometric design for naval lower surfaces is necessary, and the high loading and hence stresses raise the need for coupled hydro-structural optimisation. In order to get the most out of composite materials, the layups need to be optimised with the geometry while considering the FSI and the structural safety. Lin and Lee optimised the stacking sequence of composite propellers with a generic algorithm [70]. With generic algorithms, Plucinski et al. [71] optimised a composite propeller consisting of multiple layers by reducing the disparity of the optimised stationary angle with deflected angle under several flow situations. Recently, the work presented by Liao et al [72] showed a designed hydrofoil by optimising the shape and composite fibre orientation angle using a gradient-based optimisation method with high-fidelity CFD and FEM models.

2.3.2 Optimisation methodology

2.3.2.1 Response Surface Methodology (RSM)

Engineering systems commonly used in modern era are complex and sophisticated. Development of engineering techniques liked with numerical solutions using computation enables to predict more accurate system behaviour and to improve its performance. As a result of enormous computing cost, the numerical technique is unwilling to be utilised in the optimisation design field where a great number of simulations are necessary for optimisation. As a result, the concept with surrogate models is introduced as an efficient solution to reduce the huge computational cost and resources for computer-aided design idea. One of the solutions using the approximation model is Response Surface Method (RSM) and it has become widely attractive in recent engineering sector. Based on the Design of Experiments (DOE) methodology, the RSM is defined to solve an unknown function consisting of design variables and associated result, called response, by computing several experimental points, of which relation can be described using response surface mathematical model [73]. In general, it is difficult to find a mathematical relation between design variables and system output due to complicated interaction such as FSI. Therefore, the RSM offers the benefit of providing a deeper knowledge of each design variable's influence on the system by approximating engineering problems and optimising them with reduced calculation time. One of the recent examples of development using RSM was performed by Jian et al [74]. RSM was exploited to characterise and understand the effect of design changes on the VW Bora upper surface and their interactions. It was found that this approach allows the best possible insight to be

achieved at a minimal effort. Kim et al [75] presented the optimisation of the aerodynamic design of a commercial bus by integrating the Lattice Boltzmann Method (LBM) and the RSM in a transient CFD approach. The RSM was proven to enhance efficiency of vehicle development process when the system was affected by numerous design variables.

In wind engineering, expensive computational power caused by huge number of simulations has been preventing the aerofoil optimisation for the wing turbine blades. Therefore, significant number of studies were carried out using the RSM approach in this field [76–78]. Using a quadratic polynomial equation coupled with the RSM, Li et al [79] proposed improvement of 2D aerofoil optimisation method for the purpose of wind turbine blade. The incompressible Navier-Stokes equations and the RSM were used to investigate the effect of input variables within the design space on a wind turbine aerofoil performance [80]. For the wind blade optimisation, Lee and Shin [81] have enhanced blade design method that uses the second order RSM to evaluate several design factors including horizontal length and blade spanwise angle. The RSM approach allows the engineers to optimise the wind turbine blade out of a variety of design choices in a more efficient and accurate manner.

2.3.2.2 Multi-Objective Optimisation (MOO)

Multi-Objective Optimisation (MOO) has been widely used as a method to optimise mathematical optimisation issues considering several goal functions at the same time. In various industry sectors such as economics, engineering and logistics, MOO has been widely used when optimising more than two objectives

is required with compromise. In aerospace engineering, Multidisciplinary Design Optimisation (MDO) or MOO have been used to increase overall flight performance across a wide spectrum of current wing design [79,82,83]. The aero-structural coupled MDO was used in Kim et al [84] to produce the optimal design of supersonic flight wing over various flight conditions and multidisciplinary results were also presented. In addition, several objectives were taken care of with the weighted-sum method, and they applied the genetic algorithm to determine the weighting factors for better performance. With the fast growth of long-range unmanned aerial vehicles (UAVs), in the early design stage it has become important to consider the coupling of aerodynamic and structural disciplines, since the high aspect ratio wing enhances elastic effect.

In this sense, Long et al [85] carried out a multidisciplinary optimisation for a UAV wing with an extended range. In the first stage, the aerofoil optimisation for performance improvement was conducted and then a 3D wing based on the aerofoil optimised in previous stage was optimised for better performance of aerodynamic and structural aspect. In the second stage, the optimisation including multiple objectives were handled by the coupling technique and scaling factors. As mentioned above, due to its high degree of strength and stiffness, which is one of the important factors in aircraft design, composite material is a fantastic alternative for reducing the weight of aircraft structures. Furthermore, reinforcement of composites using different types of fibre has a lot of promise for attaining acceptable directional stiffness with little weight penalty by optimising the fibre orientations [86]. As a result, the composite wing lamination was optimised to improve aeroelastic effect according to research [87–89]. The

optimisation involving multiple objectives was proposed being subjected to numerous restrictions such as strength, damage tolerance and aeroelastic stability [90]. In this research, Guo et al developed two stages of the optimisation method in accordance with the design purpose. The objective of the first phase was to reduce the weight regarding the ply thickness and wing skin orientation under several constraint. The wing response induced by the gust was dealt with in the second phase.

2.4 Conclusion

The multi-element wing in close ground proximity has been extensively researched in experimental and numerical studies due to its significant performance advantage. However, few comparative studies have been conducted to anticipate the aerodynamic and structural performance of the wing concerning the aeroelastic characteristics. Furthermore, limitations of the FSI modelling approaches have been found in previous studies [91–93], such as that the additional resources required to develop a code for specific problems which may take a substantial amount of time. Focus should also be placed on integration of the separate code into the existing coupling process between CFD and FEA and stability of the correlation of fluid and structural algorithms. The aim of this work was to implement a two-way coupled FSI approach using commercial CFD and FEA solutions to examine the effect of aeroelastic behaviour of a double-element wing operating in close ground proximity on the wing's aerodynamic performance. This would be of great help for engineers to reduce computational resources for solving sophisticated the aero-structural problem as

well as increasing accessibility to the software usage. In order to enhance credibility of the solution and to minimise uncertainty, a grid sensitivity study was performed, followed by a turbulence model study. Numerical results are presented in terms of surface pressure distribution, aerodynamic forces, and wake profile. In the next section, details of the methodology including a modified two-way coupling method are presented that couples the aerodynamic and structural behaviour of a simplified multi-element composite front wing of an F1 vehicle in the context of high performance computing (HPC) using the ANSYS software package.

3 Research description

This chapter introduces a detailed overview of the study in terms of methodology used. Verification and validation study will be performed prior to numerical solutions followed by computational modelling and boundary condition will be discussed. Finally, the strategy and methods used for optimisation will be presented.

3.1 Research outline

This research is conducted based on numerical approach. Considering research continuity with previous studies and research limitation such as available facilities and technological possibilities, experimental results that was achieved from Zerihan's [19] work is used for validation purpose in this study. In addition, the wing model taken from his study is implemented, which is the main factor to be focused on this work. It is important to make some simplifications at the beginning. Firstly, the main focus in this research lies in the wing itself and the fundamental effect of flow characteristics induced by the flexible wing, therefore One of the most essential aerodynamic parts, the front wing, is considered in this research: the rest of aerodynamic components such as front nose, floor and front tyres is not involved. Secondly, considering efficiency of computational resources and time constraints, a symmetrical geometry is taken into account. Also, the yaw situation is not examined in this work, and the flow is considered to be symmetric over the wingspan. As discussed in Chapter 2, numerical studies with the multi-element wing have been extensively performed

considering the turbulence modelling, solver conditions, transition, etc. In spite of importance of representing the real operation conditions in the virtual world, greater focus in this research lies on improvement of accuracy of the numerical results and efficiency of computational calculation. There have been limited resources to be used for validation related to the aeroelastic behaviour of the composite wing operating in ground proximity, for example boundary layer transition and turbulence modelling. Therefore, this research would be a good cornerstone to investigate the influence of the wing flexibility on the wing aerodynamic and structural performance by starting it with fundamental study such as grid sensitivity study and turbulence model study. In addition, in the light of calculation of complicated coupled process between fluid and structure, a steady-state and incompressible solutions are selected to reduce the computational time.

The geometry of the single element wing is equivalent to the models used in Zerihan's experiments. The wing profile is a modified version of NASA GA(W) profile, type LS (1)-0413 MOD. The lower surface of this inverted wing has less camber and lowest point located forwarded which results in gradual pressure recovery. The upper surface is more levelled out so that more pressure could be generated compared to the original one. The wing itself is an 80% scaled model of the 1998 Tyrrell 026 F1 wing. In order to produce analogous effect of three dimensionality compared to the original wing, with an aspect ratio of 4.92, the wingspan is 1100 mm, and the chord length is 223.4 mm, equating to 0.007c. Due to manufacturing reasons, the trailing edge of the wing has a limited thickness of 1.65 mm. A generic rectangular endplate is fitted, of which size is

$250 \times 100 \times 4$ mm. The details of the wing are presented in Table 1 and its configuration shown in Figure 4. The distance between the lowest point of the wing and the ground is defined as the wing ride height, which is one of the most important factors in this research. The wing is tested at various ground heights ranging from h/c = 0.067 to h/c = 0.671 where the experimental data is available, and heights are of interest. As opposed to the height variation, wing incidence is fixed at the reference incident of 1°, which is measured from a line at 2.45° to the chord line.

The single element wing described above as the primary element and the single flap make up the double element wing. In racing car application, the flap is designed in order for increasing downforce within limited design space and its chord profile is not constant across the wingspan; at the tip the extended profile can be found. The identical wing from Zerihan's study is employed in this investigation, where the chord length of the flap is 165.7 mm with a thin region towards the trailing edge and fixed end trailing edge of thickness of 1 mm. The entire chord length from the main element's leading edge to the flap's trailing edge is 380.0 mm and the wing aspect ratio is 2.89. The generic rectangular endplate based on the racing car wing is used with dimensions of $400 \times 170 \times 4$ mm. Detailed dimensions of the wing is described in Table 3 and the schematic configuration of the wing is depicted in Figure 5. The variation of the ride height is also considered in the study on the double element wing with a range of h/c = 0.079 to h/c = 0.592. With the reference incident of 1° of the main elements, the angle of attack of the double element wing from the main element's leading edge to the flap's trailing edge is 5.6°, which is at the lower angle flap position in

Zerihan's study. In his study, investigation on the gap and the overlap of the flap was performed to optimise the flap location for downforce increase. The horizontal space between the trailing edge of the main element and the leading edge of the flap defined the overlap; if the flap's leading edge is positioned upstream from the main element's trailing edge, it is regarded as positive overlap. The perpendicular distance between the trailing edge of the main element and the lowest point of the flap lower surface indicated the gap; the negative gap indicates the flap is positioned beneath the main element and the positive gap is vice versa. As a result of the optimisation, the location of the overlap and the gap was chosen to be at 9 mm and 12 mm respectively, which are used in this study.

Table 2 Dimensions of a single element wing

main element chord	223.4 mm	total chord	223.4 mm
main element angle of attack	1°	span	1100 mm
endplate size	$250 \times 100 \times 4$ mm	wing planform	0.246 m^2
trailing edge thickness	1.65 mm	aspect ratio	4.92

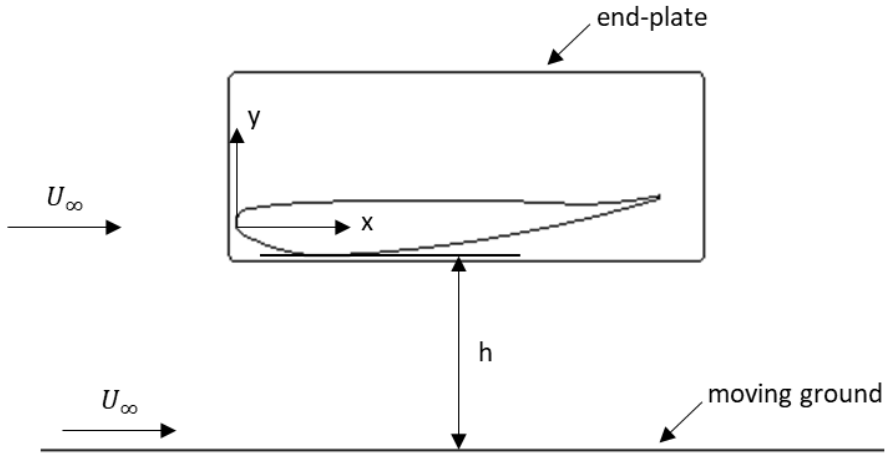

Figure 4 Configuration of a single element wing [1]

Table 3 Dimensions of a double element wing

main element chord	223.4 mm	total chord	380.0 mm
flap element chord	165.7 mm	span	1100 mm
main element angle of attack	1°	wing planform	0.418 m^2
flap element angle of attack	5.6°	aspect ratio AR	2.89
main TE thickness	1.65 mm	flap overlap	9 mm
flap TE thickness	1 mm	flap gap	12 mm
endplate size	$400 \times 170 \times 4$ mm		

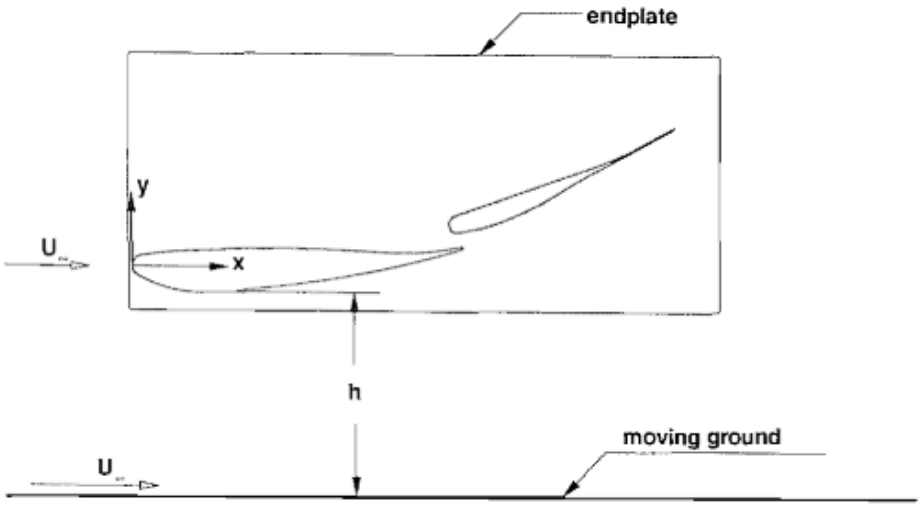

Figure 5 Configuration of a double element wing [1]

Both the single and double element wings are modelled with layers of composite materials in order for structural analysis using the ANSYS Composite PrepPost (ACP) module. It is an efficient way to represent accurate modelling of characteristics of composite structures and to provide an easy access to variation of composite layup properties including mechanical properties, ply orientations and ply properties. The composite materials used in this study are orthotropic carbon fibre-reinforced thermoplastics, which is commonly used in the motorsport industry. Moreover, for further effect of the composite structure on the aerodynamic and structural performance, this research introduces a number of key materials: Nomex and aluminium core, of which detailed material properties are shown in Appendix B. The wings are modelled being composed of different composite materials and various composite structures, which are based on the generic guideline of the ACP as the detailed composite structures used in the

motorsport application were not released in public domain due to confidentiality. Table 4 shows the configurations of the composite laminates utilised for both single and double element wings.

Table 4 Configuration of composite structure used for the inner construction of wings

Wing part	Main Skin	Main Trailing edge	Flap Skin	Flap Trailing edge	Endplate
Material	Woven	Unidirectional	Woven	Woven	Unidirectional
Configuration	$[0/90]_s$ $[45/-45]_s$ $[45/-45]_s$ $[90/0]_s$	$[45/-45]_s$	$[0/90]_s$ $[45/-45]_s$	$[0/90]_s$ $[45/-45]_s$ $[45/-45]_s$ $[90/0]_s$	$[45/-45]_s$

3.1.1 Research plan

The next phases for the study strategy are offered once the broad outline of this research is presented. First, to guarantee that the numerical uncertainty created by the computational solution is within the asymptotic range of convergence, a verification and validation study is carried out. Flexible beam inside two-dimensional flow channel is considered and solved by using various methods such as analytical solution, FSI method in monolithic approach and FSI method in partitioned approach. The details of the study will be presented in the section 3.2. Once the numerical method to be used in this research is verified and validated, a FSI study including the RANS models and the composite

structure is conducted on the single element wing. The goal of a grid sensitivity study is to enhance the quality of simulations and the accuracy of the solution by decreasing grid spacing errors. Turbulence model study is conducted to evaluate suitability of the model for purpose of this research. The influence of various ground heights on aerodynamic performance is studied and compared to the experimental data from Zerihan's study. Moreover, the influence of the composite structure of the wing on aerodynamic and structural performance is assessed and presented. A similar approach is exploited for the double element wing study: Turbulence model study and ground height study.

Once the extensive investigation on aeroelastic behaviour of the wings is completed, an optimisation routine used to develop the front wing is considered in order to enhance efficiency and durability of the design process. Because of the close link and reliance between fluid and solid structures, it is unavoidable to combine the aerodynamic and structural disciplines in the same optimisation cycle. The optimisation loop is divided into two stages: at the first stage, physical configuration of the wing, such as incidence, span length and thickness of composite lamination, is optimised under a certain vehicle operation condition. The second stage focuses on the mechanical characteristics of the composite laminates, ensuring that the previous optimisation's best outcomes are met. In order to find ‘optimal’ solutions to problems that involves more than one physics such as fluid-structure interaction, a Multi-Objective Optimisation (MOO) is used in this study to integrate the individual analysis efficiently and provide the optimum solution which satisfies both disciplines. The optimisation target and operation condition are used to establish design variables, restrictions, and

objective functions. In addition, for better prediction of the engineering problem with increased computational efficiency, the Response Surface Methodology (RSM) is exploited which can create an approximation model of the system based on individual response calculated from each design point within the design space. The optimisation results are analysed and discussed in comparison with the actual FSI simulation results. A schematic overview of the research process and the full description of optimisation methodology shown in Figure 6 can be described in section 3.4.

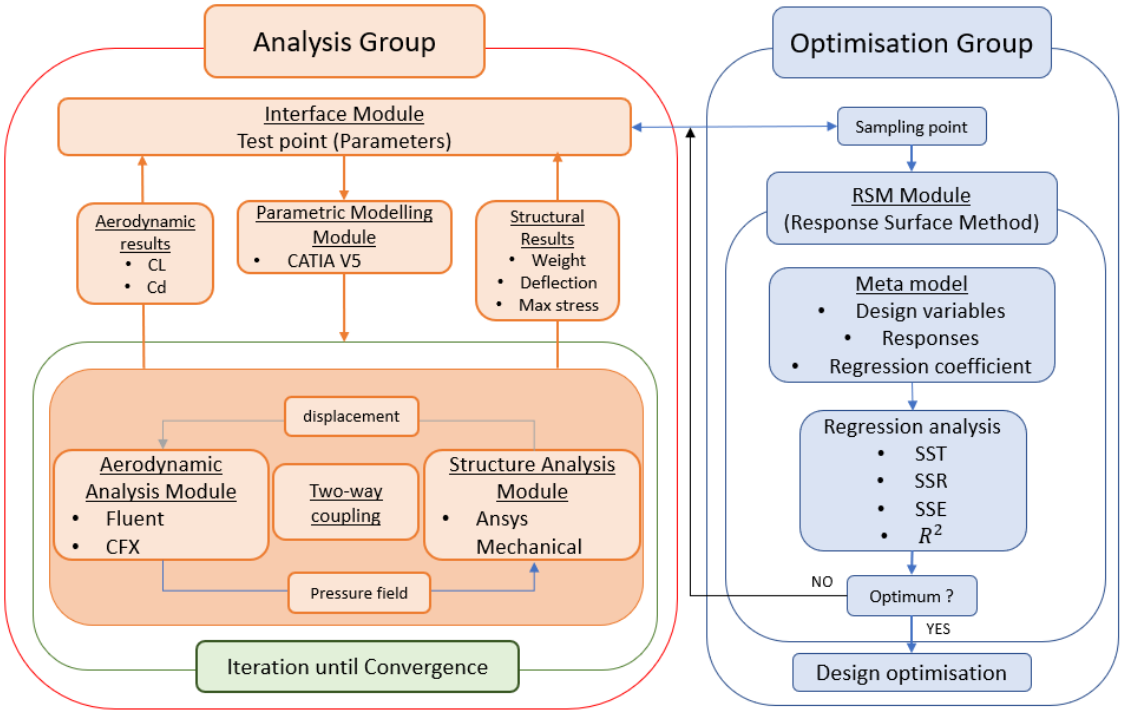

Figure 6 Schematic overview of research plan

3.2 Verification and validation

The numerical approach can be described as being based on approximation and asymptotic solutions, which inevitably produces errors because it is related to discretisation of a series of continuous governing equations. The errors caused by the computational approximation, which is called numerical errors, can also be increased by repetitive simulation cycles and nature of numerical diffusion. Error is a recognisable deficit during computation that is not due to a lack of data (i.e. boundary conditions), whereas unpredictability is a possible deficiency induced by a lack of knowledge [94–96]. The error can be categorised into three types: coding errors, user errors and numerical errors. Coding errors and user errors easily occur most of problems and through use of education and experience they are likely to be identified and reduced. Round-off and convergence errors are two types of numerical errors.

Once the errors and uncertainty are discussed in the numerical solution, it is necessary to introduce a method to evaluate the level of credibility in its results. Verification and validation are one of the most widely used procedures in order to ensure the quality of the solution obtained from the computation is met with requirements and its intended purpose. According to Roache [97], the verification and validation are defined as

- “Verification - this is the process at which it ensures that the mathematical representation of a physical system is solved correctly.”
- “Validation - this is concerned with whether the correct problem is being solved and the model is the accurate representation of the real world from

the perspective of the intended uses of the model."

In numerical modelling, code verification and solution verification may be generally involved [97,98]. Furthermore according to the recent work [99,100], It is said that code verification is separated into two parts: numerical algorithm verification and software quality assurance (SQA) (software quality assurance). By focusing on code implementation accuracy, the numerical algorithm verification ensures that all numerical algorithms are consistent. In the computational codes, this step is critical due to its influence on the numerical accuracy, so it is necessary to prove that the numerical algorithms are carried out accurately and according to plan by assembling a great deal of certified results. SQA addresses a process to ensure that the code is stable and reproducible as a software package, allowing it to deliver results of comparable quality on any computer hardware or system. At the software development stage, the SQA procedure should be considered. Solution verification is also known as computational error approximation since it focuses on determining the numerical precision of a given solution. Two fundamental approaches for the solution verification are *a priori* and *a posteriori* approach. Only knowledge on the numerical methods, as well as the beginning and boundary conditions, are used in an a priori approach. [101–105]. The knowledge from the a priori method is integrated in an a posteriori approach and a series of numerical results from the previous solution. One of the a posteriori estimate methodologies used is the Grid Convergence Index (GCI), which is originated from the Richardson's extrapolation [97,106,107]. The Grid convergence error has been evaluated

using the GCI method and several studies have proven reliability of this method [108–111].

Within the ANSYS package, the Fluent for fluid dynamics and ANSYS Mechanical for structural dynamics are employed in this work, which are one of the most widely implemented computational tools on the numerous engineering problems. It can be apparent to verify that this commercial code's numerical algorithms are dependable and sturdy to provide high accurate solutions and the code is functioning correctly. Moreover, it is proved that the software itself have been constantly developed by a great number of users and ANSYS, demonstrating its reliability and repeatability. Therefore, the GCI method will be only considered in this study.

Once the numerical code including the numerical algorithm implemented is verified, As illustrated in Figure 7, it is important to compare the computational simulation to the experimental data. As a result, it leads to measuring the numerical error caused by numerical solution and determining uncertainty from experimental results.

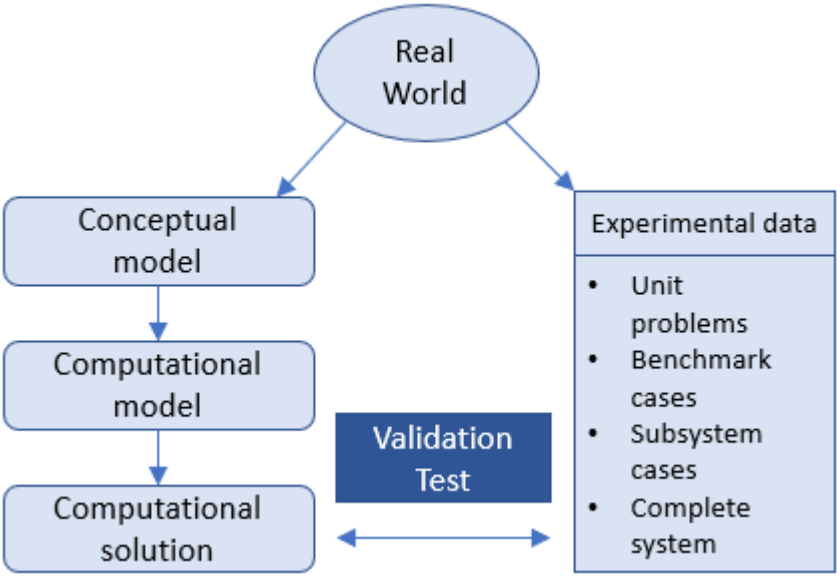

Figure 7 Validation process [112]

As a result of the fact that accurate validation experiments are impractical on most of complex engineering systems, a building block, so-called validation hierarchy approach, is recommended. The major goal of this technique is to help simplify the complexity of the issues, identify feasibility of a variety of experiments, and decompose linked engineering physics by separating the engineering system into three tiers: subsystem cases, benchmark cases, and unit problems [113–116]. This tier method demonstrates that validation studies may be conducted at a variety of levels of engineering processes, and it tackles a validation issue involving tiers that are next to one another. In this study, the validation experiment will be carried out in unit system due to lack of the experimental resources available in public domain for the intended application.

Prior to discussion about the main aero-structural problem, it is required to perform a study to ensure the credibility of the numerical approach to be implemented to carry out the research on fluid-structure interaction with regards to the numerical accuracy. The problem used in this verification and validation study is depicted in Figure 8. A flexible beam is placed inside a two-dimensional channel flow in laminar condition. The channel length is 10 m, and the height is 2 m. The beam positioned in the channel is 2.3 m away from the entrance, with a width of 0.4 m and a height of 1.2 m. The head of the beam is semi-circle with the radius of 0.1 m.

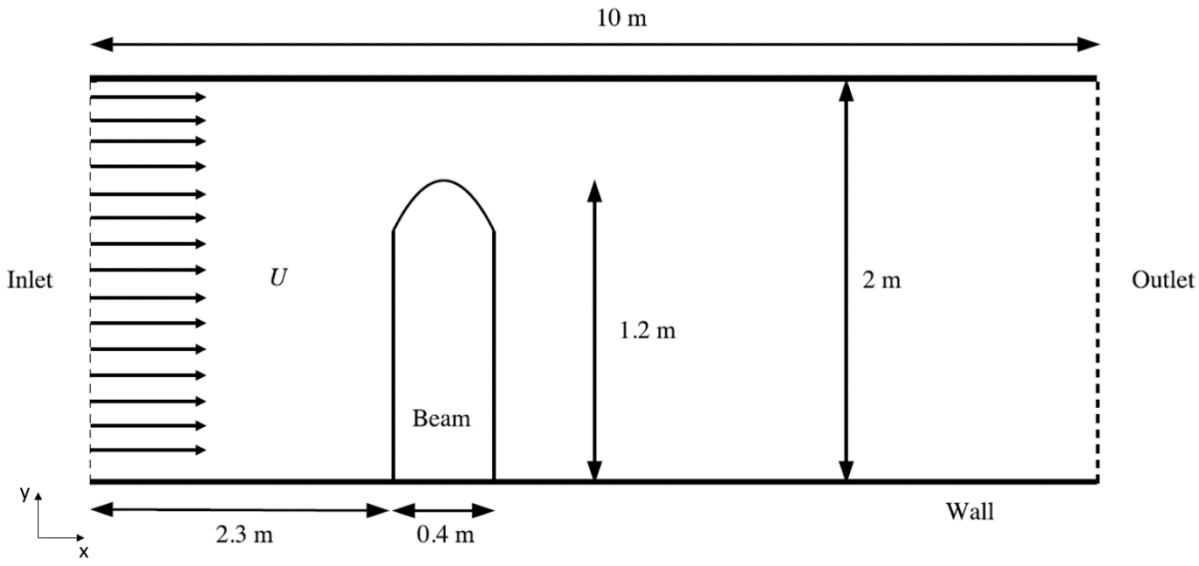

Figure 8 A schematic diagram of a flexible beam in a two-dimensional channel flow

Table 5 lists the fluid and structural parameters that will be used in the investigation. Note that the Reynolds number, referred to velocity and characteristic length, is 20, which confirms that the flow is laminar. The boundary

condition imposed on the inlet is a uniformly distributed flow and outflow condition for the outlet. On the top and bottom walls of the domain, no slip conditions are applied. The surfaces around the beam are defined as a Fluid-Structure Interaction (FSI) boundary where data transfer between the fluid and structure solver will occur as well as the mesh adapting algorithm will be updated accordingly. The beam is modelled with unrealistic material properties for better understanding of the interaction procedure as the real properties are likely to cause turbulence development and low deflection of the beam. Finally, because the flow velocity is relatively modest, the situation is deemed to be incompressible.

Table 5 Boundary conditions of the verification and validation model

	Parameter	Symbol	Value
Fluid	Flow density	ρ	1 kg/m3
	Flow viscosity	μ	0.1 Pa s
	Velocity	U	1 m/s
	Reynolds number	Re	20
Structure	Young's Modulus	E	500 – 10000 Pa
	Poisson ratio	ν	0.3
	Density	ρ	1000 kg/m3

As the verification and validation study, the problem presented above will be solved with three different approach: analytical solution and two software packages, Elmer and ANSYS. The numerical results obtained from Elmer and ANSYS will be assessed to evaluate the numerical accuracy as comparing with the analytical solution. The detailed specification of the study is presented in Appendix A.

3.3 Numerical methodology

In this study, numerical solution was used as main approach and it can be categorised into three aspects: the fluid dynamics, structural dynamics, and fluid-structure interaction. The next sections will go through the specifics of each category.

3.3.1 Fluid Dynamics

3.3.1.1 Mesh generation

The first thing to be considered in the applied CFD is to generate computational domain and discretisation process. The discretisation procedure determines where computations in the fluid domain should be performed. Both single and double element wings used in Zerihan's experiments [19] are modelled with the aid of Computer Aided Design (CAD) software package ensuring the geometry accuracy. The computational grid is generated using ICEM CFD in ANSYS and Figure 9 presents the domain meshed for both wings. Only half of the model is discretised due to the symmetry condition applied at the wing centre plane. At varied ride heights, a multiblock hybrid mesh with both structured and unstructured grids is created, and the relative grid topology and structure are preserved. Prism layers are used to properly reproduce the boundary layer of the wing and the moving ground, and an unstructured tetrahedral mesh is used to construct the rest of the domain. Refinement is applied on areas of interest. For accurate investigation of the wake profile, additional structured fine density box is positioned directly downstream the trailing edge of the wing. The first height cell within the boundary layer blocks of the wing and the ground is calculated and

set as y+ ≈ 1 to ensure a good level of grid quality. Grid sensitivity study is performed at an arbitrary ground height in order to increase credibility and accuracy of results regardless of the grid spacing. A coarse grid of 4.7 million cells, a medium grid of 9 million cells, and a fine grid of 17 million cells are created. According to the findings of the study, which are described in the next chapter, the medium grid is chosen for all fluid simulations. The overall number of cells varies somewhat depending on the ride height, with the bulk being located between the wing's trailing edge and the wake box. Once meshing the domain is completed, it is exported to Fluent for further process.

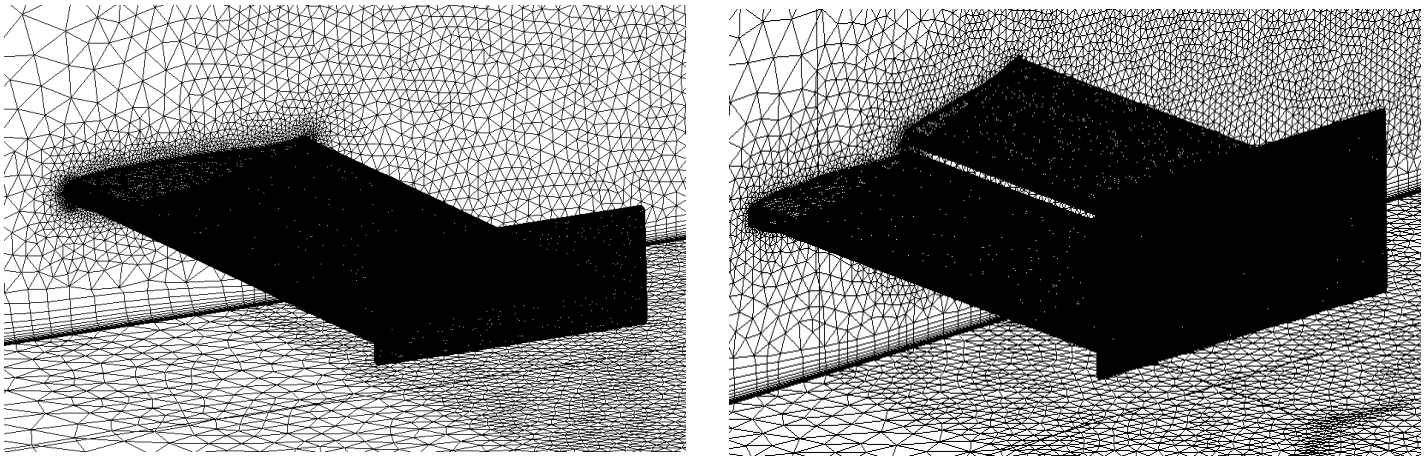

(a) (b)

Figure 9 Three-dimensional computational domain (a) single element composite wing (b) double element composite wing

3.3.1.2 Boundary conditions

The fluid domain, comprising the boundary conditions and the location of the wing model, is created as illustrated in Figure 10 to replicate the experiment

setting utilised in Zerihan's study. The upstream boundary located upstream 5c from the leading edge is modelled applying a velocity inlet boundary condition with 30 m/s uniformly distributed freestream in positive streamwise direction. 0 Pa gauge pressure at the pressure outlet boundary is used to represent the downstream boundary, which is located 15c downstream from the trailing edge. To imitate the wing and the ground, no-slip condition on the wall is utilised. In addition, to depict a moving ground, a tangential velocity of the ground is set as being equal to the freestream (30 m/s). The remainder of boundary conditions are modelled as a symmetry condition to impose zero crossflow condition and to remove the requirement of additional boundary layer resolution [94,117].

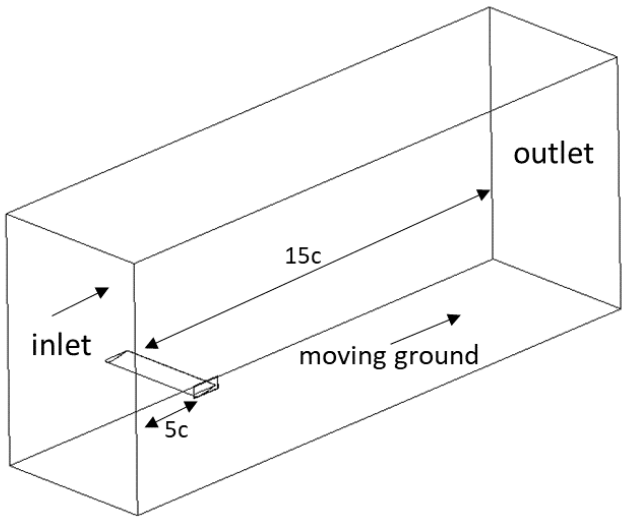

Figure 10 A schematic diagram of computational fluid domain for the single element wing

3.3.1.3 Solving stage

Once the fluid domain is constructed with the ICEM CFD, it is imported to the Fluent, which is a CFD package in ANSYS to enable to deal with a variety of flows. The manual has further information [118]. The single precision option is selected as less computational resources are required and similar results are achieved in comparison with the cases calculated with the double precision.

The Navier-Stokes equation may be used to explain fluid motion with the Newton's second law to fluid motion and incompressible fluid motion may be defined using the continuity and momentum equations in equations 3-1 and 3-2.

$$\frac{\partial u_i}{\partial x_i} = 0 \tag{3-1}$$

$$\frac{\partial u_i}{\partial t} + u_j \frac{\partial u_i}{\partial x_j} = -\frac{1}{\rho}\frac{\partial p}{\partial x_i} + \nu \frac{\partial^2 u_i}{\partial x_j \partial x_j} \tag{3-2}$$

where x_i represents the Cartesian coordinates (i = 1, 2, 3), u_i represents the velocities and p represents the static pressure. ρ and ν are the density and kinetic viscosity respectively and they remain constant since incompressible flow is assumed.

In order to model the effect of turbulence and calculate the Reynolds Stresses, the Reynolds-Averaged Navier-Stokes (RANS) equation is used in this research due to non-linearity of the equation and high-cost computing resources [101]. In

addition, FSI is coupling method between CFD and CSD so most of FSI used in many industries is performed with the RANS modelling. Time accurate solution is not required as it is in steady state condition. The Navier-Stokes equations are averaged in terms of turbulent fluctuations to obtain the RANS equations [102]. The velocity and pressure components are defined by decomposition as

$$u_i = U_i + \acute{u}_i, \quad p = P + \acute{p}, \tag{3-3}$$

where U_i and $\acute{u}_i$ represent the mean and fluctuating components. Based on the equation 3-3, the RANS equations can be obtained as

$$\frac{\partial U_i}{\partial x_i} = 0 \tag{3-4}$$

$$\frac{\partial U_i}{\partial t} + U_j \frac{\partial U_i}{\partial x_j} = -\frac{1}{\rho}\frac{\partial P}{\partial x_i} + \frac{\partial}{\partial x_j}\left(\nu \frac{\partial U_i}{\partial x_j} - \overline{\acute{u}_i \acute{u}_j}\right) \tag{3-5}$$

The instantaneous Navier-Stokes equations are comparable to them, however the averaged variables are represented and the Reynolds stresses term $\overline{\acute{u}_i \acute{u}_j}$ are added to define the effect of turbulence [94]. In many industrial applications, the RANS technique is the most commonly employed method for solving the turbulence model, which is in steady-state condition and calculates only its

greatest scales of turbulence flow [101]. Wall functions can be employed to better understand the turbulence near the wall. In this study, the flow field surrounding the wing model is studied using several turbulence models, which are perturbed by structural features in terms of surface pressure distribution, aerodynamic forces, and wake characteristics.; the one equation Spalart-Allmaras model [119], the standard k-ε model [120], the standard k-ω model [121], the k-ω SST model [122], the k-ε RNG model [123], and the Realizable k-ε model [124]. All k-ε variations receive Enhanced Wall Treatments.

Numerical analysis for all CFD simulations is performed with the implicit segregated solver using the RANS equations and is calculated in connection with a centralized Linux-based cluster. Upwind discretisation scheme satisfied with second order accuracy is used for all cases in order to interpolate the variables U_i, $\tilde{v}$ while the grid is discretised. The pressure interpolation is conducted with a second-order method, and the pressure-velocity coupling is performed with the Coupled algorithm, which is considered compatible well with the FSI application of coupling with the structural analysis. The RANS simulations use the inlet condition to initialise the flow and the solution is completed until it reaches the convergence where the residuals and coefficients of aerodynamic force are stabilised at a predetermined value.

Once the simulations were converged, the data is exported from the Fluent and transferred to the CFD-Post for post-processing. The first thing to be considered in the post-process stage is to organise and analyse the data in order to compare it with the experimental data.

3.3.2 Structural Dynamics

3.3.2.1 Mesh generation

The structural analysis employs both the single and double element wings mentioned in section 3.1. Only half of the wing is meshed by ANSYS Mechanical under the symmetrical condition to save computational resources. On the wing, three alternative meshes are utilised and examined in order to decrease the numerical error produced by the computational solution. The coarse mesh is selected, and the details of the study is presented in the next chapter.

3.3.2.2 Modelling of materials

To demonstrate the aeroelastic impact of the wing, orthotropic materials (composite) are used to create the wing structure. Continuous or discontinuous fibres inserted in a matrix make up composite materials. Because of the directional nature of these fibres in the ply, the mechanical characteristics of the composite construction are directional dependent.

The stiffness and strength qualities of composite materials are dependent on the orientation of the fibres in the laminate, which is a unique feature of composite materials. When loaded, these materials behave in a way that is distinct from that of isotropic materials. In this study, the stiffness characteristics of composite constructions made of orthotropic materials are calculated using the classical lamination theory. According to Kollar and Springer [125], the laminate stiffness matrix for a thin ply with unidirectional fibre is defined as presented from the equation 3-6 to 3-8.

$$A_{ij} = \sum_{k=1}^{N} \left(\bar{Q}_{ij}\right)_{(k)} (z_k - z_{k-1}) \quad \textbf{(3-6)}$$

$$B_{ij} = \frac{1}{2} \sum_{k=1}^{N} \left(\bar{Q}_{ij}\right)_{(k)} (z_k^2 - z_{k-1}^2) \quad \textbf{(3-7)}$$

$$D_{ij} = \frac{1}{3} \sum_{k=1}^{N} \left(\bar{Q}_{ij}\right)_{(k)} (z_k^3 - z_{k-1}^3) \quad \textbf{(3-8)}$$

The laminate membrane and bending stiffness are represented by the matrices [A] and [D], respectively, while the coupling stiffness is represented by the matrix [B]. Therefore, these three matrices represent the reaction of a laminate to in-plane forces and moments and define the stiffness of a laminate in various directions.

The ANSYS Composite PrepPost (ACP) module is used to construct the layered composite structures concerning material behaviour, ply definitions, and orientations of fibres. In the motorsport application, carbon fibre reinforced plastic (CFRP) is the most commonly utilised material because to its high strength and rigidity combined with its competitively light weight. Carbon fibre composite are mainly used in this investigation, and the details of their mechanical properties are presented in Appendix B.

3.3.3 Fluid-Structure Interaction

Fluid-structure interaction (FSI) is the shared contact between a deformable structure and an interior or surrounding fluid flow [126]. The fundamental consideration when developing a numerical simulation algorithm is the choice of appropriate governing equations of the continuum, which determines relationship between the deforming structure and fluid domain and ability of numerical method to deal with large distortions [127]. Based on the design type of scientific and engineering systems where fluid-structure interaction is concerned, different approaches of numerical procedure may be employed. One of the ways for solving these multi-physics issues may be divided into two categories: monolithic and partitioned approaches. A single solver is used to solve the monolithic method, which contains governing equations for fluid and structural dynamics inside a single mathematical framework [128,129]. This technique can yield higher accuracy for interdisciplinary issues; but developing a code for a specific mix of such problems may take a substantial amount of time. The partitioned approach, on the other hand, solves the governing equations of fluid and structure dynamics separately with two separate solvers [130]. By combining previously accessible codes or numerical methods that have been proven and utilised for complicated FSI issues, this methodology allows for faster code creation. The focus, however, should lie in correlating the fluid and structure algorithms in order to achieve stability of the coupling method. As shown in [127], the coupled FSI model can be represented by the equation 3-9.

$$\begin{bmatrix} M_s & 0 \\ \rho_0 R^T & M_f \end{bmatrix} \begin{Bmatrix} \ddot{U} \\ \ddot{P} \end{Bmatrix} + \begin{bmatrix} K_s & -R \\ 0 & K_f \end{bmatrix} \begin{Bmatrix} U \\ P \end{Bmatrix} = \begin{Bmatrix} F_S \\ F_f \end{Bmatrix}, \quad \textbf{(3-9)}$$

where M_s and K_s represent the structural mass matrix and structural stiffness matrix and U, $\ddot{U}$, F_s represent the nodal displacement, the second derivative of nodal displacement and the structural load vector, respectively. In the same manner, M_f and K_f represent the fluid mass matric and the fluid stiffness matrix, and P, F_f, $\ddot{P}$ represent the nodal pressure, the second derivative nodal pressure and the fluid load vector, respectively. R is the fluid structure interaction interface's coupling matrix.

Pressure loads induced by the fluid are exerted on the structure, causing it to deform, at the same time, the fluid geometric domain is updated considering the structural deformations. In the partitioned approach, the information acquired from each numerical technique is exchanged at the fluid structure interface, which is reliant on one-way or two-way coupling mechanisms as illustrated in Figure 11. In one-way coupling, the calculated fluid forces from CFD analysis are transferred to the structure analysis as the boundary condition and the deformation of the structure is computed until convergence is achieved. as shown in Figure 11 (a).

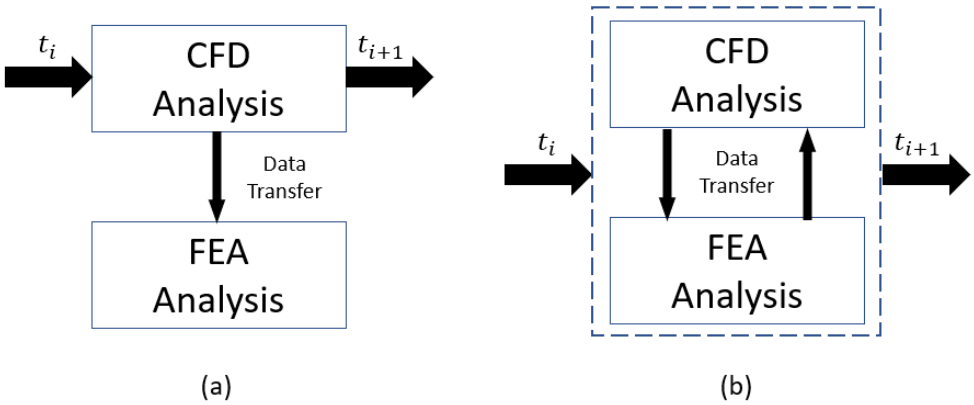

Figure 11 FSI coupling methods (a) one-way (b) two-way

In the two-way coupling technique, on the other hand, CFD solver is utilised to calculate the fluid field until the convergence requirements are fulfilled. The CFD-derived pressure loads exerted on the wing are transferred to the structural analysis as force. Then a FEA analysis is simulated to calculate the structural results including deflection and maximum stress and strain induced by aero loadings, which are subsequently interpolated into the fluid mesh. This is considered a single internal routine, and the loop continues until the iterative output value is reached below a specified threshold of tolerance, as illustrated in Figure 11 (b). This research employs the two-way coupling partitioned approach in ANSYS software to solve the FSI problem of the composite wing in ground proximity, as illustrated in Figure 12.

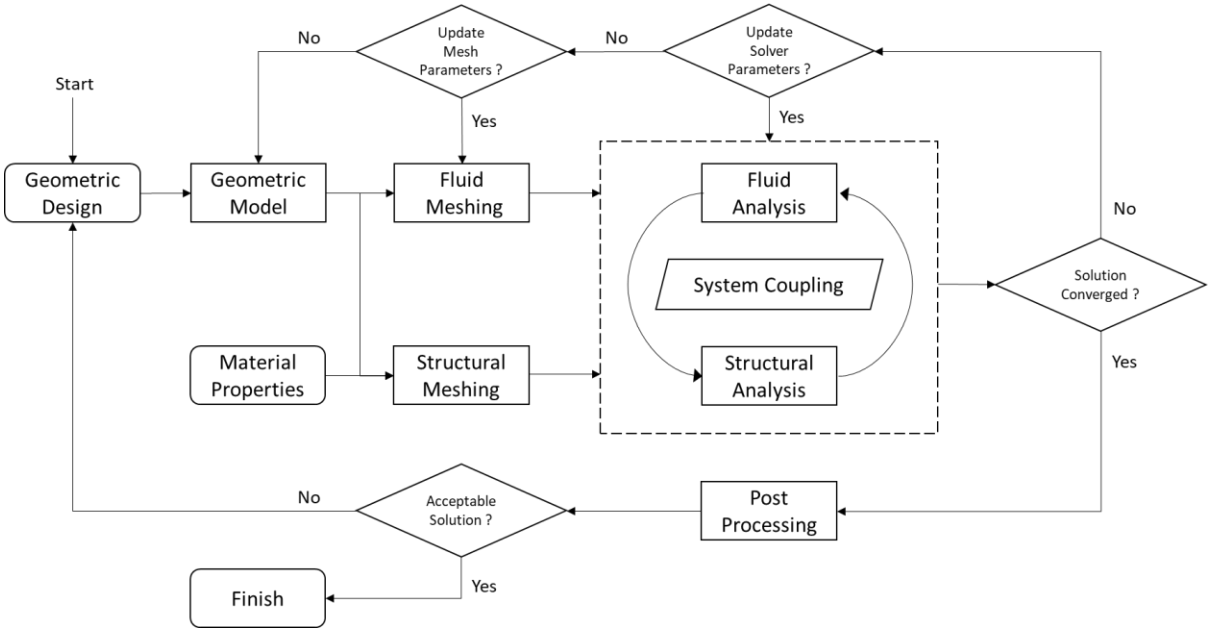

Figure 12 Workflow of fluid structure interaction system

3.4 Optimisation methodology

In this section, an optimisation algorithm to be used to achieve optimum wing performance pertaining to both aerodynamic features of the wing and structural design variables of composite structure is outlined. The details of each process will be discussed in the following.

3.4.1 Optimisation strategy

The method and operation of a design or system to offer improvement in some intended sense, based on the application, is characterised as the core concept of optimisation [131]. In the motorsport industry, at the early stage of wing development, it is critical to estimate wing performance with high precision so that labour and materials needed to build the wing model for wind tunnel testing may be minimised. With the advancements of the computational technology, the numerical approach using the FSI modelling enables to provide better estimation of the wing aerodynamics combined with the non-linear wing composite structure. Taking advantage of the coupling method for analysing the wing in ground effect, an integrated optimisation approach can be developed to solve such an aero-structural problem. Following the optimisation techniques reviewed previously, the optimisation algorithm developed in this research is integrated with several optimisation methods which are widely used in many industrial applications, so that it could be suitable for the purpose. Figure 13 shows overall process of the optimisation algorithm, which has two main stages: Response Surface

Methodology (RSM) and Multi-Objective Optimisation (MOO). Each stage is described in consecutive sequences.

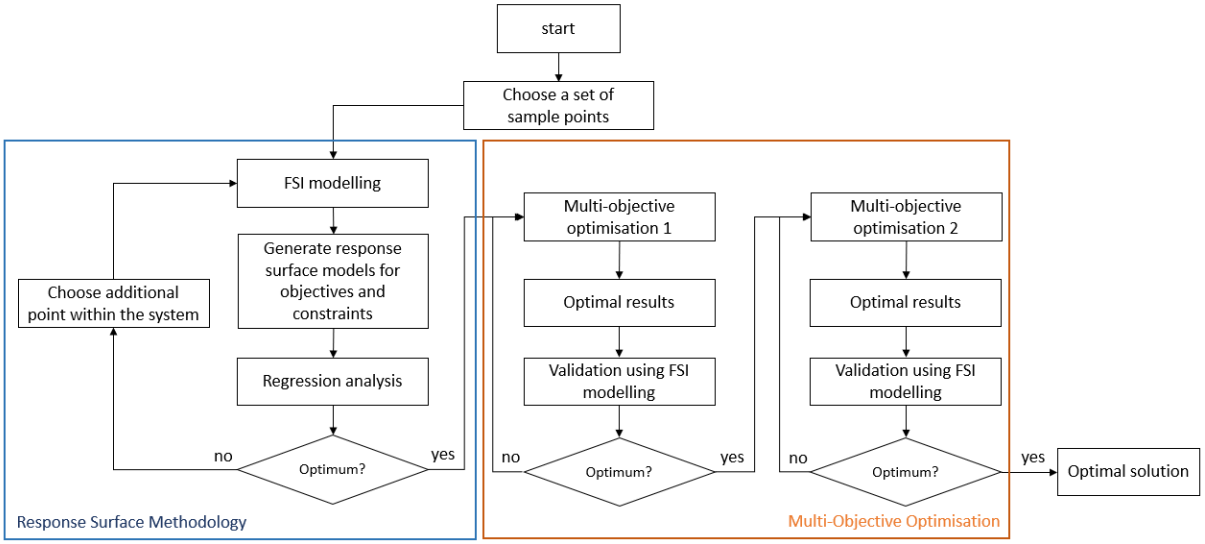

Figure 13 Flow chart of overall optimisation framework

3.4.2 Design of Experiments (DoE)

Response Surface Methodology (RSM) is a method to approximate the responses in the engineering system by calculating a function value corresponding to each independent variable in the design space [132]. Response surface, which consists of a group of the responses, is created resulting from the numerical simulations at a number of variables defined by Design of Experiments (DoE) technique [133]. DoE is a statistical method to determine the number of sampling points and their distribution within the design space so that it can maximise extraction of the amount of information required by operating the least number of calculations possible [134,135]. Effective strategy for using the DoE is

one of the key factors to create an accurate the response surface model. The objectives of the experiment need to be set prior to the DoE, followed by selecting the design variables and design space [136]. Once those parameters have been determined, a test may be run to determine the impact of changing input variables on output responses, as well as to find relationships among a variety of design factors and, ultimately, the engineering system's overall behaviour. There are a great number of sampling techniques existed and Latin Hypercube Sampling (LHS) commonly utilised engineering approaches is employed.

3.4.3 Response Surface Methodology (RSM)

Once the sampling points are selected by the DoE, six design variables are used to calculate the output responses in order to create the response surface model. Complex engineering problems including more than one independent variable such as FSI problems require a great deal of computational time and resources when carried out. Furthermore, it is an expensive process to properly setup, run, post-process and debug a single simulation. As a consequence, it can be apparent that the RSM may be appealing to reduce duration of design and development and to increase efficiency of the process. Generally, linear, or quadratic polynomial equations are presumed to be able to provide accurate response values. This is certainly not applicable for all engineering systems, however cubic and high order polynomials are not recommended due to high cost of RSM calculations and convergence insufficiency caused by more than one inflection point [137].

If n_s analyses are performed and $p = 1, \cdots, n_s$, a quadratic response surface model is characterised as

$$y^{(p)} = c_0 + \sum_{1 \le j \le n_v} c_j x_j^{(p)} + \sum_{1 \le j \le k \le n_v} c_{(n_v - 1 + j + k)} x_j^{(p)} x_k^{(p)}, \quad \textbf{(3-10)}$$

where $y^{(p)}$ is the response; $x_j^{(p)}$ and $x_k^{(p)}$ are the n_v design variables; and c_0, c_j, and $c_{(n_v-1+\mathrm{j}+\mathrm{k})}$ represent the regression coefficients. There are $n_t = (n_v + 1)(n_v + 2)/2$ coefficients in the quadratic polynomial equation. In matrix notation, this polynomial model is represented as

$$y^{(p)} = c^T \bar{x}^{(p)}, \quad \textbf{(3-11)}$$

where c represents the vector of length n_t of unknown coefficients to be calculated,

$$c = \left[c_0, c_1, \cdots, c_{n_t - 1}\right] \quad \textbf{(3-12)}$$

And $\bar{x}^{(p)}$ represents the vector of length n_t corresponding to the form of the $x_j^{(p)}$ and $x_k^{(p)}$ terms in the polynomial model presented in the equation 3-11.

Estimating the regression coefficients necessitates n_s analysis, where $n_s \geq n_t$. In these circumstances, the estimate issue may be written in matrix notation as

$$y \approx Xc, \tag{3-13}$$

where y represents the vector of n_s observed response values,

$$y = \left[y^{(1)}, y^{(2)}, \cdots, y^{(n_s)}\right] \tag{3-14}$$

And X represents the matrix formed by the p row vectors $\bar{x}^{(p)}$ which is assumed to have rank n_t. Thus, X may be described as

$$X = \begin{bmatrix} 1 & x_1^{(1)} & x_2^{(1)} \cdots & (x_{n_v}^{(1)})^2 \\ \vdots & \vdots & \vdots \ \ddots & \vdots \\ 1 & x_1^{(n_s)} & x_2^{(n_s)} \cdots & (x_{n_v}^{(n_s)})^2 \end{bmatrix} \tag{3-15}$$

The least square method can be used to solve the equation 3-15 in the form of the equation 3-16.

$$\hat{c} = (X^T X)^{-1} X^T y, \quad \textbf{(3-16)}$$

where $(X^T X)^{-1}$ exists if the rows of X are linear independent. When $\hat{c}$ is substituted for c into the equation 3-16, by mapping x into $\bar{x}^{(p)}$, the response values may be anticipated at any point x. This corresponds to in matrix notation

$$\hat{y} = \hat{c}^T \bar{x}^{(p)} \quad \textbf{(3-17)}$$

Once the response surface has been generated by calculating the quadratic polynomial model's regression coefficients, regression analysis may be used to assess the model's uncertainty. A variety of techniques exists to measure the estimation of residuals between the value of the responses predicted by the response surface model and the true value. In this study, the percentage of root mean square error (%RMSE) is used and defined as

$$\%RMSE = 100 \sqrt{\frac{1}{n_s} \sum_{i=1}^{n_s} (y_1 - y_i{}^{(p)})^2} \quad \textbf{(3-18)}$$

In addition, R^2, coefficient of determination, can be used to assess the response surface model’s fitting quality by measuring the amount of reduction in

variability of the response obtained. It has the value between 0 and 1 and is defined as

$$SST = \sum_{i=1}^{n} (Y_i - \bar{Y})^2 \quad \textbf{(3-19)}$$

$$SSR = \sum_{i=1}^{n} (\hat{Y}_i - \bar{Y})^2 \quad \textbf{(3-20)}$$

$$SSE = \sum_{i=1}^{n} (Y_i - \hat{Y}_i)^2 \quad \textbf{(3-21)}$$

$$R^2 = \frac{SSR}{SST} = 1 - \frac{SSE}{SST} \quad \textbf{(3-22)}$$

where SST stands for the total sum of squares, SSR stands for the sum of squares by the design variables and SSE means the error sum of squares. The maximum value for R^2 is 1.0 which means that the response surface model can describe all variation of the responses calculated with the independent design variables.

3.4.4 Multi-Objective Optimisation (MOO)

Once the response surface model is constructed with reasonable level of prediction accuracy, an optimisation technique can be taken into consideration in the next stage. The optimisation problem studied in this research includes more than one objective so that multi-objective optimisation method should be

considered, for example, weighted-sum method, the ε – constraint method, and the distance metric method [138,139]. The weighted-sum technique is used in this investigation and is described as

$$F^s = \sum_{i=1}^{nc} w_i f_i(\bar{X}) \tag{3-23}$$

$$\sum_{i=1}^{nc} w_i = 1 \tag{3-24}$$

$$0 \leq w_i \leq 1$$

where F^s is the final objective function combining each objective, $\bar{X}$ represents the vector of design variables, nc is the number of objectives, and w_i is the weighting factor.

The optimisation technique generates a distinct Pareto optimum depending on the weighting factor. When using the weighted sum approach to create an objective function, determining proper weighting variables to give acceptable optimal outcomes can be difficult, which is normally dependent upon the engineer's intuition or trial and errors.

3.5 Conclusion

The overview of the methodology used in this study is described. For ensuring credibility of the computational solution, verification and validation studies are

introduced, followed by both the single and double element wings are created including the composite lamination structure. The fundamentals of the Fluid-structure interaction are reviewed, as well as possible associated coupling strategies. Finally, the optimisation process used to find the optimum configuration of the single element wing is presented.

4 FSI analysis on a single element composite wing

The results of the FSI analysis on the single element composite wing with a reference incidence of α = 1° are demonstrated at various ground heights in this chapter. Starting from the grid sensitivity study, turbulence model study is carried out. The results of aerodynamic analysis regarding the surface pressure distribution, forces and wake profile are addressed and the structural analysis is finally performed.

4.1 Grid sensitivity analysis

First of all, the goal of the grid convergence research is to ensure that the numerical uncertainty created by the computing solution is within the asymptotic range of convergence. The Grid Convergence Index (GCI) suggested by Roache [97,106,140] is used to provide consistent and reliable results of the grid convergence. The Table 6 presents the grid information with three different mesh grids and the resulting drag coefficients computed from the solutions. In terms of iterations, each solution is adequately converged. Effective grid refinement ratio is calculated using total number of grid points (N) and dimension of the fluid domain. The order of grid convergence, *P*, is 1.64. The GCI values for the drag coefficient are 0.27% and 0.85% for the coarse-medium and medium-fine grid respectively. The GCI ratio is 1.005 which means that the solutions are within acceptable convergence boundary. Therefore, according to the GCI study, it can be shown that discretisation error is improved with the grid refinement.

Table 6 Summary of GCI study result

Variable	Coarse	Medium	Fine
N	1.7M	3.2M	6.1M
Cd	0.0560	0.0558	0.0545
$r_{effective,12}$		0.81	
$r_{effective,23}$		0.82	
P		1.64	
GCI_{12}[%]		0.27	
GCI_{23}[%]		0.85	
GCI ratio		1.005	

In addition to the GCI study, the effect of grid sensitivity on the surface pressure distribution and wake survey at h/c = 0.224 is shown in Figure 15. The turbulence model is created using the k-ω SST model with all three grids, which are shown in Table 6. In Figure 14 (a), the surface pressure distribution with the single element wing is presented, including the experimental work carried out by Zerihan [19] for comparison. Little variation of the pressure is found over different grid resolution. Figure 14 (b) depicts the wake flow field for three different grids at x/c = 1.2 at the same ride height and the computational results are compared with the experimental results [19] using laser doppler anemometry (LDA) techniques. Overall trends of the velocity profile among different grids are agreed, except the coarse grid showing underprediction of the velocity deficit. Therefore, with

benefits of computational efficiency and reasonable validity of the grid independence, the medium grid is selected for all numerical analysis in this study.

Following the grid sensitivity study, to investigate the aeroelastic effect, a non-FSI simulation with a rigid single element wing model is additionally performed and presented in Figure 14. The rigid wing is based on the same geometry as the flexible wing, but no other material properties are applied. Compared with the wing used in the reference experiment shown in Figure 15, the computational wings are generated based on the same geometry, but without any support system such as struts. The finest grid for the non-FSI case is selected because of little disparity of the findings obtained by different grids of the FSI modelling. The results of the surface pressure distribution are presented in Figure 14 (a), showing a similar shape of the spanwise pressure distribution with roughly 0.6% difference of the suction peak pressure on the bottom surface of the wing near the leading edge. In addition, in Figure 14 (b) the resultant velocity profile obtained by the non-FSI simulation with the rigid wing captures the general tendency of the wake profile being compared with the experiment and the FSI simulations except approximately 5% of the maximum absolute error of the velocity deficit. Despite the marginal difference between the FSI and non-FSI cases, due to the extremely sensitive operation conditions of the F1 application it could have an impact on the overall aerodynamic performance induced by the ride heights change.

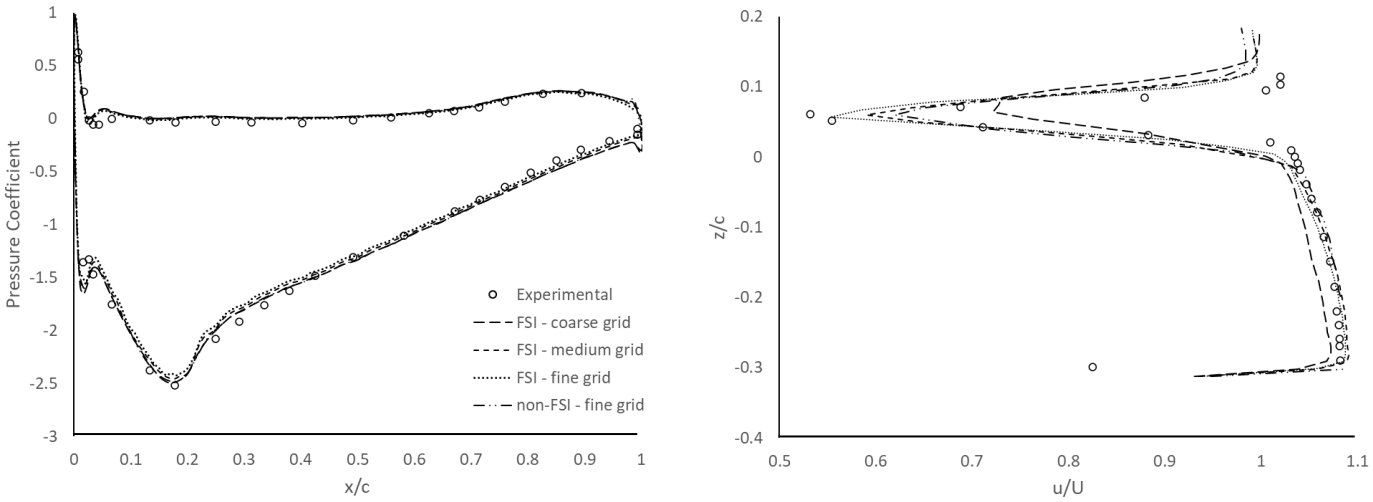

(a) (b)

Figure 14 Grid sensitivity study results of a single element wing (a) surface pressure distributions (b) wake profiles at x/c = 1.2

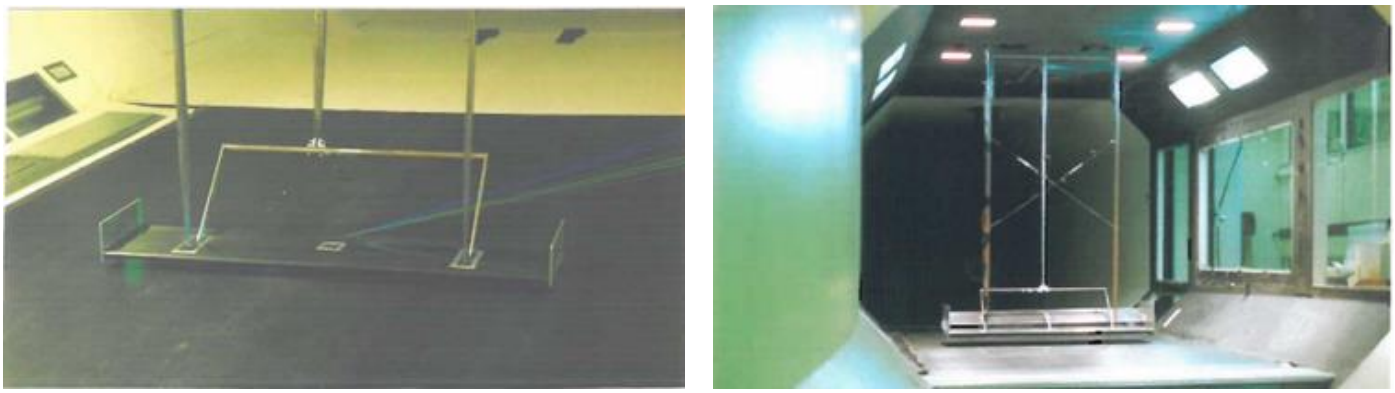

(a) (b)

Figure 15 Experimental set up of the wings [19] (a) single element wing (b) double element wing

4.2 Turbulence model study

Abovementioned, six different turbulence models are studied and for clarification, two cases are considered (h/c = 0.224 and 0.09). The flow condition at h/c = 0.224 represents a typical flow situation in which the wing's ride height is in the force enhancement area [141] and at h/c = 0.09 a significant separation zone on the trailing edge lower surface is represented. It is discussed that each turbulence model is suitable for this study by using the on-surface and off-surface flow characteristic.

Figure 16 (a) displays all of the turbulence models that describe the surface pressures' similar characteristics at h/c = 0.224 at the centre of the wing. At x/c = 0.0022 on the pressure surface, all turbulence models properly estimate the stagnation pressure near the leading edge at 1.0. Despite marginal variations of underpredicted suction peak and pressure recovery demand across the suction surface, all turbulence models capture the overall trend and basic characteristics accurately. The maximum suction appears at a point called *suction peak*. Table 7 presents detailed information about the pressure coefficient at suction peak and its location gained by each turbulence model and compares FSI results with experimental data and 2D aerofoil numerical data. The suction peak and its location are better predicted by the CFD-FEA coupled model as large discrepancy is observed with the 2D CFD results due to lack of dimensionality.

Figure 16 (b) compares the FSI numerical data with the experimental retrieved from the research on Laser Doppler Anemometry (LDA) measurement in a wind tunnel facility to demonstrate wake profile findings at x/c = 1.2 [142]. The Realizable k-ε model, which properly forecasted the lack of velocity within the

ground boundary layer, provides the most accurate prediction of the wake profile and the wake as well as the wake thickness. Table 8 summarises the results of a detailed examination of the wake characteristics obtained by each turbulence model. As the best acceptable estimation is achieved, the k-ω SST model and the Realizable k-ε model are chosen for future investigation.

Figure 16 (c) shows the surface pressure distribution at h/c = 0.09, observing a larger constant plateau is observed near the trailing edge compared to the greater height, which indicates early separated flow on the suction surface. The k-ω SST model, when compared to a range of different turbulence models, offers the best approximation of the surface pressure. Finally, the numerical results of wake measurement are presented in Figure 16 (d), however there is no experimental wake data at this height. The pattern between the turbulence models is thought to be similar to those at greater heights.

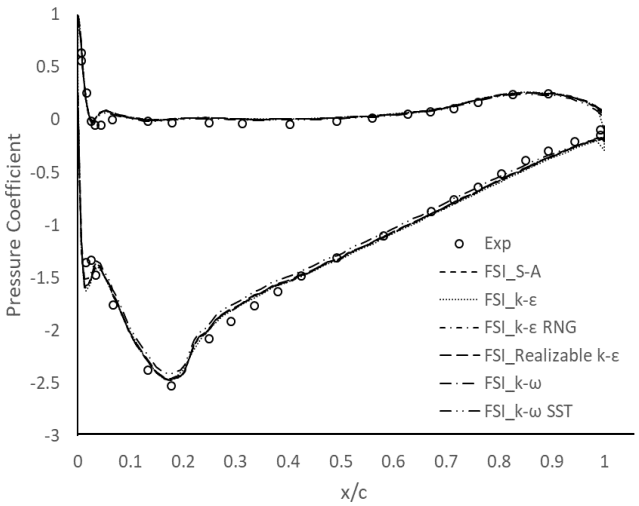

(a)

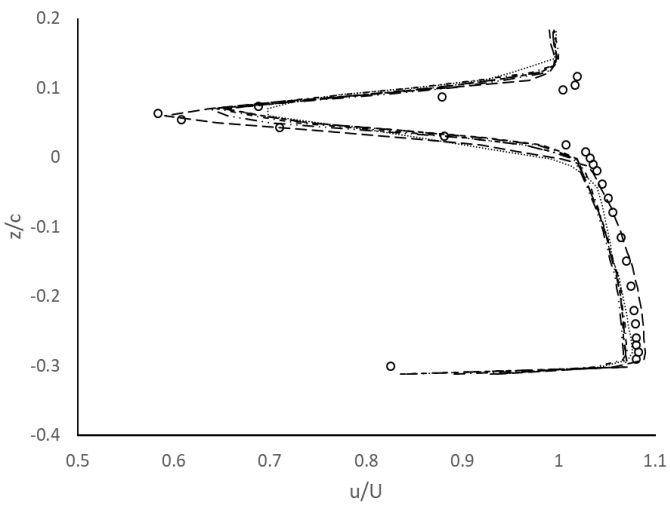

(b)

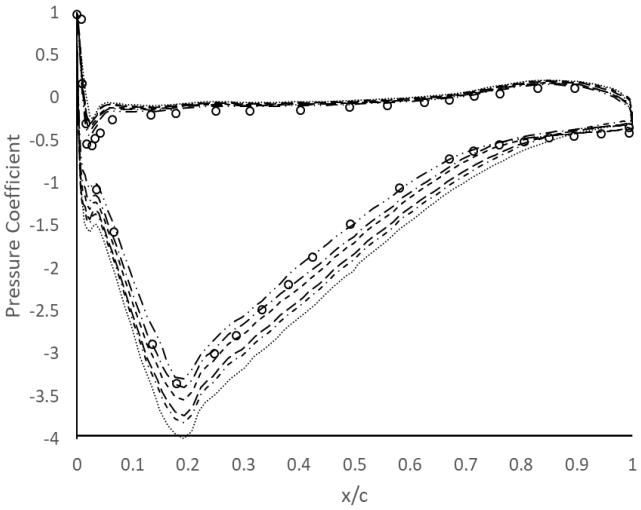

(c)

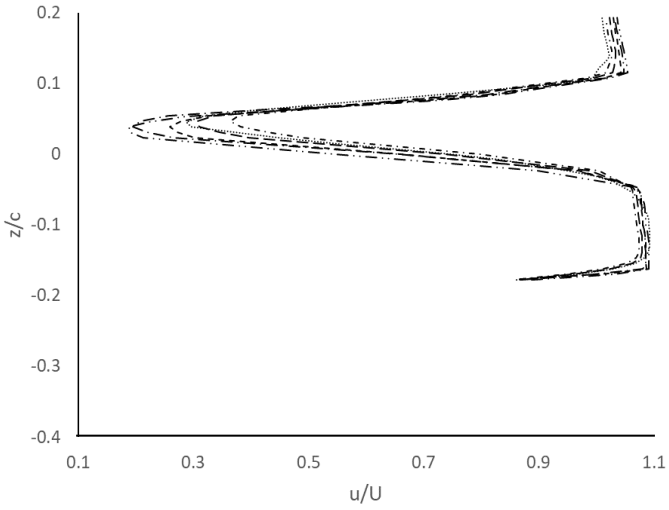

(d)

Figure 16 Turbulence model study results of a single element composite wing (a) surface pressure distributions at h/c = 0.224, (b) wake profiles at x/c = 1.2 for h/c = 0.224, (c) surface pressure distributions h/c = 0.09, (d) wake profiles at x/c = 1.2 for h/c = 0.09

Table 7 Details of the surface pressure distributions results for various turbulence models, h/c = 0.224

Turbulence model	2D CFD only [7]		3D FSI	
	$C_{P_{suc}}$	x/c at $C_{P_{suc}}$	$C_{P_{suc}}$	x/c at $C_{P_{suc}}$
Experimental	-2.53	0.18	-2.53	0.18
Spalart - Allmaras	-2.92	0.19	-2.47	0.18
Standard k - ε	-2.92	0.19	-2.47	0.17
k - ε RNG	-2.81	0.19	-2.47	0.18
Realizable k - ε	-2.94	0.19	-2.46	0.18

Standard k - ω	-2.97	0.19	-2.46	0.18
k - ω SST	-2.92	0.19	-2.46	0.18

Table 8 Details of the wake profile results for various turbulence models at x/c = 1.2 for h/c = 0.224

Turbulence model	u_{min}/U_{∞}	y/c at u_{min}	y/c at δ_{top}	y/c at δ_{bottom}	δ_{99}/c
Experimental	0.53	0.06	0.09	0.02	0.07
Spalart - Allmaras	0.65	0.07	0.10	0.02	0.08
Standard k - ε	0.69	0.07	0.10	0.02	0.08
k - ε RNG	0.65	0.07	0.10	0.02	0.08
Realizable k - ε	0.59	0.06	0.10	0.02	0.08
Standard k - ω	0.65	0.07	0.12	0.02	0.10
k - ω SST	0.64	0.07	0.12	0.02	0.10

4.3 FSI analysis

4.3.1 Chordwise surface pressures

The effect of various ride heights concerning the surface pressure distribution is investigated in comparison with the experimental pressures [13]. Figure 17

presents the chordwise surface pressures at the centre of the wing for only two ride heights h/c = 0.313 and 0.134 for fair comparison, provided by the k-ω SST and the Realizable k-ε models respectively. In general, the computed surface pressures with both turbulence models accord well with the actual pressures at all heights. The leading-edge stagnation point is accurately captured at x/c = 0.0022. The suction spike is observed at x/c = 0.019 for both turbulence models and the magnitude is slightly increased with ride height reduced. However, the experimentation doesn't present this leading-edge suction spike due to discontinuous pressure data points measured. The suction peak at x/c = 0.192 is constantly observed and its size is increased when the ride height is reduced. Downstream of the suction peak, the lower surface pressure started to recover up to the trailing edge. When the ground is approached, the suction is increased owing to the flow acceleration, which shows that the substantial pressure gains on the suction side is achieved as shown from the suction peak to x/c = 0.4, where the wing is at the lowest position with the most accelerated airflow. The overall rate of the pressure recovery along the suction surface is captured in an accurate manner with the k-ω SST model. On the other hand, overprediction of the pressure recovery rate is observed with the Realizable k-ε model at h/c = 0.09, causing inaccurate pressure difference at the end edge of the wing. Therefore, better prediction with regard to surface pressure distribution, especially to the pressure recovery rate on suction surface of the wing at lower ride height is offered by the k-ω SST model. The pressures on the pressure surface show little variation across the chord at all ride heights.

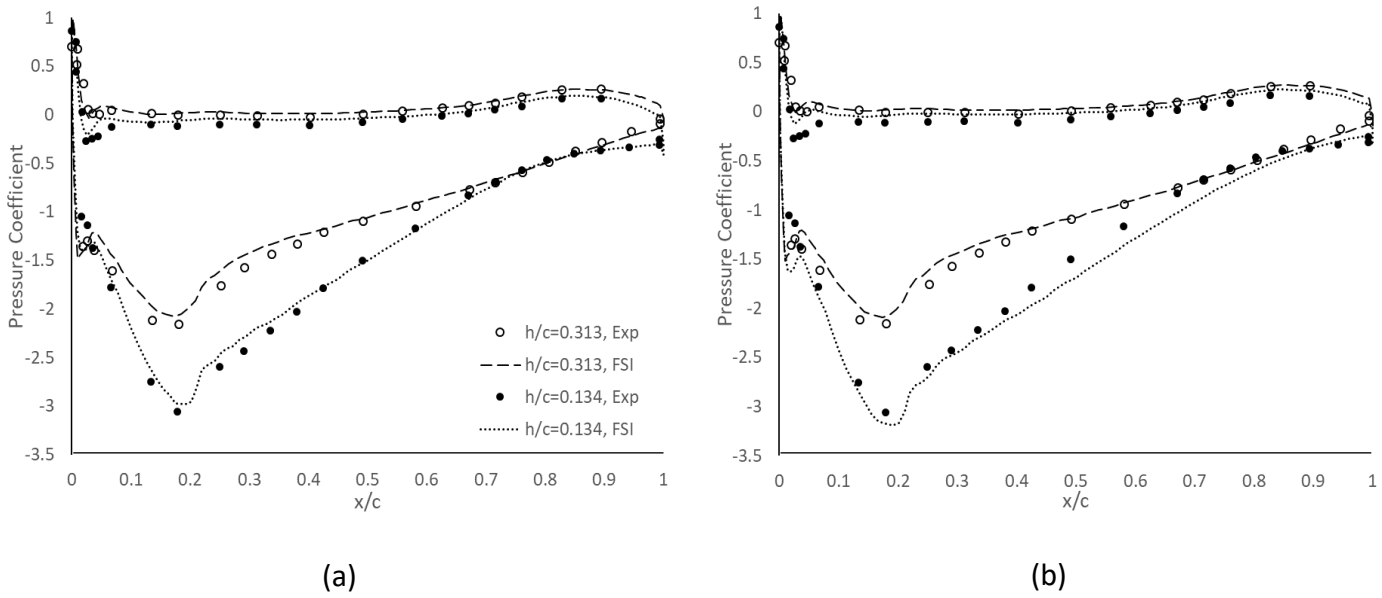

Figure 17 Chordwise surface pressure distributions at wing centre in ground effect at h/c =0.313 and 0.134 (a) k-ω SST model (b) Realizable k-ε model

The numerical results of the chordwise surface pressure distribution at the wing centre and wing tip using the k-ω SST model is presented in Figure 18 at two ground heights for clarity and compared with the experimental results [19]. In order to better investigate the aeroelastic effect of the wing, the non-FSI simulation analysis at the wing tip at both ride heights is also included. Figure 18 (a) describes the resultant surface pressure distribution at h/c = 0.395. Firstly, reduction of the suction pressure is clearly observed at the wing tip by both numerically and experimentally. At the centre of the wing, the numerical suction peak is slightly less predicted compared to the experimental results by approximately 4%. Similarly, the surface pressure distribution at the wing tip obtained by the FSI modelling is reduced compared to the experiment. The streamwise location of the suction peak at the wing centre is observed at x/c =

0.134. At the wing tip, its position is slight shifted towards the trailing edge as x/c = 0.179. The pressures on the top surfaces at both the wing centre and tip shows a good agreement with the experiment and FSI modelling, where it is not less affected by the changes of the ground heights. The non-FSI case with the rigid wing at the wing tip appears to show a comparable shape of the surface pressure distribution with the experimental results and to have slightly more suction loading than the FSI modelling case.

Figure 18 (b) presents the surface pressure distribution at h/c = 0.134. A similar pattern of the suction peak decrease from the centre to the tip found at the higher height is observed, but the suction peak at both the centre and tip of the wing significantly increases compared to the results at the higher height, indicating the ground effect enhancement due to the increased ground proximity. At this hight, it is highlighted that the experiment shows a short scale of constant pressure near the trailing edge as an indicative of flow separation, and it is also accurately captured by the numerical simulation. However, the surface pressure at the wing tip obtained by both experiments and computations does not exhibit this separation due to lower pressure recovery caused by the decreased circulation at the wing tip. The non-FSI simulation at the wing tip generally shows a good agreement with the experimental surface pressure distribution, highlighting that it can generate more suction load from the leading edge to x/c = 0.7 in comparison with the FSI modelling results. In comparison with the experimental results and non-FSI simulation, the aeroelastic-modelled wing produces dissimilar characteristics of the surface pressure distribution, especially at the wing tip. The wing is tilted backwards due to the aeroelastic effect induced by the composite

materials, resulting in reduced suction pressure and alleviating the pressure recovery.

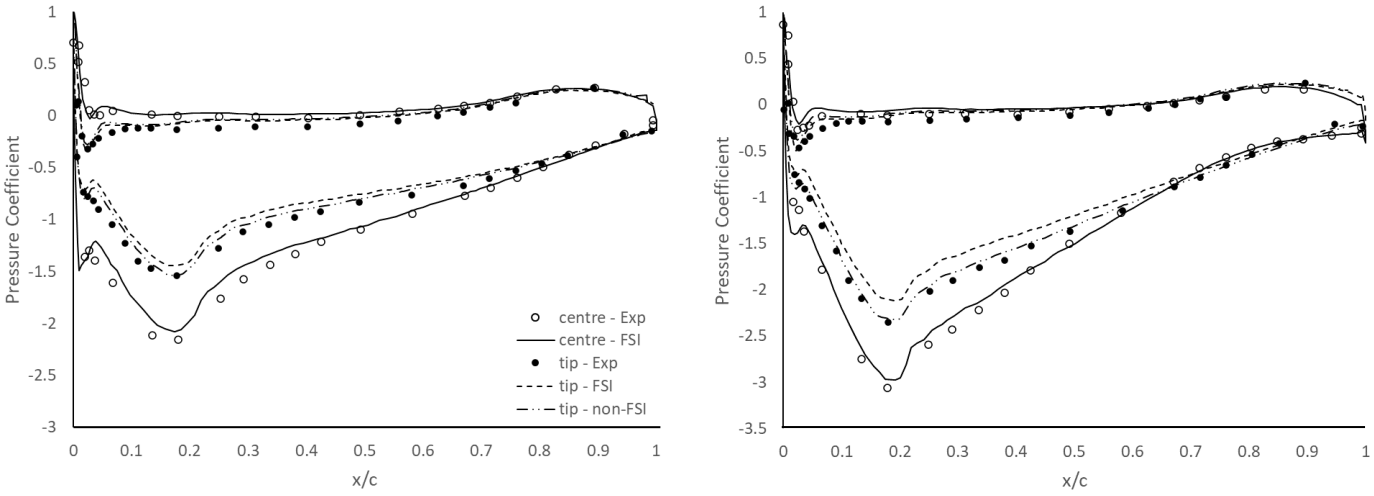

(a) (b)

Figure 18 Chordwise surface pressure distributions at wing centre and wing tip in ground effect with k-ω SST model (a) h/c=0.313 (b) h/c=0.134

4.3.2 Spanwise surface pressures

Spanwise surface pressures at the quarter-chord location are investigated with regard to various ride heights using different turbulence models and compared between experimental and computational results shown in Figure 19, which highlights the three-dimensionality of the flow. As the height is reduced, there is little fluctuation in the pressure value on the pressure surface, but the suction surface loading rises as the ground is approached. It is found that greater amount of pressures is generated across the wingspan by the FSI simulation at h/c = 0.313 for all turbulence models, which means increase in downforce. It can be

due to the stronger ground effect as the wing is temporarily deflected with increase in ground proximity. On the other hand, when the wing is lowered closer to the ground, h/c = 0.134, the computational pressures are underpredicted than the experimental pressures over the whole range of the wingspan for both turbulence models. In addition, the magnitude of this discrepancy is observed larger for the k-ω SST model. Flow separation phenomena appeared with constant pressure region near the trailing edge is not captured at the quarter-chord location as contrasted with the one shown in Figure 19 (b). It is caused by the fact that the separation point does not move this far forwards.

In this section, it can be discussed that lack of the surface pressures on the suction side across the wingspan at the lower ride height is observed with the FSI modelling. First, the effect of force reduction in ground effect becomes stronger. According to Zerihan and Zhang [13], with decreasing the height, the downforce is increased accordingly due to the ground effect. However, below a certain height, the slope of the downforce starts to be levelled off and then falls off after reaching the maximum value, which is called force reduction region. Then, as the ground proximity between the wing and the ground is increased further, the loss of downforce becomes greater. With the wing deformed in accordance with elastic characteristic of composite structure, the influence of the force reduction region on wing performance becomes severe, resulting in more loss of loadings as we can see less surface pressure in Figure 19 (a). Secondly, it can be ascribed to the wing tip vortex's decrease of effective incidence at the wing tip. As the tip vortex effect generates the upwash, the airflow surrounding the wing tip is operated at a lower effective incidence. The wing is deflected and twisted on

account of structural elasticity of the composite materials, which results in amplifying the effect.

Figure 20 illustrates the normalised maximum deflection and the twist angle of the single element composite wing over the various ride heights, which are observed at the wing tip. With decrease in the ground heights, the maximum deflection tends to show linear increase at a constant rate until h/c = 0.134. As the wing is lowered further, the deflection continues to increase at a reduced gradient, reaching approximately 0.6 mm. The maximum twist angle of the flexible wing is presents in Figure 20 (b). The twist angle is calculated with the difference of the vertical length of each reference point placed at the leading edge and trailing edge when the wing is deformed. Linear tendency of the maximum twist angle is shown over a range of the ride heights, providing the max angle of -0.047°. The variation of both maximum deflection and twist angle obtained in this research is insignificant as the boundary conditions are set based on the values from the reference experiment tests – low velocity inlet and small wing aspect ratio. Nevertheless, the aeroelastic haviour of the wing near the tip is noticeably achieved and its influence on the wing performance will be followed in the next chapter.

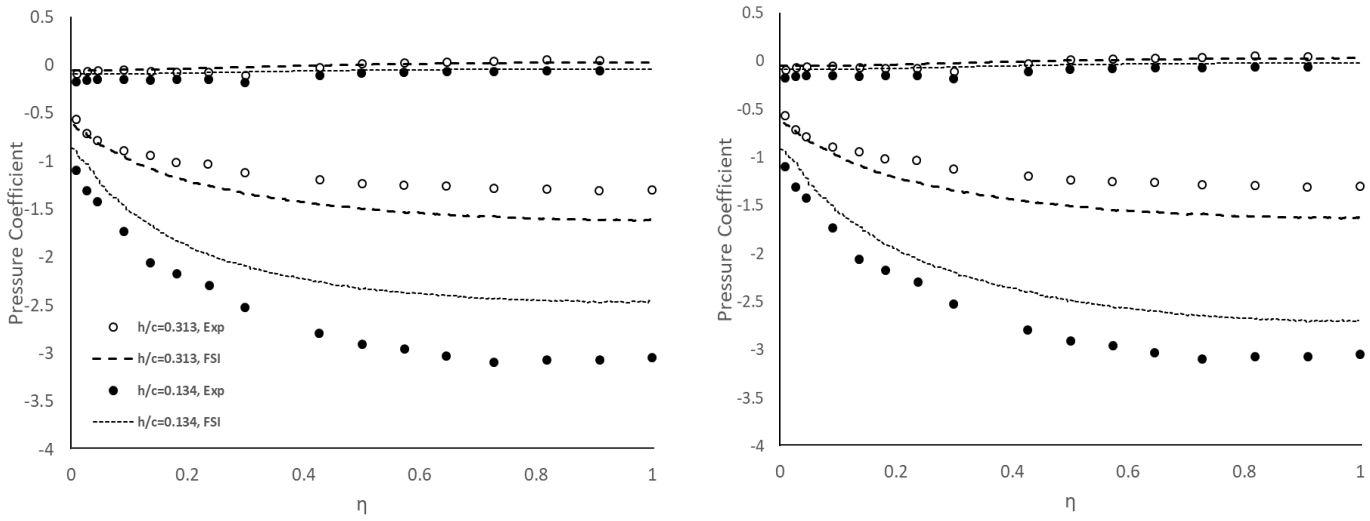

(a) (b)

Figure 19 Spanwise surface pressure distributions in ground effect for different ride heights over non-dimensional span from wing tip, η (a) k-ω SST (b) Realizable k-ε

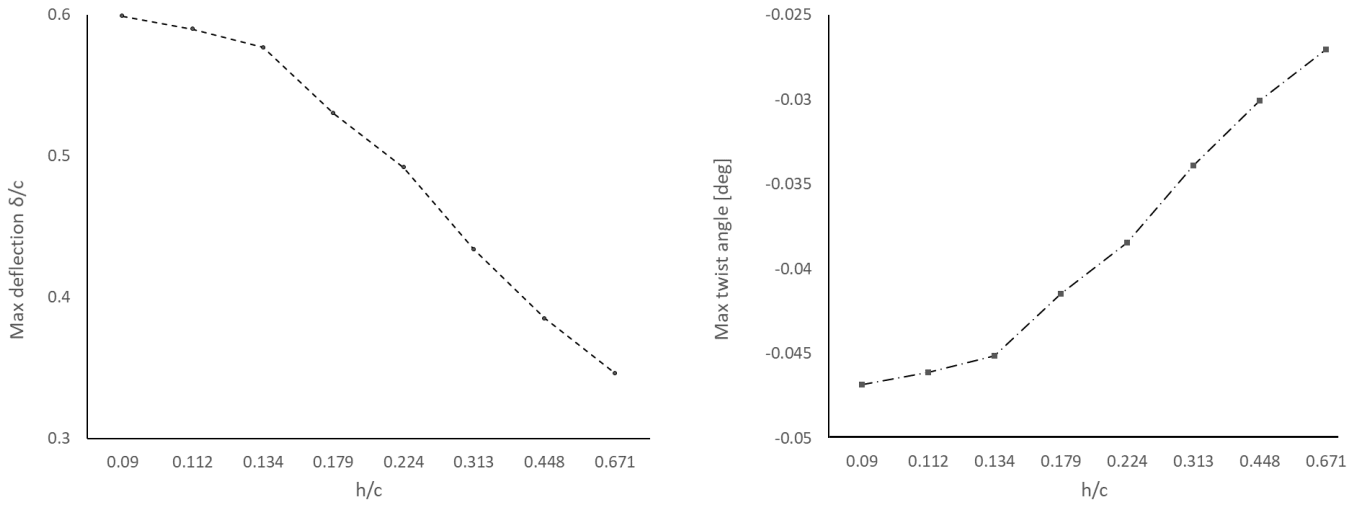

(a) (b)

Figure 20 Deflection of single-element composite wing at various ride heights (a) normalised maximum deflection, (b) maximum twist angle

4.3.3 Aerodynamic forces

Figure 21 (a) shows that the effect of non-dimensional ground heights on the downforce is quantified. The numerically calculated downforce with different turbulence models is compared with the values measured experimentally [13]. In general, in accordance with the experimental results, the gradient of downforce increases with increasing the ground proximity at large and intermediate heights. As the ride height is further lowered within a range of small heights, the slope of the line starts to slow down and finally decline with the downforce obtaining a maximum roughly at h/c = 0.111, equivalent to CL = 1.57. Comparing the results between provided by two turbulence models, the k-ω SST model is capable of catching the drop in downforce at low ride heights, thus it captures the overall trend in downforce variation more correctly. On the other hands, consistent discrepancy between the experiment and the FSI results for all ride heights is observed with both turbulence models, which might be attributed to a lower effective angle of attack induced by the wing tip deflection and wing tip vortices. The Realizable k-ε model offers analogous tendency of the downforce as the experimentation within large ride heights. However, the downforce increases as the ground gets closer within a limited range of heights, with the highest value observed at the lowest height.

The predicted downforce with ride height variations is measured and compared to the experimental forces using the aeroelastic-modelled composite wing with FSI modelling. Following the trend of the experimental results, the computational results increase gradually with decreasing ground heights across a range of large and medium heights and the gradient then starts to decrease by reaching a

maximum of CL = 1.29 at h/c = 0.134 from the ground with the k-ω SST model, whereas CL = 1.52 at h/c = 0.09 with the Realizable k-ε model. The increase in downforce with decreasing the ground height can be explained by a summation of total pressures, which is the main contribution despite the three-dimensional effect. As the height is reduced, surface pressure on the lower surface of the wing increases as well as surface pressure on the upper surface does, which results in a maximum downforce when integration of total surface pressures is a maximum. Consistent difference of downforce between experimental and computational studies is noticed throughout variation of ground heights. Two reasons can be suggested for explaining the discrepancy of downforce as the ground is approached. It is likely that a twist of the wing is the main factor. As a result of existence of the ground, there is not sufficient space between the bottom wing and ground to enable the vortex to develop. For considering the wing deflection caused by the elastic characteristics of the composite structure, as the wing is deformed and approached closer to the ground than the rigid one, it can make the distance between the wing and the ground even shorter, hindering the vortex roll up. In addition, the wing is deflected under the aerodynamic loading and also tilted backwards, following by the airflow is approaching the wing at lower effective angle of attack than the rigid case, reducing the pressure difference between upper and lower surfaces and ultimately the downforce. Another possibility is that the wing deformation might affect adversely creation of the lower edge vortex. Structural deformation may contribute to deterioration of shear layer entrainment from outboard of the endplate to feed the vortex, which leads to weakening the strength of the vortex.

Likewise, Figure 21 (b) depicts the effect of ground height variation on aerodynamic drag. The downforce grows with reduction of space between the primary element suction surface and the ground until the maximum value is reached which results in the induced drag. As a result, as the height is reduced, the drag increases for moderate and large heights. However, at a range of ground heights, the drag continues to increase until it reaches a maximum whereas the downforce decreases after the peak point. It is speculated that the drag increase at small ride heights can be attributed to other reasons as the induced drag caused by the downforce is not enhanced within the force reduction region. The numerical analysis using the different turbulence models observes a similar trend of the increase in drag force as the experimentation does. However, the discrepancy between experimental and computational results is also presented and the magnitude of the gap is decreased with increased ground proximity.

In a similar way to the experiments, the drag acquired from the numerical simulation rises for all riding heights. However, the disparity between experimental and computational results is observed and its magnitude is decreased as the ride height is lowered. At large and moderate ground heights, larger drag is generated by the computational solution due to greater amount of induced drag caused by enhancing the downforce due to the wing deflection. At the small heights, it is speculated that the increase in drag is not much affected by the wing deformation due to weakened vortex strength but likewise to the experiment, the trailing edge separation and vortex dilution might occur.

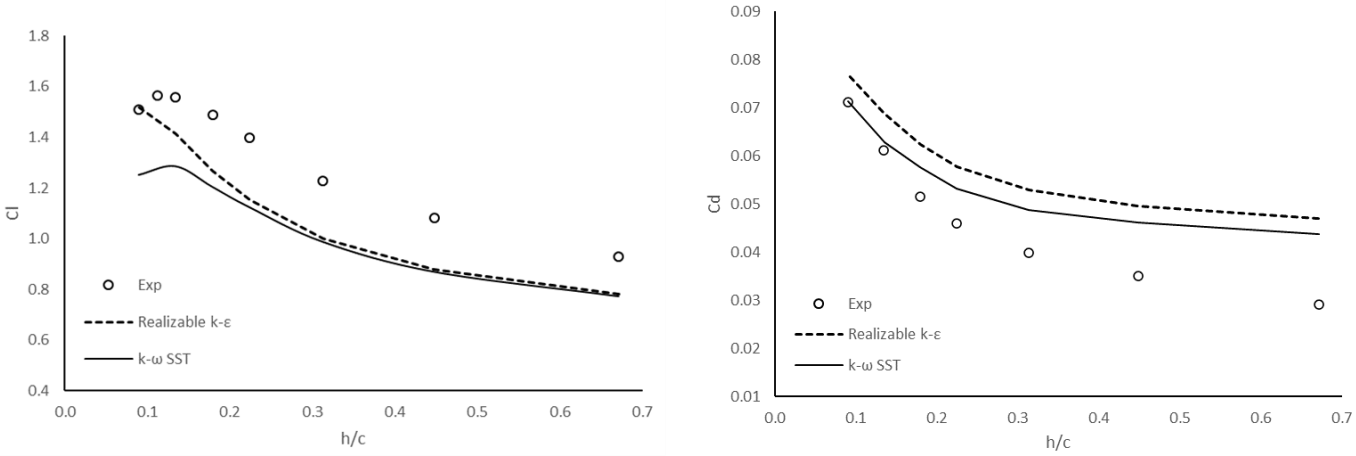

(a) (b)

Figure 21 Comparison of aerodynamic loads of single element composite wing at different ride heights using $k-\omega$ SST and Realizable $k-\varepsilon$ models (a) lift coefficient (b) drag coefficient

Following the discussion about the effect of ground heights on the aerodynamic loads in comparison with the experimental results, more detailed analysis on the fluid flow field near the wing tip using the FSI modelling is performed and compared with the non-FSI rigid wing model at the ride height of h/c = 0.134 where the aeroelastic effect could be well represented. In Figure 22, the contour of the wall shear stress on the lower surface of the wing is presented. It is firstly noticed that the non-FSI simulation produces slightly higher shear stress across the whole lower surface as shown in Figure 22 (a), which is an indicative of the fluid flow passing the surface with higher energy. On the other hand, less shear stress on the lower surface of the aeroelastically-modelled wing is depicted in Figure 22 (b), especially showing a wider region of low stress near the trailing edge highlighted in blue. It is agreed that the wall shear stress inevitably becomes decreased towards the trailing edge as the pressure recovery takes place. The

likelihood of the flow separation could increase in the area of the extended and lower stress because the flow has less energy to work against the adverse pressure gradient.

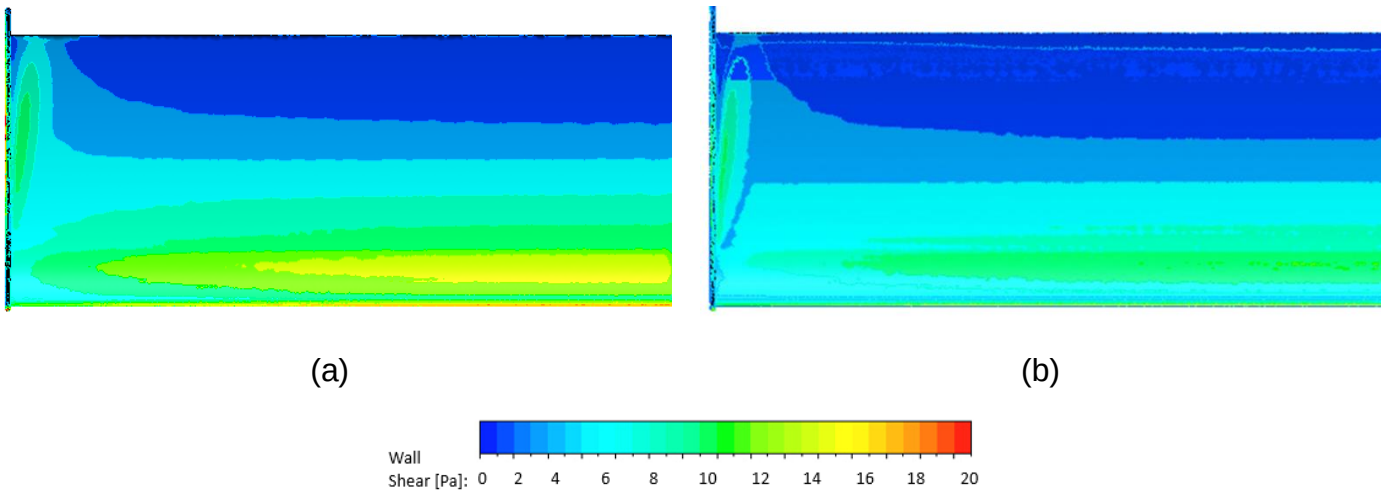

Figure 22 Wall shear stress contour on lower surface of the single element wing at h/c = 0.134 showing the leading edge lowermost (a) non-FSI (b) FSI

Another parameter to be investigated comparing the results between the FSI and the non-FSI model is the total pressure coefficient (also called total head), which is widely exploited in the motorsport aerodynamics analysis as a good way of describing the vortex energy level. The total pressure coefficients on the X plane at x/c = 0.5 at h/c = 0.134 obtained by the non-FSI and FSI models are presented in Figure 23. In both cases, two vortices shed from the top end and lower end of the endplate are well captured and a marginally more amount of loss (blue area) is observed with the aeroelastic composite wing as shown in Figure 23 (b). In addition, a certain level of the shear layers is created along the trailing edge in both cases and similar level of energy within the upper vorticities in both

wings is noticed. Under the equivalent condition, the total pressure coefficients on Y plane at y/c = 0.45 are also investigated in Figure 24. The instability behind the trailing edge in both non-FSI and FSI results is observed, and the vortex shed from the lower edge of the endplate of the FSI wing model is projected downstream of the wing, showing lower total head in Figure 24 (b). It is found that the location of the vortex created behind by the aeroelastic wing is shifted upstream compared to that of the rigid wing model due to stronger adverse pressure gradient.

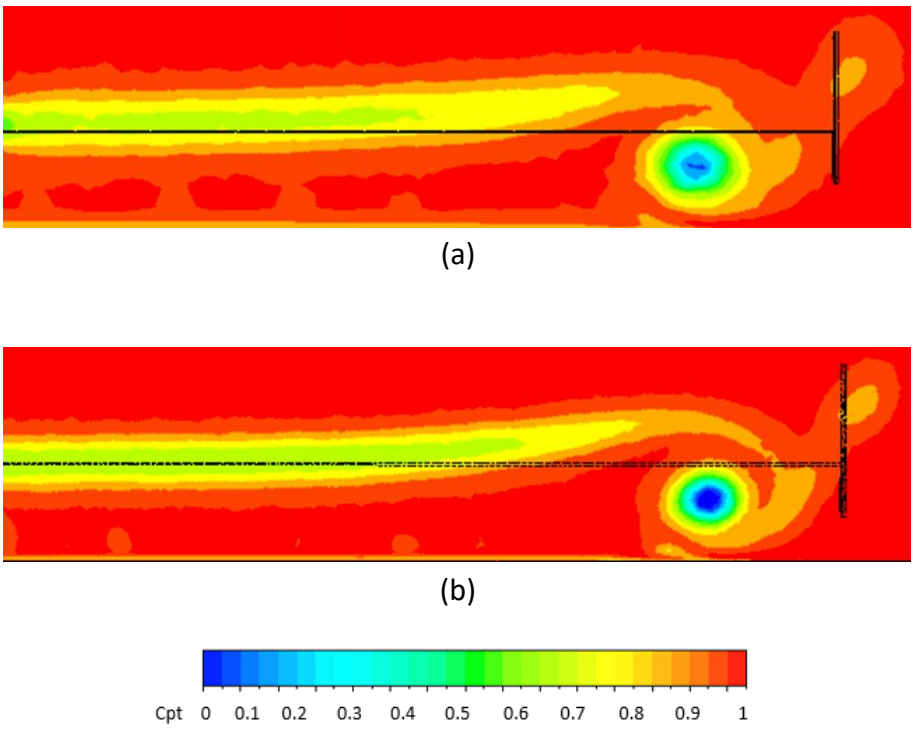

Figure 23 Total pressure coefficient contour of the single element wing at x/c = 0.5 at h/c = 0.134 on front view (a) non-FSI (b) FSI

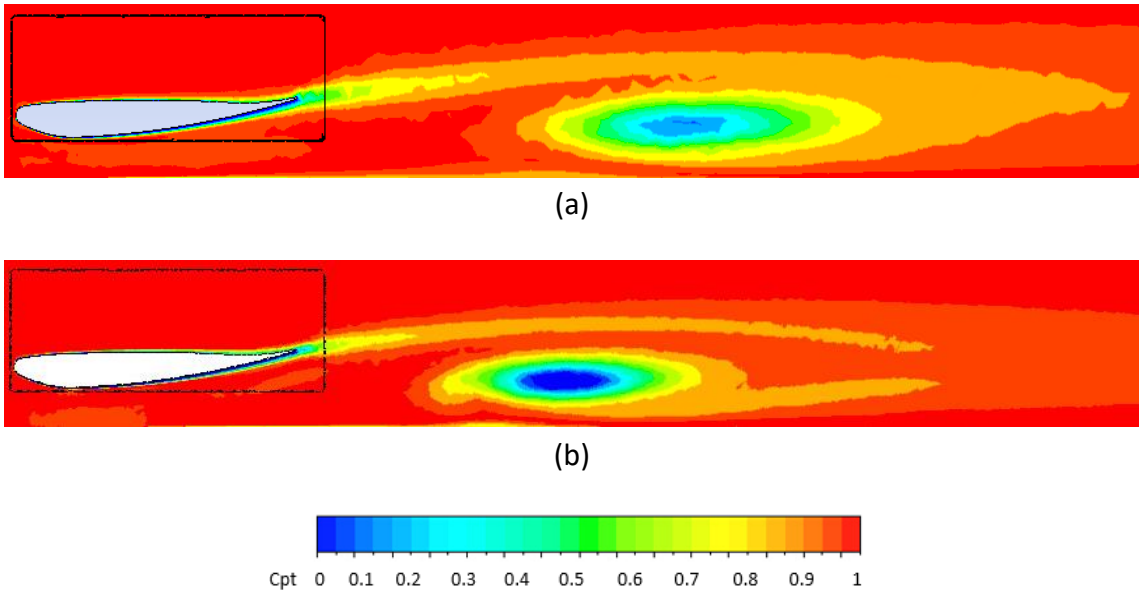

Figure 24 Total pressure coefficient contour of the single element wing at y/c = 0.45 at h/c = 0.134 (a) non-FSI (b) FSI

Along with the total pressure coefficients, Q-criterion is also one of the parameters broadly used in the motorsport application to investigate the wing tip vortex, representing the level of vorticity. In Figure 25, a two-dimensional Q-criterion on a cross plane at x/c = 0.5 at h/c = 0.134 obtained from the non-FSI and FSI simulations is illustrated, presenting the vorticities that are being shed from the bottom of the endplate. The black lines depict the outline of the wing and endplate. The high positive vorticity in red in the core of the vortex is observed with the non-FSI rigid wing in Figure 25 (a). On the ground, a small area of negative vorticity (blue) is created due to the velocities and the shear induced from the main vortex close to the ground. On the other hand, in Figure 25 (b), the aeroelastic composite wing features a significantly reduced strength of vortex shed from the lower edge of the endplate and it appears to be diffused. The strength of the secondary vortex created close to the ground is also reduced. In

order to provide further analysis of the wing tip vortex, Figure 26 presents three-dimensional vorticity with the Q-criterion for the non-FSI and FSI models at the ride height of h/c = 0.134. Both modelling techniques are capable of generating existing vortices around the wing. As discussed in Figure 25, the non-FSI rigid wing can produce stronger and healthier vortices compared to the FSI wing, showing larger thickness of the main vortex. As the wing is approached to the ground, the three-dimensionality increases being able to enhance the strength of the tip vortex. However, opposed to the flow field of the rigid wing, the aeroelastic composite wing causes lower total head and considerable reduction in the vortex strength. It could be explained that due to the increase in the ground proximity induced by the wing deflection, the distance between the lower surface of the wing and the ground is decreased, not being sufficient for the vortex to be created. In addition to the direct influence of the ground, when the wing is deflected, the decrease in the pressure difference between upper and lower surfaces of the wing caused by the reduction in the effective incidence could be another factor for the deterioration of the vortex strength. The aeroelastic effect induced by the elastic characteristics of the wing constructed with the composite materials could make the changes in the ride height dynamically and the flow field adjacent the wing could be adversely affected by the stronger adverse pressure gradient, resulting in increase the total drag.

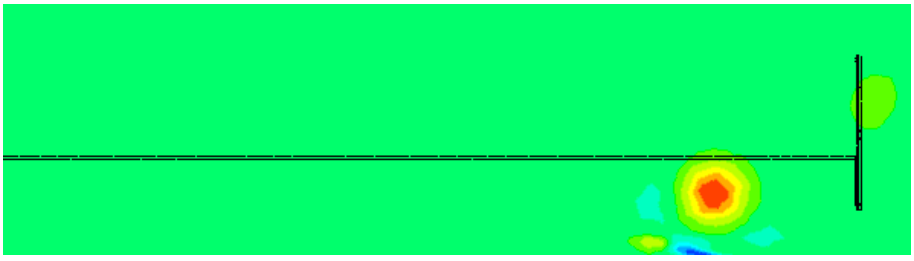

(a)

(b)

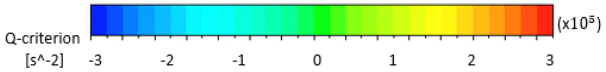

Figure 25 Q-criterion contour of the single element wing at x/c = 0.5 at h/c = 0.134 on front view (a) non-FSI (b) FSI

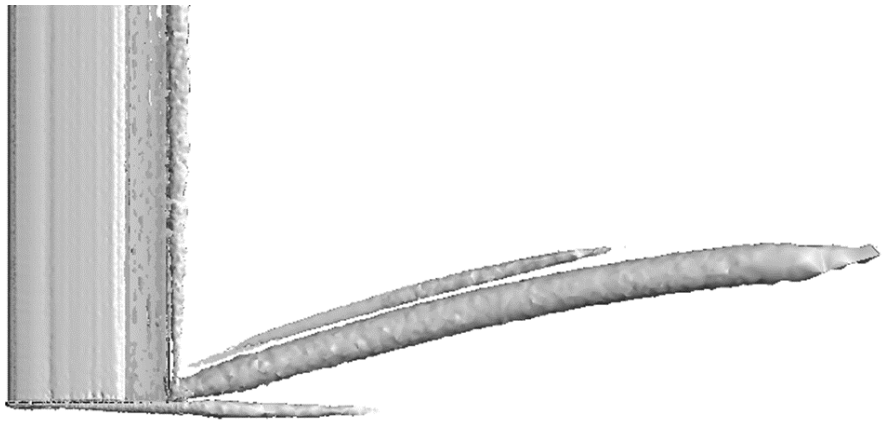

(a)

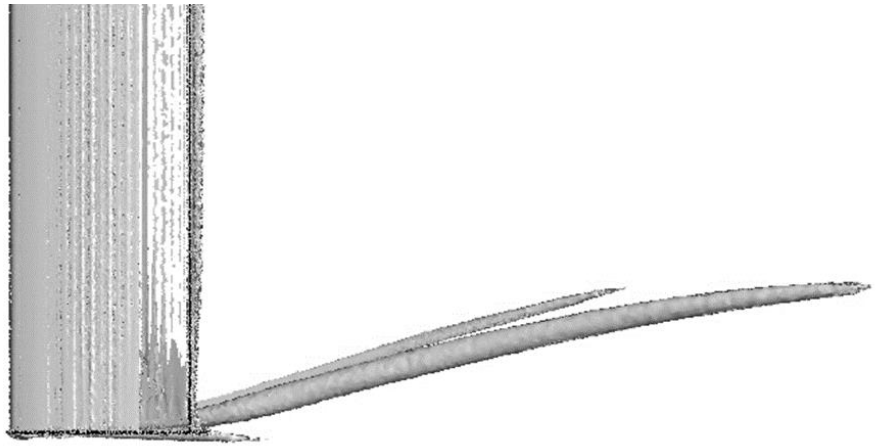

(b)

Figure 26 Three-dimensional Q-criterion contour around the single element wing at h/c = 0.134 on top view showing the leading edge left (a) non-FSI (b) FSI

4.3.4 Wake flow field

In Figure 27, u/U velocity contours obtained from computational analysis are presented for heights of the h/c = 0.448, 0.224, 0.134, and 0.09 to investigate the wing's wake pattern and near-wall flow, which is in the region of x/c = 1.0 – 1.5, comparing with the experimental results. The endplate and the back part of the wing are shown by the black lines. Compared to the experimental result performed by the Laser Doppler Anemometry (LDA) technique [19], numerical results show analogous tendency as presented. In general, the flow field of the wake is shown to change as the ride heights are varied. It can be also seen that the flow is accelerated (in red) between the trailing edge and the ground and is decelerated downstream of the trailing edge due to the unfavourable pressure gradient. At the h/c = 0.224 and 0.134, a small region at the rear of the trailing edge shows a negative velocity (in blue), indication of reversed flow, and this region becomes more obvious with increasing the ground proximity. For the h/c

= 0.09, it is observed that the negative velocity region becomes considerably larger, and its size is increased as the ground height is lowered. In addition, the path of the wake is assessed with decreasing ride heights. For the h/c = 0.448 and 0.224 cases, the wake behind the trailing edge follows an upward line of the angle of attack of the wing as it goes downstream. For the h/c = 0.134 case, where flow is separated, the path of the wake is likely to start levelling off. At the lowest height h/c = 0.09, flow separation occurs to a great extent and the path is leaned more towards a horizontal line. The size of the wake is also changed with the ground height variation. As the distance between the wing and the ground is reduced, the downforce is increased due to the flow acceleration. Accordingly, the unfavourable pressure gradient increases, resulting in a thickening of the boundary layer. When observing the wake profile at the h/c = 0.448 and at h/c = 0.09, the size of the velocity deficit is considerably increased as the ground height is lowered. In comparison with the experimental result, computational analysis presents velocity profile with slightly higher speed between the wing and the ground, which can be attributed to increasing flow acceleration caused by the wing deflection. The larger size of the velocity deficit region is observed with the FSI simulation It is believed that it may be wing deformation to deteriorate the vortex-induced effect and to develop the effect of adverse pressure gradient, which could cause larger separation.

The experimental and computational technique yielded profiles of relative velocity at streamwise position of x/c = 1.2, as shown in Figure 28 where three ride heights are shown for which experimental data is available. The detailed information about the wake profiles is given in Table 9. In general, both turbulence

models show good agreement on the wake profile estimation with the experimental data. With decreasing ride heights, the two models properly predict the velocity deficit near the ground boundary layer and the wake thickness. As representing the marginal overprediction of velocity deficit within the wake and top wake boundary and slight underprediction of the lower wake boundary thickness simulated by both turbulence models, it is believed that the computational results provide larger size of the wake profile, which can be caused by increasing the adverse pressure gradient induced by the wing deflection. The k-ω SST model slightly overpredicts the gradient of velocity recovery toward the upper wake, resulting in an overprediction in the wake thickness. The Realizable k-ε model shows similar tendency of wake profile prediction with a certain extent of underestimation in the upper boundary and in the ground boundary layer. Accordingly, the k-ω SST model produces better prediction of the wake profile with more accuracy.

Experiment [19] FSI

(a)

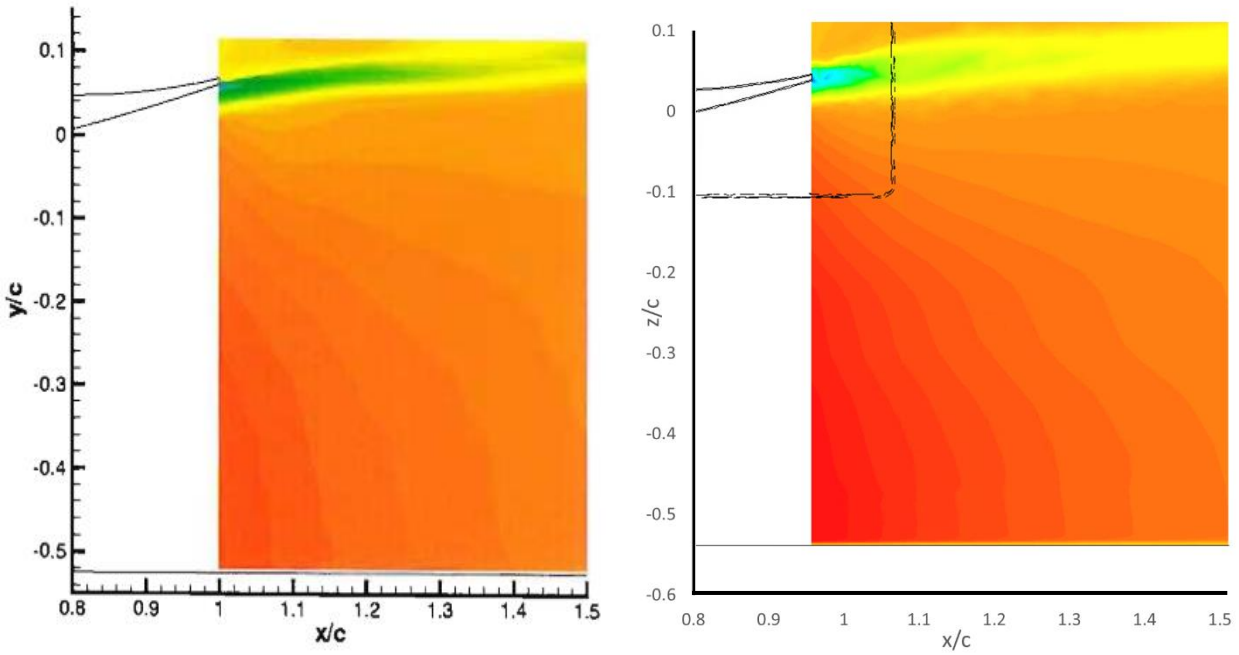

(b)

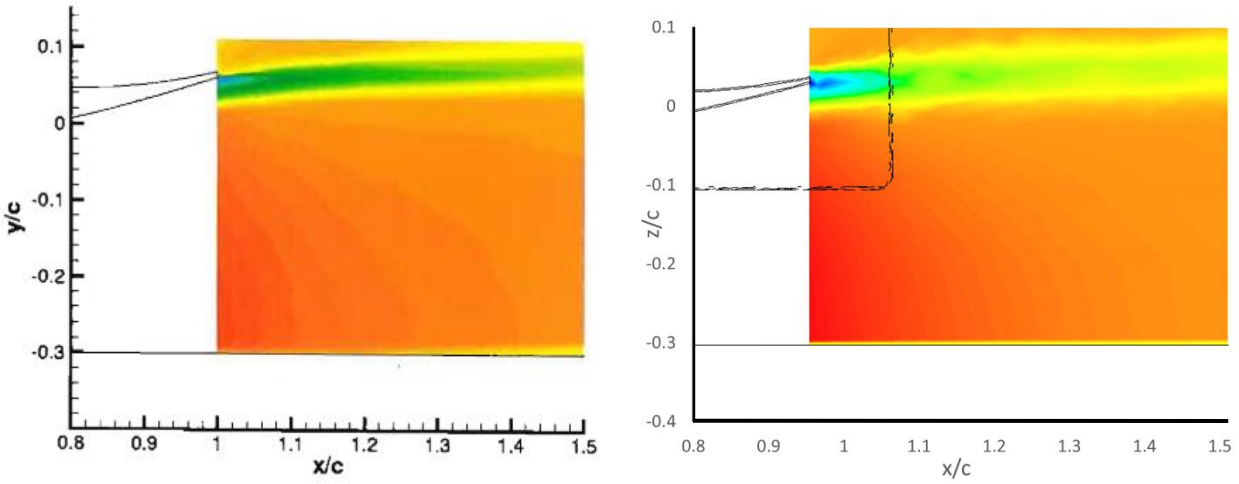

(c)

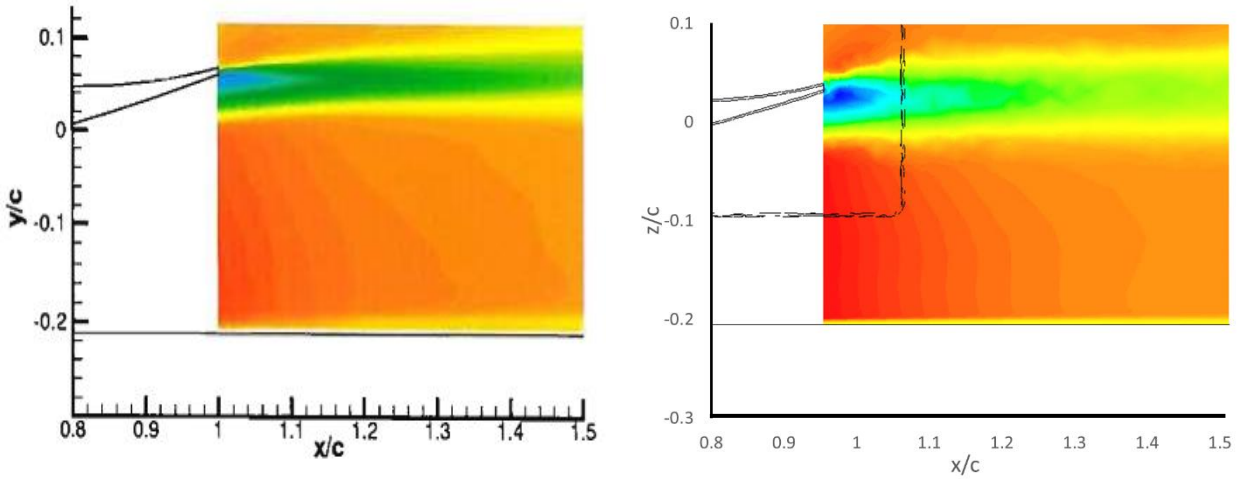

(d)

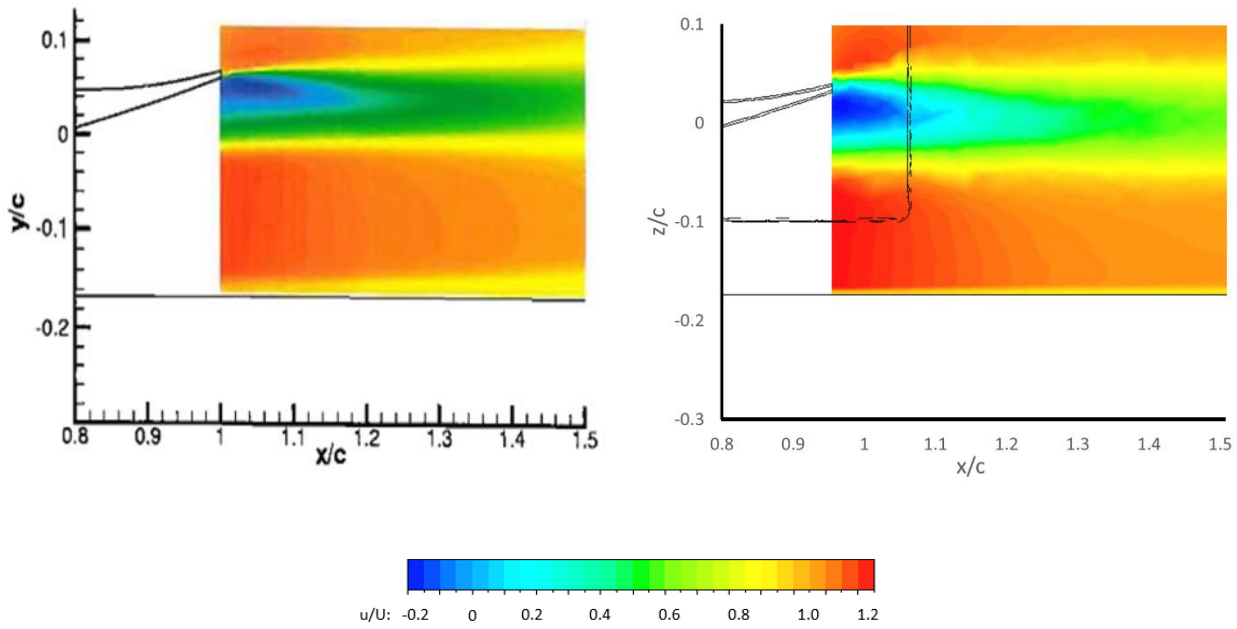

Figure 27 Comparison of u/U velocity contours at various heights between experiment and FSI results (a) h/c = 0.448, (b) h/c = 0.224, (c) h/c = 0.134, (d) h/c = 0.09

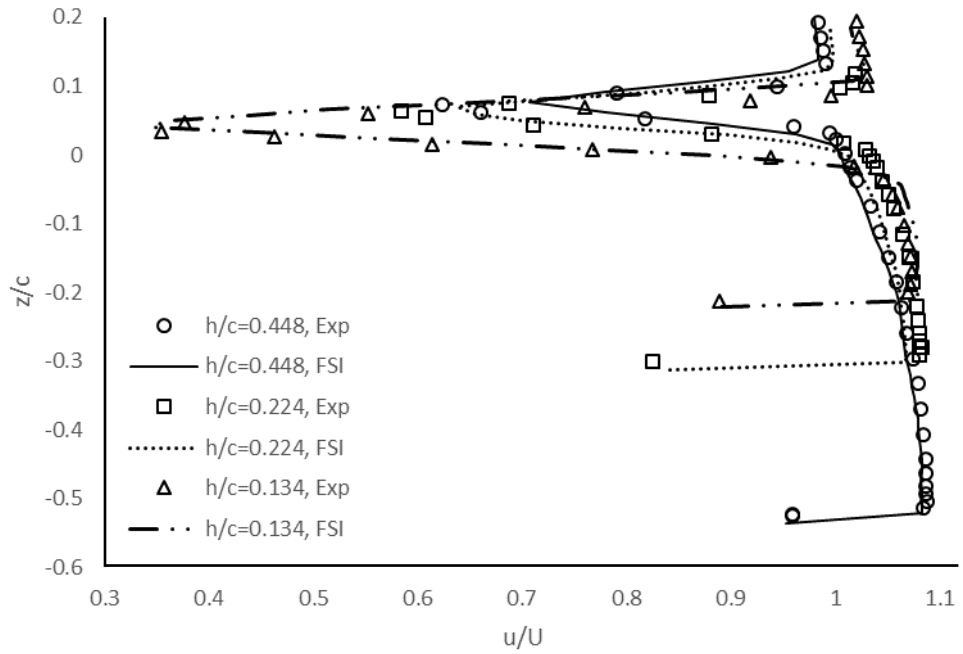

(a)

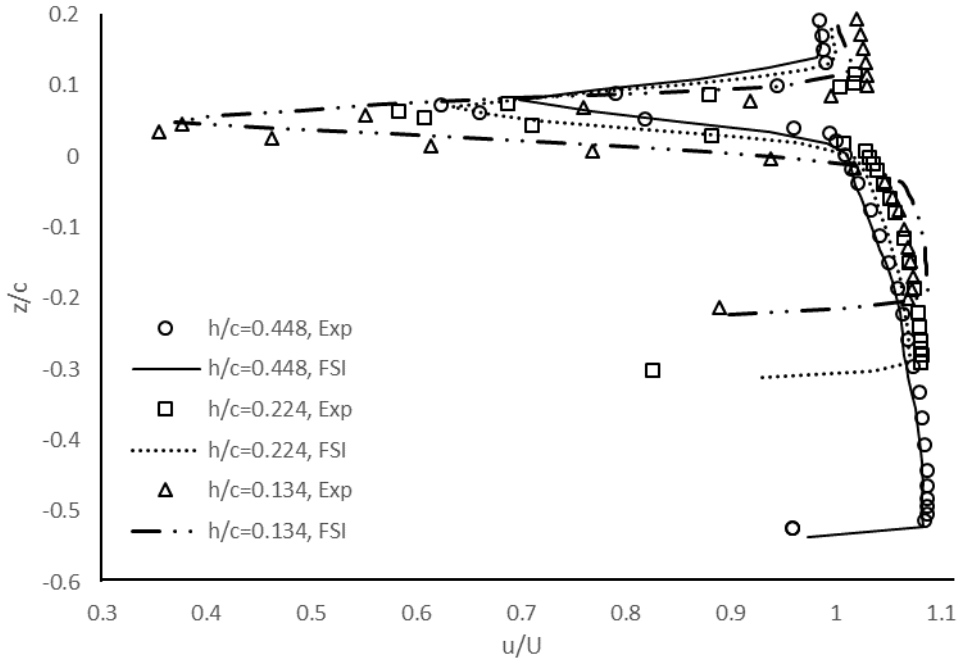

(b)

Figure 28 Wake profiles results at various ride heights at x/c = 1.2 (a) k – ω SST and (b) Realizable k – ε

Table 9 Details of wake profiles results for various ride heights at x/c = 1.2

h/c	Exp/FSI	u_{min}/U_{∞}	y/c at u_{min}	y/c at δ_{top}	y/c at δ_{bottom}	δ_{99}/c
0.448	Exp	0.62	0.07	0.10	0.03	0.07
	k – ω SST	0.70	0.08	0.12	0.02	0.11
	Realizable k – ε	0.70	0.08	0.12	0.02	0.11
0.224	Exp	0.58	0.06	0.09	0.02	0.07
	k – ω SST	0.64	0.07	0.12	0.02	0.10
	Realizable k – ε	0.63	0.07	0.11	0.02	0.09
0.134	Exp	0.35	0.03	0.09	-0.02	0.11
	k – ω SST	0.34	0.04	0.10	-0.01	0.11
	Realizable k – ε	0.37	0.04	0.11	-0.01	0.12

4.4 Structural analysis

Structural analysis of the single element composite wing is performed with variation of composite structure. In order to evaluate the aeroelastic effect under actual application conditions, this study is conducted. The span of the wing is extended up to 900 mm, compared to the previous models, being based on F1 2018 technical regulation [143] and the airflow coming from the inlet boundary for CFD analysis speeds up to 80 m/s which is regarded as high speed range in F1.

The k-ω SST turbulence model is used under the free stream condition (no ground effect) at 80 m/s, which is intended to investigate the influence on aerodynamic performance only made by the structural characteristics. The most common material used in the motorsport industry is Carbon Fibre Reinforced Polymer (CFRP) and the main material for this study is chosen to be a carbon/epoxy prepreg. The mechanical properties of uni-directional (UD) and woven prepreg are taken from the Ansys Composite Library [144] and the structure of the composite wing is created by the ANSYS Composite Prepreg. Table 10 presents a variety of composite structures in terms of different manufacturing structure (uni-directional and woven), ply orientation, and different core materials. The effects of the composite structure characteristics on the wing deflection and maximum stress are presented in the Figure 29 and additionally aerodynamic performance and weight results are shown in Table 11. The conclusion can be drawn as follows.

Comparing the UD cases with woven fabric cases, for example case 1 and 2, the wing constructed with UD structure shows more deflection of 19.2 mm and twice larger max stress shown in Figure 29, which means that the woven laminate structure has higher stiffness leading to less aeroelastic effect. Table 11 presents that the woven structured wing generates higher downforce and drag compared with the UD composite; however, difference of aerodynamic efficiency between two structures is marginal. It is concluded that, despite weight penalty, the woven structure can achieve better aerodynamic performance to avoid greater disturbance of flow field around the wing caused by larger deformation, maintaining good structural stability.

The composites structures are composed of changing ply orientations to evaluate its influence on the aerodynamic and structural performance, for example case 2 and 3 shown in Table 11. The results show that little increase in max deflection and max stress is achieved using the set [0/45] for the pile orientation shown in Figure 29 and it is speculated that the cross-ply orientation has little influence on the structural performance when most of the aerodynamic force applied on the wing is perpendicularly exerted. Along the same line, Table 6 presents that no significant changes are observed for the aerodynamic forces and efficiency by changing a sequential cross-ply orientation.

For designing the composite wing, core material can be often utilised in order to take structural advantages such as total weight reduction and strengthened mechanical characteristics. In this study, two core materials widely used in motorsport industry are evaluated, which are Nomex honeycomb and aluminum honeycomb. First, by comparing cases between Nomex and aluminum, decrease in max deflection and max stress is observed using the wing with aluminum honeycomb (case 7,8 and 9). However, the results describe that there is slight increase in total wing weight for the aluminum cases, followed by analogous level of aerodynamic performance. In comparison with the no core wing situation (cases 1, 2 and 3), significant weight reduction by 15% for UD and 22 % for woven fabric is achieved for utilising the aluminum structure replacing a couple of layers of CFRP, despite no substantial changes in aerodynamic performance and max stress. Likewise, it is shown that the Nomex core results in similar consequences as the aluminum cases, obtaining substantial reductions in weight by 20% for UD and 24% for woven fabric. In summary, it is concluded that the core material could

provide structural advantages of mechanical characteristics under the same amount of fluid loading as the no core structure, keeping the equivalent level of aerodynamic performance and weight benefit.

Table 10 Various stacking orientation of composite structures for single element wing

Case	1	2	3	4	5	6	7	8	9
Material	UD	Woven 0/90	Woven 0/45	UD	Woven 0/90	Woven 0/45	UD	Woven 0/90	Woven 0/45
ply1	0	0/90	0/45	0	0/90	0/45	0	0/90	0/45
ply2	90	0/90	0/45	90	0/90	0/45	90	0/90	0/45
ply3	0	0/90	0/45	0	0/90	0/45	0	0/90	0/45
ply4	90	0/90	0/45	90	0/90	0/45	90	0/90	0/45
ply5	0	0/90	0/45						
ply6	90	0/90	0/45						
				Nomex honeycomb			Aluminum honeycomb		
ply7	90	0/90	0/45						
ply8	0	0/90	0/45						
ply9	90	0/90	0/45	90	0/90	0/45	90	0/90	0/45
ply10	0	0/90	0/45	0	0/90	0/45	0	0/90	0/45
ply11	90	0/90	0/45	90	0/90	0/45	90	0/90	0/45
ply12	0	0/90	0/45	0	0/90	0/45	0	0/90	0/45

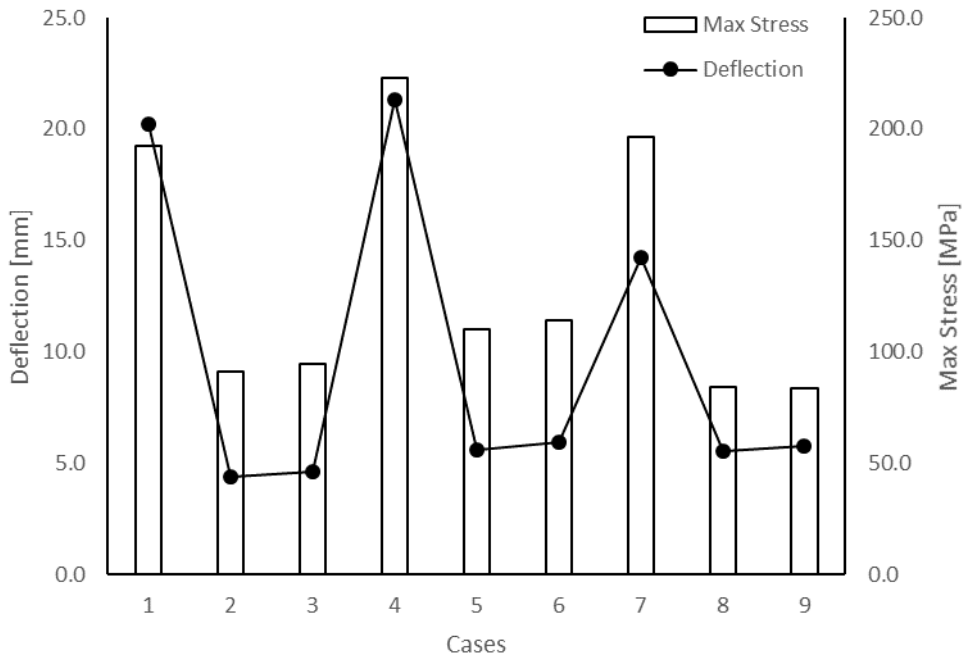

Figure 29 Results of deflection and mass stress of single element composite wing with various stacking orientations

Table 11 Results of aerodynamic performance and weights with various composite structure

Case	1	2	3	4	5	6	7	8	9
Material	UD	Woven 0/90	Woven 0/45	UD	Woven 0/90	Woven 0/45	UD	Woven 0/90	Woven 0/45
	No core			Nomex honeycomb			Aluminum honeycomb		
CL	0.774	0.811	0.815	0.761	0.782	0.784	0.778	0.785	0.785
Cd	0.034	0.036	0.036	0.033	0.035	0.035	0.034	0.035	0.035
L/D	22.95	22.65	22.48	22.87	22.66	22.66	22.78	22.62	22.62

Weight [kg]	1.13	1.97	1.97	0.90	1.49	1.49	0.96	1.54	1.54

4.5 Conclusion

FSI modelling is used to study the influence of the single element composite wing's aeroelastic behaviour. In terms of surface pressure and wake profile, the numerical method's aerodynamic performance is in good accord with experimental data. However, the aerodynamic forces calculated considering the aeroelasticity of the wing show discrepancy compared with the experiments. For further investigation on the aeroelastic effect on the wing performance, comparative analysis between the non-FSI and FSI simulations is conducted and thoroughly addressed with regards to wall shear stress, total pressure coefficients and vorticity visualising the associated results. Finally, the influence of varied composite structures on the wing's aerodynamic and structural performance is assessed and core materials provide significant structural advantages of mechanical characteristics, keeping the equivalent level of aerodynamic performance and weight benefit.

5 FSI analysis on a double element composite wing

In this chapter, the numerical results gained from FSI analysis on a multi-element wing is presented. At a reference angle of attack of 1°, the tests cover various ride heights. As described in Chapter 3, the angle of attack between the main element's leading edge and the flap's trailing edge is 5.6°. With similar approach applied for the single element wing study, the grid sensitivity study is carried out, followed by variation of turbulence models is evaluated. The FSI results are presented with regard to the surface pressure distribution, forces, and wake profile.

5.1 Grid sensitivity analysis

In this section, the grid sensitivity study of the double-element composite wing with the FSI modelling is carried out outlined to provide information on the validity of the aero-structural two-way coupling computational model and the independence of the discretisation from the grid resolution. An investigation into the grid convergence index (GCI) was conducted as recommended by Roache [97,140]. Three grids were constructed: A coarse mesh with 1.3M grid points, a medium mesh with 3.1M cells, and a fine mesh of 6.3M grid points. Each numerical solution was completely converged with respect to iterations, and the drag coefficient was obtained from the solutions. According to the procedure given by Roache, in order to obtain the grid convergence index for the flow field, the effective grid refinement ratio, $r_{effective}$, and the order of grid convergence,

p, should be calculated using the total number of grid points (N) and dimension of the fluid domain—$r_{effective,12}$ for between coarse and medium grids and $r_{effective,23}$ for between medium and fine grids. The final grid convergence ratio was obtained as shown in Table 12 in relation to the GCI values for the coarse-medium grid and the medium–fine grid determined. Because the GCI ratio is 1.001, which is close to one, the asymptotic region of convergence was effectively achieved.

Table 12 Summary of GCI study results

Variable	Coarse	Medium	Fine
N	1.3M	3.1M	6.3M
Cd	0.16302	0.16283	0.16253
$r_{effective,12}$		0.736	
$r_{effective,23}$		0.795	
P		0.701	
GCI_{12}[%]		0.227	
GCI_{23}[%]		0.370	
GCI ratio		1.001	

Followed by the grid convergence study suggested by Roache, the impact of grid resolution on computational outcomes is also explored by presenting the surface pressure distribution and the wake profile as shown in Figure 30. The turbulence model was built using the Spalart–Allmaras model with all three

instances, and the three grids indicated in Table 12 were employed in this investigation. The surface pressure distribution at h/c = 0.211 presented in Figure 30 (a) was obtained with the double-element composite wing at the reference incidence, and Zerihan's experimental work is also presented for comparison [19]. Little variation of the pressure distribution is observed over different grid resolution. In addition, Figure 30 (b) shows the wake flow field for three different grid resolutions at x/c = 1.066 at the same ride height in comparison with the experiment results obtained by Zerihan [19] using laser doppler anemometry (LDA) techniques. Between the results, the overall agreement of the velocity profile was effectively achieved for all three grids. However, the greatest velocity deficit from the main element as well as the horizontal position of the confluence point in the middle of two wakes are underpredicted by the coarse grid. Therefore, the medium grid resolution was selected for all simulations in this study, providing advantages of computational efficiency and ensuring the validity of the results.

For further analysis of the grid sensitivity study, a non-FSI simulation with a rigid double-element wing model was additionally conducted, and the associated results are presented in Figure 30. Due to the little discrepancy of the results obtained by between different grid resolutions of the FSI modelling, the finest grid was specifically selected for the non-FSI case. In Figure 30 (a), the resultant surface pressure distributions obtained by the non-FSI simulation show a similar shape to the experimental results. In comparison with the non-FSI data, the FSI results with a flexible wing generally present a comparable shape of the pressure distribution with approximately 4% difference of the suction peak pressure on the lower surface of the wing near the leading edge. As the lower surface of the wing,

especially where the flow is constrained between the wing and ground, is sensitive to small perturbation, this discrepancy of the suction peak pressure could increase the possibility of change in the flow field characteristics and may influence the wing aerodynamics. In addition, Figure 30 (b) depicts the associated results of the wake survey obtained from the non-FSI simulation with the rigid wing. The rigid wing simulation manages to capture the general tendency of the velocity profile in comparison with the experiment and the FSI cases apart from showing that the maximum error of the velocity deficit at the confluence point is roughly 9%. In the development of aircraft, there have been extensive studies on improvement of aerodynamic efficiency in order to increase the payload and reduce fuel consumption, which are sensitive to marginal changes in the aerodynamic performance [145–147]. Similarly, the ultimate goal of the F1 cars is to reduce the total time of a lap. Due to the sensitive operation conditions such as close ground proximity, a marginal difference of the aerodynamic performance caused by the ride height change would have an impact on the final lap time [148]. Thus, investigation of the aeroelastic behaviour of a double-element composite wing using the FSI modelling discussed in this research work is crucial to enhance accuracy of the wing performance associated with the complex fluid flow field.

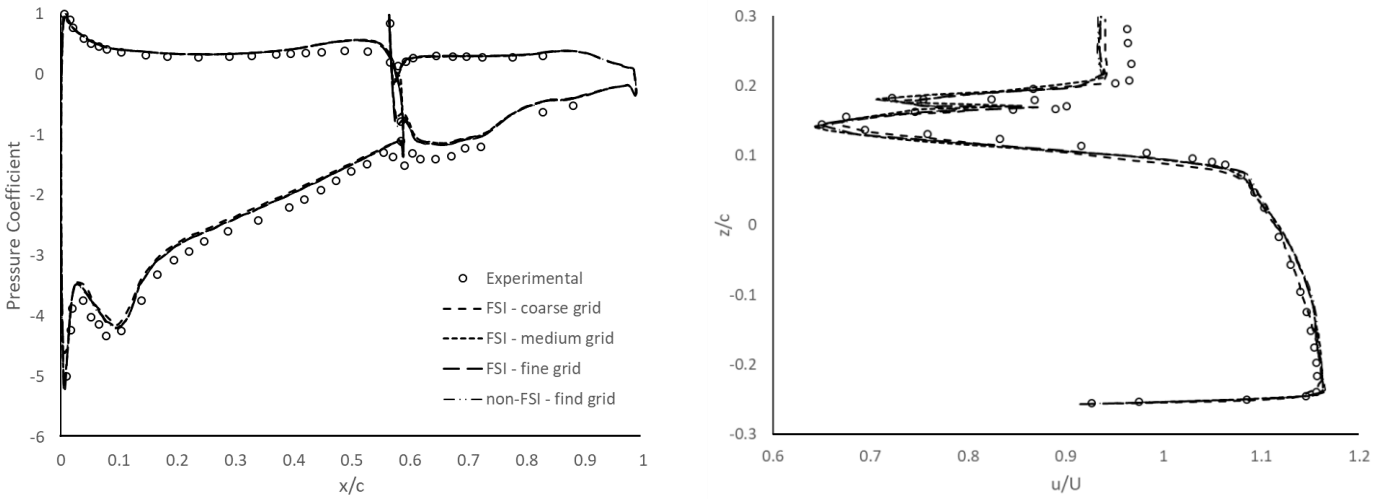

(a) (b)

Figure 30 Grid sensitivity study results of a double element wing (a) surface pressure distribution (b) wake profile at x/c = 1.066

5.2 Turbulence model study

As being carried out for the single element wing case, a study on suitability of various turbulence models is performed using the flow features near the surface and far from the trailing edge. Six turbulence models are quantitatively assessed at two particular ride height cases selected; h/c = 0.211 for a flow condition within the force enhancement region [32] and h/c = 0.079 near the maximum downforce with distinctive wake characteristics of the main element and flap. On this study, the main element wake is thought to be as the lower wake and the flap wake as the upper wake according to their location.

The surface pressure distributions on both the main element and flap are accurately captured by all turbulence models as shown in Figure 31 (a). At x/c = 0.01 for the main element and at x/c = 0.564 for the flap, the stagnation pressures

close to the leading edge, $C_{P_{stag}}$, are correctly predicted. Following by the suction spike, the suction peak, the point with the maximum downforce and fastest flow, is correctly captured by all turbulence models. The details of quantitative data of the surface pressure distribution are presented in Table 13 in comparison with the experiment and numerical aerofoil result.

Figure 31 (b) presents the velocity profile of the wake obtained by all turbulence models, which includes the LDA experimental results extracted from a research carried out by Zhang and Zerihan [32]. A variation between the numerical results and experiments, especially within the upper wake, is observed by all turbulence models. However, with the exception of the Standard $k-\varepsilon$ model, there is a good agreement between the findings obtained by individual model. Most turbulence models properly anticipate the wake below the lower wake, the vertical position of the lower wake's lower limit was underpredicted by Standard $k-\varepsilon$. A drop in non-dimensional velocity (u/U) to about 0.92 may be detected near the ground plane, followed by a dramatic rise. This trend seems correct as a strong adverse pressure gradient caused by the flow recovery in ground proximity is generated on the suction side of the main element and it brings about creation of a boundary layer near the ground in a streamwise direction. The velocity profile representing the resultant ground boundary layer is well captured by all computational models, the Spalart – Allmaras shows improvement in terms of the ground boundary layer.

The maximum velocity deficit perpendicular positions for the upper and lower wakes are well predicted by the computation, however a wide deviation is observed concerning the associated streamwise velocity (u_{low}/U and u_{top}/U) with the exception of the Spalart – Allmaras which offers improved approximation.

In addition, the confluence point between the upper and lower wakes pertaining to the location and the non-dimensional velocity is best predicted by the Spalart – Allmaras, the rest of which underpredicts the velocity. The discrepancy observed in the wake boundaries has a consequent influence on a variation within calculation of the upper ($(\delta_{99}/c)_{top}$) and lower ($(\delta_{99}/c)_{low}$) wake thickness. The Spalart – Allmaras model offers the best prediction of both upper and lower wake thickness. Table 14 shows the quantitative information of the wake profile obtained by each turbulence model at x/c = 1.066.

Figure 31 (c) and (d) present the surface pressure distribution and the wake profile at x/c = 1.066 respectively at lower ride height of h/c = 0.079. In a similar way to the higher ride height case, little variation of the surface pressure over the main element and flap obtained by the turbulence models is shown including the increased magnitude of the suction surface loading. The closest prediction to the experiment regarding the surface pressure is achieved by the Spalart – Allmaras. The actual test results of the wake profile are not available at h/c = 0.079. Nevertheless, it can be noted that the agreement between each turbulence model is observed at this height. Therefore, the best prediction of the quantitative feature of various turbulence models is achieves by the Spalart – Allmaras model, which is selected in this study.

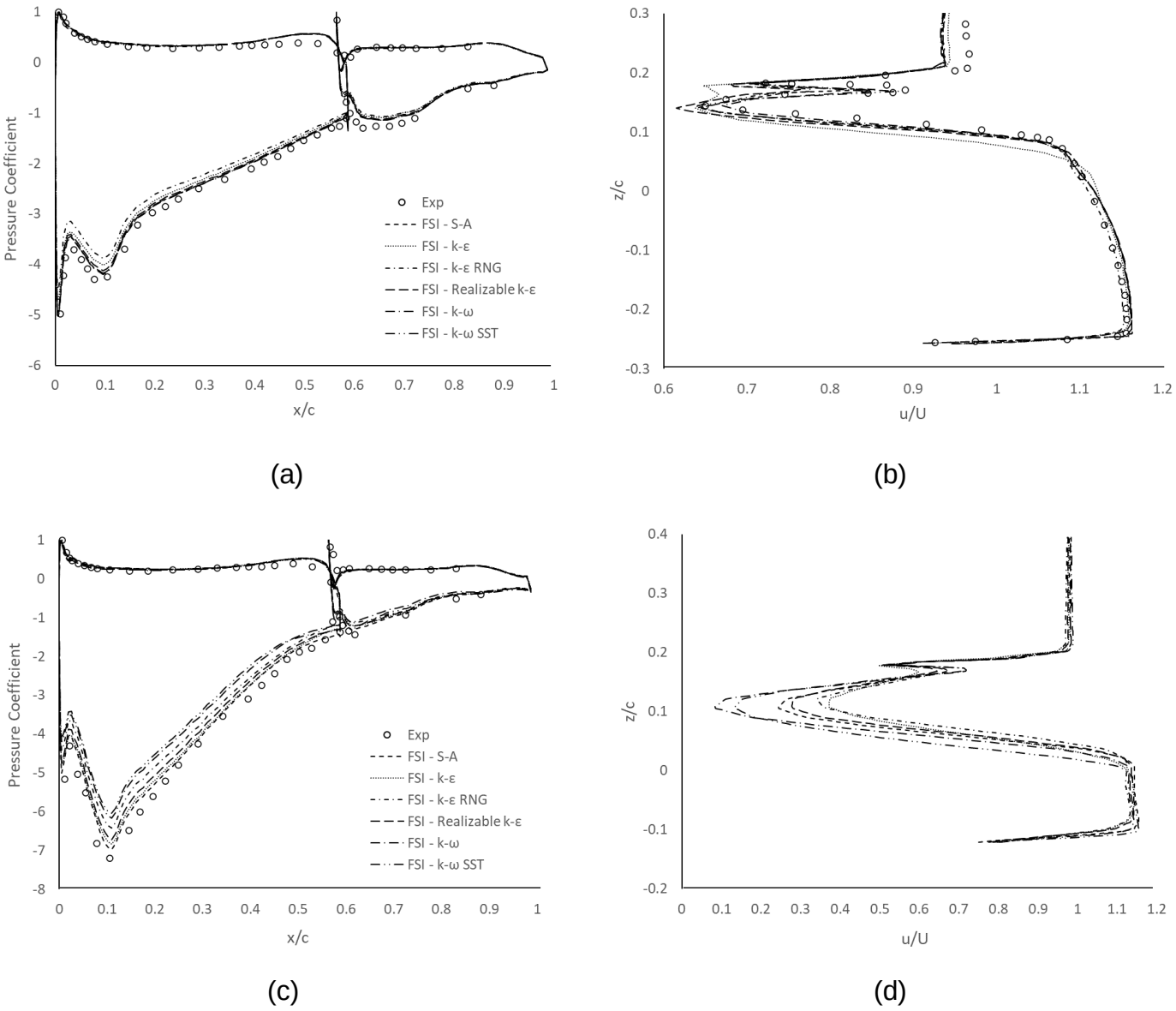

Figure 31 Turbulence models study results of a double element composite wing (a) surface pressure distributions at h/c = 0.211, (b) wake profiles at x/c = 1.066 for h/c = 0.211, (c) surface pressure distributions at h/c = 0.079, and (d) wake profiles at x/c = 1.066 for h/c = 0.079

Table 13 Details of surface pressure distributions results for experiment and various turbulence models, h/c = 0.211

	2D [38]		3D [19]	
	$C_{P_{suc}}$	$x/c\ at\ C_{P_{suc}}$	$C_{P_{suc}}$	$x/c\ at\ C_{P_{suc}}$
Experimental	-4.48	0.08	-4.48	0.08
Turbulence model	2D CFD [38]		3D FSI	
	$C_{P_{suc}}$	$x/c\ at\ C_{P_{suc}}$	$C_{P_{suc}}$	$x/c\ at\ C_{P_{suc}}$
Spalart - Allmaras	-4.96	0.11	-4.18	0.095
Standard k - ε	-4.95	0.11	-4.02	0.095
k - ε RNG	-4.93	0.11	-3.88	0.095
Realizable k - ε	-4.94	0.11	-4.13	0.095
Standard k - ω	-4.91	0.11	-4.20	0.095
k - ω SST	-4.93	0.11	-4.18	0.095

Table 14 Details of wake profiles results for experiment and various turbulence models at x/c = 1.066 for h/c = 0.211

Turbulence Model	u_{min}/U_∞		$y/c\ at\ u_{min}/U_\infty$		$y/c\ at\ \delta$		δ_{99}/c	
	Low	Top	Low	Top	Low	Top	Low	Top
Experimental [32]	0.65	0.72	0.150	0.200	0.104	0.205	0.067	0.034
Spalart - Allmaras	0.64	0.71	0.141	0.182	0.093	0.206	0.078	0.035
Standard k - ε	0.64	0.65	0.140	0.178	0.080	0.211	0.085	0.046
k - ε RNG	0.64	0.68	0.140	0.180	0.095	0.211	0.077	0.039
Realizable k - ε	0.62	0.68	0.140	0.180	0.094	0.212	0.078	0.040
Standard k - ω	0.67	0.70	0.144	0.182	0.092	0.207	0.077	0.038
k - ω SST	0.64	0.70	0.144	0.182	0.092	0.207	0.077	0.038

5.3 FSI analysis

The influence of aeroelastic behaviour of the double element composite wing in ground effect is discussed with height variation in comparison with the experimental results concerning the surface pressure distribution, aerodynamic sectional forces, and wake characteristics. Based on a prior turbulence model research, the Spalart – Allmaras turbulence model is employed in the investigation at various ride heights.

5.3.1 Chordwise surface pressures

The impact of ground proximity on the surface pressure distribution of a two-element composite wing is examined and compared to experiment observations [19] shown in Figure 32. The chordwise pressures are illustrated in Figure 32 (a) for large heights and Figure 32 (b) for small ride heights respectively. The overall shape of the surface pressures on both elements at all heights are accurately calculated. The leading-edge stagnation pressures are well captured for the main element and the flap. The pressures on the pressure surfaces of both main element and flap are correctly predicted remaining relatively independent of the ride height, whereas significant increase in pressures on the suction surfaces with increase in ground proximity is observed. In Figure 32 (a) it is shown that when the wing is approached more loading is generated on the suction surfaces of both main elements and flap. However, the main element provides greater extent of suction compared with the flap. The general feature of the pressure distributions remains constant regardless of the ride height, presenting the suction spike and suction peak near the leading edge. Figure 33 displays the pressure distribution

of each ride height respectively for clarity. Contour plot of the pressure coefficient on the suction surface is depicted in Figure 35 for the large heights, showing the leading edge lowermost and the endplate positioned left-hand side. As described, lower pressure coefficient can be found on the suction surface and the extent of the suction loading becomes greater with increasing the ground proximity. Likewise, the velocity on the lower surface increases as the wing is approached to the ground, which is illustrated in Figure 37 with the velocity contour plot.

Figure 32 (b) shows the surface pressure result at lower ride heights in comparison with the experiment. The suction loading on the suction surfaces considerably increases as the wing height from the ground is reduced, especially in a region of the suction peak, x/c = 0.11, followed by the pressure recovery downstream is correctly calculated at all heights. The main element suction pressures are slightly underpredicted. The increase in suction loading on the main element lower surface with increase in ground proximity is accurately captured. On the other hand, little change in suction loading on the lower surface of the flap is observed when the ground is approached. Figure 34 shows the detailed pressure distribution at each ride height. In terms of the pressure coefficient and velocity contour plots, Figure 36 and 38 respectively illustrate a similar trend of increase in suction pressure on the lower surface as that at higher heights. In addition, it is highlighted that at lower ride height a region of lower velocities at the main element trailing edge and underneath the flap is presented which may be an indicative of the flow separation.

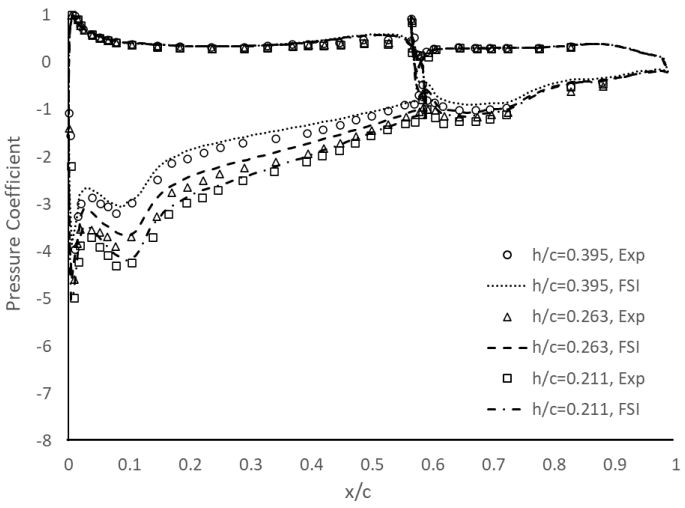

(a)

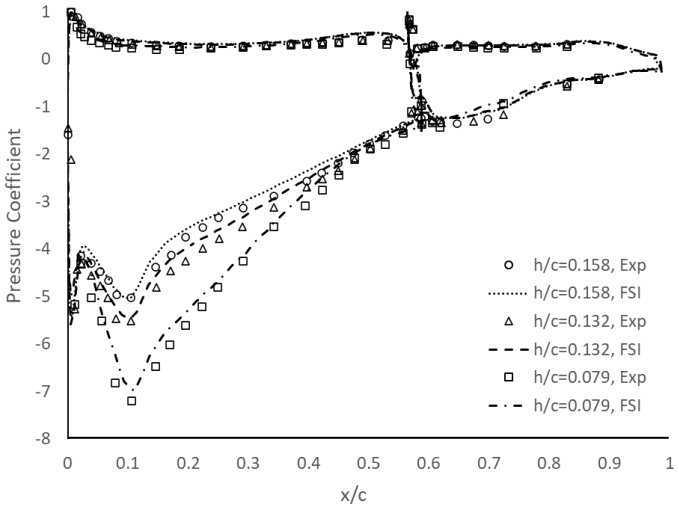

(b)

Figure 32 Chordwise surface pressure distributions at wing centre (a) high ride heights (b) low ride heights

(a)

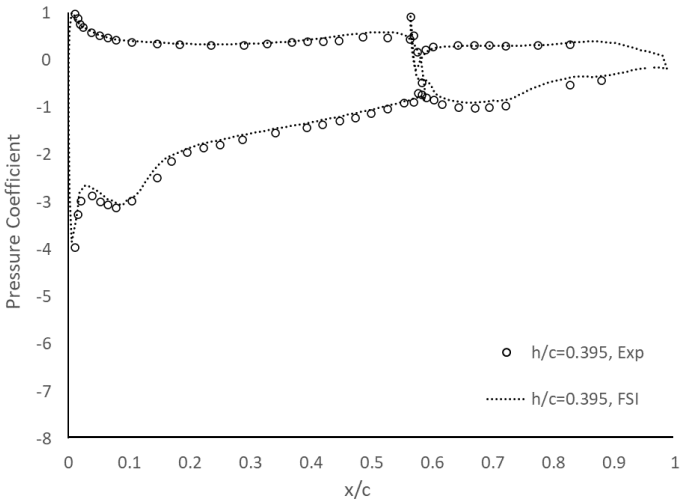

(b)

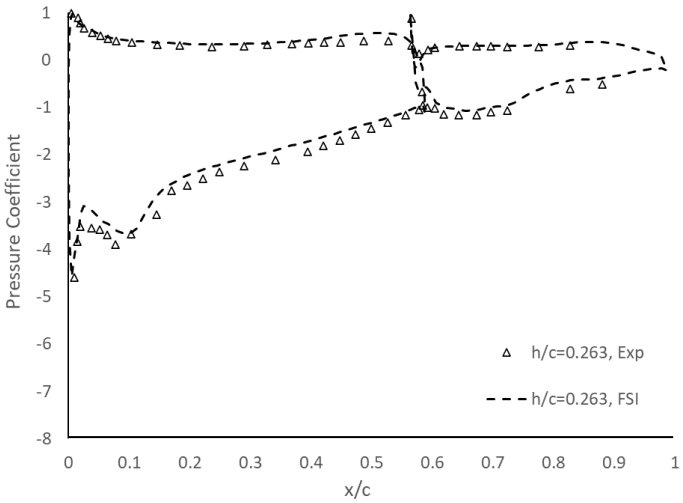

(c)

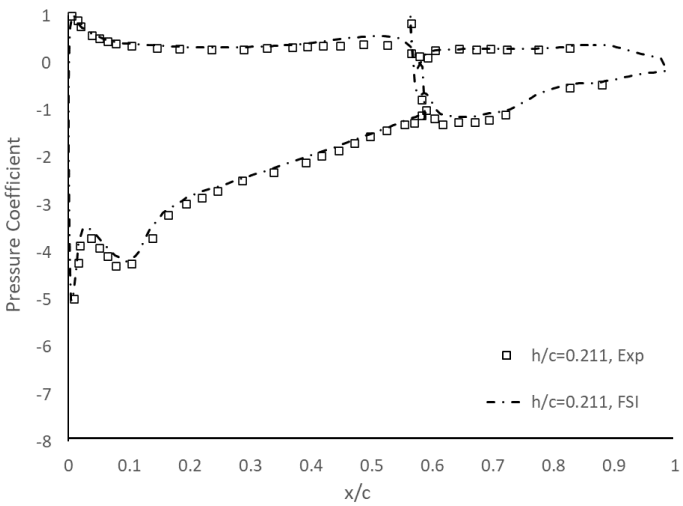

Figure 33 Chordwise surface pressure distributions at high ride heights (a) h/c = 0.395 (b) h/c = 0.263 (c) h/c = 0.211

(a)

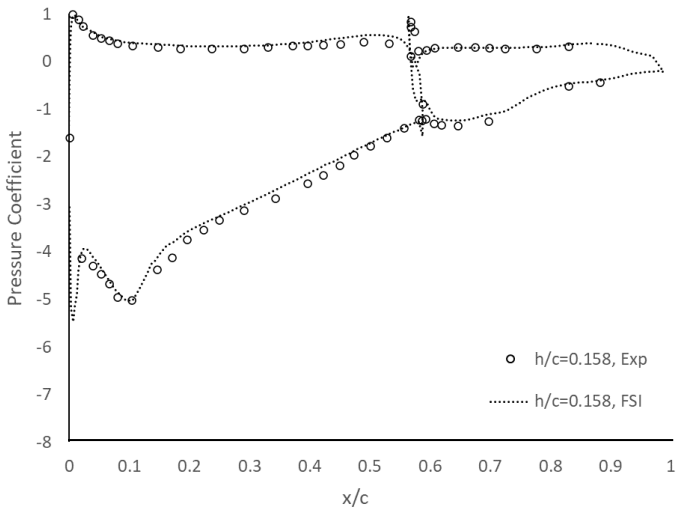

(b)

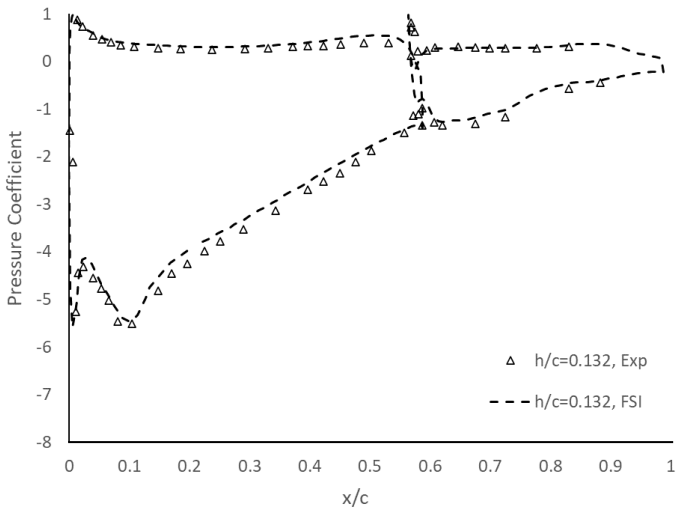

(c)

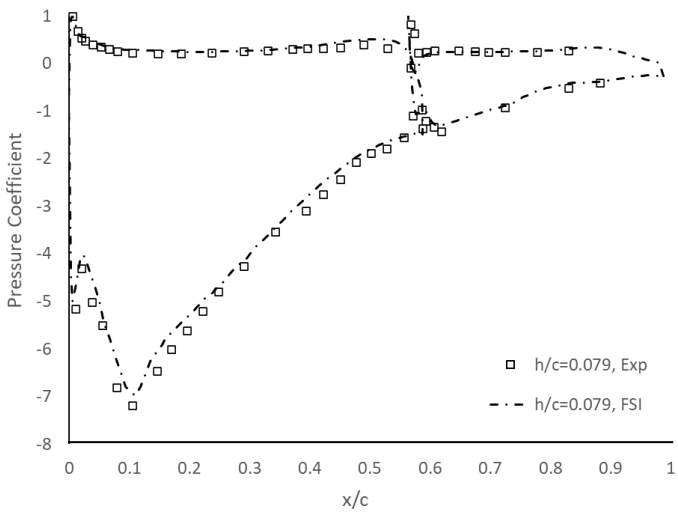

Figure 34 Chordwise surface pressure distributions at low ride heights (a) h/c = 0.158 (b) h/c = 0.132 (c) h/c = 0.105

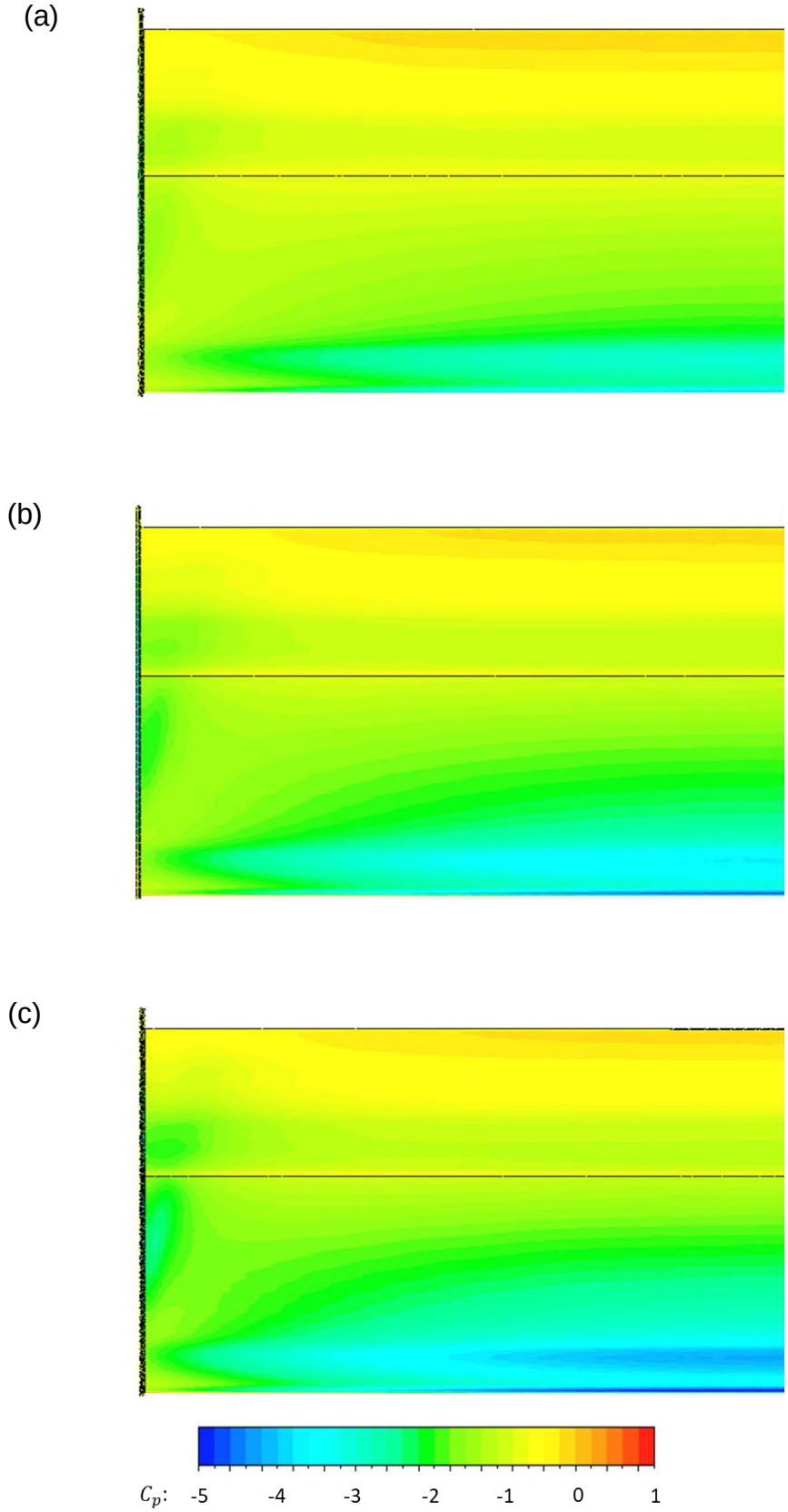

Figure 35 Pressure coefficient contours on lower surface of the wing at high ride heights showing the leading edge lowermost (a) h/c = 0.395 (b) h/c = 0.263 (c) h/c = 0.211

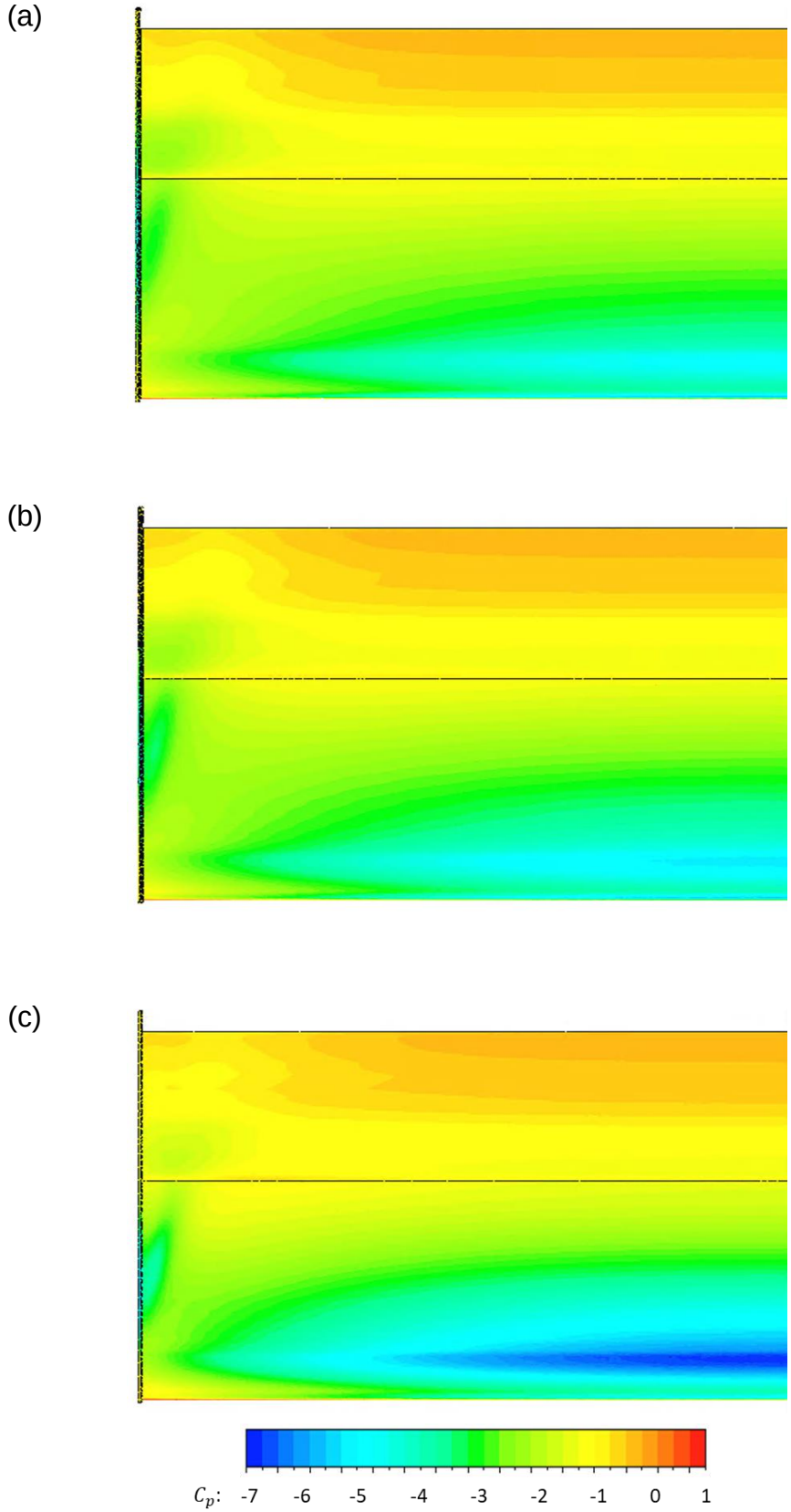

Figure 36 Pressure coefficient contours on lower surface of the wing at low ride heights showing the leading edge lowermost (a) h/c = 0.158 (b) h/c = 0.132 (c) h/c = 0.079

(a)

(b)

(c)

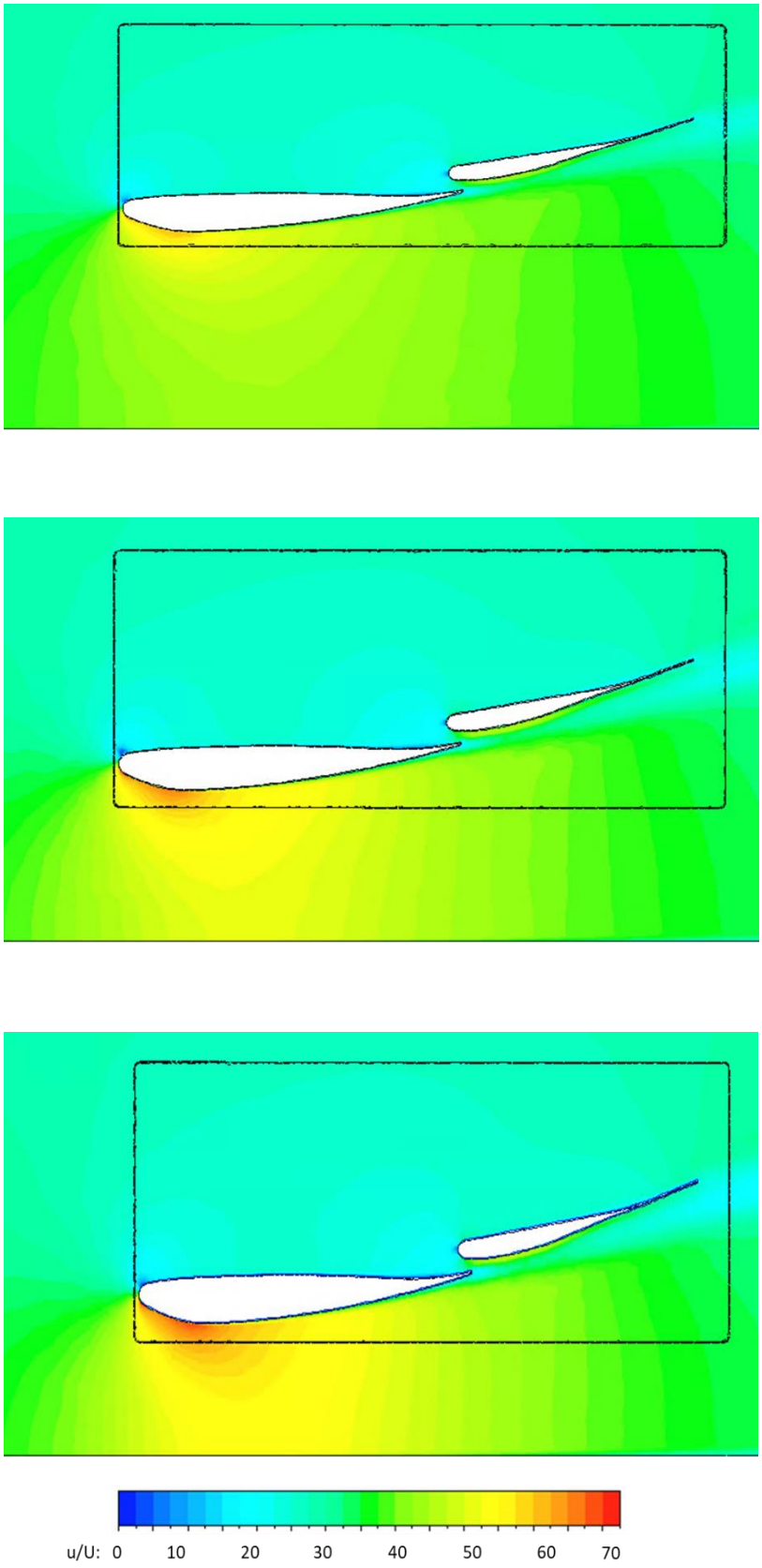

Figure 37 Velocity contours at high ride heights (a) h/c = 0.395 (b) h/c = 0.263 (c) h/c = 0.211

(a)

(b)

(c)

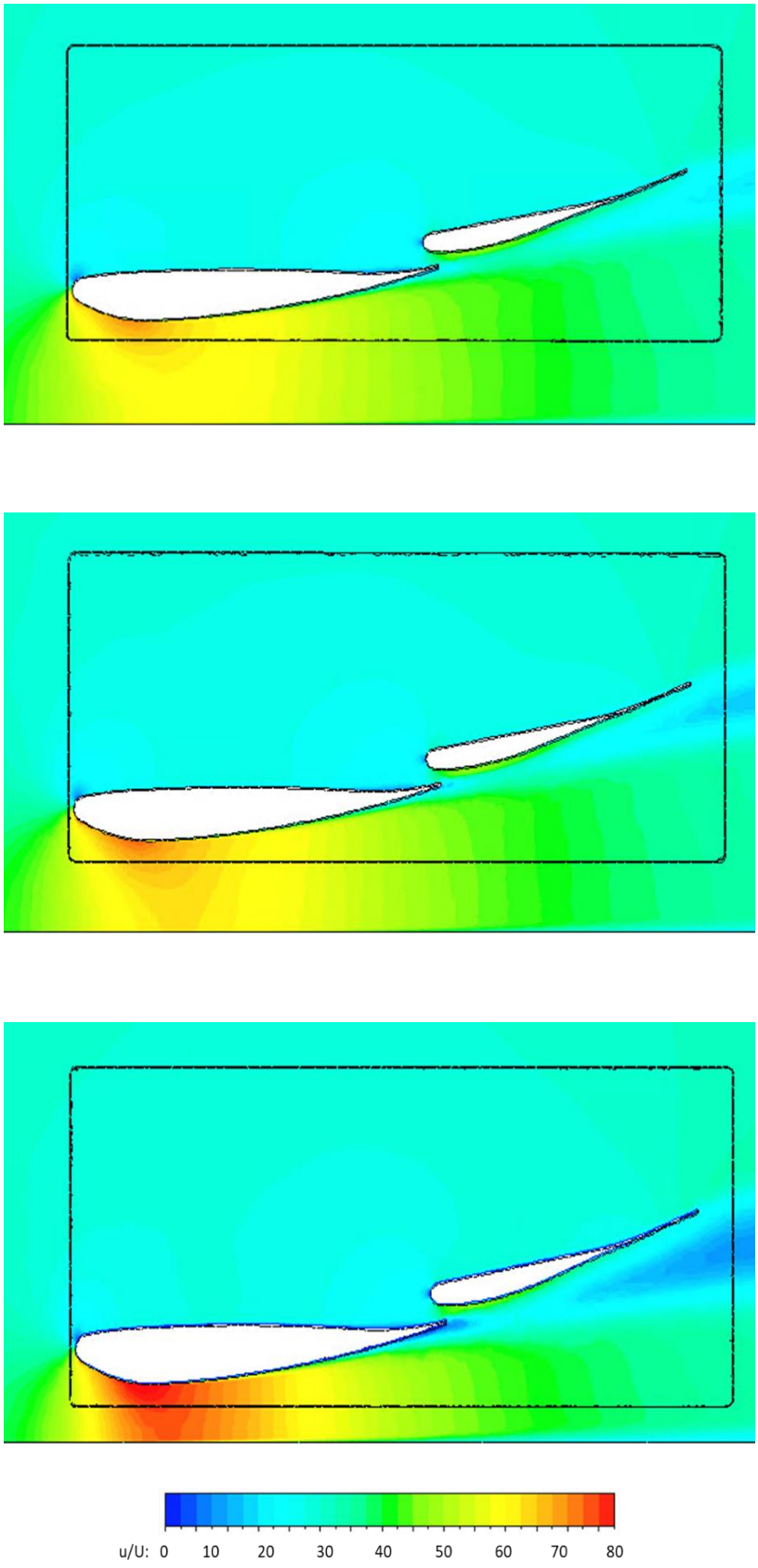

Figure 38 Velocity contours at low ride heights (a) h/c = 0.158 (b) h/c = 0.132 (c) h/c = 0.079

Figure 39 shows the chordwise surface pressures at the wing centre and towards the wing tip, which are described at two heights for clarity and compared to experimental results [19]. Non-FSI modelling results at the wing tip at both ride heights are also included, and the aeroelastic effect is better represented at the wing tip area compared to the centre of the wing. Figure 39 (a) presents the results of the surface pressure distribution at h/c = 0.395. From the centre to the tip, the suction on the bottom surface of the primary part is decreased. The spike on the leading edge has the most suction over the main part in the centre, whereas for the tip, the spike is not as sharp, and the suction peak at x/c = 0.1 is greater. The pressures on the upper surfaces of both the main element and flap are reduced from the centre to the tip. The non-FSI case with the rigid wing at the wing tip ap-pears to follow the similar trend of the pressure distribution to the experimental result. It was observed that the aeroelastic composite wing produces less suction on the main element, but marginally more suction on the flap near the wing tip in comparison with the experimental data and non-FSI data. Figure 39 (b) shows the surface pressure distribution at h/c = 0.105. The load on the main element suction surface is significantly reduced towards the wing tip, and the reduction is greater than at higher heights. From the centre to the tip, the pressure on the upper surfaces of both the main element and the flap is slightly reduced. Near the wing tip, the non-FSI simulation generally shows a good agreement with the experimental chordwise pressure distribution. It was found that with the FSI modelling, the suction peak on the lower surface of the main element is reduced and consequently alleviates the pressure recovery demand. The flap produces more suction load with the elastic wing, generating an

additional favourable pressure gradient which might result from the wing flexibility. The velocity contours at the wing centre and tip at different heights are visualised in Figure 38. As discussed above, the accelerated flow underneath the main element is presented with the ground height decreased as shown in Figure 40 (a) and (c). It is depicted that the flow speed on the bottom surface of the main element was found to be slowed from the centre to the tip as shown in Figure 40 (a) and (b). In addition, the reduction in flow speed is greater at lower ride height, and Figure 40 (d) illustrates a region of low velocity downstream underneath the trailing edge of the flap.

The double-element wing exerts extra stresses on the top and bottom surfaces of both the main element and the flap when compared to a single-element wing, the latter of which is relatively unaffected by the ride height variation. The main element suction sur-face generates more significant suction loading and the pressure recovery towards the trailing edge is less demanding. According to Smith [149], the existence of the second element, the flap, induces a larger portion of circulation on the main element, referring to as the circulation effect which is beneficial to increasing the wing performance with multiple elements. This effect may be seen in the surface pressures in the centre of the rigid wing, which shows an increase in suction pressure as the ride height decreases.

With the aeroelastic-modelled wing, the surface pressure distributions at various ride heights demonstrate the different pressure characteristics at the wing centre and tip. The suction loading on the main element lower surface reduces from the centre to the tip due to the reduced effective angle of attack caused by the wing tip vortex upwash. In comparison with the suction on the main element

of the rigid wing cases near the wing tip at both ground heights, the aeroelastic effect derived by the composite elements causes the wing to be tilted backwards, resulting in less suction pressure and stabilising the pressure recovery. On the flap, the FSI modelled-composite wing marginally increases the suction pressure near the wing tip compared to the rigid wing. As the flap is deflected by the aerodynamic loading, the angle of attack is reduced producing a more favourable pressure gradient at the first part by moving the centre of pressure rearwards, which might help to de-crease the drag. Simultaneously, additional suction may be generated by stronger interaction with the main element vortices underneath.

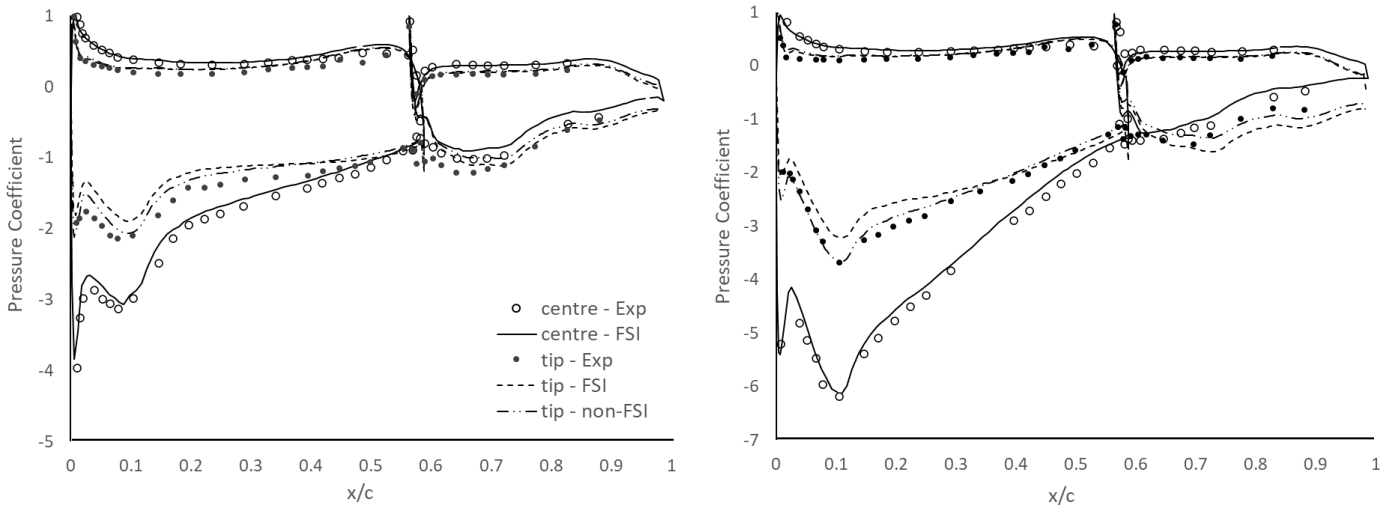

Figure 39 Comparison of chordwise surface pressure distributions at wing centre and near to wing tip (a) h/c = 0.395 (b) h/c = 0.105

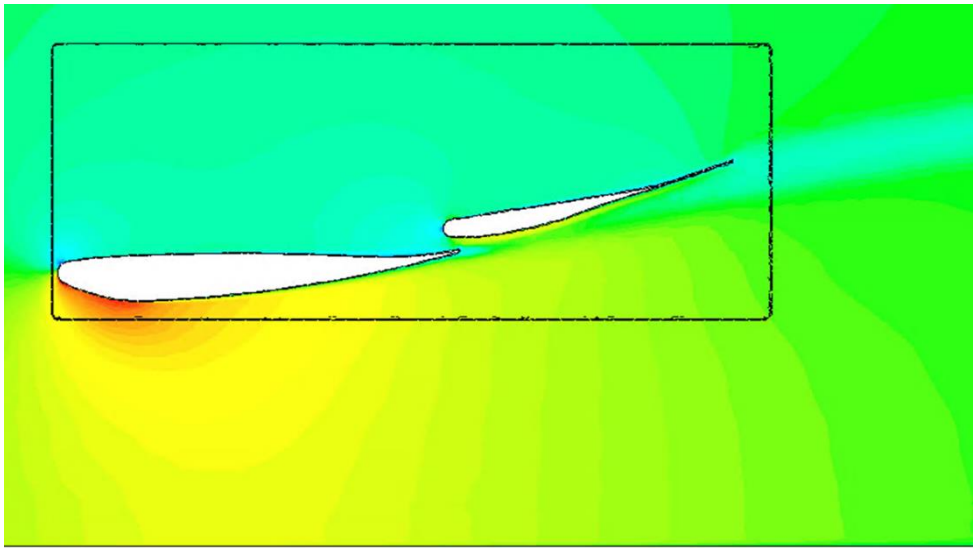

(a)

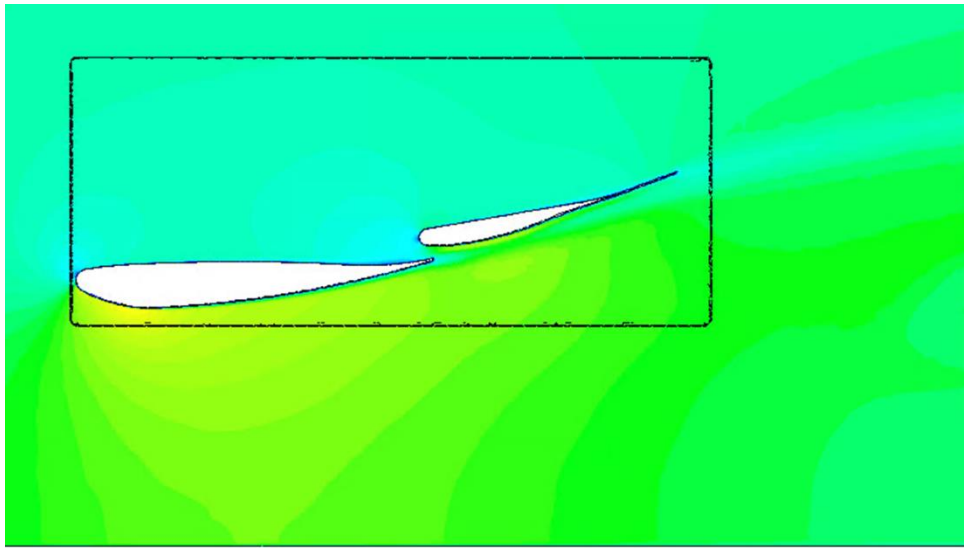

(b)

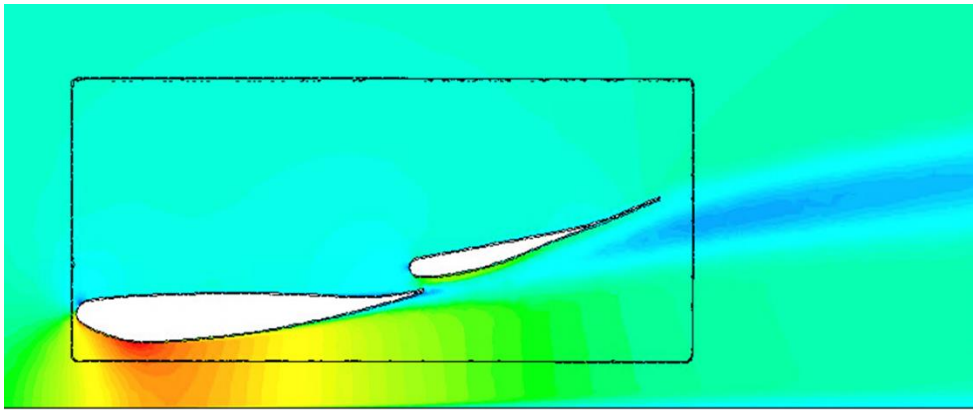

(c)

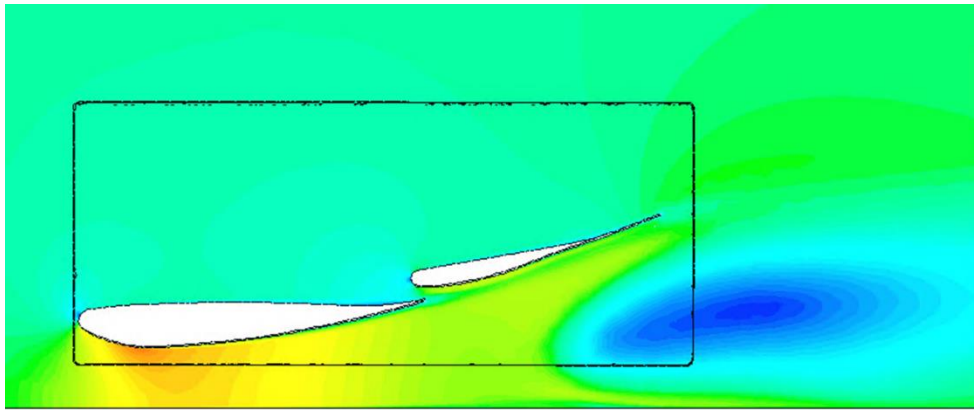

(d)

Figure 40 Velocity contours at wing centre and tip at different heights (a) h/c = 0.395, centre (b) h/c = 0.395, tip (c) h/c = 0.105, centre (d) h/c = 0.105, tip

5.3.2 Spanwise surface pressures

In addition to the chordwise pressure distribution analysis, the spanwise surface pressures are numerically calculated at the quarter-chord positions on both the main element and flap and compared with the experimental results [19]., The estimated spanwise surface pressure distribution on the main element at various ride heights is depicted in Figure 41. For the large heights shown in Figure 41 (a), it can be seen that the suction loading on the primary element suction surface increases with decreasing the distance between the wing and the ground, which shows greater rate at the wing centre. However, similar to the chordwise pressures, the pressures on the upper surfaces remain independent of a change in the height. Figure 41 (b) shows the same results for the smaller heights. As the height is lowered, a similar pattern to the upper instances may be seen, with minimal change in pressures on the pressure surfaces.

Figure 42 shows the spanwise pressure distribution on the flap in ground proximity. For the large heights shown in Figure 42 (a), a consistent increase in suction loading is observed on the lower surface of the flap near to the tip outside of around $\eta = 0.04$. Near to the centre the bottom surface suction increases with decreasing the height and little variation of suction pressures is displayed towards the central part of the wing from approximately $\eta = 0.25$. The flow on pressure surfaces stays constant when the wing height is changed. It can be seen that the gradient of suction pressures near the tip increases compared to the wing centre part, for example, at h/c = 0.211 $C_p \approx -1.12$ near the inboard part of the wing, whereas $C_p \approx -1.89$ near the tip.

Figure 42 (b) shows the same results at smaller heights. The general trend from the tip to the centre is similar to the larger cases – significant change in suction near the outboard portion and little variation of pressure from near the tip towards the inboard. On the other hand, the suction pressure increase at the tip is greater for mall heights; $C_p \approx -2.31$ compared to $C_p \approx -1.89$ for the large height. At this height, the suction at the central portion reduces with increasing the ground proximity. Furthermore, the suction surface loading near to the tip reduces at greater extent. The pressures on the upper surfaces tend to be slightly increasing towards the inboard portion of the wing and to be decreasing marginally with reducing height.

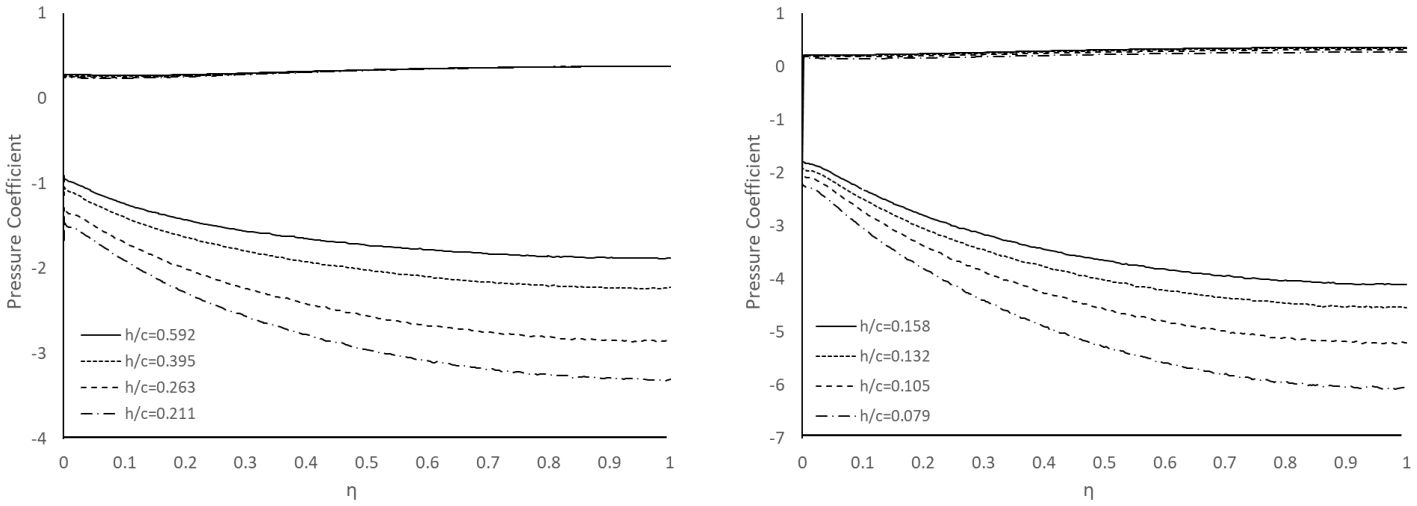

(a) (b)

Figure 41 Spanwise surface pressure distributions on main element over non-dimensional span from wing tip, η (a) large heights (b) small heights

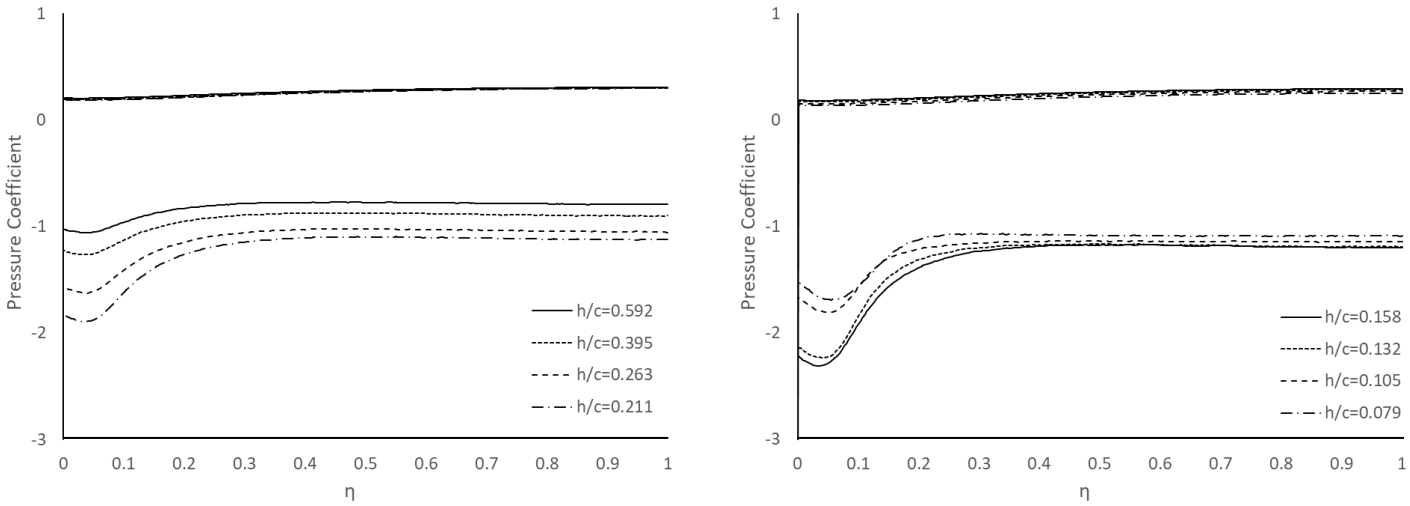

(a) (b)

Figure 42 Spanwise surface pressure distributions on flap over non-dimensional span from wing tip, η (a) large heights. (b) small heights

Following the analysis on the computational spanwise surface pressure distributions in ground proximity over the main element and flap, Figure 43 shows the numerical FSI findings at various heights in contrast to the experimental data; h/c = 0.395, 0.211 and 0.105. The spanwise pressures on the main element are shown in Figure 43 (a). As described, the general trend of the suction increase on the suction surface with decreasing the ride height is accurately captured. However, it can be noticed that the magnitude of suction loading on the lower surface is underpredicted across the span compared to the experiment and the discrepancy becomes greater towards the central portion of the wing – at h/c = 0.395, $C_p \approx -2.22$ for the numerical result compared to $C_p \approx -2.64$ for the experiment. The surface pressures on the upper surfaces are correctly predicted remaining independent of changes in ride height. Figure 43 (b) shows the flap with the same effects. Similarly, the estimated spanwise surface pressures on the

suction surfaces accurately depict the rise in suction as the wing approaches, however, as with the main element scenario, less suction is created along the span for all heights. Again, the pressure across the pressure surfaces is precisely computed, revealing that there is minimal change as the ground height decreases. Figure 44 depicts the details of the spanwise surface pressure distributions at various ride heights over both the main element and flap. As previously stated, the computational findings underpredict the pressure on the top and lower surfaces, and the amount of the discrepancy grows as the height of the wing is decreased towards the inboard portion.

Figure 45 illustrates the maximum deflection and the twist angle of the wing throughout a range of ride heights, which occur at the trailing edge of the flap. The overall trend of the deflection increase is achieved when the ground proximity is increased as shown in Figure 45 (a). With the decrease in ride height up to h/c = 0.158, the gradual increase in deflection is observed, reaching the corresponding value of 1.05 *mm*. For further reduction in the height, little variation is shown with the maximum value of 1.09 mm at h/c = 0.105. The boundary condition of the flow speed used in our investigations corresponds to the experimental conditions of the reference data. The maximum twist angle of the wing flap is also presented in Figure 45 (b). The twist angle is calculated based on the distance difference of each reference point positioned at the leading edge and trailing edge respectively. The variation of both deflection and twist angle computed in this research is marginal due to the low velocity inlet boundary condition and small wing aspect ratio. However, such variation analysed in this study indicates that the centre of pressure position is shifted downstream due to

the incidence reduction induced by the aeroelastic effect, resulting in the pressure difference and ultimately aerodynamic performance change. Note that regardless of the FSI modelling of the wing, the ground effect over the variation of ride height has a huge impact on the flow structures and overall wing performance. As discussed previously, the wing flexibility, especially near the wing tip, caused by the structural elasticity has potential to cause changes in the flow field around the wing and the discrepancy in comparison with the non-FSI simulations could prevail in this area. Therefore, it is important to consider the aeroelastic effect in ground proximity in a dynamic condition.

The flow on the main element and the flap exhibit unique three-dimensional properties for a range of ride heights as the ground is approached, as indicated in the spanwise pressures. As shown in Figure 41, when height reduction, the suction pressure on the main element increases across the span due to enhancement of the ground effect, whereas the pressure on the upper surface remains constant. The similar feature can be found at higher heights on the flap span. However, at small heights the suction pressure is reduced with decrease in the height. As briefly mentioned previously, the suction loading on the flap has strong relation with the vortex generated. For the low ride height, the vortex is likely to break down or even burst caused by the unfavourable pressure gradient. When it happens, the axial velocity of the vortex suddenly drops, resulting in reduction in the vortex strength and induced velocities. Therefore, the suction on the flap is reduced due to the weak and diffused vortex and the influence of the vortex becomes stronger with lower heights. The FSI simulations compared to the experiment show less suction pressures on the lower surfaces of both the

main element and flap, resulting from decreasing the effective incidence. The wing is constructed with the composite material which includes the elastic characteristics. When the aerodynamic loading is applied on the main element or flap, the wing is tilted backwards in a way of being such as a wash-in effect. Therefore, the FSI modelled wing may produce less suction pressures across the span.

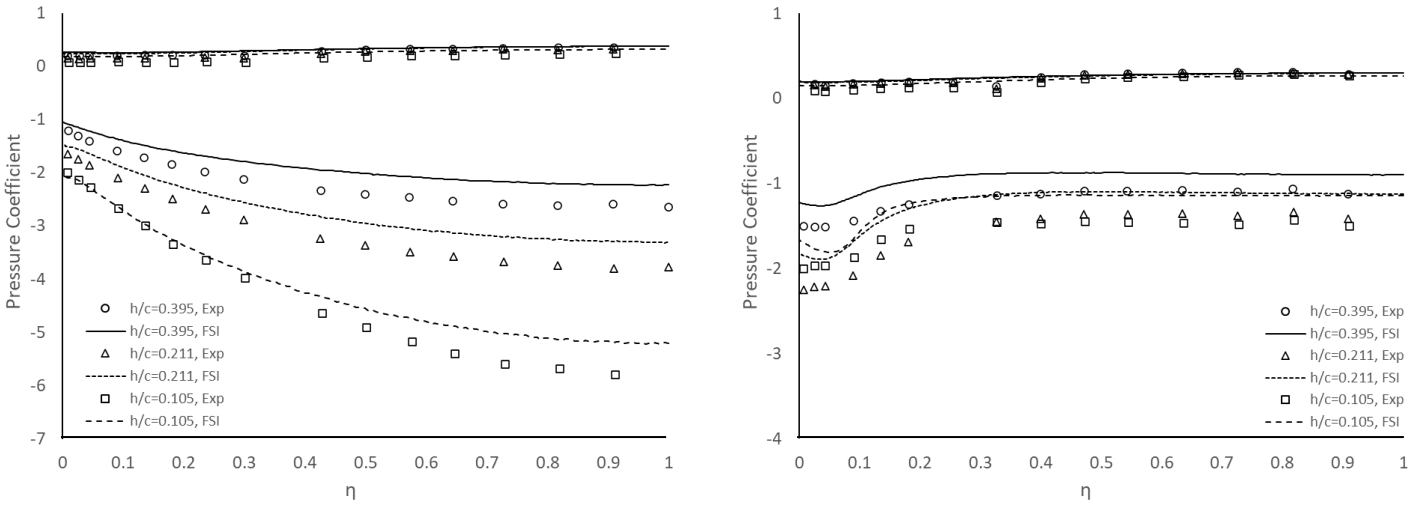

(a) (b)

Figure 43 Spanwise surface pressure distributions at various ride heights over non-dimensional span from wing tip, η (a) main element (b) flap

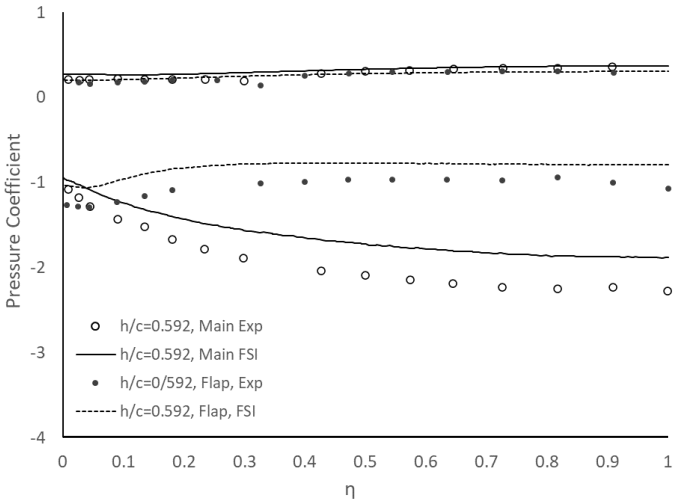
Pressure Coefficient
η
h/c=0.592, Main Exp
h/c=0.592, Main FSI
h/c=0/592, Flap, Exp
h/c=0.592, Flap, FSI

(a)

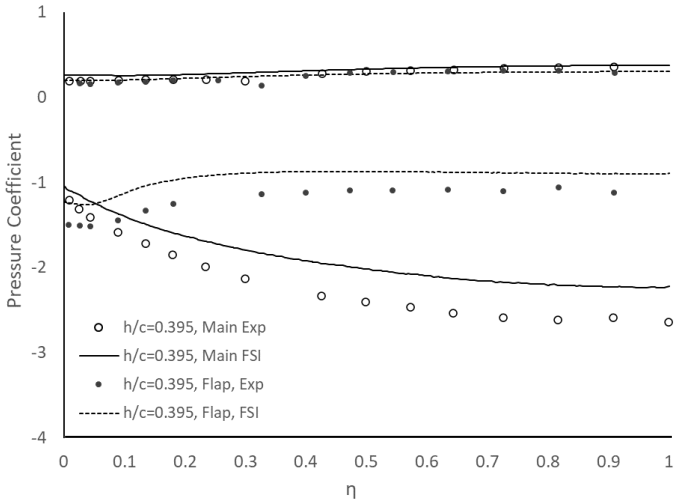
Pressure Coefficient
η
h/c=0.395, Main Exp
h/c=0.395, Main FSI
h/c=0.395, Flap, Exp
h/c=0.395, Flap, FSI

(b)

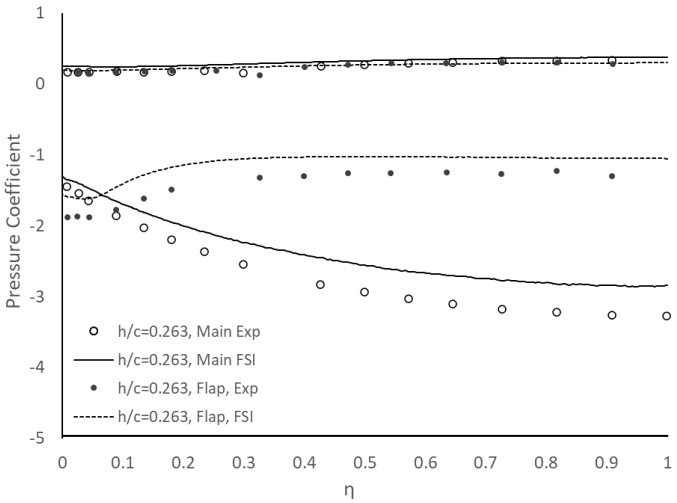
Pressure Coefficient
η
h/c=0.263, Main Exp
h/c=0.263, Main FSI
h/c=0.263, Flap, Exp
h/c=0.263, Flap, FSI

(c)

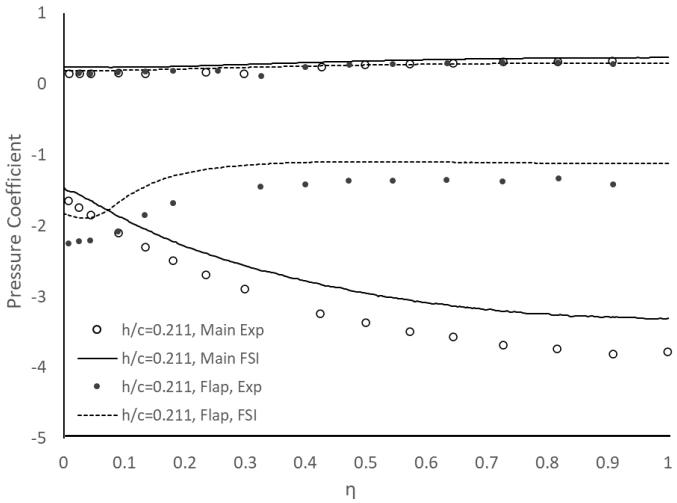
Pressure Coefficient
η
h/c=0.211, Main Exp
h/c=0.211, Main FSI
h/c=0.211, Flap, Exp
h/c=0.211, Flap, FSI

(d)

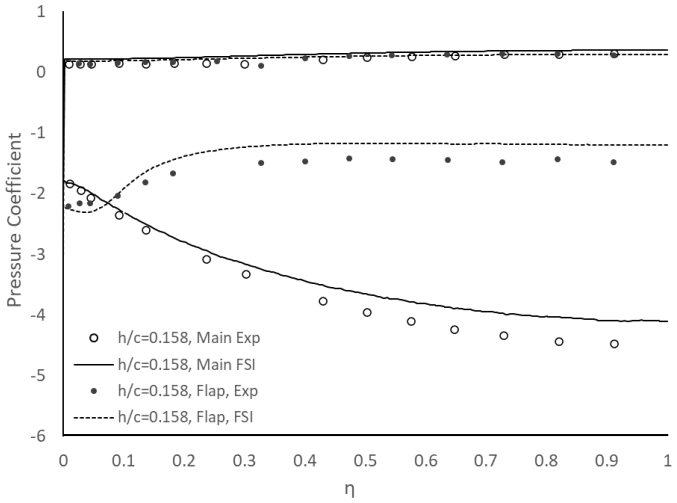

(e)

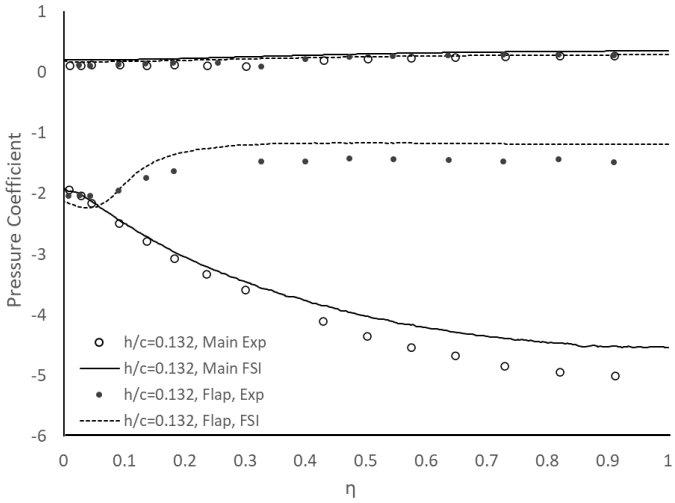

(f)

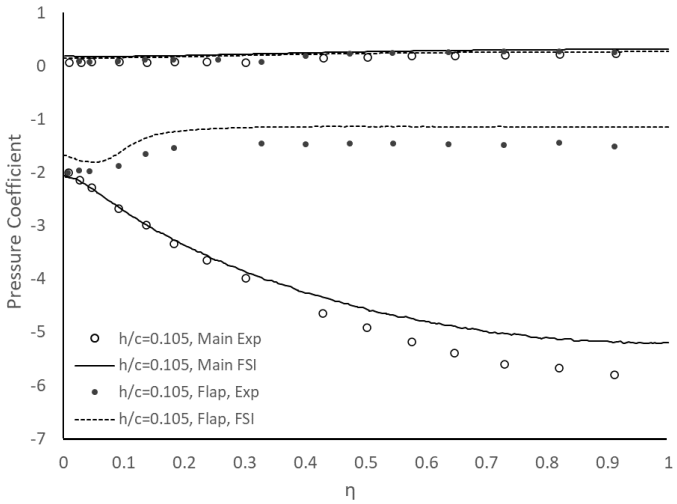

(g)

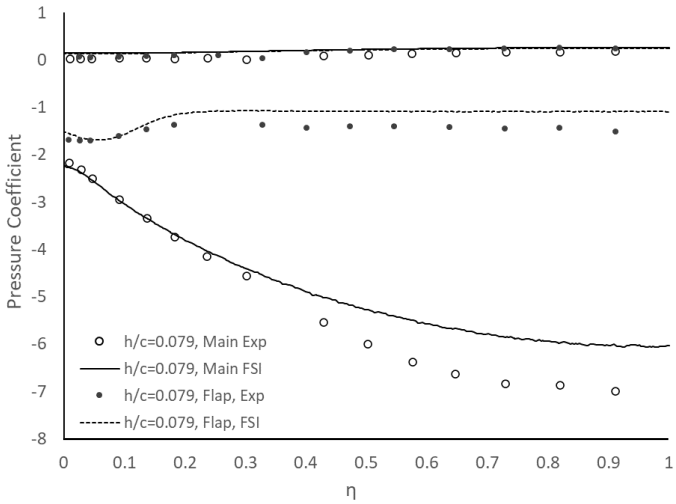

(h)

Figure 44 Spanwise surface pressure distributions on main element and flap at various ride heights over non-dimensional span from wing tip, η (a) h/c = 0.592 (b) h/c = 0.395 (c) h/c = 0.263 (d) h/c = 0.211 (e) h/c = 0.158 (f) h/c = 0.132 (g) h/c = 0.105 (h) h/c = 0.079

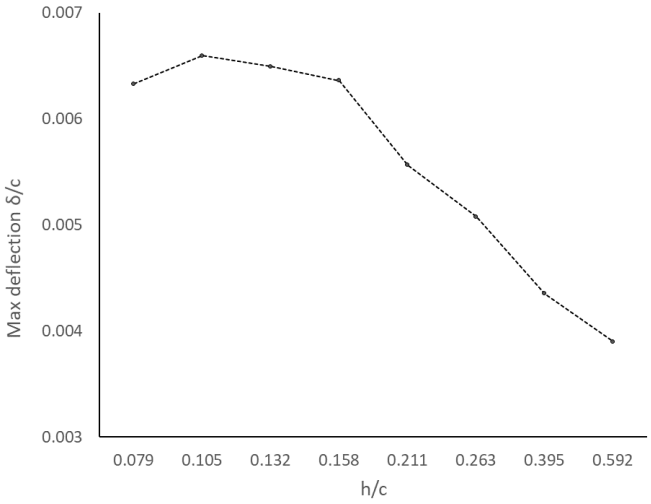

(a)

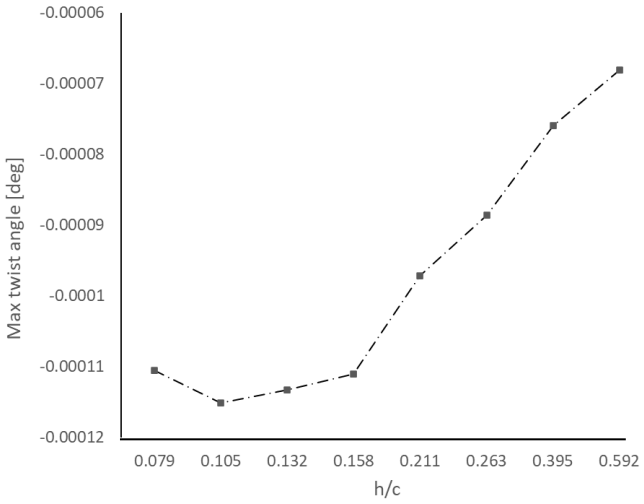

(b)

Figure 45 Deflection of double-element composite wing at various ride heights (a) normalised maximum deflection, (b) maximum twist angle

5.3.3 Aerodynamic forces

Figures 46 show the predicted aerodynamic forces created by the double element composite wing in close proximity to the ground. The experimental forces measured by integration of the surface pressures are provided together as a reference [32]. The overall characteristics of downforce with variation of ride heights shown in Figure 46 (a) are correctly calculated. As the height is lowered, the computational downforce grows until it reaches its maximum value, followed by a sudden drop of downforce further down. Up to h/c = 0.211, the gradient of the curve is gradual and smooth and above that height rather sharp rate of the line can be observed until the peak in the downforce. However, compared to the experimental results showing that the peak occurs at a height of h/c = 0.066,

corresponding to $C_L = 2.579$, the maximum value obtained by the FSI simulation is reached at a higher height of h/c = 0.079 with less amount of downforce corresponding to $C_L = 2.499$. In addition, the downforce reduction below the peak height happens at greater extent with the elastic composite wing. Figure 46 (b) shows the variation of drag force with various ride heights in comparison with the experiment. Overall trend of drag increase with increasing ground proximity is accurately predicted with a smooth and gradual gradient. However, with the numerical solution including the aeroelastic effect, a greater amount of drag force is obtained at all ride heights and lower gradient at low heights is observed.

As proved in previous section that changes of bottom surface suction pressure of the primary element are greater than those of the flap, it is reasonably surmised that the primary element is more attributed to generation of downforce, which has been previously presented [32]. It also means that the pressure changes around the flap are less sensitive than the main element to variation of the wing height as it is further above from the ground. As the wing including the main element is deflected under the aerodynamic loading, the distance between the lowest point of the wing and the ground is temporarily reduced compared to the geometrical position. The flow field very close to the ground may be sensitive to even small perturbation of changes. Consequently, as the wing is deflected at low height due to its structural characteristics under aerodynamic loading, the maximum downforce can be achieved at the higher height than the experiment. The shorted distance from the ground may cause strong adverse pressure gradient to bring forward in streamwise direction resulting in early vortex breakdown or burst. Also, this effect could impede the vortex generation and build up. For the aerodynamic

analysis on the double element aerofoil, Mahon [38] mentioned that the drag is mainly generated by the flap and the majority of it is attributed to the wake-induced drag. With the three-dimensional wing used in this study, the drag can also result from the induced drag which is a by-product of the wing tip vortices. Stronger wing tip vortices induced by enhanced flow entrainment at the lower ride height as a result of the wing deflection are created and consequently more induced drag is generated.

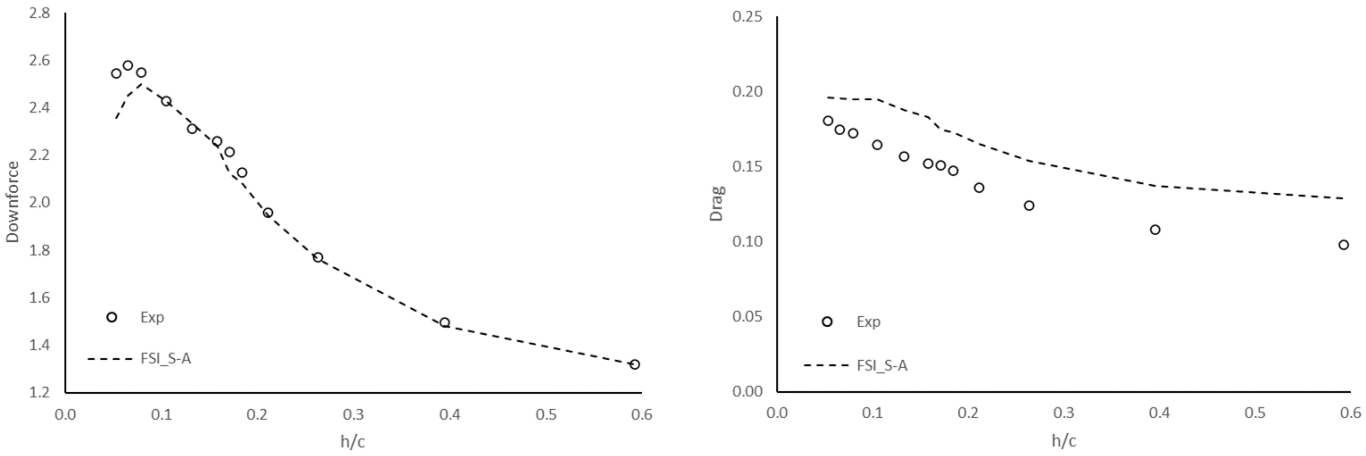

(a) (b)

Figure 46 Comparison of aerodynamic loads of double element composite wing at different ride heights between experiment and FSI model (a) lift coefficient (b) drag coefficient

In line with the FSI analysis performed with the single element wing, to investigate the influence of the wing deformation on the airflow separation, the streamwise wall shear stress on the lower surface of the double element wing model is presented at the ride height of h/c = 0.105 in Figure 47. The value of the

shear stress equivalent to 0 Pa indicates the boundary layer separation. Compared to what is discovered with the rigid wing in Figure 47 (a), the wall shear stress contour plots obtained with the flexible wing demonstrates that the bottom surface of the wing is less affected by the separation as a result of the wing deformation. It is revealed that a smaller region of low shear stress is observed near the trailing edge of the main element, but more area of the low shear on the flap. The structural flexibility causes the wing to be tilted backwards, resulting in being able to stabilise the whole system against the adverse pressure gradient.

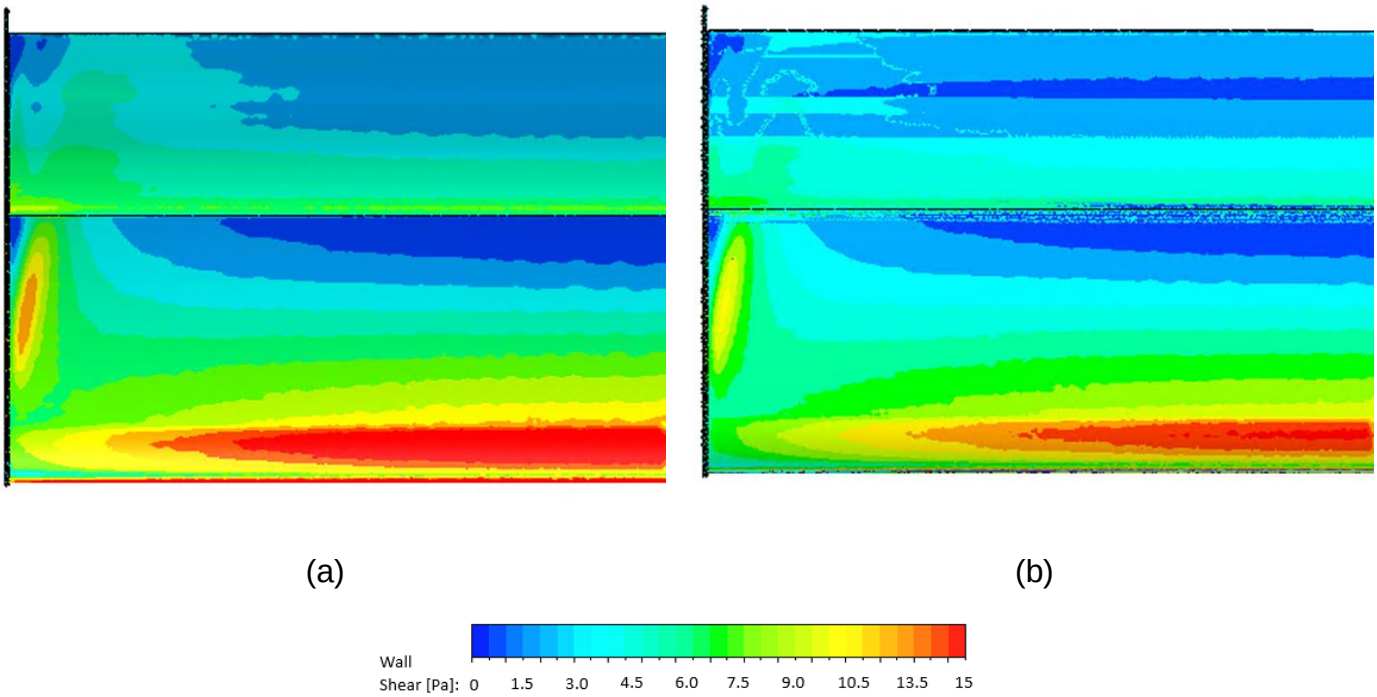

Figure 47 Wall shear stress contour on lower surface of a double element wing at h/c = 0.105 showing the leading edge lowermost (a) non-FSI (b) FSI

Following the analysis on the flow separation using the wall shear stress on the surface of the wing, Figure 48 presents the total pressure coefficients at a

cross section of x/c = 0.5 at h/c = 0.105. Top vortices coming off the top edge of the endplate appear reasonable for both the non-FSI and FSI wings and the shear layers along the trailing edge in spanwise direction are also well depicted. With regards to the lower vortices, significant amount of loss (blue area) is seen with the aeroelastic wing in Figure 48 (b), signifying lower total head behind the wing. It means that the main vortex coming off the lower edge of the endplate has less energy to be propagated further downstream. Two reasons could be proposed for reduction in the total pressure of the main vortex. It is likely that the direct influence of the ground caused by the wing deformation could be a reason. Also, when the wing is flexed and approached to the ground, separated shear layers on the ground may exist and be ingested into the main vortex. Another reason could be excessive adverse pressure gradient. Reduction in ground height due to the wing deflection causes a larger adverse pressure gradient, which slows the lower edge vortex down in axial direction. In Figure 49, the total pressure coefficients at a cross-section of y/c = 0.45 at h/c = 0.105 are presented. It is shown in Figure 49 (b) that the lower edge vortex of the flexible wing is shifted upstream, which is in agreement with the observation in Figure 47.

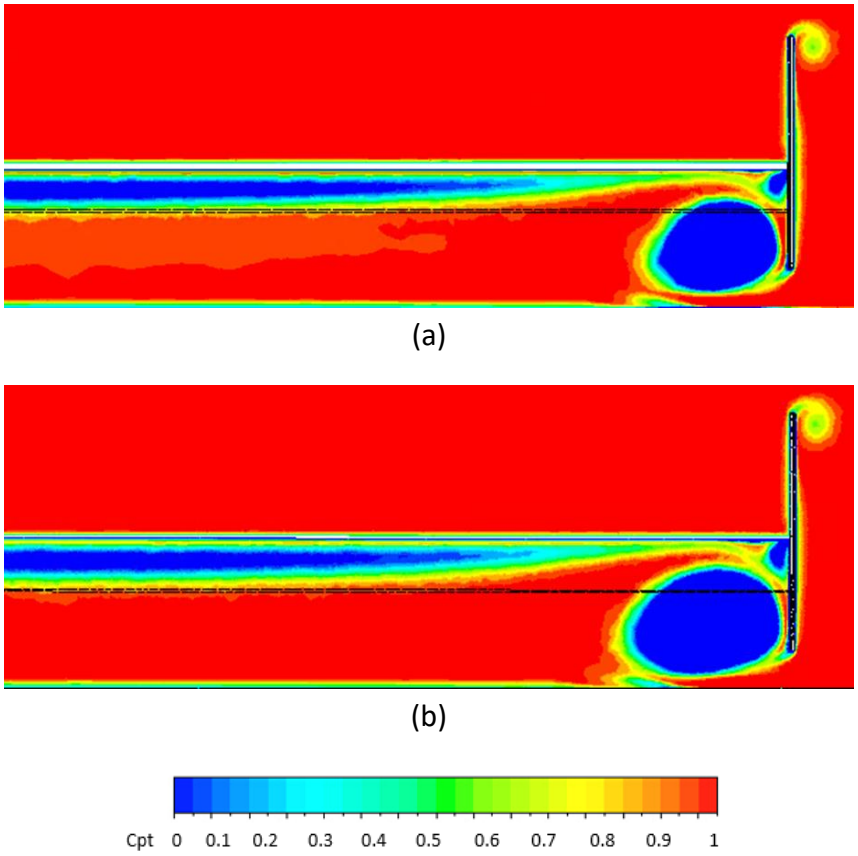

Figure 48 Total pressure coefficient contour of a double element wing at x/c = 0.5 at h/c = 0.105 on front view (a) non-FSI (b) FSI

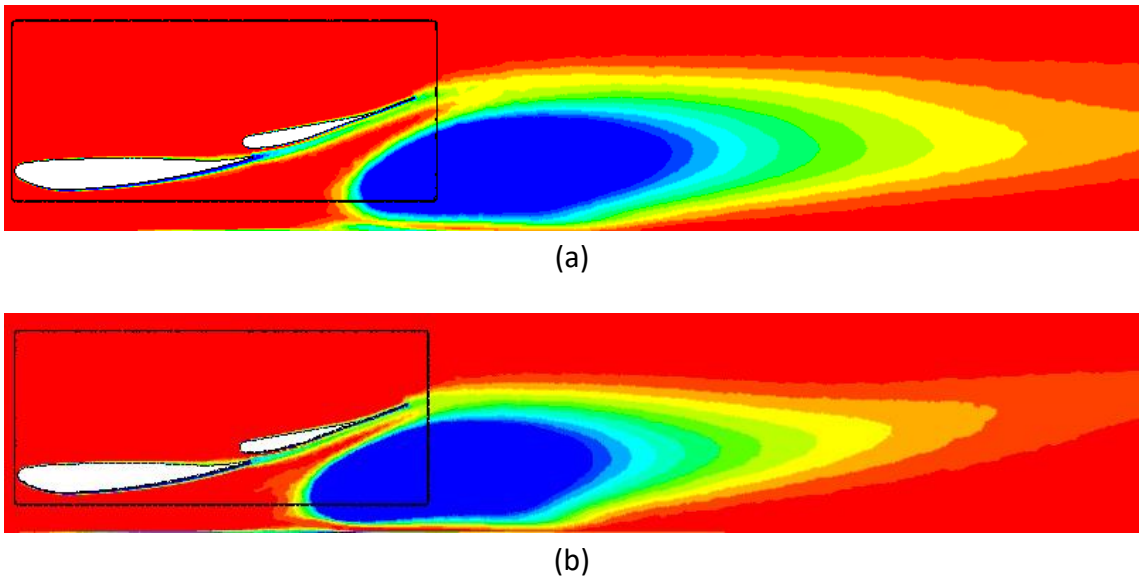

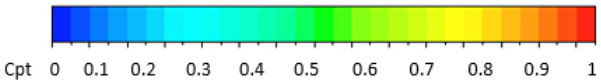

Figure 49 Total pressure coefficient contour of a double element wing at y/c = 0.45 at h/c = 0.105 (a) non-FSI (b) FSI

Contours of the planar vorticity around the double element wing at h/c = 0.105 are described in Figure 50 using the Q-criterion. The high positive strong vorticities in red can be found in both upper vortices. Along with the strong main lower vortices rolling up, a secondary area of negative vorticity (blue) due to the induced velocity and the shear layers is observed with both cases. On the other hand, the flexible wing shows tendency of the vortex dilution presenting wider area of the negative vorticity adjacent to the main vortex and its core. Further observation of the wing tip vortices is illustrated in Figure 51 using a three-dimensional Q-criterion. All existing vortices, such as upper vortices and lower vortices, around the wing are well captured with both wing models. In accordance with the discussion using the total pressure coefficient and planar vorticity analysis, the main lower vortex of the aeroelastic wing appears to be dissipated earlier than that of the rigid wing model due to the wing deformation, which results in the upstream shifted lower total head vortex and reduction in the pressure gradients between upper and lower surfaces of the wing.

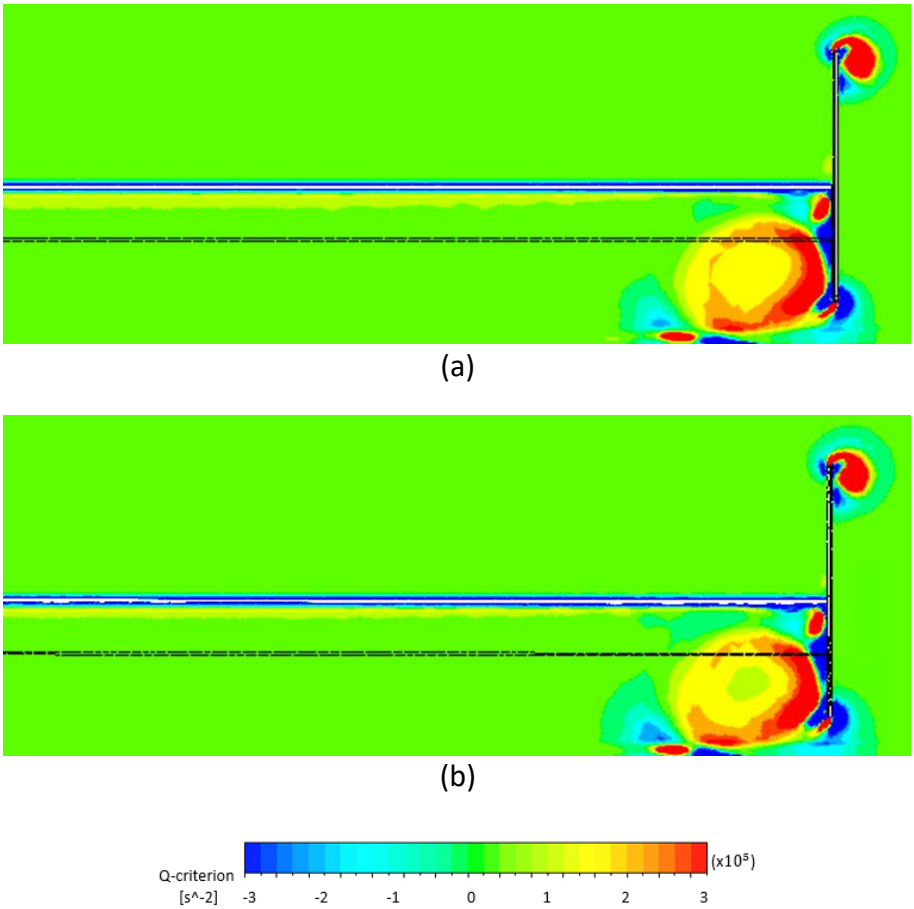

Figure 50 Q-criterion contour of the double element wing at x/c = 0.5 at h/c = 0.105 on front view (a) non-FSI (b) FSI

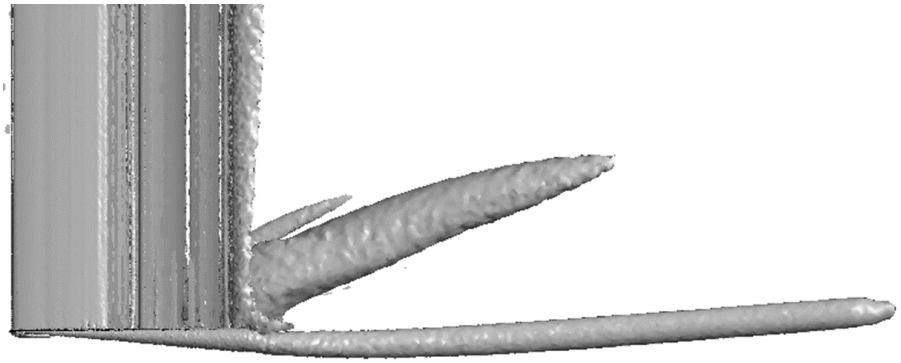

(a)

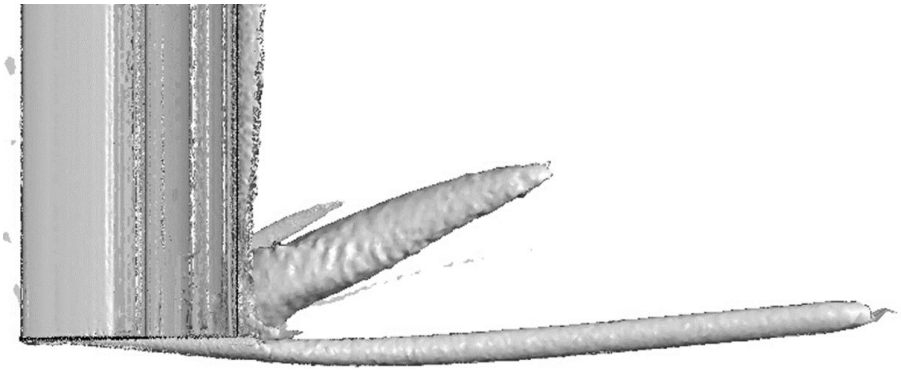

(b)

Figure 51 Three-dimensional Q-criterion contour around the double element wing at h/c = 0.105 on top view showing the leading edge left (a) non-FSI (b) FSI

5.3.4 Wake flow field

For further investigation on the flow field rising from the double element composite wing, the velocity contour plots and the wake survey are acquired at x/c = 1.066 location in terms of various ride heights in the same way that the Laser Doppler Anemometry (LDA) testing produced experimental findings [19]. The general feature of the wake profile with variation of the ride height is correctly captured in comparison with the experiment and does not represent distinct aeroelastic effect as those results are tested at the centre of the wing. Figure 52 shows the contour plots of velocity generated behind the trailing edge of the wing.

At h/c = 0.395 shown in Figure 52 (a), a wake from the wing is presented with a region of low velocity flow near the trailing edge, being deflected upwards as it develops downstream. It can also be seen that a region of flow between the wing and the ground is accelerated with a higher velocity than the freestream. As a result of the unfavourable pressure gradient, further downstream the flow in streamwise direction slows down.

Figure 52 (b) and (c) show the velocity contours at lower ride height, h/c = 0.211 and 0.105 respectively, which show a clear difference of the flow according to the height variation. As the wing is approached to the ground, one of the obvious effects is the wake increase – the wake size thickens, and the wake is more deflected. On the one hand, there is minimal change in a section of the wake from the flap as shown in Figure 53, which presents the wake profile at various ride heights. On the other hand, a substantial change in the flow profile curve caused by the main element occurs as the height is reduced – thicker wake and increased velocity deficit. As discussed previously, the primary element's suction surface causes a considerable shift in the flow field, whereas the pressure surface relatively does not attribute to the change. Therefore, it is speculated that the main element wake is the cause of the wake increase with increasing the ground proximity. Another consequence caused by reducing the height is the boundary layer growth close to the ground. Along with the surface pressure coefficient the velocity streamlines are visualised in Figure 54. As discussed above, as the wing is approached to the ground the flow speed under the main element near the centre increases. On the other hand, near to the tip it is shown

that at lower heights, a zone of reduced velocity is generated by the vortical flow starting from the primary element lower surface end edge.

The wake profile with different ride heights at x/c = 1.066 and its streamwise position are illustrated at Figure 53 and detailed information is listed in Table 15. For the sake of clarity, three ride heights are selected. The general trend between the experiment and numerical results is compromised with a few exceptions. First of all, the boundary layer thickness growth close to the ground is captured (also shown in Figure 52), however underprediction of the minimum velocity within the ground boundary layer is observed. A region of accelerated flow between the wing and the ground and associated velocities is accurately calculated for all heights, but lower boundary of the lower wake is underpredicted for h/c = 0.395 and 0.105. Also, the increase of the jetted flow with decreasing the height is well spotted.

The lower wake boundary is underpredicted for all heights. As a result, the wake thickness increases with increasing the ground proximity due to the change in vertical position of the wake boundary. The gradient of velocity recovery is correctly captured. The velocity deficit within the lower wake is accurately captured with exception of a height of h/c = 0.105, which provides overprediction of minimum velocity compared to the experiment. It can also be observed that when the ride height is reduced, the velocity deficit within the lower wake rises. Similarly, for the upper wake, the upper wake boundary is predicted correctly for all ride heights, however the velocity recovery to freestream is overpredicted, which results in less velocity values above the flap. The velocity deficit within the upper wake is underpredicted for h/c = 0.211 and 0.105 and decreases with

decrease in ride height. The wake thickness of the upper wake is overpredicted for all heights and tends to decrease as the height is reduced.

The analysis on the wake flow field at the centre of the double element composite wing is numerically carried out and compared with the LDA testing results. The overall trend is equivalent to the single element wing case which discussed in the previous chapter. As the wing is approached, the wake thickens and the velocity deficit within the wake increases which is mainly resulted from influence of the main element. Mahon [33] concluded that a region of recirculation created behind the trailing edge of the primary element is greatly attributed to the lower wake and a shape of the trailing edge of the main element could make an impact on the main element wake and further aerodynamic performance. On the other hand, the surface pressures can be used to account for this phenomenon. As discussed earlier, the suction surface pressure of the main element considerably changes and when the height is reduced, the pressure recovery increases. However, there is little perturbation of pressure found on the surface of the flap concerning variation of ride height, which means that the flap is less sensitive to ground proximity due to distance from the ground. Consequently, decreasing the wing height causes the adverse pressure gradient on the main element to increase, which can result in the flow separation and increasing the wake. In comparison with the LDA testing results, the computational wake profile shows generally similar overall feature, but not distinctive as it is taken at the centre of the wing where the aeroelastic characteristics is less effective.

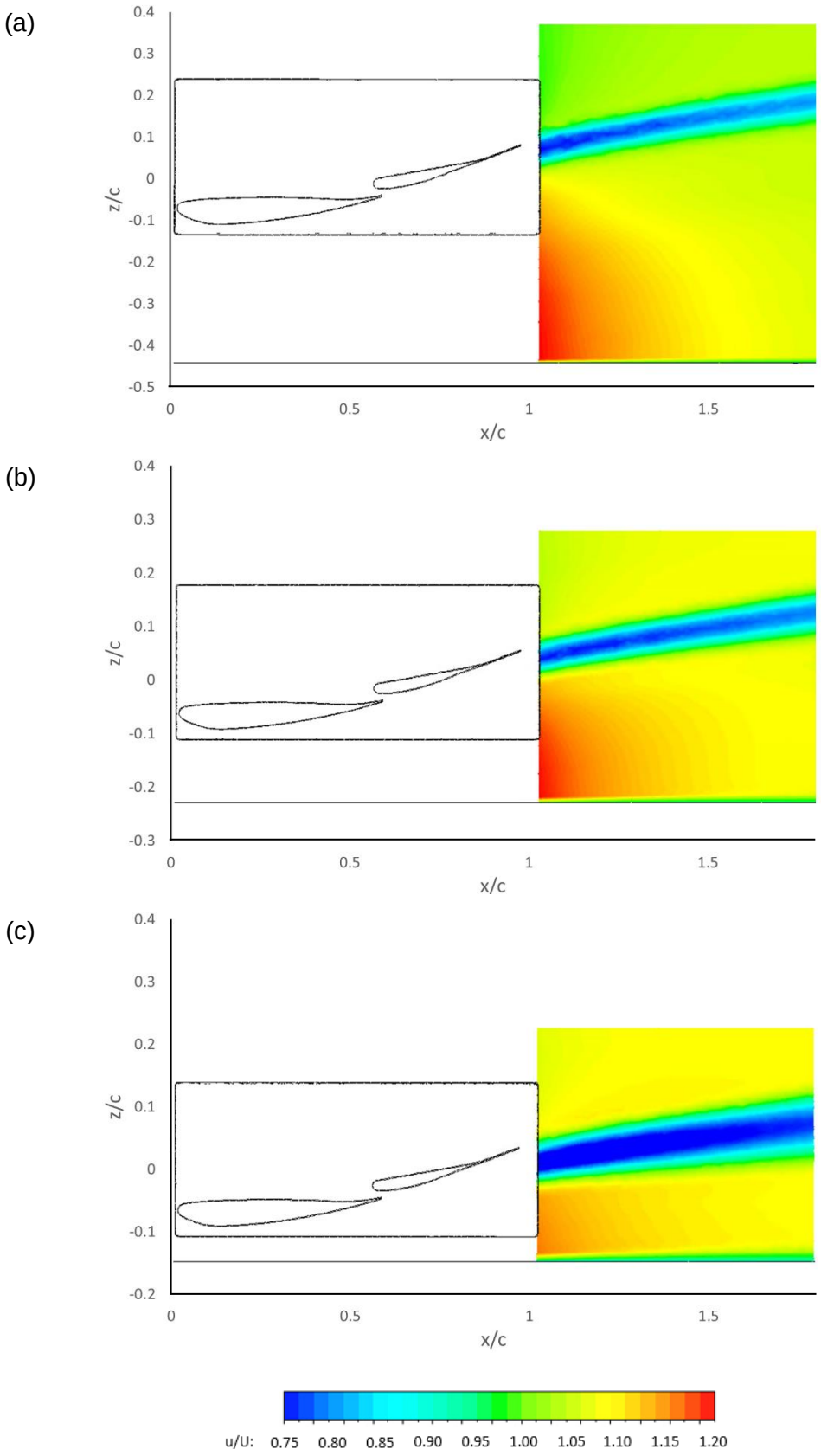

Figure 52 u/U velocity contours at heights of h/c = 0.395, 0.211, 0.105

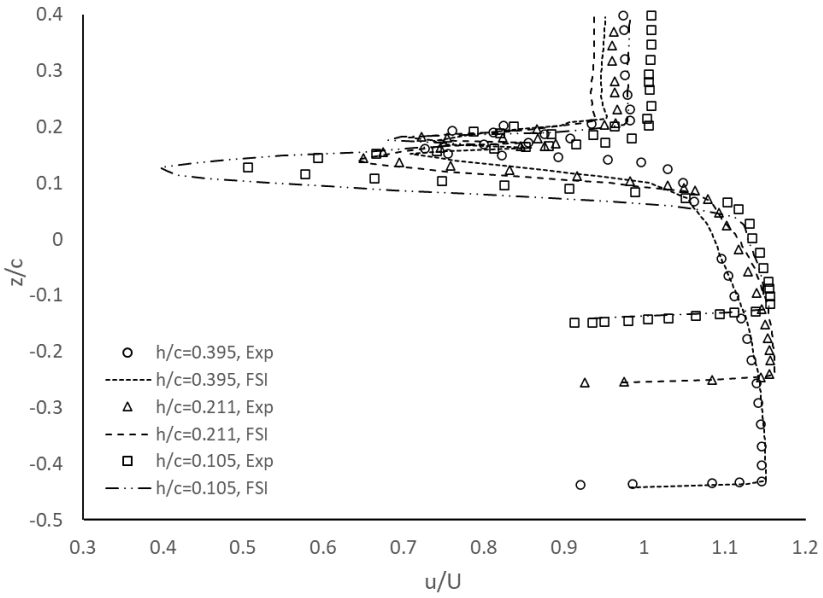

Figure 53 Comparison of wake profiles results between experiment and FSI model at various ride heights at x/c = 1.066

Table 15 Details of wake profiles results for various ride heights at x/c = 1.066

h/c	Exp/FSI	u_{min}/U_∞		$y/c\ at\ u_{min}/U_\infty$		$y/c\ at\ \delta$		δ_{99}/c	
		Low	Top	Low	Top	Low	Top	Low	Top
0.395	Experiment	0.72	0.74	0.164	0.203	0.136	0.217	0.054	0.027
	FSI	0.71	0.74	0.152	0.174	0.112	0.214	0.051	0.051
0.211	Experiment	0.66	0.76	0.150	0.200	0.124	0.207	0.060	0.023
	FSI	0.64	0.71	0.141	0.182	0.105	0.207	0.066	0.036
0.105	Experiment	0.58	0.80	0.134	0.192	0.102	0.198	0.078	0.013
	FSI	0.40	0.68	0.128	0.176	0.070	0.197	0.099	0.028

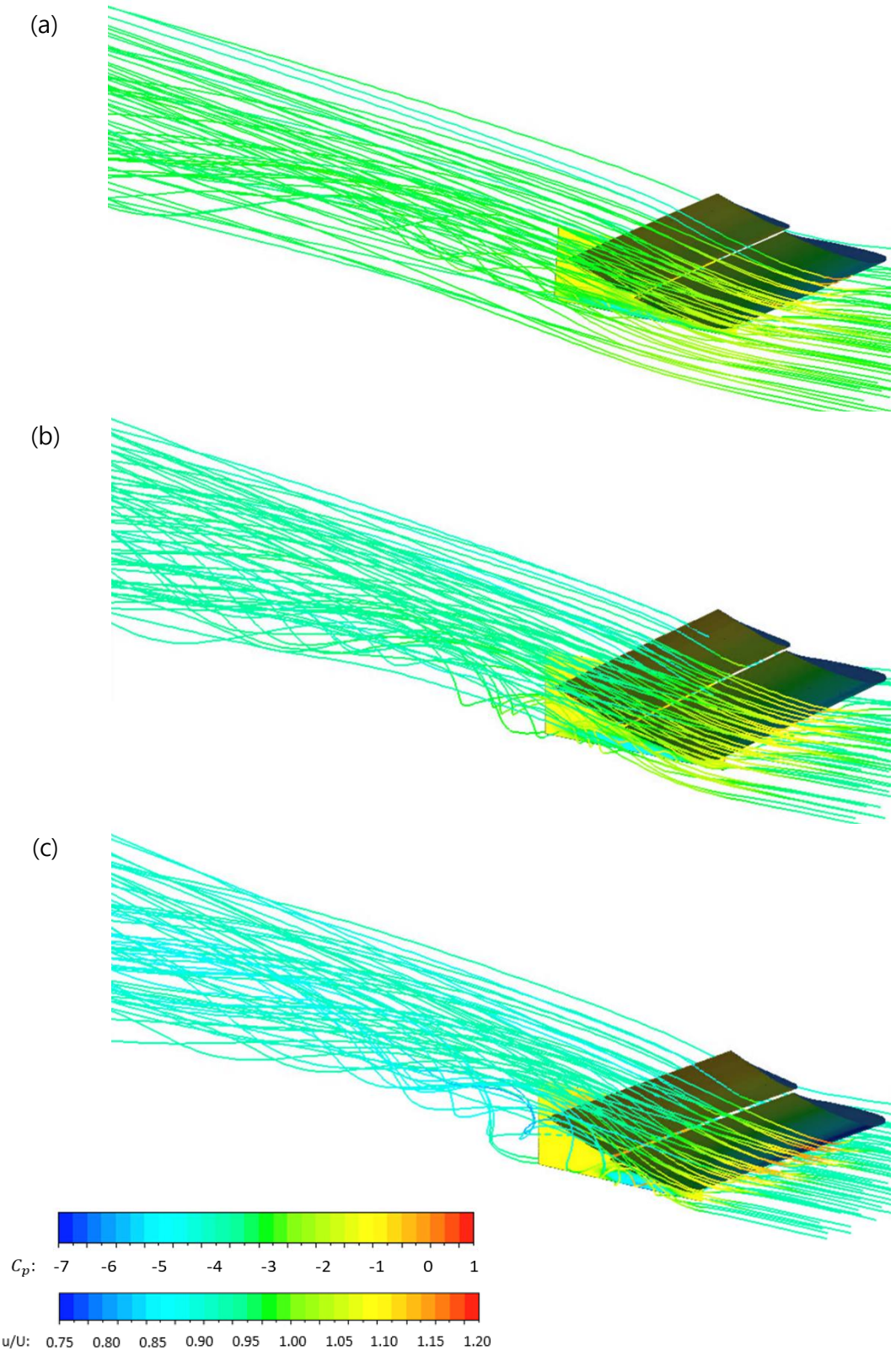

Figure 54 Velocity streamline around the wing and surface pressure coefficient at different ride heights (a) h/c = 0.395 (b) h/c = 0.211 (c) h/c = 0.105

5.3.5 High velocity

The ground effect examination of the double element composite wing is carried out at the same speed as the experiment [19] in order for accurate comparison. However, due to the low-speed range, the aeroelastic effect is not represented sufficiently to show its effect on the aerodynamic performance. In this section, the same wing model with the composite structure in ground proximity is tested using the FSI modelling at higher velocity, 80m/s, which is referred to as high-speed range in F1 application.

Figure 55 shows the maximum deflection of the wing under difference speed over a range of ride height. The overall trend of the deflection when the wing is approached is achieved between the high speed and low speed conditions. For the high speed, with decreasing the height up to h/c = 0.158 the deflection gradually increases and reaches the corresponding value of 8.1 mm. For further reduction of the height, there is a region of plateau with little changes, followed by reduced deflection at the lowest height. The wing under the low speed is deflected across the range of heights in a similar manner. Figure 56 presents the schematic diagram of the deflected wing position at the tip where the maximum deformation occurs.

Aerodynamic forces generated under different velocity regimes are presented with respect to downforce and drag in Figure 57. The downforce obtained under the low-speed increases with increasing the ground proximity. Likewise, the low-speed case follows a similar trajectory of downforce curve with the exception of slight reduction at the lowest height. The drag force steadily increases as the height is lowered, at both high and low speeds. However, there is constant

discrepancy of the resistant force occurred across the whole range of the height that less amount of the force is generated under the high velocity state.

It can be observed that the high speed gives rise to more aerodynamic loading on the wing, resulting in more deflection. When the wing is approached to the ground, the flow underneath the wing is constrained by the reduced distance between the wing and ground and accelerated to achieve faster speed, which is referred to as ground effect. Although it was expected to obtain higher value of downforce under the high-speed flow due to stronger ground effect, similar level of aero performance is created despite the enhanced ground effect caused by the wing deflection. It is speculated that the improved ground effect offered by the deflection may be cancelled out by weaker wing tip vortices resulting from the effective angle of attack reduction. The constant difference of the drag force across the ride height variation can be explained that additional aerodynamic loading induced by the higher speed provides further less incidence, so that the aero performance, such as straight-line speed, would improve.

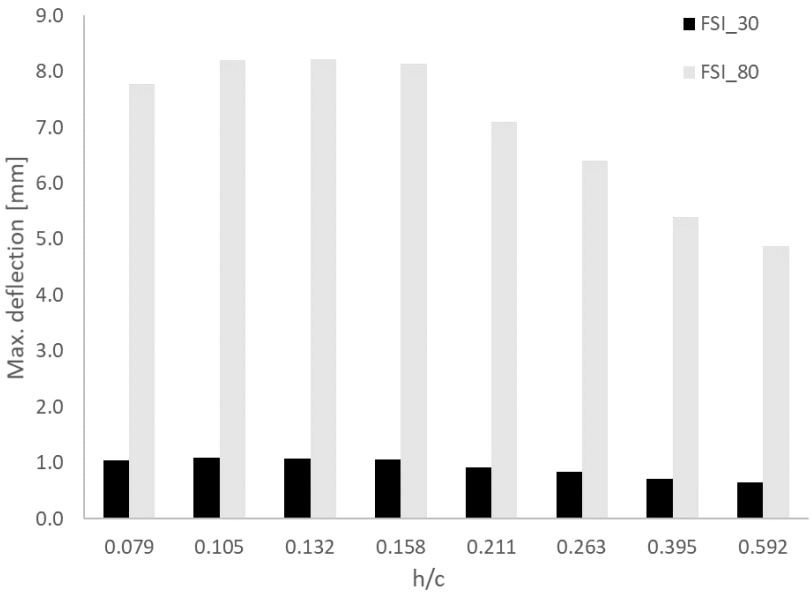

Figure 55 Maximum deflection comparison in ground proximity at different speeds

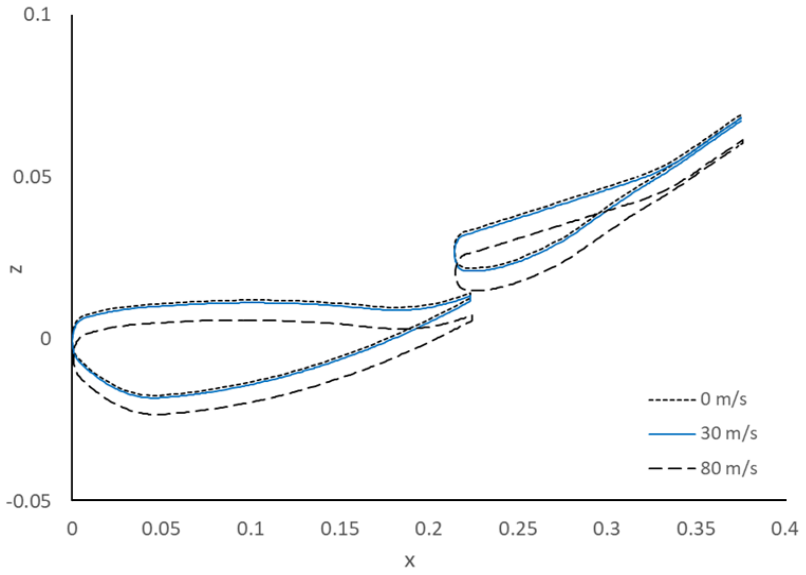

Figure 56 Schematic diagram of wing positions at different speeds at h/c = 0.211

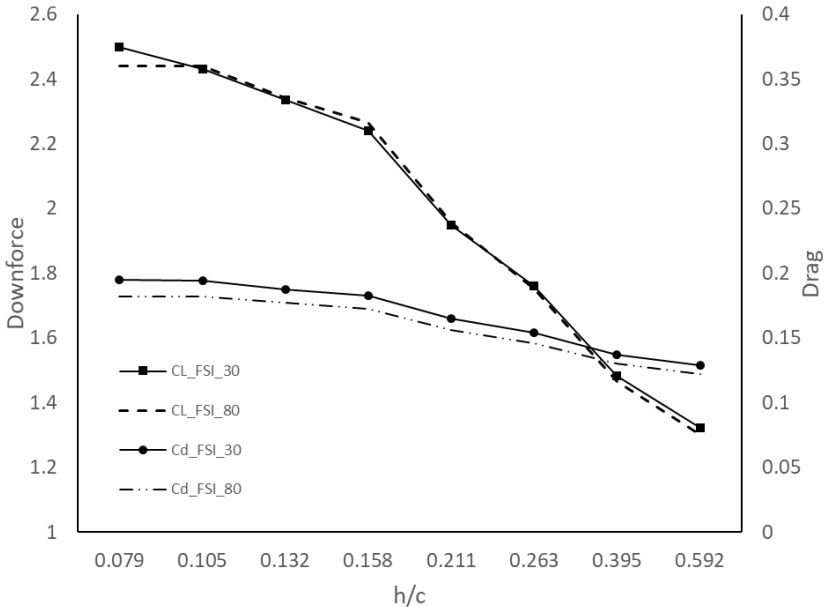

Figure 57 Comparison of aerodynamic forces at different speeds

5.4 Conclusion

Fluid Structure Interaction modelling is employed for the purpose of investigation on the flow field around the composite-material multi-element wing in order to assess the wing's aerodynamic performance induced by the aeroelastic effect. A range of ride height is included to represent the ground effect. As the wing approaches, substantial suction loading is created on the primary element's bottom surface whereas the pressure around the flap relatively remains unaffected by the ride height variation as it is far above the ground. For the spanwise pressures around the wing, due to the aeroelastic effect the suction pressures on both main element and flap are numerically less generated across the span.

Except for the fact that the greatest downforce obtained by the computation occurs at a higher ride height, followed by a greater drop in downforce at the lowest height, the numerical downforce is in good agreement with the experimental data. The FSI simulation generates additional drag compared to the experiments by broadly constant value across the ride heights. As the height of the primary element is lowered, the velocity deficit inside the wakes grows, owing to an increase in the unfavourable pressure gradient underneath it. For further investigation on the aeroelastic influence on the wing performance, a comparative study between the non-FSI and FSI wing models is performed in terms of wall shear stress, total pressure coefficient, and vorticity. The higher speed results in more deflection, causing more suction loading due to stronger ground effect. However, at h/c = 0.079 due to existence of the ground, it might not let the flow to roll up to create vortices, leading to less pressure and less loading. In addition, the downforce drop at the lowest height might be caused by a vortex burst caused by an unfavourable pressure gradient.

6 Multi-objective optimisation with FSI

The findings of optimising a single element composite wing in ground effect utilising fluid-structural interaction modelling, a response surface surrogate model, and a multi-objective optimisation method are presented in this chapter.

6.1 Optimisation problem formulation

One of the most important variables affecting the F1 car’s performance is aerodynamics. Wings are attached at the front and back of the car in order to produce aerodynamic downforce which increases the lateral and tangential forces of the tyres [150]. It causes the car's turning speed to improve, as well as its acceleration and braking capabilities, in order to minimise lap time. Additionally, aerodynamic drag created by the wings has an impact on the top speed. Therefore, it is highlighted that the design of aerodynamic devices of the F1 racing car is important in terms of the overall car performance. The front wing, placed at the very front of the car, has several functions to influence the aerodynamic performance: to generate the downforce (approximately 25-30% of the overall downforce) [151] on the front axle with high aerodynamic efficiency (high lift-to-drag ratio) [152] and to navigate and guide the airflow to the rearmost components. Concurrently, the structural design of the front wing should be carefully examined due to the large magnitude of the aerodynamic forces created by the wing. The major goal is to lower the wing's structural weight while still passing the regulation static deflection test, as demonstrated below [143].

FIA Technical Regulation 3.9.1 (2018)

“Bodywork may deflect no more than 15 mm vertically when a 1000 N load is applied vertically to it at points 675 mm and 975 mm forward of the wheel centre line and 795 mm from the car centre plane.”

The accurate parameterisation of the limit between lightweight and structural dependability is critical in a very competitive motorsport environment and it can explain why composite materials such as carbon fibres are widely used in this sector. In addition, as discussed in the previous chapter, due to the elastic characteristics of the composite materials, the front wing is deflected by the aerodynamic loading in the dynamic condition. It is realised that the wing aeroelasticity could enhance or deteriorate the wing performance depending on the ground proximity changes. Therefore, the front wing should be designed considering the aerodynamic performance as well as controlling the structural rigidity and stability [153].

The single element composite wing used in the FSI study in the previous chapter will be used as a base model for the optimisation. The F1 cars are generally manoeuvred at various driving conditions and one of the critical ones is a high-speed cornering where the high aerodynamic efficiency and the structural stability are simultaneously required. The wing is positioned at the ground proximity which enables the effect of the wing deflection on aerodynamic performance to be observed due to the ground effect. Therefore, the objective of this optimisation problem is to maximise the aerodynamic efficiency and to

minimise the weight of the wing. This study's multi-objective function and constraint may be stated as follows.

$$\text{min} \qquad F_1 = w_1 \cdot f_{aero} + w_2 \cdot f_{struc}$$

$$\text{subject to} \quad \delta_{max} \leq 15\, mm$$

$$f_{aero} = \text{min (D/L)}$$

$$\text{subject to} \quad C_L > C_{L,base}$$

$$C_D < C_{D,base}$$

$$f_{struc} = \text{min } (m_{wing})$$

$$\text{subject to} \quad \delta_{max} \leq 15\, mm$$

where F_1 is the final objective function; f_{aero} and f_{struc} are sub-functions for the aerodynamic and structural performance; w_i $(i = 1,2)$ are weighting factors; D/L is the drag-to-lift ratio; m_{wing} is the total weight of the wing; δ_{max} is the maximum deflection of the wing.

6.1.1 Optimisation process

This section shows a decomposition optimisation framework to reduce the computational complexity of the aero-structural linked with optimisation issue. The optimisation process is broken down into two parts. In the first phase, the simplified F1 front wing is optimised using a surrogate model-based optimiser to achieve the target objectives with regard to the wing geometry and global mechanical properties of the composite materials. In Stage 2, the aero-structural coupled optimisation is executed in an analogous approach focusing on the mechanical properties in the fibre level, where the geometrical shape of the wing is fixed as the optimised one obtained in the Stage 1. The suggested decomposition-based framework is depicted in Figure 58, and the key methods are outlined below.

Step 1 Wing geometry generation. In the initial design space, specimen points are selected, and the baseline wing model will be modified and updated accordingly.

Step 2 RSM module. Response Surface model is created in connection with the aero-structural analysis carried out in ANSYS. By using the quadratic polynomial equation, the response of each sampling point is obtained, and all responses are integrated to create an approximate meta model, representing the actual optimisation problem. Regression analysis of the surrogate model is performed to evaluate the accuracy of the model.

Step 3 Multi-objective optimisation module. This study's optimisation challenge is essentially a multidisciplinary design problem. As a result, many objectives that

frequently clash over a high-dimensional problem space should be optimised at the same time. The weighted-sum technique is used in this study to identify the optimal weighting factors among several multi-objective optimisation methods.

Step 4 Validation module. Once satisfactory optimum objectives are decided, they should be validated by comparing with the result obtained by the computational analysis in order to assess whether the optimisation is performed correctly.

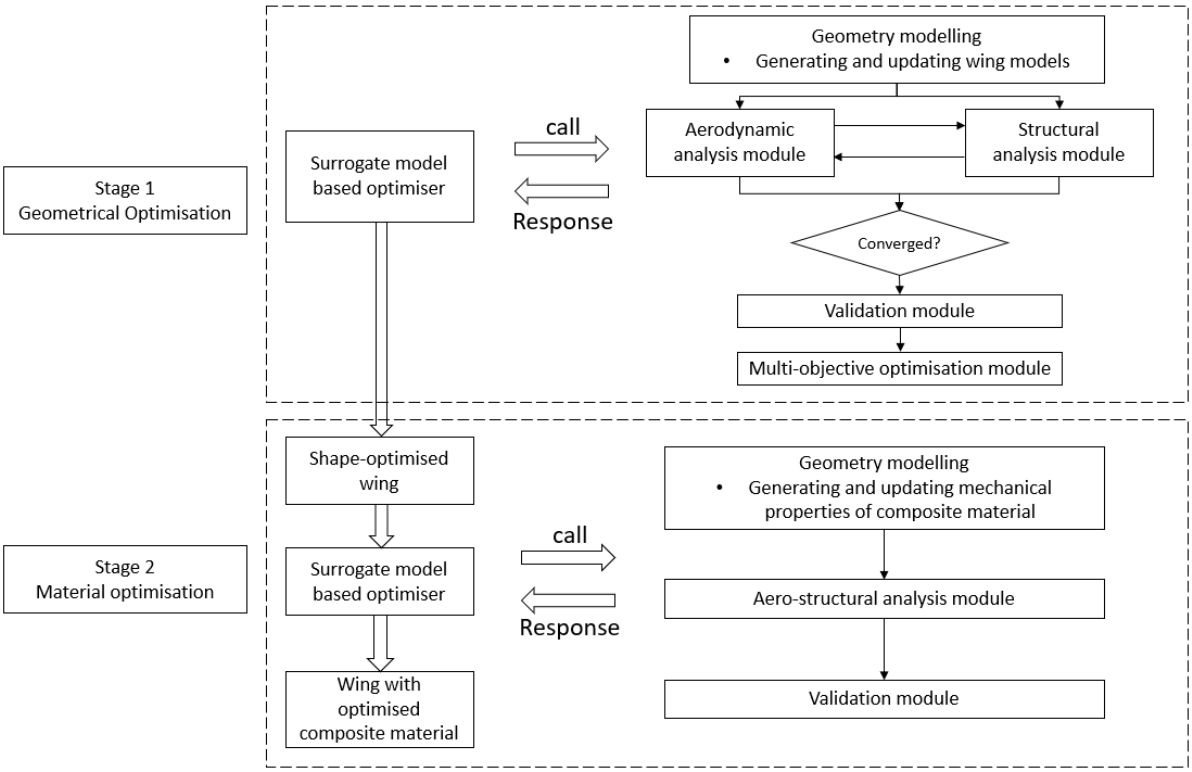

Figure 58 Decomposition-based optimisation framework using a surrogate model

Figure 59 illustrates the flowchart of how the surrogate response model is created. In the initial design space, sampling points are first selected using the Latin Hypercube Design technique. At initial or successive sample points, the aero-structural coupled analysis is carried out to assess their genuine responses, including objectives and limitations. The objective function is approximated using the sampling inputs and the output responses in current design space using the response surface model. The RSM-based optimisation is carried out using the MATLAB in order to obtain an estimated optimum point. The FSI analysis is used to acquire genuine answers at the estimated optimum point, which is considered to be the most likely global optimum value. If the termination conditions are met, the optimization process is terminated, and the current likely global optimum value is taken as the true global optimum; otherwise, by adding extra sampling points where the response surface model is created the process returns to the step.

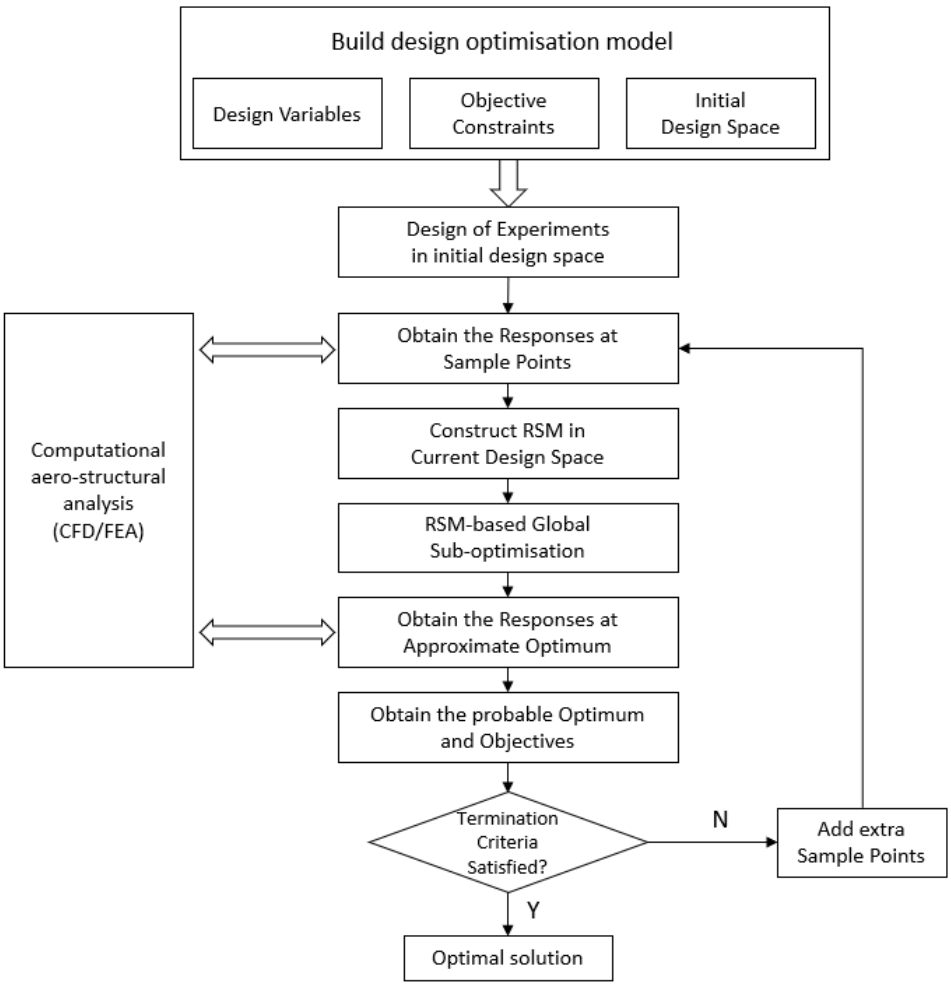

Figure 59 Flowchart of the surrogate model-based optimiser

6.1.2 Definition of design variables

The parameters of wing incidence, wingspan, and composite skin thickness of the wing, the Young's moduli and the shear modulus are all part of the design space investigated in this study, as summarised in Table 16. The baseline model is the single element composite wing which is used for FSI analysis in the previous chapter. The maximum angle of attack was initially set at 11° according to the aerodynamic study performed by Zerihan [19] that the single element wing

is stalled at 11.3°. However, multi-element wing concept is widely used in the motorsport application and this wing is represented as a main element which has a smaller boundary of incidence change [151]. The range of the wingspan is determined based on the maximum design geometry length of the wing according to the FIA technical regulations from 2018 to 2020 [143,154,155]. In consideration of thickness of a single lamina and structural stiffness under the driving condition, the total skin thickness ranges from 5.6 mm to 19.6 mm. The mechanical properties are linked to the composite materials widely used in the motorsport industry.

Table 16 Range of design variables

Design variable	Minimum	Baseline	Maximum	Unit
Angle of attack	-1	1	5	degree
Span	800	800	1000	mm
Skin thickness	5.6	14	19.6	mm
Young's modulus, E_x	50000	61340	90000	MPa
Young's modulus, E_y	50000	61340	90000	MPa
Shear modulus, G_{xy}	10000	19500	50000	MPa

6.1.3 Effect of ply orientation

According to the plate constitutive equations of the composite laminate [156], it is shown that ply orientation and thickness of a single lamina are key factors to affect the structural performance of the wing by altering characteristics of the composite structure. To achieve the optimum stacking sequences for the wing, seeking both reduction in weight and deformation without laminate failure, the structural parametric study is carried out by evaluating the influence of the ply orientation for symmetric lamination.

Results of the composite wing for the influence of the ply orientation on the deflection are summarised in Table 17, where the variation of Δ% is calculated in relation to the first stacking sequence shown. First, by changing the sequential cross-ply orientations the wing deflection is increased, one of which achieves the maximum of 9.68 mm with the set [45,90]. Regarding the maximum stress failure criteria, they are calculated using the equation [157] and no significant results are observed as all cases are within the prediction. As a result, optimum balance regarding the maximum deformation and failure performance is achieved for [0,90] case.

Table 17 Effect of the ply orientation of woven prepreg on structural performance

Orientation	Deflection[mm]	Δ%	Max. Stress FC	Δ%
$[(0,90)_3]s$	9.14	-	0.055	-
$[(30,90)_3]s$	9.57	+4.70	0.051	-6.3
$[(45,90)_3]s$	9.68	+5.91	0.050	-8.6
$[(60,90)_3]s$	9.54	+4.38	0.051	-6.3
$[(90,90)_3]s$	9.16	+0.22	0.054	-0.7

6.2 Optimisation for aero performance increase and weight reduction

6.2.1 Creation of RSM models

The numerical experiment's sample points play an essential role in determining the response surface's correctness. In general, increasing the number of points will enhance the precision and quality of the meta model, but efficiency will decrease due to expensive computational resources. As a result, extracting as much information as possible with the fewest number of simulations is important. The Design of Experiments (DoE) is a statistical method to decide variation of information including the number of points and their distribution in the design space. To identify the initial sample locations, the Latin Hypercube Sampling (LHS) methodology [158] is used in conjunction with the extensive investigation results of the FSI analysis provided in the preceding chapter. A set of beginning points for each design variable is chosen and presented in Table 18 using the variable boundaries defined in Table 16. Approximately nine-hundred simulations

are carried out accordingly. Some cases are excluded due to the linear relationship between the design variable and the response.

Table 18 Range of design variables for response surface models

Design variable	Range					Unit
Angle of attack	-1	0	1	2	3	degree
Span	800		900		1000	mm
Skin thickness	8.4	9.8	14.0	16.8	19.6	mm
Young's modulus, E_x	50000	61340	70000	90000		MPa
Young's modulus, E_y	50000	61340	70000	90000		MPa
Shear modulus, G_{xy}	10000	19500	30000	50000		MPa

After selecting the sampling points in the design space, the surrogate model based on the quadratic polynomial equation is constructed for both aerodynamic and structural responses using the Fluid-Structure Interaction modelling in ANSYS. The boundary conditions for the fluid dynamics are equivalent to the one used for the structural analysis in chapter 4 including the ground effect. Based on the definition of the quadratic polynomial equation discussed in the chapter 3, the final model can be expressed as a form of the equation 6-1 to be used in accordance with the purpose of the research, considering a significant interaction among the control design variables.

$$y_i = \beta_0 + \beta_1 x_1 + \beta_2 x_2 + \beta_3 x_3 + \beta_4 x_4 + \beta_5 x_5 + \beta_6 x_1^2 + \beta_7 x_2^2 + \beta_8 x_3^2 + \beta_9 x_4^2 \quad \textbf{(6-1)}$$
$$+ \beta_{10} x_5^2 + \beta_{11} x_1 x_2 + \beta_{12} x_1 x_3 + \beta_{13} x_1 x_4 + \beta_{14} x_1 x_5 + \beta_{15} x_2 x_3$$
$$+ \beta_{16} x_2 x_4 + \beta_{17} x_2 x_5 + \beta_{18} x_3 x_4 + \beta_{19} x_3 x_5 + \beta_{20} x_4 x_5$$

where y_i is the output responses; $x_i = [x_1, x_2, \cdots, x_5]$ is the input design variables; and $\beta_i = [\beta_0, \beta_1, \cdots, \beta_{20}]$ is the regression coefficients.

The Least Square method is used to calculate twenty regression coefficients to generate the response surface and the values are presented in Table 19. Figure 60 illustrates the response surface models fitted using the equation 6-1 and the regression coefficients obtained, being defined by two design variables: angle of attack and span for the aerodynamic objective and span and thickness for the structural objective. It is observed that each objective is influenced the most by those two variables. In Figure 60 (a), the aerodynamic response is generally influenced by all design parameters, especially the wingspan. The structural response shown in Figure 60 (b) represents across the design space strong linear characteristic with regard to the wingspan and total thickness of the composite lamination.

Table 19 Regression coefficients for response surface model of aerodynamics and structural objectives

Regression coefficient	Aero	Weight
β_0	7.1807	-1.1391
β_1	0.0714	0
β_2	-12.3807	0.9723
β_3	0.0029	0.0242
β_4	0.0075	0
β_5	0.0108	0
β_6	0.0397	0
β_7	5.04	-0.4554
β_8	-0.0002	-0.0009
β_9	-0.0014	0
β_{10}	-0.0031	0
β_{11}	-0.1569	0
β_{12}	0.0001	0
β_{13}	0.001	0
β_{14}	0.0047	0
β_{15}	0.0.056	0.0756
β_{16}	0.0259	0
β_{17}	0.0178	0
β_{18}	-0.0003	0
β_{19}	-0.0001	0
β_{20}	-0.0002	0

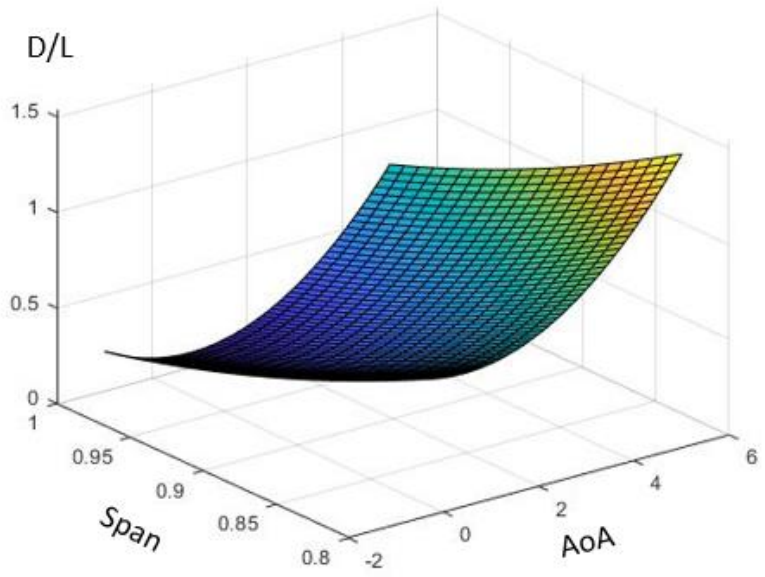

(a)

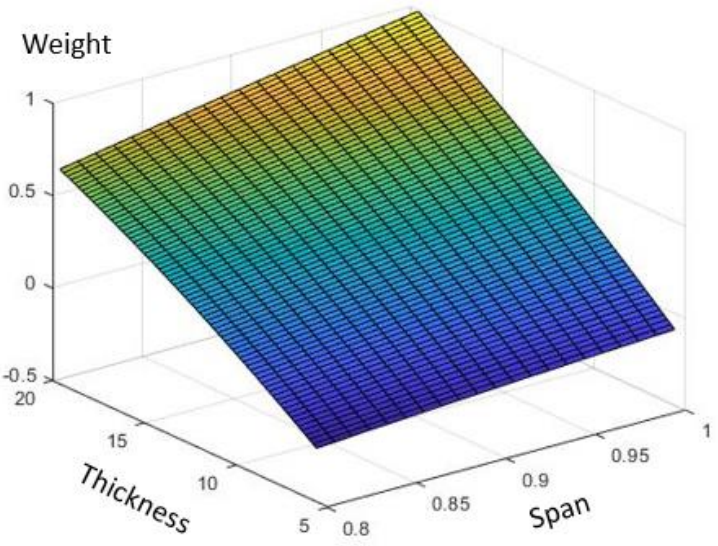

(b)

Figure 60 Illustration of response surface models (a) aerodynamic efficiency (b) weight

It is important to evaluate the model quality once the response surface models have been produced. The regression coefficients in the quadratic polynomial model are estimated using regression analysis, a statistical approach that also determines the measure of uncertainty in these coefficients. Table 20 shows the results of the model's fitting correctness as measured by the coefficient of determination of R^2 and the percentage of root mean square error. The analysis is repeated three times in order to ensure the accuracy of the model across the entire design area. Consequently, the determination coefficient for D/L and weight models is greater than 0.96, and the RMSE is close to 1%, indicating that the response surface models are fitted accurately. Therefore, for the aero-structural coupled issue, quadratic models are sufficient to model the multi-objective function and constraints.

Table 20 Fitting quality results of the response surface models

Cases	R^2		RMSE [%]	
	D/L	Weight	D/L	Weight
1	0.999	0.990	1.20	2.45
2	0.989	0.996	1.90	1.00
3	0.992	0.986	1.39	1.90

6.2.2 Optimisation results

Once the accuracy of the response surface models is assessed by performing the regression analysis, the final multi-objective optimisation function consisting of the aerodynamic and structural single objective can be solved using the weighted-sum method, which is widely used as a multi-criteria decision analysis [159]. The relative weight of importance ranging from 0 to 1 by the scale of 0.1 is assigned to each single objective, for example when w_1 is 0 and w_2 is 1.0, the structural aspect of the optimisation is fully implemented so that the design variables are only determined in accordance with the weight. The optimised design variables are obtained for each case according to a different set of the weighting factors. As a result, the performance value of the single objectives, f_{aero} and f_{struc} and the final objective F_1 are determined as shown in Table 21. In addition, for better understanding of the optimisation result, the Pareto optimality is illustrated in Figure 61 including the black circles represented as feasible choices and blue circles as the Pareto Frontier, which is based on the performance values shown in Table 21. Also, each Pareto-optimal point is specifically indicated by the broken lines.

As explained in the previous chapter, all cases in the Table 21 are potentially recognised as all Pareto efficient solutions in the aero-structural design problem within a full range of design space with respect to various weighting factors for individual objective. In this study, in order to satisfy minimisation of the multi-objective criteria, the optimal result with the weighted importance of 0.5 for each objective function is selected, yielding the minimum value of 0.9284 for the final

objective function, F_1, and it means that the aerodynamic efficiency and the structure weight are equally weighted in this application.

Table 21 Results of Pareto optimum

w_1	w_2	AoA [°]	Span [m]	Thickness [mm]	E_x [MPa]	E_y [MPa]	G_{xy} [MPa]	f_{aero}	f_{struc}	F_1
0	1.0	2.9997	0.8	12.0219	84884	84884	38955	0.9424	0.2352	1.1776
0.1	0.9	0.8590	0.8	12.0962	79816	79816	39089	0.6934	0.2399	0.9333
0.2	0.8	0.6694	0.8	12.1066	90000	90000	37345	0.6888	0.2406	0.9294
0.3	0.7	0.5888	0.8	12.1112	90000	90000	44670	0.6878	0.2408	0.9286
0.4	0.6	0.5484	0.8	12.1135	90000	90000	44265	0.6875	0.2410	0.9285
0.5	0.5	0.5025	0.8	12.1163	90000	90000	44426	0.6872	0.2412	0.9284
0.6	0.4	0.4901	0.8014	12.2156	90000	90000	45104	0.6815	0.2490	0.9305
0.7	0.3	0.5360	0.8229	14.2244	90000	90000	45777	0.5956	0.3997	0.9953
0.8	0.2	0.5562	0.8269	15.306	90000	90000	45660	0.5689	0.4736	1.0425
0.9	0.1	0.5665	0.8320	15.9876	90000	90000	45343	0.5589	0.5171	1.0760
1.0	0	0.6560	0.8789	17.604	90000	90000	45652	0.3922	0.6805	1.7027

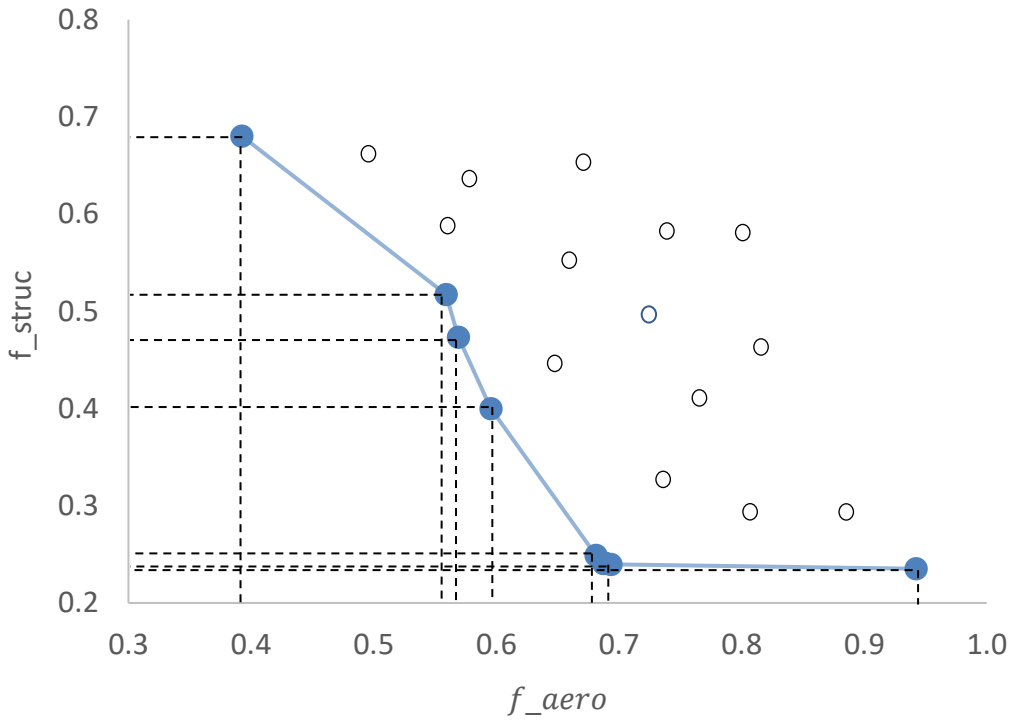

Figure 61 Illustration of Pareto optimality. The Pareto Front is represented by blue points and feasible choices as black points. The broken lines are indicative of each Pareto Optimal point.

The FSI design optimisation problem is solved by the surrogate model-based optimiser and the optimised results of the design parameters are presented in Table 22 in comparison with the baseline. It can be seen that the total thickness is reduced by approximately 14% and all mechanical properties are increased up to the maximum within the design space in order to compensate lack of stiffness of the wing which is decreased due to the thinner skin. In addition, it is found that the angle of attack is lowered towards 0° and the wingspan remains unchanged.

Table 23 presents the optimisation results in terms of the wing performance and constraint. The maximum deflection is calculated by the static structural simulation according to the FIA Technical regulations [143,154,155]. The aerodynamic efficiency of the optimised wing model is enhanced by around

0.63% above the baseline, while the weight is decreased by 11.5%, simultaneously satisfying the constraint of the maximum deflection. It is concluded that the optimised wing has a slightly better level of aerodynamic performance over the baseline model, while significant weight reduction can be achieved by optimising the composite structure and its mechanical properties. In addition, it is important to validate the optimum results by performing the FSI analysis as the optimised wing is achieved using the approximation meta model. In Table 23, the FSI results of the optimised wing are shown and a similar trend in the aerodynamic performance and weight is presented in comparison with that of the surrogate model-based optimisation results. However, due to the pre-determined thickness of a single lamina, the wing for the FSI analysis is modelled with the total thickness of 12.6mm, which results in a slight increase in the weight and less deflection compared to the analytical solution.

Following the discussion based on the tabulated results, further comparative analysis between the base wing and the optimised wing is performed using the computational solution and the associated results are visualised. In Figure 62, the wall shear stress on the bottom surface of the wing is presented. Overall variation of the wall shear for both models have similarity across the surface, showing a region of high shear stress in red near the leading edge and low shear stress at the trailing edge. However, it is found that certain level of difference of the wall shear stress between the base wing and optimised wing can be seen near the wing tip where the influence of the wing flexibility is strong. The larger area of lower shear stress at the trailing edge obtained by the optimised wing indicates higher likelihood of the boundary layer separation which could lead to

increase in the total drag. Three-dimensional vorticity is shown in Figure 63 in order to represent the strength of vortices. Both models generally produce equivalent level of vorticities around the wing tip, but slightly longer propagation of the upper vortex is observed by the base case. Lastly, the chordwise surface pressure distributions obtained from both models are shown in Figure 64. The only difference of the surface pressure could be found around the suction peak near the leading edge, providing that the suction loading calculated by the optimised wing is reduced. In other words, the general shape of the surface pressure distribution is equivalent for both cases. As a result of the optimisation stage 1, although aerodynamic performance of the wing is slightly increased by 1.7% compared to the base case, more benefit could be provided on the structural performance such as the weight reduction.

Table 22 Optimisation results of design variables in Stage 1

	Incidence [°]	Span [mm]	Skin thickness [mm]	Ex [MPa]	Ey [MPa]	Gxy [MPa]
Base	1	800	14	61340	61340	19500
Optimum	0.5025	800	12.1	90000	90000	44426

Table 23 Optimisation results of output in Stage 1

		L/D	ΔL/D [%]	Weight [kg]	ΔWeight [%]	Deflection [mm]
	Base	25.58	-	3.13	-	14.567
RSM	Optimum	25.74	+0.63	2.77	-11.5	15.000
FSI	Optimum	26.02	+1.72	2.87	-8.3	14.517

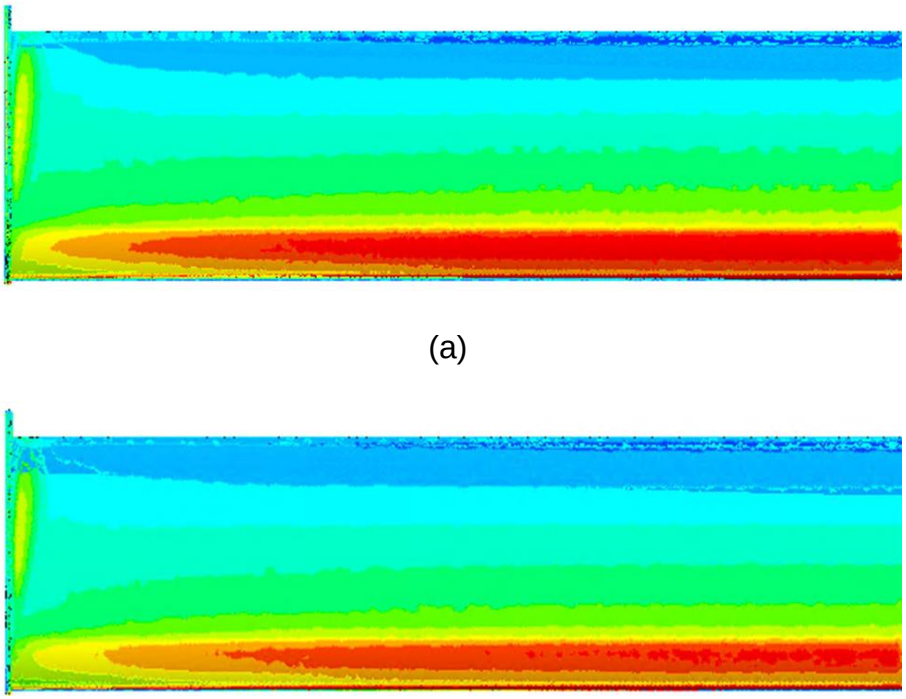

Figure 62 Comparison of wall shear stress contour on lower surface of a single element composite wing showing leading edge lowermost (a) base case (b) optimised case

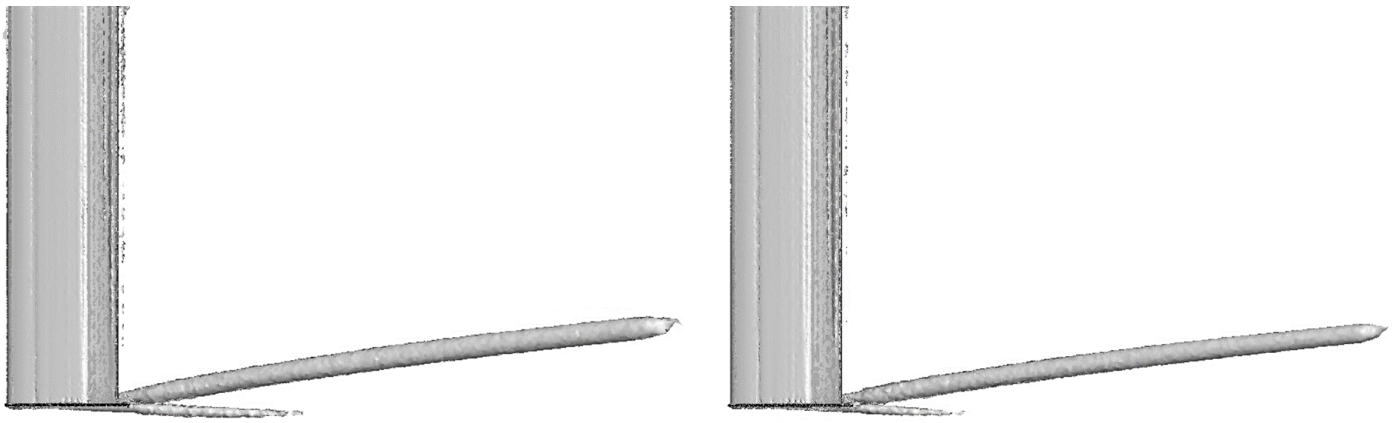

(a) (b)

Figure 63 Three-dimensional Q-criterion results of a single element composite wing on the top view showing leading edge left (a) base case (b) optimised case

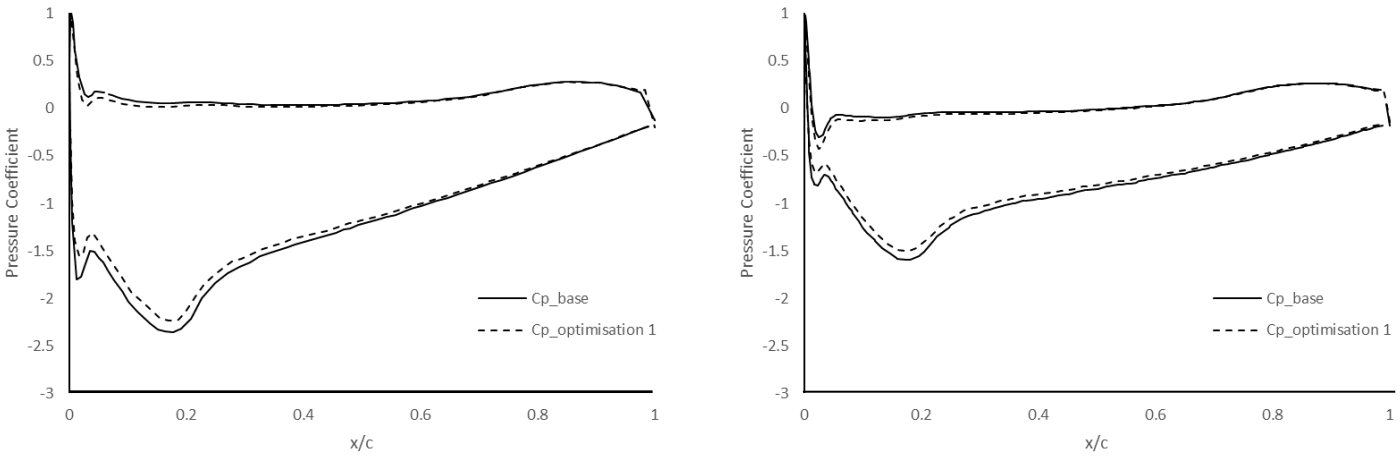

(a) (b)

Figure 64 Comparison of surface pressure distribution of a single element composite wing between base case and optimised case at (a) wing centre (b) wing tip

6.3 Optimisation for material property of composite structure

Following the geometrical optimization, the composite material's mechanical characteristics are the focus of the following stage. Laminated carbon-fibre layers are piled up inside in order to construct the wing model, which are capable of describing structural advantages of the composite such as the low specific weight of the material and considerable rigidness. For purpose of the reverse engineering process, Stage 2 optimisation aims to search for the most appropriate composite structure construction at the constituent level, satisfying the objective function and constraints shown below and maximising static strength of the laminates for a given thickness.

$$\text{min} \qquad F_2 = (E_x - E_{x,target})^2 + (E_y - E_{y,target})^2 + (G_{xy} - G_{xy,target})^2$$

$$\text{subject to} \quad \delta_{max} \leq 15\ mm$$

$$t_{total} = constant$$

where $E_{x,target}$, $E_{y,target}$ $G_{xy,target}$ are the optimised values obtained in Stage 1 optimisation; δ_{max} is the maximum deflection of the wing; t_{total} is the total thickness of the composite structure.

The design variables for the Stage 2 are the mechanical properties of a lamina, which consists of the fibre and matrix. The Rule of Mixtures theory related to the properties of the composite is applied [160] to calculate the moduli in global directions presented as follows.

$$E_1 = E_f V_f + E_m V_m \quad \textbf{(6-2)}$$

$$\frac{1}{E_2} = \frac{V_f}{E_f} + \frac{V_m}{E_m} \quad \textbf{(6-3)}$$

$$\nu_1 = \nu_f V_f + \nu_m V_m \quad \textbf{(6-4)}$$

$$\frac{1}{G_{12}} = \frac{V_f}{G_f} + \frac{V_m}{G_m} \quad \textbf{(6-5)}$$

where f represents fibre and m is matrix. E and G represent Young's modulus and Shear modulus respectively. Lastly, V means volumetric fraction and Poisson's ratio is represented by v.

$$[S] = \begin{bmatrix} \frac{1}{E_1} & -\frac{\nu_{21}}{E_2} & 0 \\ -\frac{\nu_{12}}{E_1} & \frac{1}{E_2} & 0 \\ 0 & 0 & \frac{1}{G_{12}} \end{bmatrix} \quad \textbf{(6-6)}$$

$$[Q] = \begin{bmatrix} \frac{E_1}{1-\nu_{12}\nu_{21}} & \frac{\nu_{12}E_2}{1-\nu_{12}\nu_{21}} & 0 \\ -\frac{\nu_{12}}{E_1} & \frac{1}{E_2} & 0 \\ 0 & 0 & G_{12} \end{bmatrix} \quad \textbf{(6-7)}$$

where $[S]$ is the compliance matrix and $[D]$ is the stiffness matrix. On the other hand, a woven layer becomes orthotropic when the fibres are placed in the +θ and -θ directions and therefore, the elements of the stiffness matrix for woven fabrics lamina and extensional stiffness matrix can be expressed as:

$$Q_{ij,woven} = \frac{1}{2}\left[\overline{Q_{ij}}(\theta) + \overline{Q_{ij}}(-\theta)\right] \quad \textbf{(6-8)}$$

$$[A] = \sum_{f=1}^{F} [\bar{Q}]_f (h_f - h_{f-1}) \quad \textbf{(6-9)}$$

where $h_f - h_{f-1}$ is thickness of a single lamina as the extensional stiffness matrix is calculated by adding the product of thickness and $[\bar{Q}]$ for each ply. Finally, the properties of the laminate are determined as below:

$$E_x = \frac{1}{a_{11}h} \quad \textbf{(6-10)}$$

$$E_y = \frac{1}{a_{22}h} \quad \textbf{(6-11)}$$

$$G_{xy} = \frac{1}{a_{66}h} \quad \textbf{(6-12)}$$

where the extensional compliance matrix [a] for the laminate is obtained by inversion of [A] and h is thickness of laminate.

Table 24 presents the design variables (input parameters) and their bounds, which are based on various types of the composite materials largely used in the motorsport industry [161–167].

Table 24 Range of design variables of mechanical properties of composite materials

	Minimum	Maximum
Ef [GPa]	200	600
Em [GPa]	2.5	7
Vf	0.3	0.65
Vm	0.35	0.7
vf	0.1	0.4
vm	0.35	0.45
Gf [GPa]	5	15
Gm [GPa]	1	1.6

6.3.1 Optimisation results

The optimisation results in Stage 2 are presented in Table 25, 26 and 27. Table 25 shows the optimised design variables of the mechanical properties, demonstrating that the maximum volume fraction of the fibre is required and both

Shear moduli of the fibre and matrix are obtained. The dependency of the composite fibre is increased to take the performance level up to the target values. The outputs are calculated using the parameters in Table 26 and also compared with the target values from Stage 1. It shows a good agreement in Young's moduli, however significant discrepancy of the Shear modulus is obtained; it means that the required mechanical properties for the objective function and constraints cannot be satisfied with the existing carbon fibre composite materials in the market. Table 27 shows the aerodynamic and structural performance data from Stage 2. The results gained from the optimisation Stage 2 present that the maximum deflection of the wing is over the pre-defined value, 15mm, despite slight increase of the aerodynamic performance compared to both the base case and optimisation Stage 1. Following the calculated results, the FSI validation analysis is performed implementing the optimised design variables in Table 26 and comparison between the metamodel-based analytical solution and FSI is made; marginal increase in aerodynamic efficiency by roughly 3% is observed and the wing is deflected over 24 mm, which means constraints are not met. Due to lack of the Shear stiffness caused by limitation of available composite material spectrum, the optimisation is unable to find the appropriate solution for satisfying the objective function and constraints in this application.

Table 25 Optimisation results of design variables in Stage 2

	Ef [GPa]	Em [GPa]	Vf	Vm	vf	vm	Gf [GPa]	Gm [GPa]
RSM	253.04	2.5	0.65	0.35	0.1	0.35	15	1.6

Table 26 Comparison of optimisation results between stage 1 and stage 2

		Ex [MPa]	Ey [MPa]	Gxy [MPa]
RSM	Optimum 1	90000	90000	44426
RSM	Optimum 2	90000	90000	3973.7

Table 27 Comparison of optimisation results of aerodynamics efficiency and weight at different optimisation stages

		L/D	ΔL/D [%]	Weight [kg]	ΔWeight [%]	Deflection [mm]
	Base	25.58	-	3.13	-	14.567
RSM	Optimum 1	25.74	+0.63	2.77	-11.5	15.000
RSM	Optimum 2	25.86	+1.09	2.77	-11.5	24.400
FSI	Optimum 2	26.27	+2.70	2.87	-8.3	24.024

6.3.2 Further analysis

Excessive deflection of the wing is observed in FSI result due to the less stiffness caused by the reduced Shear modulus. According to the FIA Technical regulations, any aerodynamic components which does not comply with the regulation are not homologated to be used. Therefore, the optimised wing is not acceptable despite improved aerodynamic performance.

In order to increase the stiffness of the wing by increasing the Shear modulus, further analysis is carried out using the sandwich structure, which is widely used in the motorsport industry. In this study, core material of aluminium 5052

honeycomb is inserted in the middle of the wing, surrounded by the carbon-fibre skins in order to increase the shear stiffness as shown in Table 28. With help of additional reinforcement inside the wing, the thickness of skins is reduced by 24% while the core thickness of 13.3 mm is created. Table 29 presents the performance output obtained from the FSI model including the core material. It is concluded that the sandwich structure with additional core material could enhance structural stiffness of the wing, resulting in less maximum deflection within the constraint. In addition, physical benefit of the weight reduction can be achieved compared to the previous design by adding the smart structure.

Table 28 Comparison of design variables in further analysis

	Incidence [°]	Span [mm]	Skin thickness [mm]	Core thickness [mm]	Ex [MPa]	Ey [MPa]	Gxy [MPa]
Optimum 2	0.5025	800	12.1	-	90000	90000	3973.7
Optimum 2a	0.5025	800	9.2	13.3	90000	90000	3973.7

Table 29 Comparison of optimisation results of aerodynamic and structural performance at different optimisation stages

		L/D	ΔL/D [%]	Weight [kg]	ΔWeight [%]	Deflection [mm]
RSM	Optimum 2	25.74	+0.63	2.77	-11.5	24.400
FSI	Optimum 2	26.27	+2.70	2.87	-8.3	24.024
FSI	Optimum 2a	25.93	+1.37	2.42	-22.7	14.201

6.4 Conclusion

To tackle the design challenge of a single element composite wing in ground effect, an efficient and unique decomposition-based optimisation framework employing the response surface model integrated with computational aero-structural coupled analysis is suggested. The recommended approach is shown to be both accurate and efficient, with a significant cost benefit, when the design variables outnumber the objective functions.

7 Conclusions and Recommendations for Future Work

7.1 Conclusions

The influence of aeroelastic analysis on the aerodynamic performance of a multi-element composite wing in ground proximity has been fully explored. The structural construction of the wing using the composite material was achieved with the Fluid-Structure Interaction modelling method and the interaction between fluid and structure was evaluated by the two-way coupling method using the ANSYS software. As the first objective of this research, validation and verification of the Fluid-Structure Interaction modelling was carried out. The numerical results of a two-dimensional flexible beam within a channel gained from two different FSI computational solutions showed a good agreement with the analytical solution. In addition, prior to thorough investigation the grid sensitivity study and turbulence model study were performed to minimise the numerical uncertainty and to make sure that the computational solution is within acceptable range of convergence. In order to perform the Fluid-Structure Interaction simulations efficiently, the workflow of the FSI analysis using a commercial software ANSYS was created in connection with the high-performance computing system at Cranfield university which enables to save a huge amount of computational time to calculate the coupling phenomenon.

The FSI analysis on the single element composite wing in ground effect was conducted in order to investigate and quantify the effect of aeroelastic behaviour of the wing on its aerodynamic performance. Among six different turbulence models evaluated, the k-ω SST model and the Realizable k-ε model were

selected to be used as a result of achieving the most acceptable prediction with regard to the surface pressure distribution and the wake profile. With the exception of the spanwise pressure difference induced by the wing's aeroelastic behaviour, there was a good agreement between the numerical FSI findings and the experiment for the surface pressures recorded at the centre and tip of the wing. Regarding the aerodynamic forces gained by the FSI simulations, the calculated downforce and drag showed similar features of the force curves to the experiment, showing influence of the wing deflection on the flow field around the flexible wing. To investigate the aeroelastic effect on the wing performance, a thorough comparative study between the non-FSI and FSI wing models was conducted. Finally, the influence of varied composite structures on the aerodynamic and structural performance of the wing is assessed and core materials provide significant structural advantages of mechanical characteristics, keeping the equivalent level of aerodynamic performance and weight benefit.

Likewise, the single element wing FSI analysis, the effect of aeroelasticity on the double element wing in ground effect was studied with respect to surface pressure distribution, aerodynamic forces, and wake profile, followed by the grid convergence study and turbulence model analysis. As the wing is approached, there is significant suction loading generated on the suction surface of the primary element whereas the pressure around the flap relatively remains unaffected by the ride height variation as it is far above the ground. For the spanwise pressures around the wing, due to the aeroelastic effect the suction pressures on both main element and flap are numerically less generated across the span. Except for the fact that the greatest downforce obtained by the computation occurs at a higher

ride height, followed by a greater drop in downforce at the lowest height, the numerical downforce is in good agreement with the experimental data. The FSI simulation generates additional drag compared to the experiments by broadly constant value across the ride heights. In addition, as a results of the comparative study on the aeroelastic effect using the non-FSI rigid wing, the wing flexibility, especially near the wing tip, has an impact on the fluid flow field in either advantageous or disadvantageous way depending on the variation of the ride heights. As the height of the primary element is lowered, the velocity deficit inside the wakes grows, owing to an increase in the unfavourable pressure gradient underneath it.

Based on thorough investigation on the aeroelastic effect of the composite wings in ground effect on the wing performance, an efficient and innovative decomposition-based optimisation framework was proposed in order to solve the design problem of a single element composite wing in ground effect. The optimisation procedure was established using the response surface model combined with the computational aero-structural coupled analysis. The geometrical parameters of the wing (angle of attack, span and thickness) and various composite material properties (ply orientation, number of plies, core material, and mechanical properties) were optimised in order to maximise the aerodynamic efficiency and to minimise the weight of the wing under certain constraints. This multi-objective optimisation method was found to be an accurate and efficient way of solving a complicated design problem of aerodynamic components when considering fewer functions over a great number of design variables.

In the present work, a modified two-way coupling method was employed for the purpose of investigation into the fluid flow field around the composite-material multi-element wing to assess the aerodynamic performance of the wing induced by the aeroelastic effect. The computational approach focused on a novel coupling of the aerodynamic and structural behaviour of the multi-element composite wing of an F1 vehicle in the context of high performance computing (HPC) to simulate a steady-state fluid-structure interaction (FSI) configuration using the ANSYS software package. The objective of these investigations was to understand the suitability of computational techniques for FSI modelling and to quantify the influence of aeroelastic behaviour of the composite wing on the aerodynamic performance in ground effect. It is important to note that the practical contribution of this investigation was to quantify the couple effect on the aerodynamic and structural performance of the wing because the quantification of these physical processes is in the mainstream research focus. Overall, I focused on the development of an accurate FSI numerical modelling framework in conjunction with computational fluid dynamics (CFD) techniques and structural finite element analysis (FEA) for an F1 application.

7.2 Recommendations for Future Work

Implementation of various methods to study complicated flow field would be vital requirement to enhance understanding of the flow and associated effects. The numerical approach used in this research provides sufficient assessment of the wing performance considering the aeroelastic effect in an efficient way. In addition to this, a variety of experimental methods such as force measurement

system, Particle Image Velocimetry or Flow-viz could be exploited to examine the Fluid-Structure Interaction phenomenon physically and help the computation method to improve accuracy of the findings. Even a physical testing with a small-scale model would be a great resource to provide cross-reference data.

The steady-state Reynolds Averaged Navier-Stokes (RANS) turbulence models were used in this research. If sufficient computer capacity is available, the Detached-Eddy Simulation (DES) or the Large Eddy Simulation (LES) might be an alternative for additional research in order to improve the accuracy of the numerical solution, which would improve prediction of the complicated flow field around the wing and the ground as well as the three-dimensional effect such as the wing vortices and near and far field wakes.

In order to evaluate the general applicability of the wing models utilised in this study, they are a simplified version of the Formula One car front wing. On a basis of what has been discovered in this research, modern aerodynamic components of the Formula One car could be investigated exploiting the equivalent principle and method to make the study more realistic. Under the current technical regulation, the recent front wing has a longer span and a tapered planform. The front wing is crucial not only to generate a certain amount of downforce, but also more importantly to control the wake that it creates influencing the rest of the car downstream. Small perturbations in the flow field around the front wing could be altered by its deflection under the aerodynamic loading and could affect adversely the aerodynamic performance of other components downstream due to revised wakes. In addition, it would be of interest to study the interaction of the front wing with other components of the car, for example front wheels. The wheels of a

Formula One car produce roughly 40% of drag force and generate a great deal of adverse wake flows. Thus, as the front wheels are affected by the flow directed by the front wing it is necessary to investigate the interaction of these two components which are in proximity.

BIBLIOGRAPHY

[1] Dominy, J.A. and Dominy, R. G., 1984, “Aerodynamic Influences on the Performance of the Grand Prix Racing Car,” Proc. Inst. Mech. Eng. Part P J. Sport. Eng. Technol., pp. 87–93.

[2] Wright, P., 1982, “The Influence of Aerodynamics on the Design of Formula One Racing Cars,” Int. J. Veh. Des., 3, pp. 4:383-397.

[3] Agathangelou, B. and G., 1998, “Aerodynamic Considerations of a Formula 1 Racing Car,” SAE Publ., 980399, p. 8.

[4] Jeffrey, D. and Alperin, M., 2000, “Aspects of the Aerodynamics of Year 2000 Formula One Racing Cars,” *3rd Mira International Vehicle Aerodynamics Conference*.

[5] Somerfield, M., 2016, “‘Analysis: Is F1 Set for Another Flexi-Wing War?,’” Motorsport.com.

[6] Bazilevs, Y., Takizawa, K., and Tezduyar, T. E., 2013, “Challenges and Directions in Computational Fluid-Structure Interaction,” Math. Model. Methods Appl. Sci., 23(2), pp. 215–221.

[7] Auza, R., McNamara, J., Kimbrell, A., Rupp, T., and Kang, P., 2020, “High-Fidelity Modeling and Prediction of Hood Buffeting of Trailing Automobiles,” SAE Tech. Pap., pp. 1–11.

[8] Wang, L., Quant, R., and Kolios, A., 2016, “Fluid Structure Interaction Modelling of Horizontal-Axis Wind Turbine Blades Based on CFD and FEA,” J. Wind Eng. Ind. Aerodyn., 158, pp. 11–25.

[9] Ozcatalbas, M., Acar, B., and Uslu, S., 2018, “Investigation of Aeroelastic Stability on AGARD 445.6 Wing at Transonic Regime,” Proc. 2018 9th Int. Conf. Mech. Aerosp. Eng. ICMAE 2018, pp. 565–569.

[10] Katz, J., 1995, “High-Lift Wing Design for Race-Car Applications,” SAE Publ., p.

951976.

[11] Knowles, K., Donahue, D., and Finnis, M., 1994, “A Study of Wings in Ground Effect,” *Loughborough University Conference on Vehicle Aerodynamics*, pp. 22.1-22.13.

[12] Ranzenbach, R., Barlow, J. B., and Diaz, R. H., 1997, “Two-Dimensional Airfoil in Ground Effect- an Experimental and Computational Study,” 942509.

[13] Zerihan, J., and Zhang, X., 2000, “Aerodynamics of a Single Element Wing in Ground Effect,” AIAA J., **37**(6).

[14] Mahon, S., and Zhang, X., 2005, “Computational Analysis of Pressure and Wake Characteristics of an Aerofoil in Ground Effect,” J. Fluids Eng. Trans. ASME, **127**(2), pp. 290–298.

[15] Ranzenbach, R., and Barlow, J. B., 1994, “Two-Dimensional Airfoil in Ground Effect, an Experimental and Computational Study,” SAE Tech. Pap. 942509, p. 9.

[16] Ranzenbach, R., and Barlow, J. B., 1995, “Cambered Airfoil in Ground Effect-Wind Tunnel and Road Conditions,” 13th Appl. Aerodyn. Conf., pp. 1208–1215.

[17] Ranzenbach, R., and Barlow, J., 1996, “Cambered Airfoil in Ground Effect an Experimental and Computational Study,” SAE Tech. Pap. 960909.

[18] Zhang, X., and Zerihan, J., 2000, “Turbulent Wake behind a Single Element Wing in Ground Effect,” Proc. 10th Int. Symp. Appl. Laser Tech. to Fluid Mech.

[19] Zerihan, J., 2001, “An Investigation on the Aerodynamics of a Symmetrical Airfoil in Ground Effect,” University of Southampton.

[20] Zerihan, J., and Zhang, X., 2001, “A Single Element Wing in Ground Effect; Comparisons of Experiments and Computation,” 39th Aerosp. Sci. Meet. Exhib.

[21] Zhang, X., Zerihan, J., Ruhrmann, A., and Deviese, M., 2002, “Tip Vortices Generated by a Wing in Ground Effect,” *11th International Symposium on Applications of Laser Techniques to Fluid Mechanics*.

[22] Doig, G., Barber, T. J., and Neely, A. J., 2011, “The Influence of Compressibility

on the Aerodynamics of an Inverted Wing in Ground Effect," J. Fluids Eng. Trans. ASME, **133**(6), pp. 1–12.

[23] Diasinos, S., Barber, T. J., and Doig, G., 2013, "Influence of Wing Span on the Aerodynamics of Wings in Ground Effect," Proc. Inst. Mech. Eng. Part G J. Aerosp. Eng., **227**(3), pp. 569–573.

[24] Diasinos, S., Barber, T., and Doig, G., 2017, "Numerical Analysis of the Effect of the Change in the Ride Height on the Aerodynamic Front Wing-Wheel Interactions of a Racing Car," Proc. Inst. Mech. Eng. Part D J. Automob. Eng., **231**(7), pp. 900–914.

[25] Keogh, J., Doig, G., Diasinos, S., and Barber, T., 2015, "The Influence of Cornering on the Vortical Wake Structures of an Inverted Wing," Proc. Inst. Mech. Eng. Part D J. Automob. Eng., **229**(13), pp. 1817–1829.

[26] Roberts, L. S., Correia, J., Finnis, M. V., and Knowles, K., 2016, "Aerodynamic Characteristics of a Wing-and-Flap Configuration in Ground Effect and Yaw," Proc. Inst. Mech. Eng. Part D J. Automob. Eng., **230**(6), pp. 841–854.

[27] Roberts, L. S., Finnis, M. V., and Knowles, K., 2016, "Characteristics of Boundary-Layer Transition and Reynolds-Number Sensitivity of Three-Dimensional Wings of Varying Complexity Operating in Ground Effect," J. Fluids Eng. Trans. ASME, **138**(9), pp. 1–10.

[28] Roberts, L. S., Finnis, M. V., and Knowles, K., 2017, "Forcing Boundary-Layer Transition on a Single-Element Wing in Ground Effect," J. Fluids Eng. Trans. ASME, **139**(10), pp. 1–12.

[29] Roberts, L. S., Finnis, M. V., and Knowles, K., 2019, "Modelling Boundary-Layer Transition on Wings Operating in Ground Effect at Low Reynolds Numbers," Proc. Inst. Mech. Eng. Part D J. Automob. Eng., **233**(11), pp. 2820–2837.

[30] Ranzenbach, R., Barlow, J. B., and Diaz, R. H., 1997, "Multi-Element Airfoil in Ground Effect- an Experimental and Computational Study," AIAA Pap. no.

972238.

[31] Jasinski, W. J., and Selig, M. S., 1998, “Experimental Study of Open-Wheel Race-Car Front Wings,” SAE Tech. Pap. 983042.

[32] Zhang, X., and Zerihan, J., 2003, “Aerodynamics of a Double-Element Wing in Ground Effect,” AIAA J., **41**(6), pp. 1007–1016.

[33] Mahon, S., 2005, “The Aerodynamics of Multi_element Wings in Ground Effect,” University of Southampton.

[34] Van Den Berg, M. A., and Zhang, X., 2009, “The Aerodynamic Interaction between an Inverted Wing and a Rotating Wheel,” J. Fluids Eng. Trans. ASME, **131**(10).

[35] Pegrum, J. M., 2006, “Experimental Study of the Vortex System Generated by a Formula 1 Front Wing,” Imperial College, London.

[36] Van Den Berg, M. A., 2007, “Aerodynamic Interaction of an Inverted Wing with a Rotating Wheel,” University of Southampton.

[37] Heyder-Bruckner, J., 2011, “The Aerodynamics of an Inverted Wing and a Rotating Wheel in Ground Effect,” University of Southampton.

[38] Mahon, S., and Zhang, X., 2006, “Computational Analysis of a Inverted Double-Element Airfoil in Ground Effect,” J. Fluids Eng. Trans. ASME, **128**(6), pp. 1172–1180.

[39] Henri J.-P. Morand, R. O., 1995, *Fluid-Structure Interaction: Applied Numerical Methods*.

[40] S.K. Chakrabarti, 2005, *Numerical Models in Fluid-Structure Interaction*.

[41] Dowell, E. H., and Hall, K. C., 2001, “Modelling of Fluid-Structure Interaction,” Annu. Rev. Fluid Mech., **33**, p. pp 445-490.

[42] Yurkovich, R., 2003, “Status of Unsteady Aerodynamic Prediction for Flutter of High Performance Aircraft,” J. Aircr., **40**(5), pp. 832–842.

[43] Sangeetha, C., 2015, “Fluid Structure Interaction on AGARD 445.6 Wing at Transonic Speeds,” J. Aircr., **2**(4), pp. 28–34.

[44] Chen, X., 2007, “Numerical Simulation of 3D Wing Flutter with Fully Coupled Fluid Structural Interaction,” J. Aircr., **36**, pp. 856–867.

[45] Krawczyk, P., Beyene, A., MacPhee, D., 2013, “Fluid Structure Interaction of a Morphed Wind Turbine Blade,” Int. J. Energy Res., **37**, pp. 1784–1793.

[46] Bagheri, E., Nejat, A., 2015, “Numerical Aeroelastic Analysis of Wind Turbine NREL Phase VI Rotor,” Energy Equip. Syst., **3**, pp. 45–55.

[47] Gaylard, A., Beckett, M., Gargoloff, J. I., and Duncan, B. D., 2010, “CFD-Based Modelling of Flow Conditions Capable of Inducing Hood Flutter,” SAE Int. J. Passeng. Cars - Mech. Syst., **3**(1), pp. 675–694.

[48] Ratzel, M., and Dias, W., 2014, “Fluid - Structure Interaction Analysis and Optimization of an Automotive Component,” SAE Tech. Pap.

[49] Patil, S., Lietz, R., Woodiga, S., Ahn, H., Larson, L., Gin, R., Elmore, M., and Simpson, A., 2015, “Fluid Structure Interaction Simulations Applied to Automotive Aerodynamics,” SAE Tech. Pap.

[50] Andreassi, L., Mulone, V., Valentini, P. P., and Vita, L., 2004, “A CFD-FEM Approach to Study Wing Aerodynamics under Deformation,” SAE Tech. Pap.

[51] Björn, H., Elmar, W., and Dieter, D., 2004, “A Monolithic Approach to Fluid–Structure Interaction Using Space–Time Finite Elements,” Comput. Methods Appl. Mech. Eng., **193**, pp. 23–26.

[52] P. B. Ryzhakov, R. Rossi, S. R. Idelsohn, and E. Oñate, 2010, “A Monolithic Lagrangian Approach for Fluid–Structure Interaction Problems,” Comput Mech, **46**, pp. 883–899.

[53] Rossi, R., and Oñate, E., 2010, “Analysis of Some Partitioned Algorithms for Fluid-structure Interaction,” Eng. Comput., **27**(1), pp. 20–56.

[54] ANSYS, 2020, “ANSYS System Coupling User’s Guide.”

[55] M. M Munk, 1949, “Propeller Containing Diagonally Disposed Fibrous Material.”

[56] James J. Joo, Christopher R. Marks, L. Z. and A. J. C., 2015, “Variable Camber

Compliant Wing - Design," AIAA Conf., pp. 2015–1050.

[57] NASA, 1981, *Aeroelastic Tailoring with Composites Applied to Forward Swept Wings*.

[58] Georghiades, G. A., 1997, "Aeroelastic Behaviour of Composite Wings," City University.

[59] Shirk, M. H., Hertz, T. J., and Weisshaar, T. A., 1986, "Aeroelastic Tailoring-Theory, Practice and Promise," J. Aircr., **23**(1), pp. 6–18.

[60] Haftka, R. T., 1986, "Structural Optimisation with Aeroelastic Constraints: A Survey of US Applications," Int. J. Veh. Des., **7**.

[61] Weisshaar, T. A., and Ryan, R. J., 1986, "Control of Aeroelastic Instabilities through Stiffness Cross-Coupling," J. Aircr., **23**, pp. 148–155.

[62] Eschenauer, H. A., Schuhmacher, G., and Hartzheim, W., 1992, "Multidisciplinary Design of Composite Aircraft Structures by Lagrange," Comput. Struct., **44**(4), pp. 877–893.

[63] Popelka, D., Lindsay, D., Jr, Parham T., Berry, V., and Baker, D. J., 1995, "Results of an Aeroelastic Tailoring Study for a Composite Tiltrotor Wing," *51st Annual Forum of the American Helicopter Society*.

[64] Gimmestad, D., 1981, "Aeroelastic Tailoring of a Composite Winglet for KC-135," AIAA J., pp. 1981–607.

[65] Eastep, F. E., Tischler, V. A., Venkayya, V. B. and Knot, N. S., 1999, "Aeroelastic Tailoring of Composite Structures," J. Aircr., **36**(6), pp. 1041–1047.

[66] Miura, H., Chattopadhyay, A., and Jha, R., 1997, *Development of a Composite Tailoring Technique for Airplane Wing*.

[67] Knot, N. S., Zweber, J. V., Veley, D. E., Öz, H., and Eastep, F. E., 2002, "Flexible Composite Wing with Internal Actuation for Roll Maneuver," J. Aircr., **39**(4), pp. 521–527.

[68] Young, Y. L., Motley, M. R., Barber, R., Chae, E. J., and Garg, N., 2016, "Adaptive

Composite Marine Propulsors and Turbines: Progress and Challenges," Appl. Mech. Rev., **68**(6).

[69] Young, Y. L., 2019, "Hydroelastic Response of Lifting Bodies in Separated Flows," *NATO-AVT-307: Symposium on Separated Flow: Prediction, Measurement and Assessment for Air and Sea*.

[70] Lin, C., and Lee, Y., 2004, "Stacking Sequence Optimization of Laminated Composite Structures Using Genetic Algorithm with Local Improvement," Compos. Struct., **63**(3), pp. 339–345.

[71] Plucinski, M. M., Young, Y. L., and Liu, Z., 2007, "Optimization of a Self-Twisting Composite Marine Propeller Using Genetic Algorithms," *16th International Conference on Composite Materials*.

[72] Yingqian Liao, Sicheng He, Joaquim R. R. A. Martins and Yin L. Young., 2020, "Hydrostructural Optimization of Generic Composite Hydrofoils," *AIAA SciTech Forum*.

[73] G. Wang, Z. Dong., P. A., 2001, "Adaptive Response Surface Method - a Global Optimization Scheme for Approximation-Based Design Problems," Eng. Optim. Appl. Optim. Des., **33**, pp. 707–733.

[74] Y. Jiang, J. Liu, Q. Chi, F. Lu, B. Li, A., Learned, R. S., and Friz, H., 2014, "Aerodynamic Characterization of the Design Changes for the Facelift of the VW Bora," SAE Tech. Pap. 2014-01-0601.

[75] Kim. , M., Jeong, Y., and Jimin, K., 2018, "Aerodynamic Optimization of Rear End Parameters in a Commercial Bus Utilizing Statistical Response Surface Method," Korean Soc. Automot. Eng., **26**(2).

[76] Sun, H. and Lee, S., 2005, "Response Surface Approach to Aerodynamic Optimization Design of Helicopter Rotor Blade," Int. J. Numer. Meth. Eng., **64**, pp. 125–142.

[77] Madsen, J., Shyy, W., Haftka, R., and Liu, J., 1997, “Response Surface Techniques for Diffuser Shape Optimization,” AIAA Pap. no. 97-1801.

[78] Steffen, C. J., 2002, “Response Surface Modeling of Combinedcycle Propulsion Components Using Computational Fluid Dynamics,” AIAA Pap. no. 2002-0542.

[79] Li, G., and Grandhi, R., 2000, “Accuracy and Efficiency Improvement of Response Surface Methodology for Multidisciplinary Design Optimization,” AIAA Pap. 2000-4715.

[80] Hyosung Sun, 2011, “Wind Turbine Airfoil Design Using Response Surface Method,” J. Mech. Sci. Technol., **25**(5), pp. 1335–1340.

[81] Lee, S. L., and SangJoon Shin, 2020, “Wind Turbine Blade Optimal Design Considering Multi-Parameters and Response Surface Method,” Energies, **13**(7), p. 1639.

[82] Sobieszczanski-Sobieski, J and Haftka, R. T., 1996, “Multidisciplinary Aerospace Design Optimization: Survey of Recent Developments,” AIAA-96-0711.

[83] Giesing, J. P. and Barthelemy, J. M., 1998, “Summary of Industry MDO Applications and Needs,” AIAA J.

[84] Kim, Y., Jeon, Y. H., and Lee, D. H., 2006, “Multi-Objective and Multidisciplinary Design Optimization of Supersonic FighterWing,” J. Aircr., **43**(3).

[85] Teng Long, Li Liu, Jiabo Wang, and Sida Zhou, L. M., 2008, “Multi-Objective Multidisciplinary Optimization of Long-Endurance UAV Wing Using Surrogate Models in ModelCenter,” *AIAA/ISSMO Multidisciplinary Analysis and Optimization Conference*.

[86] Liu, I. W., and Lin, C. C., 1991, “Optimum Design of Composite Wing Structures by a Refined Optimality Criterion,” Compos. Struct., **17**(1), pp. 51–65.

[87] Georghiades, G. A., Guo, S., and Banerjee, J. R., 1996, “Flutter Characteristics of Laminated Wings,” J. Aircr., **33**, pp. 1204–1206.

[88] Lillico, M., Butler, R., Guo, S.,Banerjee, J. R., 1997, “Aeroelastic Optimization of

Composite Wings Using the Dynamic Stiffness Method," Aeronaut. J., **101**, pp. 77–86.

[89] Guo, S., Banerjee, J. R., Cheung, C. W., 2003, "The Effect of Laminate Lay-up on the Flutter Speed of Composite Wings," Proc. IMechE, Part G J. Aerosp. Eng., **217**, pp. 115–122.

[90] S Guo, D Li, and Y. L., 2012, "Multi-Objective Optimization of a Composite Wing Subject to Strength and Aeroelastic Constraints," Proc. Inst. Mech. Eng. Part G J. Aerosp. Eng., **226**(9), pp. 1095–1106.

[91] Pedrol, E., Massons, J., Díaz, F., and Aguiló, M., 2018, "Two-Way Coupling Fluid-Structure Interaction (FSI) Approach to Inertial Focusing Dynamics under Dean Flow Patterns in Asymmetric Serpentines," Fluids, **3**(3).

[92] Nonino, M., Ballarin, F., and Rozza, G., 2021, "A Monolithic and a Partitioned, Reduced Basis Method for Fluid–Structure Interaction Problems," Fluids, **6**(6), p. 229.

[93] Lassila, T., Quarteroni, A., and Rozza, G., 2012, "A Reduced Basis Model with Parametric Coupling for Fluid-Structure Interaction Problems," SIAM J. Sci. Comput., **34**(2).

[94] Versteeg, H. K., and Weeratunge, M., 2007, *An Introduction to Computational Fluid Dynamics: The Finite Volume Method*, Pearson.

[95] Antonio, F., and Zulfaa, M.-K., 2010, "Fuel Savings on a Heavy Vehicle via Aerodynamic Drag Reduction," Transp. Res. Part D Transp. Environ., **15**(5), pp. 275–284.

[96] Buil, R. M., and Luis, C. H., 2009, "Aerodynamic Analysis of a Vehicle Tanker," J. Fluids Eng., **131**(4).

[97] Roache, P. J., 1998, *Verification and Validation in Computational Science and Engineering*, Hermosa Publishers.

[98] Patrick J. Roache, 2012, "Verification of Codes and Calculations," AIAA J., **36**(5).

[99] Oberkampf, W. L., and Trucano, T. G., 2000, “Validation Methodology in Computational Fluid Dynamics,” *Fluids 2000 Conference and Exhibit*.

[100] Oberkampf, W. L., and Trucano, T. G., 2002, “Verification and Validation in Computational Fluid Dynamics,” Prog. Aerosp. Sci., **38**(3), pp. 209–272.

[101] Charles Hirsch, 2007, *Numerical Computation of Internal and External Flows: The Fundamentals of Computational Fluid Dynamics*, Elsevier Science.

[102] Ferziger, J. H., and Milovan, P., 2012, *Computational Methods for Fluid Dynamics*, Springer Science & Business Media.

[103] Laney, C. B., 1998, *Computational Gasdynamics*, Cambridge University Press.

[104] K.W. Morton, 1996, *Numerical Solution Of Convection-Diffusion Problems*, Chapman and Hall/CRC.

[105] Oden, J. T., 1993, *Error Estimation and Control in Computational Fluid Dynamics, in the Mathematics of Finite Elements and Applications*, John Wiley.

[106] Roache, P. J., 1993, “A Method for Uniform Reporting of Grid Refinement Studies,” *Proceedings of Quantification of Uncertainty in Computation Fluid Dynamics*.

[107] P. J. Roache, 1997, “Quantification of Uncertainty in Computational Fluid Dynamics,” Annu. Rev. Fluid Mech., **29**, pp. 123–160.

[108] Cadafalch, J., Pe´rez-Segarra, C. D., Co`nsul, R., and Oliva, A., 2002, “Verification of Finite Volume Computations on Steady-State Fluid Flow and Heat Transfer,” J. Fluids Eng., **124**(1), pp. 11–21.

[109] Chen, C.-F. A., Lotz, R. D., and Thompson, B. E., 2002, “Assessment of Numerical Uncertainty around Shocks and Corners on Blunt Trailing-Edge Supercritical Airfoils,” Comput. Fluids, **31**(1), pp. 25–40.

[110] Eca, L., and Hoekstra, M., 2002, “An Evaluation of Verification Procedures for CFD Applications,” *The 24th Symposium on Naval Hydrodynamics*.

[111] Roy, C. J., 2012, “Grid Convergence Error Analysis for Mixed-Order Numerical

Schemes," AIAA J.

[112] AIAA, 2002, *Guide for the Verification and Validation of Computational Fluid Dynamics Simulations*, American Institute of Aeronautics and Astronautics.

[113] Oberkampf, W. L., Trucano, T. G., and Hirsch, C., 2004, "Verification, Validation, and Predictive Capability in Computational Engineering and Physics," Appl. Mech., **57**(5), pp. 345–384.

[114] Raymond Cosner, 2012, "CFD Validation Requirements for Technology Transition," *AIAA Fluid Dynamics Conference*.

[115] Joseph G. Marvin, 2012, "Perspective on Computational Fluid Dynamics Validation," AIAA J.

[116] M. Sindir, S. Barson, Chan, D., and Lin, W., 2012, "On the Development and Demonstration of a Code Validation Process for Industrial Applications," AIAA J.

[117] John, W. S., 2012, *Mechanics of Fluids*, CRC Press.

[118] ANSYS, 2019, *ANSYS FLUENT 2019 R1 Manual*.

[119] Spalart, P. R., and Allmaras, S. R., 1992, "A One-Equation Turbulence Model for Aerodynamic Flows," AIAA Pap. no. 92-0439.

[120] Launder, B. E., and Spalding, D. B., 1974, "The Numerical Computation of Turbulent Flows," Comput. Methods Appl. Mech. Eng, **3**, pp. 269–289.

[121] Wilcox, D. C., 1988, "Multiscale Models for Turbulent Flows," AIAA J., **26**(11), pp. 1311–1320.

[122] Menter, F. R., 1994, "Two-Equation Eddy-Viscosity Turbulence Models for Engineering Applications," AIAA J., **32**(8), pp. 1598–1605.

[123] Yakhot, A., and Orszag, S., 1986, "Renormalisation Group Analysis of Turbulence: I Basic Theory," J. Sci. Comput, **1**(1), pp. 1–51.

[124] Shih, T-H, Liou, W. W, Shabbir, A., Yang, Z., and Zhu, J., 1995, "A New k −ε Eddy Viscosity Model for High Reynolds Number Turbulent Flows," Com- put. Fluids, **24**, pp. 227–238.

[125] Kollar, L. P., and Springer, G. S., 2009, *Mechanics of Composite Structures*, Cambridge University Press.

[126] Bungartz, H. J., Schäfer, M. Eds., 2006, *Fluid-Structure Interaction: Modelling, Simulation, Optimization*, Springer-Verlag Berlin Heidelberg.

[127] Sigrist, J. F., 2015, *Fluid-Structure Interaction: An Introduction to Finite Element Coupling*, Wiley.

[128] Ryzhakov, P. B., Rossi, R., Idelsohn, S. R., and Onate, E., 2010, "A Monolithic Lagrangian Approach for Fluid-Structure Interaction Problems," Comput. Mech., **46**, pp. 883–899.

[129] C. Michler, S.J. Hulshoff, E.H. van Brummelen, and R. de Borst, 2004, "A Monolithic Approach to Fluid-Structure Interaction," Comput. Fluids, **33**(5–6), pp. 839–848.

[130] Piperno, S., Farhat, C., and Larrouturou, B., 1995, "Partitioned Procedures for the Transient Solution of Coupled Aeroelastic Problems, Part I: Model Problem, Theory and Two-Dimensional Application," Comput. Methods Appl. Mech. Eng., **124**(1–2), pp. 79–112.

[131] Faber, T. E., 1995, *Fluid Dynamics for Physicists*, Cambridge University Press.

[132] Venter, G., Haftka, R. T., and Starnes, J. H., J., 1996, "Construction of Response Surfaces for Design Optimization Applications," AIAA Pap. 96-4040.

[133] Cavazzuti, M., 2012, *Optimization Methods: From Theory to Scientific Design and Technological Aspects in Mechanics*, Springer-Verlag Berlin Heidelberg.

[134] Lorriaux, E., Bourabaa, N., and Monnoyer, F., 2006, "Aerodynamic Optimization of Railway Motor Coaches," 7th World Congress on Railway Research Queen Elizabeth in Montreal, Canada.

[135] D. Ghate, 2005, "Using Automatic Differentiation for Adjoint CFD Code Development," Comput. Sci.

[136] Bizzarrini, N., Grasso, F., and D.P. Coiro, 2011, “Genetic Algorithm in Wind Turbine Airfoil Design,” *The EWEA 2011*.

[137] Myers, R. H., Montgomery, D. C., and Christine M. Anderson-Cook, 2016, *Response Surface Methodology: Process and Product Optimization Using Designed Experiments*.

[138] Eschenauer, H., Koski, J., and Osyczka, A., 1990, *Multicriteria Design Optimization*, Springer-Verlag Berlin Heidelberg.

[139] Lewe, J. H., 2002, “Spotlight Search Method for Multi-Criteria Optimization Problems,” AIAA Pap. 2000-5432.

[140] Roache, P.J., Ghia, K.N., White, F. M., 1986, “Editorial Policy Statement on Control of Numerical Accuracy,” J. Fluids Eng. Trans. ASME, **108**.

[141] Katz, J., 1985, “Calculation of the Aerodynamic Forces on Automotive Lifting Surfaces,” ASME J. Fluids Eng., **107**, pp. 438–443.

[142] Zhang, X., and Zerihan, J., 2003, “Off-Surface Aerodynamic Measurements of a Wing in Ground Effect,” J. Aircr., **40**(4), pp. 716–725.

[143] FIA, 2018, “2018 Formula One Technical Regulation.”

[144] ANSYS, 2018, “Ansys Composite Library.”

[145] Bushnell, D. M., 2003, “Aircraft Drag Reduction—a Review,” Proc. I MECH E Part G J. Aerosp. Eng., **217**(1), pp. 1–18.

[146] Bushnell, D. M., 1990, “Supersonic Aircraft Drag Reduction,” AIAA J.

[147] Neittaanmaki, P., Rossi, T., Korotov, S., Onate, E., Periaux, J., and Knorzer, D., 2004, “Overview on Drag Reduction Technologies for Civil Transport Aircraft,” *European Congress on Computational Methods in Applied Sciences and Engineering (ECCOMAS)*, pp. 24–28.

[148] Zhang, X., Toet, W., and Zerihan, J., 2006, “Ground Effect Aerodynamics of Race Cars,” Appl. Mech. Rev., **59**(1–6), pp. 33–48.

[149] Smith, A. M. O., 1975, “High-Lift Aerodynamics,” J. Aircr., **12**(6).

[150] Katz, J., 1995, *Race Car Aerodynamics: Designing for Speed*, Robert Bentley.

[151] Wright, P. G., and Matthews, T., 2001, *Formula 1 Technology*, SAE International.

[152] Obeid, S., Jha, R., and Ahmadi, G., 2017, "RANS Simulations of Aerodynamic Performance of NACA 0015 Flapped Airfoil," Fluids, **2**(2).

[153] Landvoqt, B., 2016, "Fluid-Structure Interaction of Racing Car Spoilers," *The NAFEMS European Conference: Multiphysics Simulation*, Copenhagen.

[154] FIA, 2019, "2019 Formula One Technical Regulation."

[155] FIA, 2020, "2020 Formula One Technical Regulation."

[156] Tesinova, P., 2011, *Advances in Composite Materials - Analysis of Natural and Man- Made Materials*, InTech.

[157] Sun, C. T., Quinn, B. J., and Tao, J., 1996, *Comparative Evaluation of Failure Analysis Methods for Composite Laminates.*

[158] McKay, M. D., Beckman, R. J., and Conover, W. J., 1979, "A Comparison of Three Methods for Selecting Values of Input Variables in the Analysis of Output from a Computer Code," Technometrics, **21**(2), pp. 239–245.

[159] Triantaphyllou, E., 2002, *Multi-Criteria Decision Making Methods:A Comparative Study*, Kluwer Academic Publishers.

[160] Kaw, A. K., 2006, *Mechanics of Composite Materials*, CRC Press.

[161] Minus, M. L., and Kumar, S., 2005, "The Processing, Properties, and Structure of Carbon Fibers," JOM, **57**, pp. 52–58.

[162] Kewate, A. D., Ghade, R. R., and Kewate, S. R., 2017, "Stress and Deflection Analysis of Composite Cantilever Beam Using Software– A New Trend Approach," J. Mater. Sci. Mech. Eng., **4**(3), pp. 126–130.

[163] Quadrant, 2016, *Ketron 1000 PEEK*.

[164] Duan, S., Liu, F., Pettersson, T., Creighton, C., and Asp, L., 2019, "Determination of Transverse and Shear Moduli of Single Carbon Fibres," Carbon N. Y.

[165] Aktas, A., 2001, "Determination of the Deflection Fuction of a Composite

Cantilever Beam Using Theory of Anisotropic Elasticity," Math. Comput. Appl., **6**(1), pp. 67–74.

[166] Azzam, A., and Li, W., 2014, "An Experimental Investigation on the Three-Point Bending Behavior of Composite Laminate," *Materials Science and Engineering*.

[167] Cruz, J. R., Shah, C. H., and Postyn, A. S., 1996, *Properties of Two Carbon Composite Materials Using LTM25 Epoxy Resin*, Hampton, Virginia.

[168] Gere, J. M., and Goodno, B. J., 2012, *Mechanics of Materials*, ENGAGE Learning Custom Publishing.

[169] Henningson, D., and Berggren, M., 2005, *Fluid Dynamics: Theory and Computation*, KTH, Stockholm.

[170] Raback, P., Malinen, M., Ruokolainen, J., Pursula, A., and Zwinger, T., 2018, "Elmer Models Manual."

[171] NASA, 1998, "NPARC Alliance CFD Verification and Validation Web Site," Natl. Aeronaut. Sp. Adm.

APPENDICES

Appendix A Verification and validation of Fluid-Structure Interaction (FSI)

A.1 Governing equations and numerical procedure

A.1.1 Analytical solution

Despite the widespread use of computational fluid dynamics (CFD) in a variety of applications, it is claimed that there is no consensus on techniques for evaluating the credibility of CFD. Therefore, it is essential to assess the uncertainty and errors of the computational results as comparing with the theoretical and experimental ones. The main principles to do this is verification and validation. “Verification is the process of determining if a computational simulation accurately represents the conceptual model; but no claim is made of the relationship of the simulation to the real world. Validation is the process of determining if a computational simulation represents the real world” [97].

The case presented in this study is a unique example provided from the tutorial of the Elmer package, and It is difficult to carry out the validation of its forecast by comparing it to an existing reference. Therefore, the classical beam theory is used for the validation of the results. However, it might be a challenge to draw reasonable results from the theoretical calculation due to limitation; the size of the beam is an unusual ratio of width to length (1:3) and elasticity modulus is relatively small.

In the structure analysis, deflection of a beam is an important parameter to be considered and It is based on the deflection curve differential equations as well

as the material and geometrical parameters of the beam. The beam used in this study is a cantilever beam. The differential equations may be stated in the following terms when the flexural rigidity EI (where I – moment of inertia) is constant [168]:

$$\mathrm{EI}\frac{\partial^4 v}{\partial_y{}^4} = -\mathrm{q} \tag{A-1}$$

$$\mathrm{EI}\frac{\partial^4 v}{\partial_y{}^4} = -\mathrm{q} \tag{A-2}$$

$$\mathrm{EI}\frac{\partial^2 v}{\partial_y{}^2} = \mathrm{M} \tag{A-3}$$

Where v is a deflection with respect to distributed load q, shear force V, and bending moment M. EI is the product of the Young's Modulus E and the inertia of the section I, and it is known as bending stiffness.

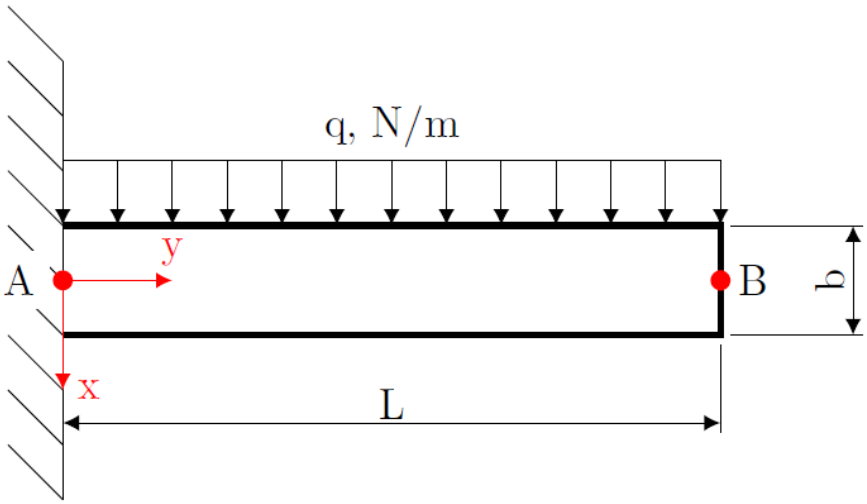

Figure A-1 Schematic drawing of distributed load over a cantilever beam

Figure A-1 shows the cantilever beam model that is used to calculate the deflection of the beam (neglecting the effect of the circumference of the beam) and the equation (A-3), referred as bending-momentum equation, is applied. To solve the differential equation, you must first establish the boundary conditions, and these can be stated as follows:

- The derivative of the deflection, or the angular deflection (v'), is known an d equal to zero:

$$v'_A\,(\mathrm{y}{=}0) = 0, v'_B\,(\mathrm{y}{=}1.2) = 0 \qquad \textbf{(A-4)}$$

- The deflection v is known on the fixed point (A), and it is equal to zero

$$\mathrm{v}\,(\mathrm{y}{=}0) = 0 \qquad \textbf{(A-5)}$$

- q is the uniformly distributed load over the beam. It is defined as the deriv ative of the force distribution:

$$\mathrm{q(y)} = \frac{dF(y)}{dy} \qquad \textbf{(A-6)}$$

The Navier-Stokes equations are used to a discrete control volume as illustrated in Figure A-2 to determine the load over the beam. Considering the height of differential dy, limitless control volume will be incorporated. Notice that p_i indicates the pressure on face i and n_i indicates the normal vector of that face.

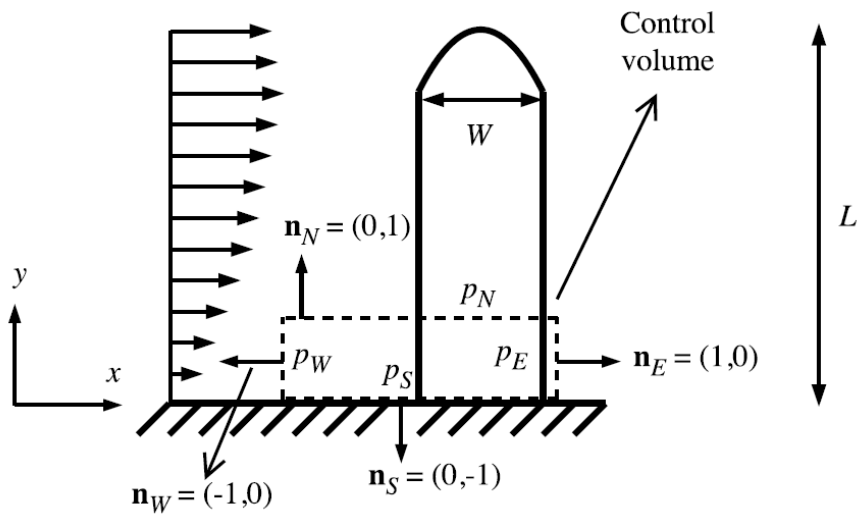

Figure A-2 Control volume around the beam

The control volume is bordered by four distinct faces that follow the Cartesian axis: east (e), west (w), north (n), and south (s). Each face has its own normal vector n_i and a pressure p_i. The integral Navier-Stokes equations for an incompressible flow in a two-dimensional situation (ignoring viscous forces and transient effects) are as follows [169]:

$$\mathrm{d}F_i = -\iint_S \left[\rho\left(u\frac{\partial u_i}{\partial x} + v\frac{\partial u_i}{\partial x}\right) + \frac{\partial p}{\partial x_i}\right] dS \qquad \textbf{(A-7)}$$

where F_i is the vector force exerted by the fluid on the solid. The integral is over the surface of control volume contour S.

As the force to be interested is in x direction, the equation (A-7) is particularised about the x direction putting i = 1 (equivalent to x) in Einstein notation:

$$\mathrm{d}F_x = -\iint_S \left[\rho\left(u\frac{\partial u}{\partial x} + v\frac{\partial u}{\partial x}\right) + \frac{\partial p}{\partial x}\right] dS \qquad \textbf{(A-8)}$$

To find the analytical solution, the effect of the vertical velocity v is neglected:

$$\mathrm{d}F_x = -\iint_S \left[\rho\left(u\frac{\partial u}{\partial x}\right) + \frac{\partial p}{\partial x}\right] dS \qquad \textbf{(A-9)}$$

As all equations on the right-hand side are put inside one integral, the Stokes theorem can be applied:

$$\mathrm{d}F_x = -\iint_S \frac{\partial}{\partial x}\left(\frac{1}{2}\rho uv + p\right) dS \tag{A-10}$$

In the simplified 1D example, the integral is then split into the two contours illustrated. The contribution of the south and north sides may be omitted since the vertical velocity is ignored. Therefore, equation (A-10) becomes as follows when the normal vectors indicated in Figure 2 are taken into consideration.:

$$\mathrm{d}F_x = \int_y^{y+dy}\left(\frac{1}{2}\rho u^2 + p_w\right) dy - \int_y^{y+dy}\left(\frac{1}{2}\rho u^2 + p_e\right) dy \tag{A-11}$$

To ignore the top and bottom faces, not only the vertical velocity but also the pressure variation must be insignificant regarding the y coordinate $\left(\frac{\partial p}{\partial y}\right) = 0$, leading to $p_n = p_s$. In addition, on the right face, the velocity profile u(y) is considered to be zero. Therefore, the equation remains as follows:

$$\mathrm{d}F_x = \int_y^{y+dy}\left(\frac{1}{2}\rho u^2 + p_w - p_e\right) dy \tag{A-12}$$

where the velocity profile at the east face is now u. The differential force is eventually written as follows if the integral is assumed to be constant inside the differential control volume.

$$\mathrm{d}F_x = \left(\frac{1}{2}\rho u^2 + p_w - p_e\right) dy \tag{A-13}$$

Applying the equation (A-13) into the equation (A-6), the uniformly distributed load over the beam with the length of L is as follows:

$$\mathrm{q(y)} = \frac{1}{2}\rho u(y)^2 L + (p_w - p_e)L \tag{A-14}$$

Note that in order to obtain $\mathrm{q(y)}$, it is required to know the inlet velocity profile $\mathrm{u(y)}$ and the pressure p_w and p_e. However, in this simplified case, the inlet velocity is constant as 1m/s.

It is impossible to compute the pressure analytically, even for the simple case because the existence of a barrier has a significant impact on the pressure distribution in a channel flow, resulting in a massive drop in this magnitude. For this reason, a case with the rigid beam without the FSI modelling is simulated using the Ansys Fluent in order to calculate the pressure on the control volume's west and east sides. Figure A-3 shows the pressure contours on the west face, which is considered as the inlet in this simulation and on the east face as the rear

of the beam. For the purpose of validation, the result gained from the Elmer is also presented on Figure A-3 and it shows good agreement between two solution.

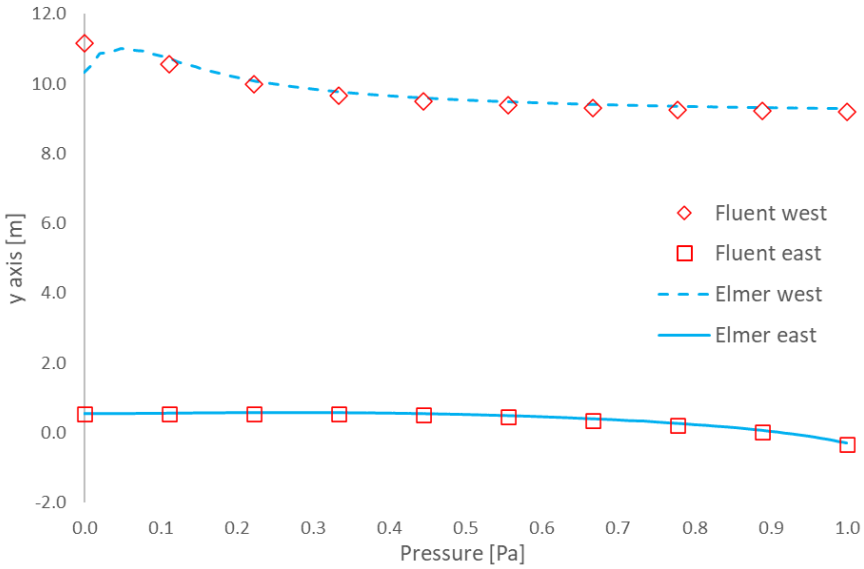

Figure A-3 Pressure profile on the control volume's west and east faces

The average of the pressure profiles in Figure 3 is used as a first estimate of the solution for calculating, $\mathrm{q(y)}$, p_w and p_e for the final computation of the distributed load. It is noted that during the derivation of the equations, the pressure is considered to be constant with respect to the y coordinate.:

$$p_w = 9.7204\ Pa\ , \quad p_e = 0.3318\ Pa \tag{A-15}$$

Lastly, with $\mathrm{q}(\mathrm{y})$ force acting on the y surface of the beam at the length of y/2, the bending moment equation turns to be as follows:

$$\mathrm{EI}\frac{\partial^2 v}{\partial_y{}^2} = -\mathrm{q}\frac{y^2}{2} \tag{A-16}$$

After calculating the double integration applying the initial conditions (A-4) and (A-5),

$$\mathrm{EI}v = -\frac{qy^4}{24} + \frac{qL^3}{6} - \frac{qL^4}{8} \tag{A-17}$$

The equation (A-17) is the equation of deflection of cantilever beam with uniformly distributed load. Because the greatest deflection occurs at y = L, it may be written as:

$$\delta_{max} = \frac{-qL^4}{8EI} \tag{A-18}$$

where E is Young's modulus and I is the moment of inertia for a square-cross sectioned beam, which is $\mathrm{I} = \frac{b^3}{12}$ in this case.

A.1.2 Introduction to Elmer

The study is carried out with the help of open-source solver, Elmer. In fluid modelling, it employs a Eulerian method, whereas in structural modelling, it employs a Lagrangian approach. The problem is addressed using an ALE (Arbitrary Lagrangian-Eulerian) frame of reference. Elmer uses a time-consuming method for FSI modelling called one-way coupling, in which he adapts the grid with each iteration (or strongly coupled method). Because the task was two-dimensional and used a small number of grid elements, there is no difficulty in terms of computing expenses in this investigation. Elmer is said to employ three solvers at once, according to the manual: a fluid solver, a structural solver, and a mesh solver.

The flow parameters of the issue are obtained using the fluid solver in Elmer, which is based on the Navier-Stokes equation. To avoid numerical instability, Elmer linearises the NS equation's convective component. The linearisation is performed in one of two ways: Picard iteration,

$$(\vec{u}\cdot\nabla)\vec{u} \approx (\vec{U}\cdot\nabla)\vec{u} \qquad \textbf{(A-19)}$$

or the Newton iteration,

$$(\vec{u}\cdot\nabla)\vec{u} \approx (\vec{U}\cdot\nabla)\vec{u} + (\vec{u}\cdot\nabla)\vec{U} - (\vec{U}\cdot\nabla)\vec{U} \qquad \textbf{(A-20)}$$

where U is the velocity vector at preceding step. The convective term is presented using the ALE frame of reference and assuming mesh velocity is C.

$$\left((\vec{u}-\vec{c})\cdot\nabla\right)\vec{u} \approx \left(\left(\vec{U}-\vec{c}\right)\cdot\nabla\right)\vec{u} \qquad \textbf{(A-21)}$$

While the Picard iteration has a slower rate of convergence, it is more robust, and Newton iteration has a quicker rate of convergence. With the Elmer, the Picard method solves the problem first and starts off the solution using the Picard method and then progresses to the Newton method after convergence has been obtained [170].

The structural solver is the second solver, and it possesses non-linear elasticity properties, by which the deformation produced on the structure by fluid is calculated. Any detailed information including the associated equations is not provided in the Elmer manual [170]. This solution is engaged when the mesh starts to deform and the structure's behaviour is no longer linear, regardless of whether the material characteristics are provided as constant values.

Finally, as the solution progresses, the mesh solver is utilised to recompute the mesh based on the deformation that happens as a result of interacting with the fluid. The built-in meshing functionality of the Elmer programme was utilised to generate the grids used in this investigation. Delaunay-type triangular components are used to produce grids, maintaining the geometry’s form and the curvatures. Three meshes used in this study are presented in Figure A-4.

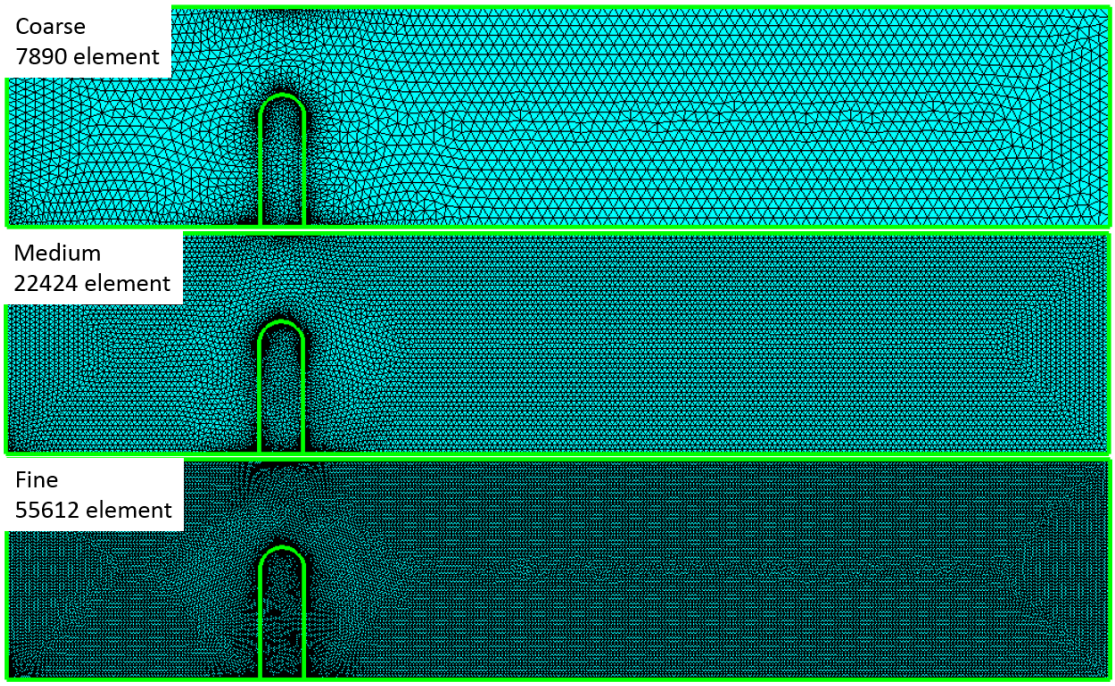

Figure A-4 Mesh generation in Elmer

A.2 Results and discussion

The results of the computations using Elmer and ANSYS are shown in this section.

A.2.1 Numerical verification

As mentioned above that the computational methods give approximate results, to verify that the findings produced are independent of the domain discretisation, a grid sensitivity analysis should be carried out. For different Young's Modulus values within the range to be evaluated, the Grid Convergence Index (GCI) technique [171] is employed in the current study.

Table A-1 Information about the grid sensitivity study with Young's Modulus 1000 Pa, representative of the range from 500 Pa to 2500 Pa.

Node	Mesh size [m]	Ref. ratio	Deflection [m]	p	GCI [%]	GCI ratio
28294	0.0266	1.5662	0.2630	-	0.43	-
11534	**0.0416**	**1.6691**	**0.2627**	**0.4150**	**0.57**	**1.0012**
4140	0.0695	1.4380	0.2623	1.0000	0.29	1.0015
2002	0.1000	1.4024	0.2621	4.0444	4.72	1.0010
1018	0.1402	1.5953	0.2588	-	-	-
400	0.2236	-	0.2560	-	-	-

Table A-2 Information about the grid sensitivity study with Young's Modulus 4000 Pa, representative of the range from 3000 Pa to 5000 Pa

Node	Mesh size [m]	Ref. ratio	Deflection [m]	p	GCI [%]	GCI ratio
28294	0.0266	1.5662	0.0740	-	1.52	-
11534	**0.0416**	**1.6691**	**0.0737**	**0.4150**	**2.04**	**1.0041**
4140	0.0695	1.4380	0.0733	0.3219	3.41	1.3406
2002	0.1000	1.4024	0.0728	1.5850	1.29	0.3382
1018	0.1402	1.5953	0.0713	-	-	-
400	0.2236	-	0.0711	-	-	-

Table A-3 Information about the grid sensitivity study with Young's Modulus 7000 Pa, representative of the range from 5500 Pa to 7500 Pa.

Node	Mesh size [m]	Ref. ratio	Deflection [m]	p	GCI [%]	GCI ratio
28294	0.0266	1.5662	0.0461	-	1.08	-
11534	**0.0416**	**1.6691**	**0.0459**	**0.5850**	**1.63**	**1.0043**
4140	0.0695	1.4380	0.0456	0.4150	3.29	1.5102

2002	0.1000	1.4024	0.0452	1.0000	2.21	0.3362
1018	0.1402	1.5953	0.0444	-	-	-
400	0.2236	-	0.0434	-	-	-

Table A-4 Information about the grid sensitivity study with Young's Modulus 10000 Pa, representative of the range from 8000 Pa to 10000 Pa.

Node	Mesh size [m]	Ref. ratio	Deflection [m]	p	GCI [%]	GCI ratio
28294	0.0266	1.5662	0.0334	-	0.37	-
11534	**0.0416**	**1.6691**	**0.0333**	**1.0000**	**0.75**	**1.0030**
4140	0.0695	1.4380	0.0331	0.5850	2.27	2.0119
2002	0.1000	1.4024	0.0328	1.0000	2.29	0.5046
1018	0.1402	1.5953	0.0322	-	-	-
400	0.2236	-	0.0320	-	-	-

The results of the GCI research with various Young's Modulus across the study's range are presented in Tables A-1 to A-4. It is worth noting that the mesh refinement is accomplished by changing the Elmer's maximum cell size. However, because the number is not reflective of the mesh's real size, it cannot be utilised to calculate the refinement ratio for future results. Therefore, the mesh mean size is computed using the equation as below [171]:

$$h_{mean} = \left(\frac{H}{N}\right)^{1/D} \quad \textbf{(A-22)}$$

where H is the typical domain size depending on the problem dimension D and N is the number of nodes. H is 20m^2 referred to the area of the channel.

The calculation of the refinement ratio is performed using ratio of two consecutive grid refinements $\mathrm{r} = h_2/h_1$, but in this case, due to lack of uniformity of spacing refinement the effective grid refinement ratio can be written as [171]:

$$r_{eff} = \left(\frac{N_1}{N_2}\right)^{1/D} \quad \textbf{(A-23)}$$

where N is the total number of elements and D is the spatial dimension of the problem.

In every case, the bolded row refers to the mesh that is used to run the rest of the simulations based on the GCI results. It shows that the GCI error is lower than 5% and the GCI ratio is close to 1, which means that results from the simulations will reach within the asymptotic range [171] as well as considering the accuracy and computational cost trade-off.

Finally, Figure A-5 shows results of the grid convergence analysis with various Young's modulus study for Young's Modulus. Based on the Young's Modulus, the maximum deflection, which is a distinctive variable, is shown in streamwise. The graph represents how the results are likely to be concluded in the asymptotic way to the final estimated value when minimum mesh size tends to 0 and all of them are within the expected range meaning that the mesh size is irrelevant of

are further unpredictability. Moreover, the grid sensitivity is shown to be independent of Young's Modulus.

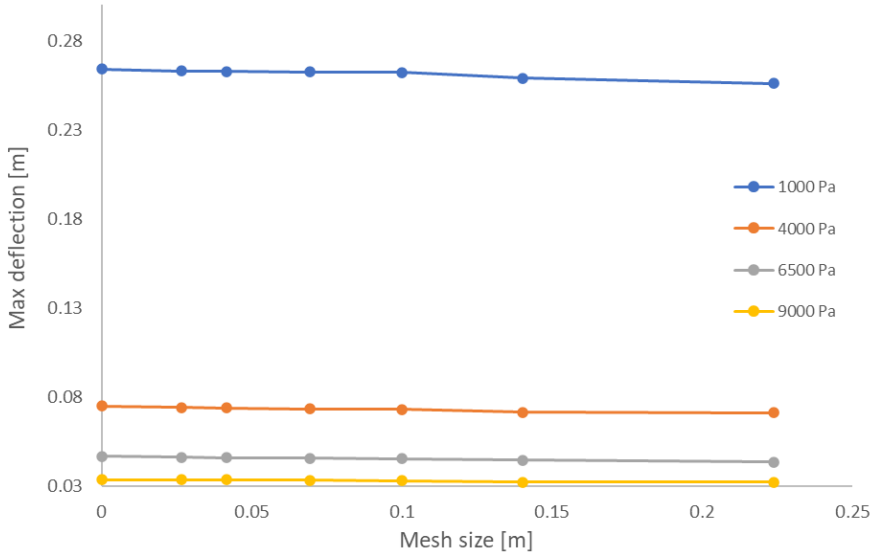

Figure A-5 Grid sensitivity study results for various Young's Modulus

The influence of various Young's Moduli on the greatest horizontal deflection is examined in this section. On the basis of the grid sensitivity study, the medium mesh is chosen to be used. Figure A-6 shows the result of deflection analysis for the Young's Modulus range from 500 Pa to 10,000 Pa. The divergence of the numerical result for 500 Pa is caused by an over-deformed mesh, as can be observed. Therefore, importantly when the elasticity modulus is less than a specific value, the simulation becomes very unstable and false results may by produced owing to substantial mesh deformation. The deflection of the beam over the whole range of Young's Modulus is presented in Figure A-7. Due to the heavily distorted mesh, the result for E=500 Pa is anticipated with the incorrect

deflection value. The findings show that the deflection reduces as the elasticity modulus increases, as predicted by the analytical solution.

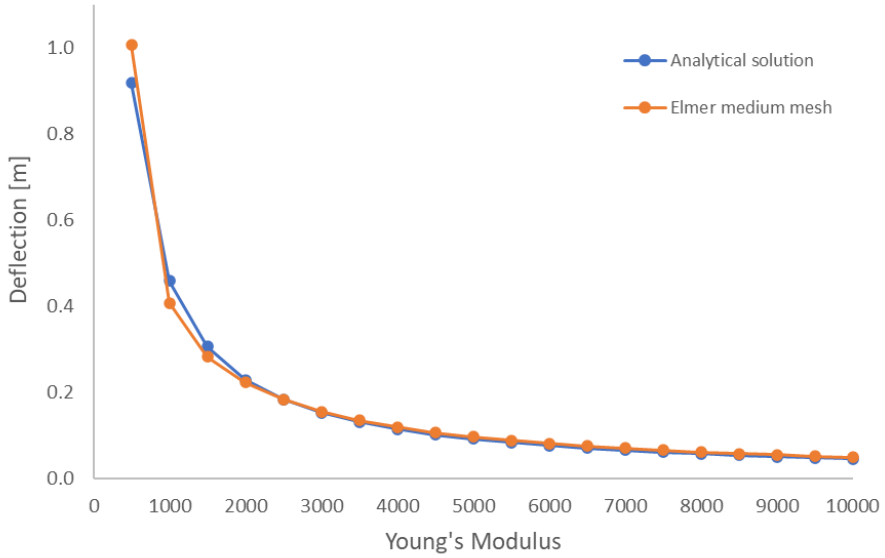

FigureA-6 The result of deflection analysis for the Young's Modulus

(a) (b)

Figure A-7 Beam deflection over various Young's Modulus (a) 500 Pa to 5000 Pa (b) 5500 Pa to 10000 Pa

In this section, the same problem is dealt with using a commercial software, Ansys Mechanical and Ansys Fluent. The two different packages within the Ansys are performed as being combined with the coupling function, System coupling, so that the structure and fluid solutions are calculated within the same iteration, referring to as the Fluid-Structure Interaction (FSI).

First, time step sensitivity is considered as the accuracy of the results would be varied depending on setting up the appropriate time step in transient simulation. Figure A-8 shows how much the beam is deflected with three different time steps (0.1s, 0.2s, 0.5s) for the total simulation of 500s. The mesh sizes of fluid and structure domain are identical for all three cases. It is obviously noticed that the time step would not be one of the factors to have an impact on the solution as the difference is insignificant. Therefore, for the further simulations, time step 0.5s is used considering efficient computation running time. In the similar way, Figure A-9 presents that there is less discrepancy of the results regarding the pressure and velocity for three different time steps.

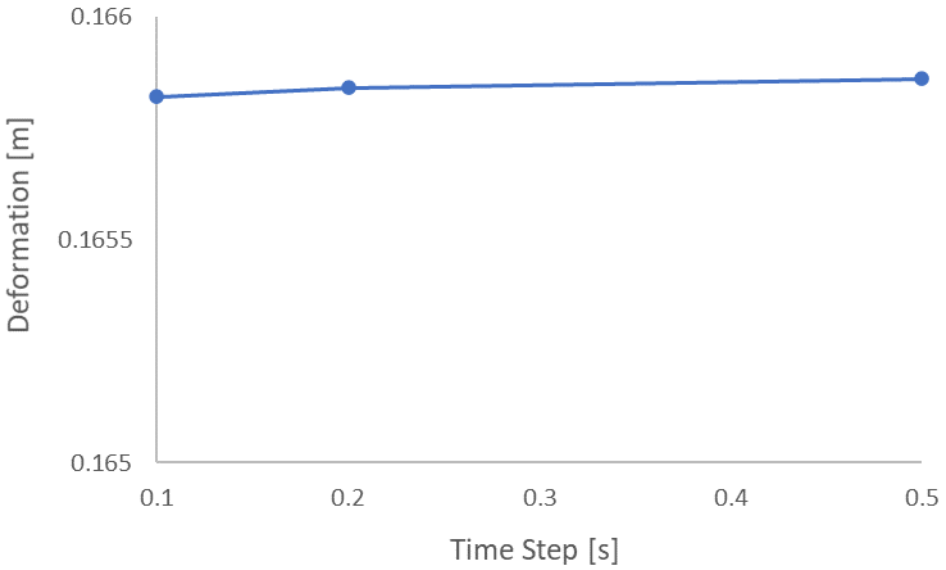

Figure A-8 Deflection of the beam with different time steps

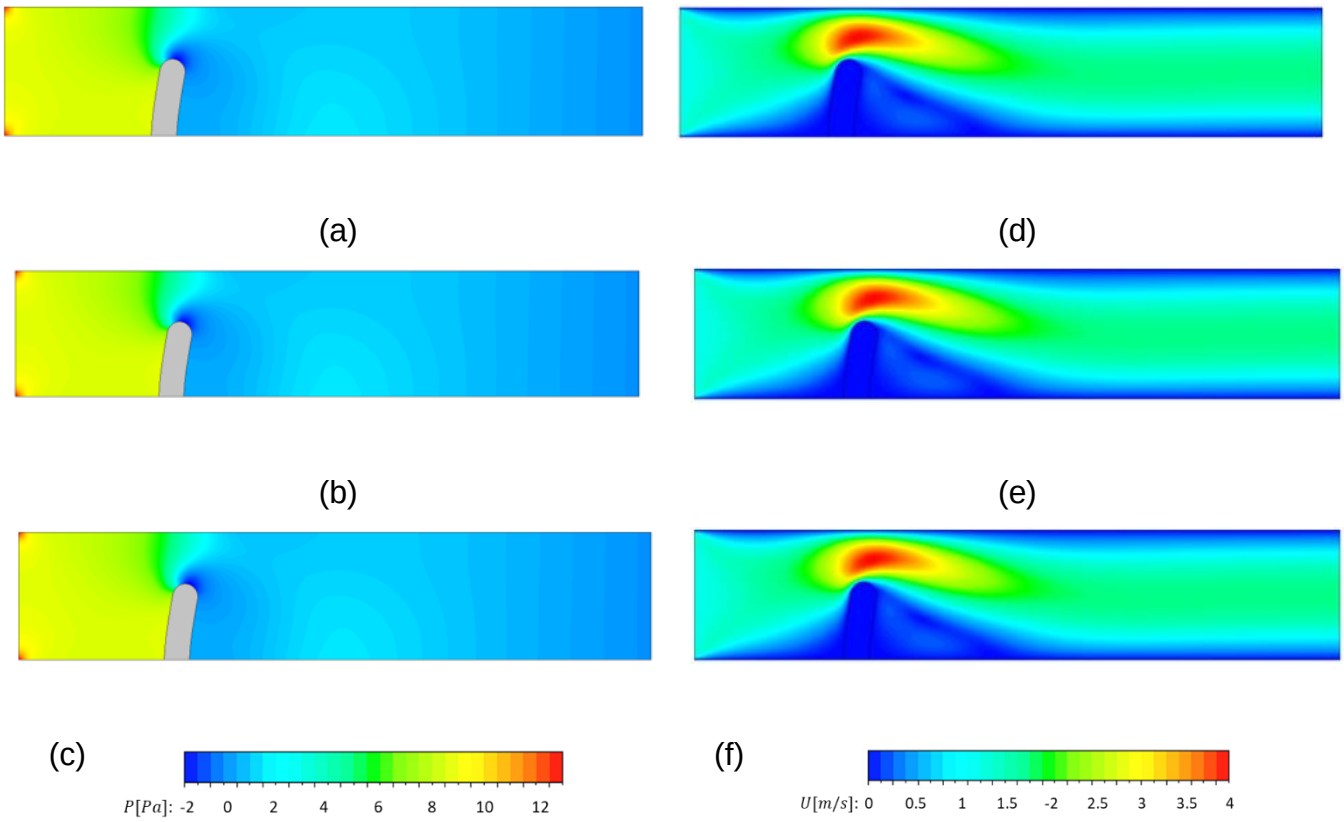

Figure A-9 Time sensitivity results (a) Pressure, 0.1s (b) Pressure, 0.2s (c) Pressure, 0.5s (d) Velocity, 0.1s (e) Velocity, 0.2s (f) Velocity, 0.5s

The grid should be independent of the findings in order to assess the trustworthiness of the calculation. Table A-5 shows the grid details of fluid domain. Fluid-Structure Interaction manages to solve the fluid and structure modelling respectively, so it is important to investigate the impact of mesh size on an individual basis. Note that the Young's Modulus (E = 3000 Pa) and time step (0.5s) are the same. Figure A-10 presents the resultant contours of pressure and velocity of all three meshes. It can be shown that the velocity is characterised through the channel regardless of the grid resolution. However, regarding the pressure feature around the beam, the pressure contour with the finer mesh shows more asymptotic range of solution. Moreover, it can be seen that there is minor increase in the deflection with the finest mesh compared with between coarse and medium meshes. Therefore, in consideration of the computational time, medium mesh is used for the fluid domain in this study.

Table A-5 Variation of grid details and deflection result of fluid domain

	Fluid		
	Node	Element	Deflection [m]
Coarse	1230	543	0.15694
Medium	16330	7903	0.16586
Fine	44886	22011	0.16590

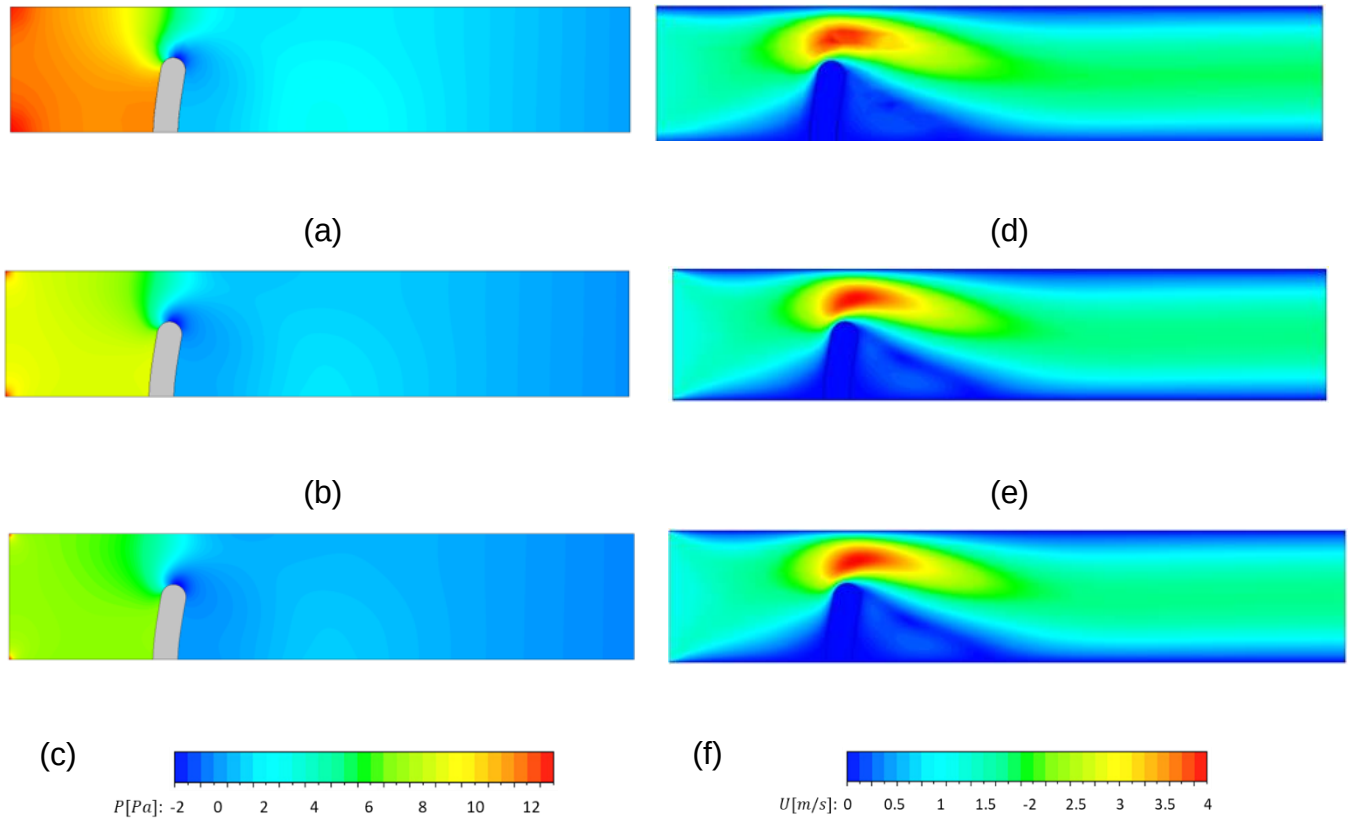

Figure A-10 Mesh sensitivity results of fluid domain (a) Pressure, coarse (b) Pressure, medium (c) Pressure, fine (d) Velocity, coarse (e) Velocity, medium (f) Velocity, fine

In the similar manner, the mesh quality of the structure domain is assessed investigation three different meshes shown in Table A-6. Unlike the fluid domain, the deflection of the beam is completely identical in all three cases, which means that if the structure domain has a certain level of grid resolution the result will be independent from it. At the same time, in terms of overall FSI simulation, the fluid domain has more influence on the consequence of the simulation. Figure A-11 shows the contours of pressure and velocity for three different meshes and it can be presented that they result in the same pattern of pressure and velocity characteristics.

Table A-6 Variation of grid details and deflection result of structure domain

	Structure		
	Node	Element	Deflection [m]
Coarse	4920	984	0.16585
Medium	10484	2210	0.16585
Fine	44043	9928	0.16585

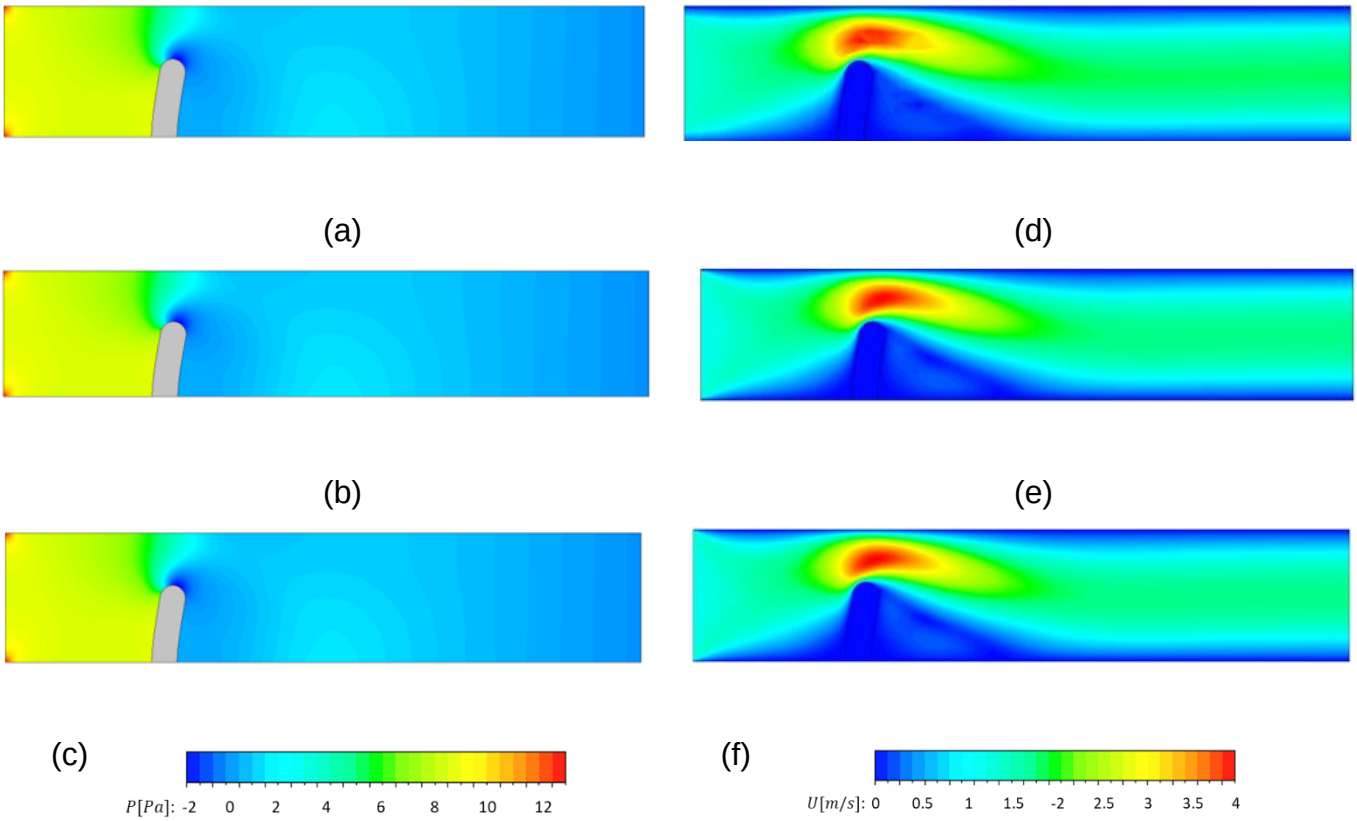

Figure A-11 Mesh sensitivity results of structure domain (a) Pressure, coarse (b) Pressure, medium (c) Pressure, fine (d) Velocity, coarse (e) Velocity, medium (f) Velocity, fine

A.2.2 Validation

In this chapter, the comparison of the results using Elmer and Ansys is shown. The findings are also compared to the analytical solution to determine the computational tools' correctness.

To cross-reference the data and corroborate the results, the pressure contours generated from the Elmer and Ansys simulations are compared, shown in Figure A-12. It is highlighted that the conditions such as boundary conditions and Young’s Modulus (E=3000 Pa) are identically applied. Despite the varied dimensional degrees used, they appear to have a good agreement in terms of pressure distribution. The pressure decrease happens above the beam in both situations, generating a region of suction behind the back. In addition, it can be observed that there is a huge pressure drop caused by the beam in both cases, which could result in a change of the flow characteristics. The pressure upstream on the left side of the beam remains constant as the rise in static pressure generated by the flow's interaction with the beam compensates for the pressure decrease caused by the wall's viscosity.

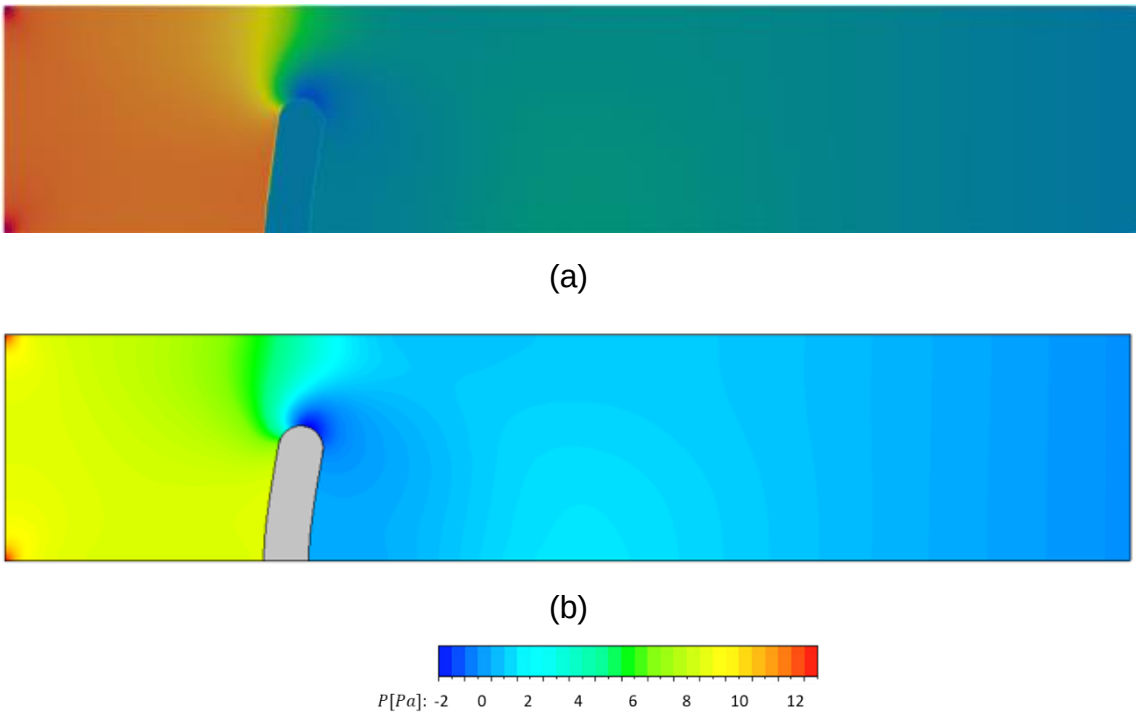

Figure A-12 Contours of pressure around the beam with Young's Modulus 3000 Pa (a) Elmer (b) Ansys

Regarding the velocity results, Figure A-13 illustrates the velocity contours and flow streamline around the flexible beam. As seen in Figure A-12, both cases make a good agreement in terms of velocity features. Due to the contraction of the channel above the beam, the velocity increases. However, it is interesting to notice that there is significant recirculation region formed at the back of the beam which results from the low pressure caused by the beam blocking the flow. The beam in the channel flow is treated as a bluff body, which leads to flow separation and turbulent region. During the simulation, it is investigated that the beam is bounced back after the initial deflection, which could be attributed to force exerted by the recirculation region.

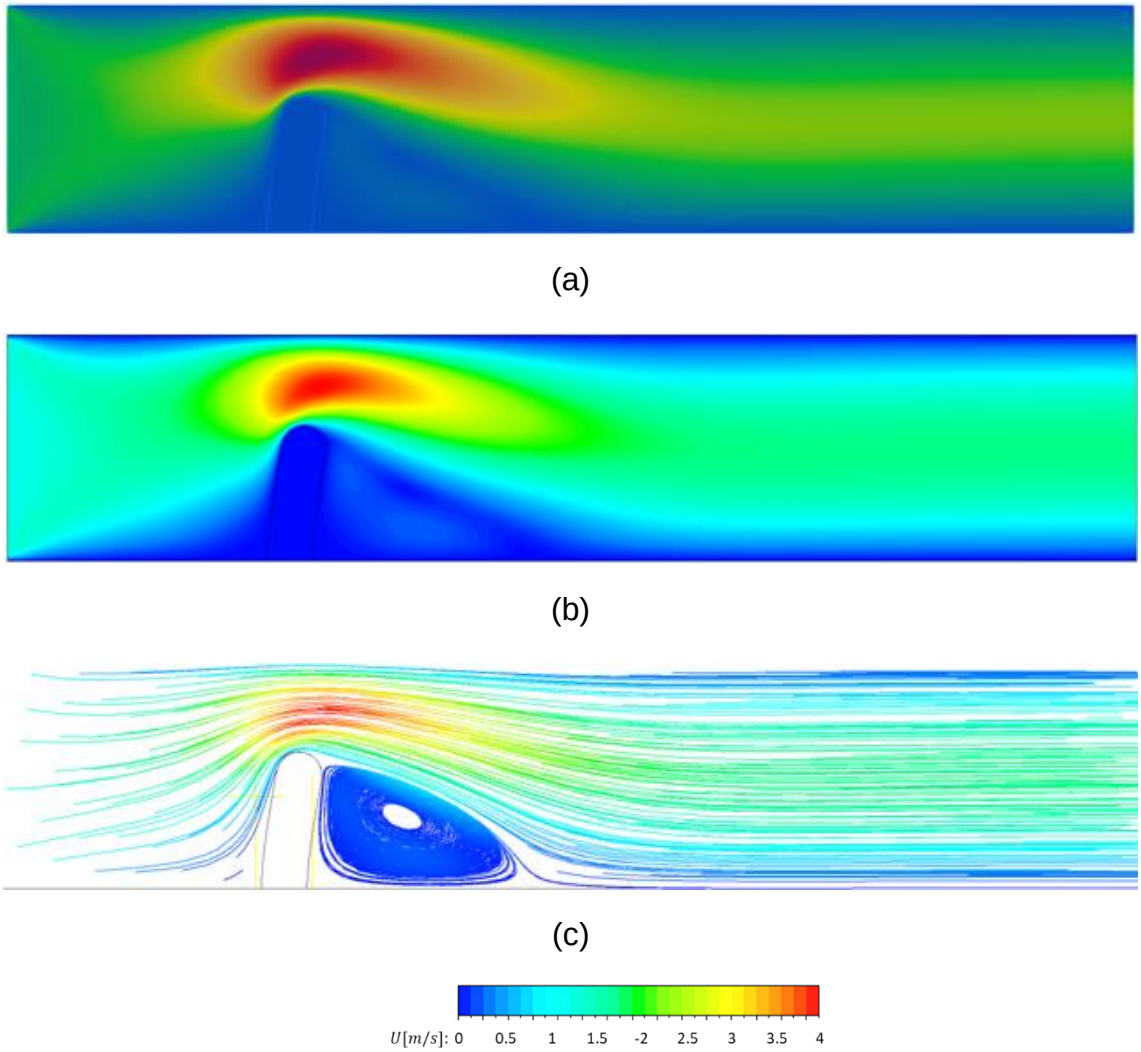

Figure A-13 Contours of Velocity around the beam with Young's Modulus 3000 Pa (a) Elmer (b) Ansys (c) Streamline from Ansys

According to the chapter A.1, it is impossible to achieve an exact calculation in an analytical way. Therefore, as explained above, by exploiting the beam theory equations and the pressure drop from the Ansys simulation, Table A-7 represents the analytical solution as well as the results from the Elmer and Ansys. Both cases have a good level of solutions and the errors compared to the analytical solution are 1.63% and 8.33% respectively. The reason why the error for the Ansys is higher is that the Ansys case deals with the three-

dimensional model which has more detailed grids so that it could lead to be in a larger range of errors including discretisation error or residual error. Nevertheless, the Ansys solution is still within an acceptable range.

Table A-7 Beam deflection results

	Deflection [m]	Error [%]
Analytical Solution	0.1531	-
Elmer	0.1556	1.63
Ansys	0.1659	8.33

A.3 Conclusion

The Fluid-Structure Interaction (FSI) problem of a flexible beam within a 2D channel flow is analysed using two different solvers, Elmer and Ansys. It is proved that the engineering solution related to FSI problem is proved to be valid and accurate by cross referencing the results in a situation where validation data is not available. Chapter A-2 demonstrates a good agreement between the Elmer and Ansys results, as well as an acceptable level of errors when compared to the analytical solution. The error could be derived from several reasons; assumption made to calculate the analytical solution and different dimensional models used for Elmer and Ansys. Moreover, by investigating the potential factors which could affect the results, it is shown that the solvers have capability to be assessed being accurate and reliable for computational simulations. The accuracy of the

computational findings is assessed by comparing them to the analytical answer, thus this technique should be used to boost trust in the computational model's prediction capacity.

Appendix B Mechanical properties of CFRP

B.1 Mechanical properties of carbon fibre

Table B-1 Mechanical properties of carbon fibre [144]

		Epoxy Carbon UD 230GPa Prepreg	Epoxy Carbon woven 230GPa Prepreg	Epoxy Carbon UD 395GPa Prepreg	Epoxy Carbon woven 395GPa Prepreg
Orthotorpic Elasticity [Mpa]	Density[kg/m3]	1490	1420	1540	1480
	YM_x	121000	61340	209000	91820
	YM_y	8600	61340	9450	91820
	YM_z	8600	6900	9450	9000
	PR_x	0.27	0.04	0.27	0.05
	PR_y	0.4	0.3	0.4	0.3
	PR_z	0.27	0.3	0.27	0.3
	SM_x	4700	19500	5500	19500
	SM_y	3100	2700	3900	3000
	SM_z	4700	2700	5500	3000
Orthotorpic Stress Limits [Mpa]	Tensile_x	2231	805	1979	829
	Tensile_y	29	805	26	829
	Tensile_z	29	50	26	50
	Compressive_x	-1082	-509	-893	-439
	Compressive_y	-100	-509	-139	-439
	Compressive_z	-100	-170	-139	-140
	Shear_xy	60	125	100	120
	Shear_yz	32	65	50	50
	Shear_xz	60	65	100	50
	Tensile_x	0.0167	0.0126	0.0092	0.0086
	Tensile_y	0.0032	0.0126	0.0031	0.0086

Orthotorpic Strain Limits	Tensile_z	0.0032	0.008	0.0031	0.007
	Compressive_x	-0.0108	-0.0102	-0.0053	-0.0055
	Compressive_y	-0.0192	-0.0102	-0.0172	-0.0055
	Compressive_z	-0.0192	-0.012	-0.0172	-0.012
	Shear_xy	0.012	0.022	0.016	0.022
	Shear_yz	0.011	0.019	0.014	0.018
	Shear_xz	0.012	0.019	0.016	0.018
Tsai-Wu	xy	-1	-1	-1	-1
	yz	-1	-1	-1	-1
	xz	-1	-1	-1	-1

B.2 Mechanical properties of core materials

Table B-2 Mechanical properties of core materials [144]

		Nomex honeycomb	Al honeycomb
Density [kg/m^3]		29	50
Orthotorpic Elasticity [Mpa]	YM_x	0.6	5.2
	YM_y	0.6	5.2
	YM_z	60	517
	PR_x	0.001	0.001
	PR_y	0.001	0.001
	PR_z	0.001	0.001
	Shear Modulus XY	0.2	4
	Shear Modulus YZ	17	496
	Shear Modulus XZ	25	310
Orthotorpic Stress Limits [Mpa]	Tensile_x	0	0
	Tensile_y	0	0
	Tensile_z	0.9	2.07
	Compressive_x	0	0
	Compressive_y	0	0
	Compressive_z	-0.9	-2.07
	Shear_xy	0	0
	Shear_yz	0.35	0.9
	Shear_xz	0.5	1.45